

Optical Label-Free Methodologies for Characterization of Extracellular Vesicles

Meruyert Imanbekova

Biological and Biomedical Engineering Graduate Program

McGill University, Montreal



June 2023

A thesis submitted to McGill University in partial fulfillment of the requirements of the degree of Doctor of Philosophy in Biological and Biomedical Engineering

Table of Contents

Abstract.....	6
Resume.....	8
Acknowledgments.....	10
Contribution to original knowledge.....	11
Contribution of authors.....	13
List of Publications.....	15
First-author publications.....	15
Co-author publications (contributions to other projects).....	15
Conferences.....	15
List of figures and tables.....	17
Chapter I. Introduction.....	18
Transition to chapter II.....	29
Chapter II. Comprehensive literature review.....	31
Recent advances in optical label-free characterization of extracellular vesicles.....	31
2.1 Abstract.....	31
2.2 Introduction.....	32
2.3 Biology and functions of EVs.....	37
2.3.1 Exosomes.....	38
2.3.2 Microvesicles.....	41
2.3.3 Apoptotic bodies.....	42
2.3.4 Exomeres.....	42
2.3.5 MISEV2018 guidelines.....	43
2.4 Particle counting, sizing, and morphology characterization.....	44
2.4.1 Nanoparticle tracking analysis.....	44
2.4.2 Dynamic light scattering.....	49
2.4.3 Atomic force microscopy.....	51
2.4.4 Flow cytometry.....	54
2.4.5 Single particle interferometric reflectance imaging sensor.....	57
2.4.6 Super resolution microscopy.....	59

2.5 Characterization of EVs molecular content	60
2.5.1 Raman spectroscopy	60
2.5.2 Surface enhanced Raman spectroscopy	65
2.5.3 Surface plasmon resonance spectroscopy	70
2.5.4 Infrared spectroscopy	74
2.5.5 Multiphoton microscopy	74
2.6 Applications	75
2.6.1 Neurodegenerative diseases	75
2.6.2 Cancer	80
2.6.3 Data analysis	84
2.7 Conclusions and perspectives	85
Funding source	86
Author contributions	87
Conflict of interest statement	87
References	87
Transition to chapter III	104
Chapter III. Lensless, reflection-based dark-field microscopy (RDFM) on a CMOS chip	106
3.1 Abstract	106
3.2. Introduction	106
3.3 Experimental methods	109
5.3.1 Chemicals	109
3.3.2 Lensless imaging platform	109
3.3.3 Bead-size quantification based on shadow images	112
3.3.4 Characterization via Scanning Electron Microscopy	112
3.3.5 Characterization via Atomic Force Microscopy	113
3.3.6 Preparation of Microorganisms	113
3.4 Results and discussions	113
3.4.1 3D geometrical measurements from shadow imaging	113
3.4.2 Dark-field microscopy on the CMOS sensor	116
3.4.3 Imaging of biological samples on the CMOS sensor	120
3.5 Conclusion	126

3.6 Author contributions	128
3.7 Conflict of interest.....	128
3.8 Acknowledgements	128
References	128
Transition to chapter IV	133
Chapter IV. Complementary Metal-Oxide-Semiconductor - Based Sensing Platform for Trapping, Imaging, and Chemical Characterization of Biological Samples	135
Abstract	135
Introduction	136
Materials and Methods	139
Materials	139
Fabrication of the CMOS-SERS substrates.....	139
Structural characterization of the uncoated CMOS imaging sensors and SERS substrates	139
SERS Measurements	139
SERS hot spot characterization	140
EVs isolation and characterization	140
Simulations	141
Data pre-processing and analysis	141
Results and discussion.....	142
Results	142
Discussion	151
Conclusions	153
Author contributions	154
Acknowledgments.....	154
References	154
Transition to chapter V	160
Chapter V. Identification of amyloid beta in small extracellular vesicles <i>via</i> Raman spectroscopy.	162
5.1 Abstract	162
5.2 Introduction	163
5.3 Materials and methods	165

5.3.1 A β ₁₋₄₂ pure protein preparation	165
5.3.2 Cell culture models	166
5.3.2.1 MC65 AD cell culture model	166
5.3.2.2 Midbrain organoids 3D cell culture	166
5.3.3 Isolation of sEVs from cell culture media	167
5.3.4 sEVs characterization	167
5.4 Results	170
5.4.1 sEVs characterization by NTA and TEM	171
5.4.2 Raman spectroscopy analysis of sEVs isolated from MC65 (TC -/+) cells and midbrain organoids cell culture media	174
5.5 Discussion	183
Conflict of interest	186
Acknowledgments	187
References	187
Chapter VI. Discussion	192
6.1 Morphological and biochemical characterization of micro- and nanoparticles including EVs using developed techniques	195
6.2 Optical label-free technologies for identification of EV-associated disease biomarkers..	199
7. Conclusions and outlook	203
Reference list	206

Abstract

Extracellular vesicles (EVs) are complex membrane-bound particles secreted by cells into the extracellular space. EVs molecular cargo contains proteins, lipids, and nucleic acids derived from the cell of origin. EVs are found to play important roles in normal physiology and pathology and are recognized as a rich source of biomarkers for disease diagnostics, drug delivery vehicles, and therapeutic agents. Therefore, a thorough characterization of the biochemical composition of EVs is a matter of great importance. Recent research efforts have focused on the detection and characterization of EVs, with an emphasis on label-free methodologies that simplify sample preparation and are free of interfering signals. Thus, the main goal of this thesis is to develop novel versatile technologies for the optical label-free characterization of EVs and use an established methodology, Raman spectroscopy, for the detection of an EV-associated disease biomarker.

First, we identified the niche for technological improvements by conducting a comprehensive review. The review showed the existing demand in the research field to conduct a label-free characterization of EVs in low volumes, perform analysis of a single/few EVs, and develop less expensive technologies to complement existing traditional methods. To address this need in the EV research field, we developed technologies to characterize the EV morphology and biochemical composition.

The initial research method, lensless reflection-based dark-field microscopy, enables the morphological characterization of particles using two modalities: a) shadow-based height measurement and b) oblique illumination dark-field microscopy. The performance of this technology is validated by using it to determine the shape and size of polystyrene spheres and single or clustered microorganisms.

Next, we developed a novel approach for trapping, imaging, and biochemical characterization of the EVs. For this, a complementary metal oxide semiconductor (CMOS) imaging sensor was converted to a Surface Enhanced Raman spectroscopy (SERS) substrate by coating its surface with a thin layer of silver. This creates areas of plasmonic enhancement localized in the crevices between adjacent microlenses. The small size of these wells enables size-based trapping of EVs in plasmonic hot spots followed by their spectroscopic analysis. Using this approach, we determined the biochemical content of small particles, including polystyrene nanospheres and

small EVs.

Finally, we applied Raman spectroscopy to detect an amyloid-beta ($A\beta$) molecular fingerprint in the biochemical content of EVs. Here, we used small EVs isolated from an Alzheimer's disease (AD) cell culture model along with control EVs. Raman spectroscopy characterization detected clear differences in the AD EVs spectra compared to the control EVs. The Amide I region and "high-wave-number region" are the regions of the EV Raman spectra that reflected the main differences. These regions describe the protein content of EVs, and the additional contribution from lipids indicated in the "high wavenumber region". Subsequent analysis of the Raman spectra using Principal Component Analysis (PCA) differentiated EVs associated with $A\beta$ from the control group EVs. Peak analysis shone a light on the secondary structure of EV-associated $A\beta$ and the lipid content of EVs. Importantly, we confirmed the presence of $A\beta$ in EVs containing pellet using mass spectrometry analysis. While these results are promising for the EV-based liquid biopsy AD diagnosis, they remain to be validated using clinical samples.

Overall, the findings of the thesis broaden the available toolbox for the study of EVs by adding new optical label-free techniques that allow the noninvasive analysis of low volumes of EVs and validate the use of Raman spectroscopy for the detection of biomarkers associated with EVs. The rapid technological advancement in optical detection instruments and the employment of advanced data processing methods suggest a leading role of optical label-free techniques in the perspective of EV characterization in preclinical and clinical studies.

Resume

Les vésicules extracellulaires (VE) sont des particules complexes liées à la membrane sécrétée par les cellules dans l'espace extracellulaire. La cargaison moléculaire des VE contient des protéines, des lipides et des acides nucléiques dérivés de la cellule d'origine. Les VE jouent un rôle important dans la physiologie et la pathologie normales et sont reconnus comme une riche source de biomarqueurs pour le diagnostic des maladies, les véhicules d'administration de médicaments et les agents thérapeutiques. Par conséquent, une caractérisation approfondie de la composition biochimique des VE est d'une grande importance. Les efforts de recherche récents se sont concentrés sur la détection et la caractérisation des VE, en mettant l'accent sur les méthodologies sans étiquette qui simplifient la préparation des échantillons et sont exemptes de signaux interférents. Ainsi, l'objectif principal de cette thèse est de développer de nouvelles technologies polyvalentes pour la caractérisation optique sans étiquette des VE et de valider l'utilisation d'une méthodologie établie, la spectroscopie Raman, pour la détection d'un biomarqueur de maladie associé aux VE.

Tout d'abord, nous avons identifié le créneau des améliorations technologiques en procédant à un examen complet. L'examen a montré la demande existante dans le domaine de la recherche pour effectuer une caractérisation sans étiquette des VE en faibles volumes, effectuer l'analyse d'un seul/quelques EV et développer des technologies moins coûteuses pour compléter les méthodes traditionnelles existantes. Pour répondre à ce besoin dans le domaine de la recherche sur les VE, nous avons développé des technologies pour caractériser la morphologie et la composition biochimique des VE.

La méthode de recherche initiale, la microscopie à fond noir basée sur la réflexion sans lentille, permet la caractérisation morphologique des particules en utilisant deux modalités: a) la mesure de la hauteur basée sur l'ombre et b) la microscopie à fond noir à illumination oblique. La performance de cette technologie est validée en l'utilisant pour déterminer la forme et la taille des sphères de polystyrène et des micro-organismes simples ou groupés.

Ensuite, nous avons développé une nouvelle approche pour le piégeage, l'imagerie et la caractérisation biochimique des VE. Pour cela, un capteur d'imagerie semi-conducteur à oxyde métallique complémentaire (CMOS) a été converti en un substrat SERS en revêtant sa surface d'une fine couche d'argent. Cela crée des zones de renforcement plasmonique localisées dans les crevasses entre les microlentilles adjacentes. La petite taille de ces puits permet le piégeage en

fonction de la taille des VE dans les points chauds plasmoniques suivi de leur analyse spectroscopique. En utilisant cette approche, nous avons déterminé le contenu biochimique des petites particules, y compris les nanosphères de polystyrène et les petits VE.

Enfin, nous avons appliqué la spectroscopie Raman pour détecter une empreinte moléculaire bêta-amyloïde ($A\beta$) dans le contenu biochimique des VE. Ici, nous avons utilisé de petits VE isolés à partir d'un modèle de culture cellulaire de la maladie d'Alzheimer (MA) avec des VE témoins. La caractérisation par spectroscopie Raman a détecté des différences nettes dans les spectres des VE AD par rapport aux VE témoins. La région Amide I et la «région à nombre d'ondes élevé» sont les régions des spectres Raman des VE qui reflétaient les principales différences. Ces régions décrivent la teneur en protéines des VE et la contribution supplémentaire des lipides indiquée dans la «région à nombre d'onde élevé». Une analyse ultérieure des spectres Raman à l'aide de VE différenciés par PCA associés à $A\beta$ à partir des VE du groupe témoin. L'analyse des pics a mis en lumière la structure secondaire de l' $A\beta$ associé aux VE et la teneur en lipides des VE. Fait important, nous avons confirmé la présence d' $A\beta$ dans les VE contenant des granulés à l'aide d'une analyse par spectrométrie de masse. Bien que ces résultats soient prometteurs pour le diagnostic de la DA par biopsie liquide basée sur l'VE, ils restent à valider à l'aide d'échantillons cliniques.

Dans l'ensemble, les résultats de la thèse élargissent la boîte à outils disponible pour l'étude des VE en ajoutant de nouvelles techniques optiques sans étiquette qui permettent l'analyse non invasive de faibles volumes de VE et valident l'utilisation de la spectroscopie Raman pour la détection de biomarqueurs associés aux VE. Les progrès technologiques rapides dans les instruments de détection optique et l'utilisation de méthodes avancées de traitement des données suggèrent un rôle de premier plan des techniques optiques sans étiquette dans la perspective de la caractérisation des VE dans les études précliniques et cliniques.

Acknowledgments

First and foremost, I would like to express my sincere gratitude to my esteemed supervisor, **Prof. Sebastian Wachsmann-Hogiu** for granting me this unique opportunity to study at McGill University and work under his supervision, for his invaluable advice, continuous support, and patience during my PhD study. His immense knowledge and plentiful experience have encouraged me in all the time of my academic research and daily life.

I would also like to thank **Dr. Ayyappasamy Sudalaiyadum Perumal, Dr. Sara Kheireddine, Dr. Tatu Rojalin, Dr. Sorina Suarasan, and Dr. Juanjuan Liu** for their insightful comments, suggestions, and contributions. I also would like to extend my gratitude to **Dr. Maria LaCalle, Ms. Laura Montermini, Dr. Kelly Sears, and Ms. Jeannie Mui** for their technical support of my study. I am also thankful to **Dr. Diane Dechief** and **McGill Writing Center tutors** for their editorial help. I am deeply grateful to members of my **PhD committee Dr. Christine Tardif, Dr. Amine Kamen, and Dr. Satya Prakash**. It is their kind support and guidance that helped keep me on a good track. I am thankful to the Bolashak International scholarship, the FRQNT award, and the McGill Engineering graduate excellence award for financial support during my PhD studies.

I would like to thank my friends and lab mates for the cherished time spent together in the lab and social settings.

Finally, **I would like to dedicate this thesis to my family**, for their tremendous support and endless love: my parents, Mom and late Papa, and my little sister who always believed in me; my dear beloved husband and my darling children, who bring joy, infinite love and meaning to every single day of my life.

Contribution to original knowledge

During my PhD studies, my focus was on the development of novel optical label-free methodologies to characterize EVs that will help to address some of the current challenges in the field and to employ them for the detection of EV-associated biomarkers of AD. Specifically, I performed a comprehensive literature review of optical label-free methodologies currently applied for EV characterization with emphasis on the specifics of the working principle of each technology and how they have been used to analyse EVs. In addition, I fabricated multifunctional CMOS imaging sensor-based techniques for EV trapping and characterization. Moreover, the first Raman spectroscopic fingerprint of A β associated with EV molecular cargo is presented and discussed. These results are reflected in the four published first-author articles. In addition, I have also contributed to the development of superhydrophobic SERS substrates for EV concentration and characterization. The details of my contribution to this study will be described in the following section.

The details of each work in my first-author publications are presented below.

In the first publication¹, a comprehensive review of optical label-free methodologies for EV characterization is presented. The review summarizes all currently applied label-free optical methods, describes their basic working mechanisms, and discusses their advantages and limitations for the EV research field. Moreover, the study presents recent advances in the application of EVs as biomarkers of neurodegenerative diseases and cancer. Finally, this review offers a perspective to research directions in EV heterogeneity characterization and the accuracy of EVs as biomarkers of pathology.

In the second publication², a novel lensless reflection-based dark-field microscopy (RDFM) technique has been developed. It consists of a CMOS imaging sensor and a custom-built multi-angle imaging platform. The RDFM introduces a new imaging modality to the field of lensless microscopy – direct-on-chip dark-field microscopy. The modality is used to perform dark-field microscopy of biological and non-biological samples over a large field-of-view. Another novel modality is a measurement of the height of micrometer-sized objects such as polystyrene microspheres and microorganisms placed directly on the CMOS sensor. From a practical viewpoint, this platform provides a useful tool for label-free optical characterization of 3D morphological features of cells and potentially large EVs or small EVs clusters.

*The third published article*³ introduces a novel CMOS-based sensing platform for EV trapping, label-free imaging, and chemical characterization (CMOS TrICC). The combination of SERS with lensfree on-chip microscopy enables both high spatial resolution over the wide field-of-view imaging and chemical content characterization. This inexpensive and easy-to-build platform generates even distribution of hot spots with large SERS active area resulting in consistent SERS intensity enhancement. The platform is used to characterize the biochemical content of EV and, due to the distribution of the field enhancement, probes both EV membrane and intraluminal cargo. Finally, the imaging capability of the CMOS imaging sensor is maintained which enables direct on-chip lensless imaging with spatial resolution limited by the pixel size and wide field-of-view. CMOS TrICC is used to acquire optical images of particles placed directly on CMOS imaging sensor. This opens new directions for integrated (bio)sensing devices.

*The fourth article*⁴ presents the first Raman spectroscopic fingerprint of the A β present in the molecular cargo of small EVs. The study confirms the presence of A β protein in sEV molecular cargo and that it can be detected *via* Raman spectroscopy, paving the way for other studies on this topic. Moreover, this study indicates that A β associated with secreted sEVs has an α -helical secondary structure and the size of a monomer or small oligomer, which has not been shown previously. Furthermore, analysis of the lipid content of sEVs shows altered fatty acid chain lengths in sEVs that carry A β which may affect the fluidity of the EV membrane. Future studies using clinical samples of AD patients will be necessary to demonstrate the potential of sEVs for early AD diagnosis.

Contribution of authors

- **Chapter II**

In this chapter, a review of optical label-free methodologies is presented. Specifically, fundamental working principles and applications in the EV research field are introduced. Moreover, applications for the characterization of EVs related to neurodegenerative diseases and cancer are highlighted, and a thorough discussion of the current status of the field and future considerations are outlined.

The contribution of the authors is listed as follows:

MI and SWH conceived the idea and defined the structure and content of the manuscript. MI wrote the manuscript. SS, YL, and SJ contributed to the parts of the manuscript. SWH supervised the project. All authors reviewed and approved the manuscript in its current form.

- **Chapter III**

In this chapter lens-free reflection-based dark-field microscopy technique is presented. The technique is used for dark-field microscopy and shadow-based measurements of unstained micrometer-sized analytes, polystyrene microspheres, and microorganisms, placed directly on CMOS imaging sensor surface.

The contributions from the authors are as below:

ASP and SWH conceived the idea. MI, ASP, and SWH designed experiments. MI and ASP conducted the experiments and analysed the results. MI wrote the main text of the manuscript with input from all co-authors. SWH supervised the project. All authors reviewed and approved the manuscript in its current form.

- **Chapter IV**

This chapter introduces a CMOS imaging sensor-based platform for trapping, imaging, and chemical characterization of EVs. We demonstrated the use of this platform for parallel trapping of 100 nm nanospheres and EVs in the hot spots created in the gaps between the microlenses, and SERS characterization of these particles. The imaging capability of the CMOS imaging sensor is maintained and provides the opportunity for direct on-chip lensless imaging with spatial

resolution limited by pixel size. This unique feature opens up new directions for integrated (bio)sensing devices.

The contributions from the authors are as follows:

SWH conceived the idea. MI and SWH designed the experiments. MI and JL performed the substrate fabrication and hot spots localization characterization. MK and AMS performed the substrate morphology characterization and EF calculation experiments. HC conducted simulations. MI conducted experiments for the application of the platform for nanospheres and EV characterization. MI wrote the main body of the manuscript with input from all the co-authors. SWH supervised the project. All authors reviewed and approved the manuscript in its current form.

- **Chapter V**

In this chapter, Raman spectroscopy has been employed to identify A β that is associated with sEVs. We isolated sEVs from AD cell-culture model and thoroughly characterized their morphology, concentration, surface markers, and biochemical content. The findings of this study provide evidence supporting the use of Raman spectroscopy for the identification and characterization of sEVs associated with potential biomarkers of neurological disorders such as toxic proteins.

The contribution of the authors is listed as follows:

MI and SWH conceived the idea and experimental design of the project. SH, MM, PL, MN, NM, TD, and JV provide cell culture media for EV isolation. MI and TR performed EV isolation. MI, TR, RM, and RC conducted EV characterization. MI, SS, and SWH performed an analysis of the data. MI wrote the main text of the manuscript with contributions from all the co-authors. SWH supervised the project. All authors reviewed and approved the manuscript in its current form.

List of Publications

First-author publications

1. **Imanbekova, M.**; Perumal, A. S.; Kheireddine, S.; Nicolau, D. V.; Wachsmann-Hogiu, S., Lensless, reflection-based dark-field microscopy (RDFM) on a CMOS chip. *Biomed Opt Express* **2020**, *11* (9), 4942-4959. (IF: 3.562, citations: 3)
2. **Imanbekova M.**, Suarasan S., Rojalin T., Mizenko R.R., Hilt S., Mathur M., Lepine P., Nicouleau M., Mohamed N.V., Durcan T. M., Carney R.P., Voss J.C, and Wachsmann-Hogiu S. "Identification of amyloid beta in small extracellular vesicles *via* Raman spectroscopy", *Nanoscale Advances*, **2021**, *3*, 4119-4132. (IF: 5.598, citations: 9)
3. **Imanbekova, Meruyert**, Suarasan, Sorina, Lu, Yao, Jurchuk, Sarah and Wachsmann-Hogiu, Sebastian. "Recent advances in optical label-free characterization of extracellular vesicles" *Nanophotonics*, vol. 11, no. 12, 2022, pp. 2827-2863. (IF: 7.923, citations: 6)
4. **Imanbekova M.**, Saridag A.M., Kahraman M., Liu J., Caglayan H., and Wachsmann-Hogiu, S. Complementary-metal-semiconductor-based sensing platform for trapping, imaging, and chemical characterization of biological samples. *ACS Applied optical materials*, **2022**.

Co-author publications (contributions to other projects)

1. Suarasan, S.; Liu, J.; **Imanbekova, M.**; Rojalin, T.; Hilt, S.; Voss, J. C.; Wachsmann-Hogiu, S., Superhydrophobic bowl-like SERS substrates patterned from CMOS sensors for extracellular vesicle characterization. *Journal of Materials Chemistry B* **2020**. (IF: 5.344, citations: 14)

Conferences

1. **Imanbekova. M.**, P. Sudalaiyadum A., Kheireddine S., and Wachsmann-Hogiu S. "Direct on-sensor imaging for shadow-based microparticle characterization and bioluminescence imaging" SPIE, 2020

(Presented by SWH due to inability to travel)

Date: February 2, 2020

2. **Meruyert Imanbekova**, Tatu Rojalin, Silvia Hilt, Randy P. Carney, John C. Voss, Ayse Mine Saridag, Mehmet Kahraman, Humeyra Caglayan, and Sebastian Wachsmann-Hogiu. “Raman and SERS spectroscopy for EV characterization: detection of amyloid beta and bulk chemical analysis” SPIE, 2023

(Presented by SWH due to inability to travel)

Date: January 30, 2023

Research exchange

During my short-term research exchange at the University of California Davis in the lab of Prof. James Chan in August 2019, where I learnt about various optical techniques such as line scan Raman imaging and multifocal Raman imaging. This research exchange expanded my knowledge about Raman spectroscopy and its application for analysis of biological samples. This research exchange was funded by a Graduate Mobility Award (GMA).

List of figures and tables (non-manuscript sections)

List of tables

Table 1. 1 Analysis of EV-associated A β as a biomarker of AD

Chapter I. Introduction

The EV research field is a rapidly evolving field that expanded exponentially over the past two decades. This growing interest follows the recognition of EVs as mediators of cell-cell communication⁵. EVs are heterogeneous lipid membrane-bound vesicles shed by cells into the extracellular space⁶⁻⁸. Exosomes, microvesicles, and apoptotic are the three main subtypes categorized based on biogenesis and release pathways, content, function, and size⁹. Exosomes are the EVs that have endosomal biogenesis pathway and the size range from 30-200 nm in diameter^{5, 10}. Microvesicles are formed as a result of the inward budding of the plasma membrane and their size ranges from 100 nm to 1000 nm in diameter. Apoptotic bodies (ABs) are 50 nm to 5 μ m in diameter and are released during apoptosis as a result of caspase-mediated cleavage¹¹. Subsequently, the molecular content of EVs including proteins, lipids, nucleic acids, and other bioactive molecules differ depending on the type of EVs¹². For example, exosomes are enriched in tumor susceptibility gene 101 protein (TSG101), syntenin, ALG-2-interacting protein X (ALIX), and various tetraspanins, while microvesicles are enriched in proteasomes, mitochondria, and endoplasmic reticulum proteins¹³. Fatty acids and glycolipids predominate in the composition of exosomes in comparison to microvesicles which are rich in ceramides and sphingomyelins¹⁴. ABs contain cell degradation products such as organelle fragments, DNA, histones, and cytoplasmic components^{15, 16}. The transfer of a functional cargo by EVs and its influence on biological mechanisms in recipient cells has both been shown previously¹⁷⁻²⁰. Exosomes are studied as potential biomarker carriers for the diagnosis of various diseases including cancer, infectious and neurodegenerative diseases⁸. Other studies suggested the use of exosomes as drug delivery vehicles, vaccines, and therapeutics. Despite their seeming homogeneity, exosomes can provoke a plethora of effects in recipient cells, which can explain their multifunctional nature^{8, 17, 21}. Microvesicles have been suggested to be involved in the promotion of angiogenesis, transfer of oncogenic receptor protein, and metastasis²². Additionally, microvesicles are shown to be involved in the progression of cardiovascular²³ and neurological disorders^{24, 25}. Since the formation of ABs promotes cell debris removal without triggering inflammatory reactions, the alterations in ABs clearance have been found to contribute to autoimmune disorders^{26, 27}. Their role in intercellular communication remains to be explored but it is suggested that they contribute to cell-cell communication by delivering their molecular cargo²⁸⁻³⁰.

The overall impact of EVs in a variety of cellular functions and disease states holds potential for improved diagnostics and therapeutics. Therefore, it is essential to establish characterization methodologies that are able to analyze three EV aspects: morphology, biochemical composition, and functions.

Given the vast heterogeneity of EVs discussed before, there are extensive challenges in their isolation and characterization³¹. No single characterization technique or isolation method can capture the full-size range of EVs³². Current isolation methods entail trade-offs in terms of reproducibility, throughput, and ease of operation³³. The choice of isolation methods often depends on the scientific question to be answered. For example, commercially available polymer-based methods are efficient in recovering nano- and microparticles from a sample. However, these methods tend to precipitate cell debris, non-vesicular proteins, and nucleic acids. Moreover, residues of the polymer may also interfere with EV characteristics.

Differential ultracentrifugation is another widely used EV isolation method³⁴. The method is very reproducible and EV yield is good. Yet, the resulting pellet may contain co-isolation contaminants such as low- and high-density lipoproteins. Also, the process is laborious and lengthy. Therefore, often complementary methods, including density gradient ultracentrifugation and size exclusion chromatography, are used to help achieve higher purity EVs.

Ultrafiltration³⁵ and asymmetric flow field-flow fractioning³⁶ are emerging methods that showed promising results in terms of ease of use and efficiency in isolating EVs from clinical samples. Additionally, an affinity purification technique is proposed. In this method, EV-specific surface markers including transmembrane proteins CD9, CD63, and CD81 are used to selectively capture particles that express them. While the method ensures the purification of vesicles, the resulting yield will not represent the entire vesicle population in the analysed sample.

Following isolation and purification, EVs are characterized in terms of their size, morphology, and content. A large variety of labeling and non-labeling characterization techniques have been developed to address the processing and testing needs of EVs^{37, 38}. The label-based techniques rely on the use of molecular tags or markers that bind to EVs. Label types can include fluorescent dyes and molecules³⁹, radionuclides⁴⁰, and lipophilic tracer dyes⁴¹. Using labels is advantageous in EV visualization and tracking, single molecule detection, and in high-throughput settings such as flow cytometry⁴². Despite these useful functions, label-based

technologies have some fundamental limitations. To begin, using labels may result in potential unwanted interaction of labels with EVs and may affect EV functions and uptake^{41, 43}. The next important point is that using EV surface protein markers for EV recognition would affect the characterization of EV heterogeneity as there is no established single EV marker⁴⁴. Finally, the low specificity of some labels and their aggregation may cause false conclusion⁴³.

Recent advances in label-based technologies are genetically encoded labels^{45, 46}. These labels offer greater specificity compared to lipid dyes and in the case of fluorescent tetraspanins ensure the vesicular origin of the analysed particles, plus they are useful to study EV biogenesis and functions. However, there is a risk of alterations of the EV functions due to overexpression of such proteins. Moreover, the selectivity of this approach limits its application for EV heterogeneity analysis.

On the other hand, label-free techniques offer direct non-invasive analysis of EV morphology and molecular cargo. Elimination of the tags or dyes allows conducting of experiments that require less time and wet-lab complexity compared to labeling techniques. Importantly, a non-invasive approach for characterizing EV molecular cargo, including proteins conformation and lipids structures, is a great advantage for EV functionality studies in both fundamental and applied research.

Among label-free techniques, particular interest is paid to optical methods that utilize light and optical properties for analysis of EVs. Lens-based microscopes are the most broadly used light microscopy systems. However high spatial resolution imaging at enhanced magnification leads to limited FOV and optical aberrations that distort the resulting image. Image stitching is implemented to form mosaics with a large overall FOV of high-resolution images. Yet, such techniques are time consuming and result in artifacts.

Lens-free approaches that typically use CMOS imaging sensors further simplify the hardware of imaging systems. One example is in-line holography, where the sensor detects shadows and diffraction interference patterns generated by the object placed between the image sensor and the illumination source, and the final image is reconstructed using computational algorithms. Whereas the FOV is limited by the sensor area, the spatial resolution can reach sub-pixel proportions using ptychographic imaging, where multiple images of the sample are taken at different illumination angles followed by image reconstruction. Such approaches can serve as

portable and adaptable devices with minimal hardware requirements. Main drawback of such methods is computationally heavy holographic reconstruction that makes the system more complex.

Non-holographic on-chip imaging addresses the above-mentioned limitations. This methodology takes advantage of the conventional hardware design of lens-free imaging without the need to perform complicated image reconstruction. Transmission-based imaging is the main imaging mode performed using direct on-chip lens-free microscopy. New modality such as dark-field microscopy will expand the existing range of methods of direct on-chip lens-free microscopy.

Dark-field microscopy is an optical technique, that allows contrast enhancement of unstained objects due to its very low background. This elegant technology has many advantages including high contrast and high-resolution images of unstained and transparent objects and subsequent simplicity of sample preparation. The oblique illumination used in dark-field microscopy causes the darkening of the background while the object is visible due to the scattering of the oblique light. This particular phenomenon is used to develop dark-field microscopy modality directly on CMOS imaging sensor and described in details in Chapter III. The darkening of the background that leads to contrast reversal is explained through Fresnel equations. The Fresnel equations describe the transmission and the reflection coefficients of light in the interface between different optical media. Light is an electromagnetic wave that has an oscillating electromagnetic field (E-vector). The E-vector posses amplitude components that are parallel to the plane of incidence or perpendicular. The reflection coefficient is the ratio of the amplitude of the reflected light to the incident light (r). The transmission coefficient is a ratio of amplitude of the transmitted light to the incident light (t).

$$r_p = \frac{\tan(\theta_1 - \theta_2)}{\tan(\theta_1 + \theta_2)} \quad (1)$$

$$r_s = \frac{\sin(\theta_1 - \theta_2)}{\sin(\theta_1 + \theta_2)} \quad (2)$$

$$t_p = \frac{2\sin\theta_2 \cos\theta_1}{\sin(\theta_1 + \theta_2) \cos(\theta_1 - \theta_2)} \quad (3)$$

$$t_s = \frac{2\sin\theta_2 \cos\theta_1}{\sin(\theta_1 + \theta_2)} \quad (4),$$

Where r_p and r_s are the reflection coefficients of a parallel and perpendicular amplitude components, respectively; and t_p and t_s are transmission coefficients of a parallel and perpendicular amplitude components, respectively. Θ_1 is a reflection angle and Θ_2 is a transmission angle, and these angles are related by Snell's law.

$$n_1 n_1 \sin \Theta_1 = n_2 \sin \Theta_2$$

The intensity of the reflected light at the interface between air (refractive index of 1) and the surface of the CMOS imaging sensor (plastic, with a refractive index approximately 1.5) obeys the Fresnel equations such that at large angles of incidence, almost total reflection at this interface is expected.

Overall label-free optical technologies have been widely applied for characterization of EV morphology and molecular content. The morphological characterization including determination of the EV size, concentration and shape is performed using Nanoparticle Tracking Analysis (NTA), Atomic Force Microscopy (AFM), Dynamic Light Scattering (DLS). The molecular content of EVs is characterized using Fourier Transformed Infrared spectroscopy (FTIR), Single Particle Interferometric Reflectance Imaging Sensor (SP-IRIS), SERS and Raman spectroscopy. In particular, this thesis highlights the use of Raman spectroscopy for EV characterization.

Raman spectroscopy is a label-free spectroscopy technique based on inelastic scattering of laser light that interacts with molecular vibrations. The scattered light consists of Rayleigh scattering and Raman scattering. Rayleigh scattering has the same frequency as the incident light. Raman scattering, on the other hand, reflects the vibrational frequencies of the molecules. Raman spectroscopy measures the vibrational frequency as a shift from incident frequency. When the molecule moves from the ground state to a more excited vibrational state it requires energy from the absorbed from the incident light. Hence, it causes a decrease in the energy for the scattered light, which further leads to a decrease in frequency. This downshift in frequency for scattering is called Stokes scattering. On the other hand, when the molecule moves to a less vibrational state, it leads to an increase in energy and frequency for the scattering. And this upshift in frequency is called anti-Stokes scattering. Raman scattering is used in Raman spectroscopy for the characterization of the sample chemical content at molecular level. Raman spectrometer consists of several components including excitation source, edge filter, dispersion element and

CCD detector. Typically, in modern Raman instruments solid state laser with wavelengths of 532 nm, 633 nm, 785 nm, 830 nm and 1064 nm are used to induce Raman scattering. In order to separate Raman scattered light from Rayleigh scattering Raman spectrometers are equipped with filters. The laser energy is collected by fiber optics cables. Holographic grating is used to disperse the scattered light that is further captured by CCD detector. Currently there are more than 25 different types of Raman spectroscopy techniques including SERS, coherent anti-stokes Raman scattering, tip-enhanced Raman scattering, and Raman tweezers. Among which SERS and Raman tweezers are mostly applied for EV characterization. Raman tweezers is a technique that combines Raman spectroscopy and optical tweezers. The technology is used to trap EVs in a laser beam and obtain their chemical components. An optical trapping is a result of a tightly focused laser beam achieved by the use of a lens with high numerical aperture.

The methodologies described above have certain shortcomings including low signal, low reproducibility, high cost, and laborious data acquisition process.

The technical challenges associated with EV analysis are well-described elsewhere³³. Among which is the necessity to use a large amount of EVs in most bulk methods such as Western blot. Another ongoing challenge is an analysis of EV heterogeneity based on single-EV characterization: the current single-EV characterization techniques are low throughput or lack sensitivity. The overlap in size of EVs with non-EV isolation contaminants introduces additional challenges in analysing both EV morphology and molecular content. Therefore, addressing these challenges is the focus of this thesis.

Another important direction that is explored in this thesis is the application of label-free optical methods for the characterization of disease-associated markers enveloped in EV molecular cargo. As has been described above the molecular content of EVs has attracted great interest from the scientific community as it reflects the state of the releasing cell⁸. In pathological conditions, including cancer and neurodegeneration, EVs are found to contribute to disease progression^{47, 48}. It has been suggested that EVs may be used as potential carriers of disease markers for early diagnosis of neurodegenerative diseases such as AD⁴⁹. AD is the most common form of dementia and has an overwhelming impact on patients' lives and their families. Over 747,000 Canadians are living with AD or another form of dementia, and the number is expected to rise to 937 000 cases by 2031⁵⁰. While the cause of AD is still not clear, A β and hyperphosphorylated

tau are molecules that form amyloid plaques and tau tangles, respectively, accompanied by neuroinflammation, which are characteristics of neuropathology⁵¹. The toxic effect of these misfolded proteins might be explained by the disruption of multiple mechanisms such as the loss of functions of aggregated proteins, mitochondrial dysfunction, synaptic toxicity, endoplasmic reticulum stress, free radicals of reactive oxygen species (ROS); the promotion of depolarization of synaptic membrane; and the formation of neurofibrillary tangles⁵². Moreover, elevated level of A β activates microglia and chronic inflammation that led to the neuronal loss by direct phagocytosis⁵³. Amyloid plaques may contain various forms of A β such as soluble A β , A β oligomer, and A β , that may contribute to a neurodegeneration process at different stages of AD⁵⁴. The current diagnosis of AD is based on the patient's mental decline degree, which is not obvious until severe and permanent brain damage has occurred⁵⁵. The state-of-the-art clinical assessment of A β depositions in the brain are positron emission tomography (PET) imaging and /or by measurements of A β in cerebrospinal fluid (CSF)^{56, 57}. While these methods are proven to be useful to stratify symptomatic AD patients from healthy subjects with high specificity and sensitivity these methods are expensive, invasive, and depend on the skills of the operator. In addition, these methods are used to confirm the diagnosis rather than predict preclinical patients. Moreover, even though amyloid plaque-associated proteins can be detected in the CSF and blood of AD patients, their extremely low concentrations that are less than one-millionth of total CSF proteins and one ten-billionth of total blood proteins, limit their use as biomarkers⁵⁸. Therefore, the discovery of new AD biomarkers in fluids other than CSF (such as blood, urine, and saliva) that can help detect and monitor disease progression is essential for non-invasive diagnosis and the development of new therapies.

EVs possess properties that can make them excellent candidates as AD biomarkers. Their cargo of proteins and nucleic acids is a molecular fingerprint of secreting cells and can reflect intracellular processes. EVs secreted from the cell can have an autocrine function as well as an endocrine effect by transfer to CSF and bloodstream, from which blood is more convenient for repeated sampling to monitor therapeutic responses. EVs from brain cells can be found in circulating blood⁵⁹. Interestingly, exosome markers such as ALIX and Flotillin 1 have been detected in the amyloid plaque area suggesting exosome cargo contribution to plaque formation⁶⁰. However, the movement of EVs from the systemic circulation to the CNS remains unclear. L1 cell adhesion molecule (L1CAM) that is expressed by cells in CNS has been used to

differentiate CNS-derived EVs from other EV populations⁶¹⁻⁷⁴. Yet, it is important to mention that this protein is expressed by other cells in the body and has soluble forms⁷⁵, and found to be upregulated in several cancer types⁷⁶.

Multiple studies indicate the involvement of EVs in the pathogenesis of AD and particular attention has been paid to neurotoxic proteins A β and tau^{48, 77-79}. Some studies have shown that oligomeric A β and tau can be transferred by exosomes and lead to prion-like spreading of misfolded proteins^{60, 80, 81}. C. Lim and co-authors reported that exosome bonded A β protein measured directly from AD patients' blood better reflects neuroimaging results in comparison with total circulating A β . Further, they showed that exosomes are preferentially bound to large prefibrillar A β aggregates. This finding is similar to positron emission tomography (PET) tracers that particularly bind to large A β aggregates and demonstrate the lower binding activity to a small aggregate⁸².

Most of the reported studies identify and characterize EV-associated A β using Western blot, enzyme-linked immunosorbent assay (ELISA), mass spectrometry, and electron microscopy (EM)^{72-74, 83-85} (Table 1).

Table 1. 1 Analysis of EV-associated A β as a biomarker of AD

Type of EVs	Experimental design of the study	Detection method	Outcome	Reference
1. Exosomes	Mouse neuroblastoma N2a that expresses Swedish mutant of APP	Western blot, immunoelectron microscopy	Packaging of A β into MVBs and secretion within exosomes	⁶⁰
2. Exosomes	Human neuroblastoma cell line that expresses APP	Western blot, immunoelectron microscopy, mass spectrometry	APP derivatives (full-length APP, APP-CTFs, AICD) are found in secreted exosomes	⁸⁶
3. Exosomes	Chinese-hamster ovary (CHO)-APP695 cell line	Western blot	APP-CTFs and A β are found in exosomal cargo	⁸⁷
4. Exosomes	APP transgenic mice (Tg2576) and age- and gender-matched wild-type controls, human brain tissue of AD patient and control	Immunoelectron microscopy, Western blot	Higher levels of full length APP, APP CTFs are identified in brain-derived exosomes compared to control exosomes	⁸⁸

	subject			
5. Neuronal EVs	Blood of AD (n=57) and frontotemporal dementia (n=16) patients	ELISA	The level of A β is higher in neuronal EVs compared to case-controls	⁸⁹
6. Neuronal exosomes	Plasma samples of AD (n=10), MCI (n=20) and control (n=10)	ELISA	The level of A β is higher in neuronal EVs compared to case-controls	⁷⁴
7. Neuronal EVs, astrocyte EVs	Plasma samples of MCI (n=12), FTD (n=14), and healthy control (n=20)	ELISA	The level of A β is higher in astrocyte EVs compared to neuronal EVs and healthy control-derived EVs	⁶³
8. Exosomes	Brain tissue of AD patients and healthy individuals	ELISA	Increased level of A β in exosomes derived from AD patients	⁸⁰
9. Neuronal exosomes	Plasma samples of AD (n=101), MCI (n=96), healthy control (n=101)	ELISA	Higher level of A β ₁₋₄₂ in AD neuronal exosomes compared to MCI and control derived exosomes	⁹⁰
10. Neuronal EVs	Plasma samples from AD patients (n=128) and controls (n=222)	ELISA	Increased level of A β	⁹¹
11. Neuronal EVs	Plasma samples Of AD (n=45), MCI (n=45) and control (n=156)	Single-molecule array	Gradual increase in the levels of A β from MCI to AD	⁹²
12. Exosomes	Blood samples of AD (n=36), MCI (n=12), control (n=12)	Luminex	Increased level of A β ₄₂	⁹³

MCI – Mild Cognitive Impairment; APP – Amyloid Precursor Protein; APP-CTFs- Amyloid Precursor Protein C-terminal fragments; AICD – Amyloid Precursor Protein Intracellular Domain.

While these methods allow the detection of certain molecules in EVs, there are a few shortcomings that need to be addressed. For example, EM (Transmission Electron Microscopy (TEM) and cryo-TEM) is one of the well-established methods for single EV analysis. It enables analysis of the size and morphology of EVs. By using immunostaining, it is possible to detect certain molecules of interest including A β . However, the technique is low-throughput and

laborious. Moreover, it requires expensive equipment and a specially operated facility. Mass spectrometry analysis of EVs is an excellent tool for the characterization of EVs' global content and is beneficial in biomarker discovery studies. Yet low reproducibility of the results, in addition to complex sample preparation steps, limits its application. Finally, ELISA is currently a method of choice for the detection of A β due to its accessibility and quantitative measurements, yet the method could be less sensitive to low concentrations of EV-associated A β ⁹⁴. While Raman spectroscopy or SERS has not been used previously to detect A β in EVs, these techniques have been employed to stratify AD patients from healthy controls based on blood plasma and serum, CSF, and saliva analysis⁹⁵⁻¹⁰⁰. The fact that Raman-based techniques offer label-free and sensitive detection, with a small amount of analyte required, makes them a favorable tool in the AD research field.

We *hypothesize* in this thesis that optical label-free methodologies enable characterization of membrane and intraluminal biochemical content of EVs, and identify specific disease-related molecules in EV cargo. To verify this hypothesis this thesis *aims* to:

1. perform a comprehensive literature review of evidence-based state-of-the-art technologies in the field and identify a potential niche for further developments;
2. develop a label-free optical method for imaging and morphological characterization of EVs. To achieve this goal, a CMOS imaging sensor was prepared by removing the original lens and (infrared) IR filter. Then, the surface morphology of the CMOS sensor was thoroughly characterized by SEM and AFM. Furthermore, the multi-angle illumination platform was designed to attain certain angles of illumination. Finally, analytes, such as polystyrene microspheres of various sizes and microorganisms, were detected, and their morphological features were examined;
3. develop a CMOS-based sensing platform for trapping, imaging, and chemical characterization of EVs and other biological samples (CMOS-TrICC). The developed CMOS imaging sensor platform is expanded to a new platform by coating the surface of the CMOS imaging sensor with a thin metallic layer. The surface morphology and metal coating were examined *via* AFM and Energy Dispersive X-ray (EDX) analysis, respectively. The distribution of hot spots was characterized using 4-Aminothiophenol (4-ATP) and Rhodamine 6G (R6G) molecules. Finally, the performance of the CMOS-TRiCC platform was evaluated by using 100 nm polystyrene nanospheres and EVs;

4. characterize molecular cargo of small EVs *via* Raman spectroscopy and identify EV-associated A β . To achieve this goal, first, EVs were isolated from AD model cell line MC65, that under certain conditions overexpress A β . EVs isolated from the Neuro-2a cell line were used as a control in this study. The size distribution and morphology of isolated EVs were examined using NTA and TEM. The expression of EV surface markers including CD9, CD63, and CD81 was determined by ExoView. Finally, Raman spectroscopy was used to characterize the biochemical composition of EVs and identify EV-associated A β . The presence of A β in EV containing pellet was validated by mass spectrometry.

Transition to chapter II

As has been highlighted in Chapter I, EVs have attracted increasing interest in biomedical research and therapy. Their unique properties, along with their role in normal physiology and pathology, make EVs desirable candidates as biomarkers and targets of disease, drug delivery vehicles, and therapeutics. Therefore, the detection of EVs, and the characterization of molecular cargo enveloped in EVs, is important to determine their potential functions. Current methodologies used for EV characterization can use labels or be completely label-free. In most studies, more than one technique is used to characterize EV morphology, biochemical cargo, and functions. While the choice of the most suitable technique for each specific scientific question can differ, analysis of EVs in conditions close to physiological is always desirable. Therefore, label-free optical technologies offer a non-invasive characterization of EVs.

The aims of Chapter II are to 1) systematically review state-of-the-art literature on optical label-free methodologies for EV characterization with evidence from basic research to biomarker investigations using clinical samples, and to 2) determine a niche for further technological developments.

The review includes published studies up to March 2022 that are relevant to the topic of the thesis. First, it describes the biology of EVs, their main subtypes, biogenesis, molecular content, and a brief description of their uptake and functions. Then the review emphasizes the working principles and key characteristics of each currently available optical label-free methodology as well as advantages for addressing specific EV-related questions. The limitations of each technique for EV analysis application are thoroughly discussed. Moreover, through the lens of the latest developments in the aforementioned techniques, this review examines the compelling hypothesis and data-driven rationale for EV-based diagnosis of neurodegenerative diseases and cancer. Finally, the review outlines key questions and existing challenges and provides recommendations on how to address them. Since the review article has been published, a few more studies were issued validating the benefit of label-free optical analysis of EVs and associated biomarkers and supporting further developments of such techniques¹⁰¹⁻¹⁰⁴.

This chapter is based on my recently published first-author article. The contributions of the authors are as follows:

MI and SWH conceived the idea and defined the structure and content of the manuscript; MI wrote the manuscript with a partial contribution of SS, YL, and SJ. SWH supervised the project. All authors reviewed and approved the manuscript in its current form.

Chapter II. Comprehensive literature review

Recent advances in optical label-free characterization of extracellular vesicles

Meruyert Imanbekova, Sorina Suarasan, Yao Lu, Sarah Jurchuk, Sebastian WachsmannHogiu*

Corresponding author: Sebastian Wachsmann-Hogiu, Bioengineering, McGill University Faculty of Engineering, 3480 University St., MC362, Montreal, H3A 0E9I, Canada, E-mail: sebastian.wachsmannhogiu@mcgill.ca. <https://orcid.org/0000-0002-3761-3834>

Meruyert Imanbekova, Bioengineering, McGill University Faculty of Engineering, Montreal, QC, Canada

Sorina Suarasan, Nanobiophotonics and Laser Microspectroscopy Center, Interdisciplinary Research Institute in Bio-Nano-Sciences, Babes-Bolyai University, T. Laurian 42, 400271, Cluj-Napoca, Romania

Yao Lu, Bioengineering, McGill University Faculty of Engineering, 3480 Rue Universite, 1006, Montreal, QC, H3C6W1, Canada

Sarah Jurchuk, Bioengineering, McGill University Faculty of Engineering, 3480 Rue Universite, Rm#350, Montreal, QC, H3A 0E9, Canada.

2.1 Abstract. EVs are complex biological nanoparticles endogenously secreted by all eukaryotic cells. EVs carry a specific molecular cargo of proteins, lipids, and nucleic acids derived from cells of origin and play a significant role in the physiology and pathology of cells, organs, and organisms. Upon release, they may be found in different body fluids that can be easily accessed *via* noninvasive methodologies. Due to the unique information encoded in their molecular cargo, they may reflect the state of the parent cell and therefore EVs are recognized as a rich source of biomarkers for early diagnostics involving liquid biopsy. However, body fluids contain a mixture of EVs released by different types of healthy and diseased cells, making the detection of the EVs of interest very challenging. Recent research efforts have been focused on the detection and characterization of diagnostically relevant subpopulations of EVs, with emphasis on label-free methods that simplify sample preparation and are free of interfering signals. Therefore, in this paper, we review the recent progress of the label-free optical methods

employed for the detection, counting, and morphological and chemical characterization of EVs. We will first briefly discuss the biology and functions of EVs, and then introduce different optical label-free techniques for rapid, precise, and non destructive characterization of EVs such as nanoparticle tracking analysis, dynamic light scattering, atomic force microscopy, surface plasmon resonance spectroscopy, Raman spectroscopy, and SERS spectroscopy. In the end, we will discuss their applications in the detection of neurodegenerative diseases and cancer and provide an outlook on the future impact and challenges of these technologies to the field of liquid biopsy *via* EVs.

Keywords: early disease diagnosis; extracellular vesicles; label-free detection; liquid biopsy; optical methods

2.2 Introduction

EVs are heterogeneous lipid membrane-enclosed, nanometer-sized vesicles shed by all cells in the human body. Their molecular cargo contains lipids, proteins, nucleic acids, and sugars, and may carry biomarkers of certain diseases [1]. The uptake of EVs by recipient cells triggers intercellular signaling and can further activate intracellular metabolic pathways [2]. Determining the role and impact of EVs in a variety of cellular functions and disease states holds potential for improved diagnostics and therapeutics. In this context, it is important to establish quantitative characterization methodologies related to the three aspects of EV research: morphology, biochemical composition, and functions. While EVs exhibit significant heterogeneity, establishing distinct subpopulations of EVs has been a persistent problem in the EV research field. EVs are known to vary in size, biogenesis pathways, cells of origin, morphology, molecular cargo, and functions [1, 3]. EVs range in size from 50 to 2000 nm and are commonly divided into three main types based on their biogenesis pathway: exosomes, microvesicles, and apoptotic bodies. These will be discussed more in-depth later in this review. Briefly, exosomes or small EVs have an endosomal origin and are typically less than 150 nm, microvesicles formed by outward budding and fission of cell plasma membrane and their size ranges between 50 nm and 2000 nm, and apoptotic bodies are a heterogeneous population of EVs formed during apoptosis [2–4]. However, due to overlapping size ranges, current EV isolation methods are not able to precisely differentiate between subtypes of EVs. In addition, resulting EV pellets may contain other co-isolated particles present in the cell culture media or biofluids such as viruses

and protein aggregates. Therefore, to uncover EV heterogeneity, a comprehensive assessment of their morphology and biochemical composition is needed.

The morphological heterogeneity of EVs is mainly described by their differences in size, shape, and elasticity (Figure 1). The wide range in size, from 50–2000 nm, offers a particularly unique window for exploration. In terms of shape, exosomes and microvesicles are generally spherical or ellipsoid shapes [1], while apoptotic bodies have heterogeneous morphologies and are present in a wide variety of shapes and sizes [5].

The variations in EV biochemical composition are ultimately the result of their different biogenesis and subsequent cargo loading [6] and reflect the state of releasing cells [7, 8]. Specifically, the molecular cargo of EVs includes proteins [9], lipids [10], various subpopulations of RNA [11], and DNA [12]. Hence, an accurate assessment of EV biochemical composition is important for anticipation of their potential functions in normal physiology as well as to uncover their relevance to disease.

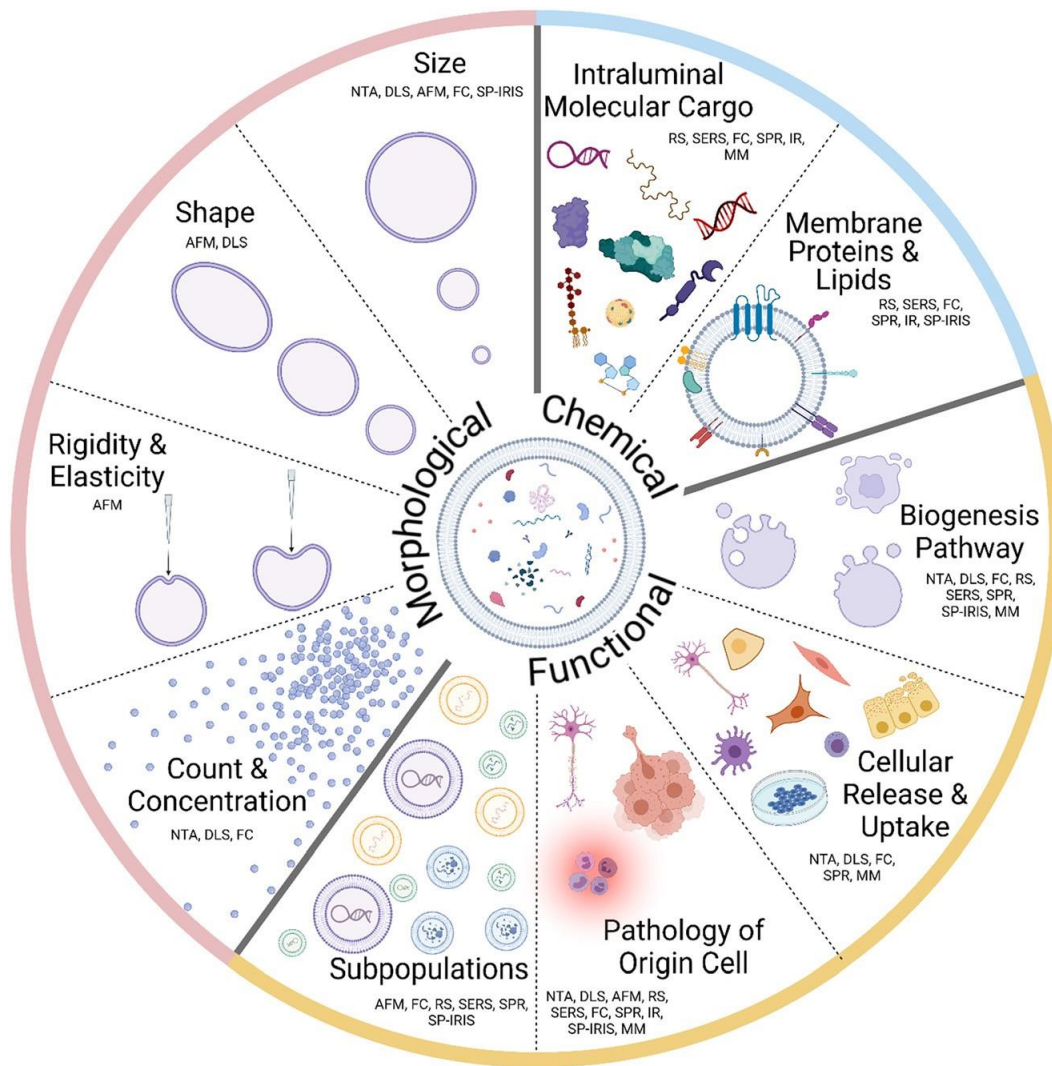


Figure 1: Optical label-free characterization methodologies for EV heterogeneity characterization. Categories of EV heterogeneity are divided into morphological, biochemical, and functional heterogeneity. *Morphological heterogeneity* category includes size, shape, rigidity, elasticity, count, and concentration. Size of individual EVs can be determined by NTA, DLS, AFM, FC, and SP-IRIS. The size distributions within a population of EVs, as well as the count and concentration of EVs can be determined with NTA, DLS, and FC. The shape of EVs can be characterized using AFM and DLS. EVs rigidity and elasticity can only be determined by AFM. *Biochemical heterogeneity* of EVs is derived from intraluminal molecular cargo and membrane molecules. RS, SERS, FC, SPR, IR-FTIR, SP-IRIS, and MM are the methods that are applied to characterize EVs biochemical content. *Functional heterogeneity* of EVs derives from the state of the cell of origin, biogenesis pathway and heterogeneity of EVs within subpopulations (exosomes, microvesicles, and apoptotic bodies). EV biogenesis pathway is commonly determined by combining size and biochemical content characterization methods including NTA, DLS, FC, RS, SERS, SPR, SP-IRIS, and MM. The cells of EV origin as well as their physiological state are determined by analyzing EV morphological features and their biochemical content, where the differences in EV counts, shape, rigidity, and elasticity can indicate disease triggered alterations in the cell of origin. NTA,

DLS, AFM, RS, SERS, FC, SPR, IR-FTIR, SP-IRIS, and MM are applied to study the pathological functions of EVs. The dynamics of EV release and uptake may be characterized *via* NTA, DLS, FC, MM, and SPR. Finally, EVs are found to vary in size, morphology, and biochemical cargo even within one specific subpopulation. These differences are currently studied using AFM, RS, SERS, SPR, FC, and SP-IRIS.

Given the vast heterogeneity of EVs discussed before, there are extensive challenges in their isolation and characterization. No single characterization technique or isolation method can capture the full-size range of EVs. Some morphological characterization and counting techniques have also been shown to be biased towards certain size ranges, due to technical limitations and calibration issues [13, 14]. EVs samples are rarely fully purified or isolated [14]. The overlap in size and chemical composition makes the separation of specific EV subpopulations challenging. In addition, the variations in protein, lipid, and nucleic acid profiles mean that labelling and affinity methods can only capture some information within limited populations of EVs. Therefore, combinations of methods are often used to extract EVs and further explore their biochemical composition [13]. This leads to the need of standard methodologies for quantitative EVs characterization. However, the repeatability of results is a common weakness within the field. Therefore, the International Society for Extracellular Vesicles (ISEV) has established guidelines for the Minimal Information for Studies of Extracellular Vesicles, most recently updated in 2018 (MISEV2018) [14]. The guidelines outline the need for specific EVs terminology as well as detailed reporting on the isolation and EV characterization techniques used.

Current methodologies of EV characterization may employ labels or can be label-free. A large variety of labeling and nonlabeling characterization techniques have been developed to address the processing and testing needs of different EV subgroups [15].

The field of label-based techniques is rapidly expanding with advancements in high-resolution microscopy techniques as well as improvements in EV labeling strategies. Labeling involves the use of molecular tags or markers that bind to EVs. Label types can include fluorescent dyes and molecules [16], radionuclides [17], and lipophilic tracer dyes [18]. The presence of the label is measured downstream and can be used to characterize the EVs. Label-based methods offer a range of advantages such as simple differentiation, visualization, and tracking of different EVs. They can be implemented into high-throughput strategies, such as flow cytometry. Labeling is also applied for experimental validation when combined with techniques for single-molecule characterization, such as high-resolution microscopy [19–21]. Moreover, labels are also highly

practical for acting as positive or negative markers to ensure adequate measurement and characterization of individual target particles [22]. Despite these useful functions that labels can fulfill, there are some fundamental concerns that may arise when using label-based methods. First, because of the vast heterogeneity of the surface proteins and molecular content of EVs, there is no established single optimal positive or negative marker for EV recognition or characterization [14] that can be used in label-based methods. Furthermore, one of the main drawbacks of label-based techniques is the potential unwanted and unanticipated interaction of labels with EVs which can compromise the obtained data and lead to false conclusions. Moreover, EV functions or their interaction with cells can be impaired or obstructed by the label itself, leading to misleading data on EVs uptake [23]. Another potential problem is the aggregation of labels or consequent labeling of non-EV particles that may cause false-positive results [24, 25]. Finally, labels may also degrade or change over time including photobleaching of fluorescent tags [26], or end up as hazardous waste, such as radiolabels. These limitations of the labelling methodologies necessitate the use of label-free methods for certain applications.

Label-free techniques are a variety of methods that do not use tags or labels to detect and characterize the analyte of interest. These methods are often based on direct and noninvasive probing of the inherent features of the analyte. Elimination of the need for tags or dyes results in numerous advantages. First, the lack of a tag allows performing measurements in conditions close to physiological which are beneficial for both fundamental and applied research. For example, identification, quantification, and characterization of proteins in native conformation by label-free mass spectrometry and Raman spectroscopy. Furthermore, label-free techniques require less time and wet-lab complexity compared to labelling techniques which consequently leads to fewer wet lab errors. In the field of EVs research, label-free methods offer a non-invasive approach for studying EVs molecular cargo including proteins conformation, and lipids structures that may further affect EVs functions. However, these technologies have some challenges and limitations that will be extensively discussed in this review.

Among label-free techniques, optical methods that utilize light and optical properties for noninvasive analysis of EV size, morphology, concentration, and molecular content are particularly interesting. Raman spectroscopy, SERS, and FTIR spectroscopy are examples of optical methods that have been used for characterization of EV biochemical content, while

techniques such as NTA, AFM, and DLS are often applied to reveal morphological features of EVs. In addition, there are novel emerging optical single-vesicle characterization approaches such as Raman tweezers microspectroscopy, AFM coupled infrared (IR) spectroscopy, and SP-IRIS that are capable to reveal specific features of a single vesicle and shine light on EVs heterogeneity.

In this review, we summarize current optical label-free methods used to study EVs and their contributions to understanding EV biology and EV-associated pathology of various diseases. We will first elaborate on EV biology and functions (Section 2). This section will break down the main classifications of EVs into exosomes, microvesicles, and apoptotic bodies, with a focus on their biogenesis pathways, molecular cargo, and their functions. Next, we will discuss morphological characterization, counting, and sorting methods such as NTA, AFM, flow cytometry (FC), DLS, and SP-IRIS (Section 3). This section will first explain their working principles and key characteristics, and then we will discuss main advantages and disadvantages of each method. In Section 4 we will describe optical technologies that are applied for EV molecular content characterization including Raman spectroscopy, SERS, surface plasmon resonance (SPR) spectroscopy, IR spectroscopy, and multiphoton microscopy (MM). Subsequently, in Section 5 we will define application of the aforementioned techniques for exploration of pathophysiology and diagnostics of various diseases. Finally, Section 6 will overview our perspectives and conclusions on label-free optical characterization techniques and applications within the rapidly growing field of EV research.

2.3 Biology and functions of EVs

The current state of knowledge identifies EVs as small lipid-membrane enclosed heterogeneous structures. There are a number of review articles that describe in great detail the aspects of EV biology [27, 28]. For the purpose of this review, we will briefly outline EV subtypes and their main characteristics. Their size ranges from 50 nm to 2000 nm in diameter depending on a subtype of EVs. The three major subtypes of EVs based mainly on their biogenesis are exosomes (less than 150 nm in diameter), microvesicles, and AB (both considered to be larger than 200 nm) [29]. Some studies classify EVs according to their origin (ectosomes, prostasomes, cardiosomes, and mitovesicles). All EVs subtypes share important characteristics such as lipid bilayer membrane, ability to carry intraluminal cargo of proteins and nucleic acids, and their release into

extracellular space [2]. Although the amount of research aimed to study the biology of EVs has increased over the past few decades, the detailed mechanisms of their biogenesis, cargo loading, trafficking, and release are not completely understood.

2.3.1 Exosomes

Exosomes, or small sEVs are membrane-bound EVs that originate from an endosomal pathway and are proposed to carry intercellular cargo for cell-to-cell communication as seen in Figure 2A [29]. Exosomes are released into the extracellular space upon fusion of the MVBs or late endosomes with the plasma membrane [2]. This tightly regulated process of intraluminal vesicles (ILVs) formation and cargo loading depends on the endosomal sorting complex required for transport (ESCRT) machinery (ESCRT-0, -I, -II, -III) [30, 31]. The initial step in this process is the formation of an early endosome (EE) by fusion of the primary endocytic vesicles containing receptors and proteins, which are regulated by clathrin- or caveolin mediated formation of inward budding of the plasma membrane [32]. Rab 5 protein plays a crucial role in the early stages of EE formation and the conversion to late endosome or MVB [33]. Next step is the formation of ILVs in late endosomes. ESCRT-0 and ESCRT-I cluster ubiquitinated proteins on the MVBs membrane and generate inward budding and scission of the limiting membrane *via* ESCRT-II and ESCRT-III subunits [34] as well as syntenin, and ALIX [35].

Additionally, there is another possible way of exosome formation known as the ESCRT-independent mechanism that involves ceramide [36, 37] and tetraspanins [38]. Ceramide forms membrane subdomains that can be spontaneously budded inside the MVB [37]. In addition, proteins of the tetraspanin family such as CD63, CD9, CD81, and CD82 are involved in exosome formation and cargo sorting [38]. These proteins are suggested to have a cone-shaped structure that contains cholesterol molecules and their enrichment in specific microdomains can induce inward budding of the membrane [39]. Both described pathways seem to be active in exosome formation and their contribution may be affected by the cell type. Little is known about the molecular mechanisms that regulate the fate of MVBs after their formation. The MVBs may be degraded by a lysosome or fuse with the plasma membrane which further leads to exosome release. The exosome biogenesis pathway requires transport of MVBs to the plasma membrane. This step involves association of MVBs with cytoskeleton components such as actin and microtubules, molecular motors, and molecular switches (Rab family proteins) [34]. Rab 7 and

dynein are further promoted to transport MVBs toward the plasma membrane [40]. Another protein of the Rab family, Rab 27, is found to regulate fusion of MVBs with plasma membrane by rearranging actin cytoskeleton [41]. It has been shown that this process is determined by soluble factors such as N-ethylmaleimide-sensitive factor (NSF) and soluble NSF-attachment protein (SNAP) as well as membrane complexes such as SNAP-attachment protein receptor (SNARE). The release of exosomes into the extracellular matrix may be regulated by Ca^{2+} and is based on ATP-dependent interaction of actin and myosin leading to cytoskeleton contraction [42, 43].

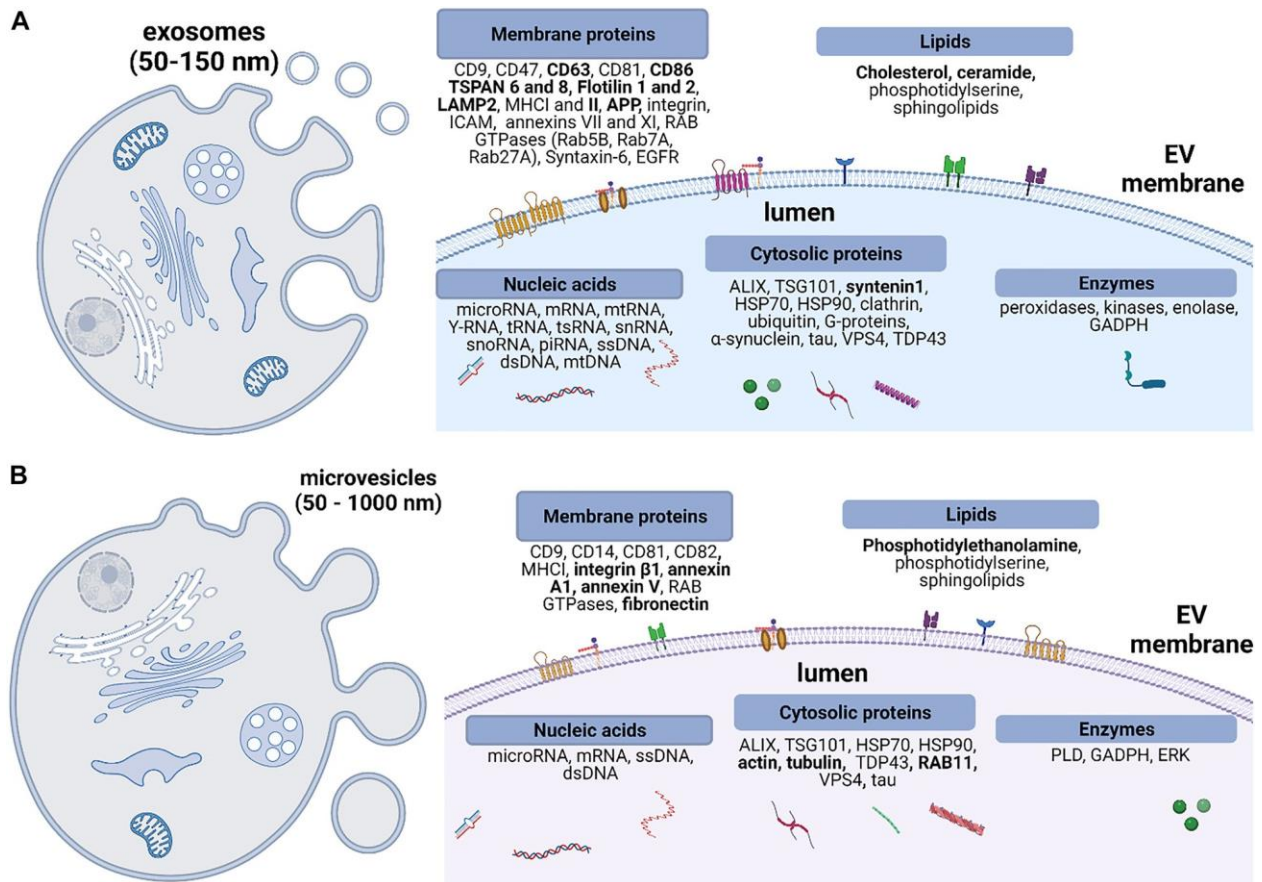


Figure 2: Biogenesis and chemical composition of a single EV.

(A) Exosomes are released upon fusion of multivesicular bodies (MVBs) to an extracellular matrix. Exosomes have a phospholipid bilayer membrane and carry various species of proteins, nucleic acids, and metabolites. (B) Microvesicles form *via* outward budding of the cell plasma membrane. Their biochemical content has some similarities with exosomes' and includes a variety of membrane proteins, cytosolic proteins, lipids, and nucleic acids. Bold fonts in both panels represent EVs molecular cargo that is uniquely found or enriched either in exosomes or in microvesicles. TSPAN, tetraspanins; APP,

amyloid precursor protein; LAMP2, lysosomal associated membrane protein 2; MHC, major histocompatibility complex; ICAM, intercellular adhesion molecule; EGFR, epidermal growth factor receptor; ALIX, ALG-2 interacting protein; TSG101, tumor susceptibility gene 101 protein; HSP, heat shock protein; VPS, vacuolar sorting associated protein; TDP43, TAR DNA-binding protein 43; GADPH, glyceraldehyde-3-phosphate dehydrogenase; PLD, phospholipase D; ERK, extracellular receptor kinase.

Subsequently, the molecular cargo of exosomes includes a large variety of proteins that are involved in their biogenesis, such as membrane proteins including tetraspanins (CD9, CD63, CD81, CD86, TSPAN 6 and 8, flotillin 1 and 2, and annexin II) as well as cytosolic proteins such as ALIX, GTPases (Rab5/Rab7), TSG101 [44], and syntenin (Figure 2A). In addition, exosomes may carry metabolic enzymes, heat shock proteins, and MHC molecules (MHC class I and class II). Due to their enrichment in exosomal cargo, TSG101, syntenin, ALIX, and various tetraspanins have been used as potential markers of exosomes [45, 46]. A recent study by Kugeratski et al. reported results of proteomic analysis of exosomes isolated from different cellular origins and highlighted a cohort of universally enriched 22 proteins, where syntenin1 was the most abundant protein and therefore identified as a potential universal exosome marker [47].

Importantly, Lötvall et al. measured in 2007 the presence of functional mRNAs and microRNAs (miRNAs) in exosomes and showed that exosomal mRNA can be translated into proteins in target cells [10]. Further studies reported the presence of DNA, small interfering RNAs (siRNAs), transferring. RNA, small cytoplasmic RNA and mitochondrial DNA, and RNA [10, 48, 49]. Lipidomic analysis of exosomes revealed an abundance of sterols (cholesterol and cholesteryl esters), sphingolipids (sphingomyelin and ceramide), glycosphingolipids, and phospholipids (phosphatidylserine, phosphatidylcholine) within exosomes compared to their releasing cells [10].

After release, exosomes can transmit information to the same cell (autocrine function) or target neighboring or distant cells, herewith exerting their intercellular communication function. There are two generally accepted ways of EV-based cell-cell communication. They can bind to the surface of the recipient cell and initiate intracellular signaling pathways, or they can be internalized by target cells and release their molecular cargo. Cells can internalize exosomes by clathrin-dependent endocytosis, pinocytosis, phagocytosis, and caveolin-mediated endocytosis. The discovery of such compositional variety in proteins and nucleic acids has led to an increased interest in exosomes as mediators of intercellular communication and pathogenesis over a diverse

range of cell types.

2.3.2 Microvesicles

The outward budding of the plasma membrane causes the formation of particles 50–2000 nm in diameter known as microvesicles (also known as ectosomes, oncosomes, or shedding vesicles) (Figure 2B) [50]. While significant effort has been dedicated to the understanding of the biogenesis of exosomes, less is currently known about microvesicles. It has been shown that the release of microvesicles depends on the lipid content of the plasma membrane of releasing cell, as well as on the intracellular calcium concentration [51]. Elevated levels of Ca^{+2} stimulate rearrangement of the phosphatidylserine from the inner leaflet of the plasma membrane to the cell surface result in plasma membrane curvature and cytoskeletal changes. This further supports membrane pinching and the formation of microvesicles. This described process of microvesicles formation is regulated by several enzyme groups that regulate the membrane asymmetry such as aminophospholipid translocases including flippases and floppases, scramblases, and calpain [52]. Some studies showed the importance of lipid rafts, cholesterol-rich domains of the plasma membrane, in microvesicles formation [53]. Another described way of microvesicles formation involves interaction between TSG101 and arrestin domain-containing protein 1 (ARRDC1) [54]. The molecular cargo of microvesicles includes enzymes, signaling molecules, miRNAs, mRNAs, growth factors, and cytokines. The proposed surface protein markers are annexin A1 and A2 which are found to be abundant in the lower flotation density region of EVs that correspond to microvesicles [49].

Following the release from the cell of origin, microvesicles interact with target cells *via* membrane receptors and either fuse with the recipient cell or trigger signaling pathways in the cell in a contact dependent manner [3]. Therefore, microvesicles function as mediators of intercellular communication by transferring bioactive molecules such as nucleic acids, proteins, and lipids between cells. They have been suggested to be involved in the promotion of angiogenesis, transfer of oncogenic receptor protein, and metastasis [55]. Additionally, microvesicles are shown to be involved in the progression of cardiovascular [56] and neurological disorders [57, 58]. This further suggests their possible clinical application as biological markers of the aforementioned diseases.

2.3.3 Apoptotic bodies

ABs are a class of highly diverse EVs that can range in size from 50 nm to 5000 nm and have variable morphology. They are formed during the apoptosis of cells and contain cell degradation products such as organelle fragments, DNA, histones, and cytoplasmic components. ABs clearance is performed by professional phagocytes or by neighboring cells [59].

Little is known about their functions, yet it is clear that the formation of ABs promotes the efficient removal of cell debris and may regulate cell-cell communication. Their role in intercellular communication is yet to be explored but it is suggested that they contribute to the cell-cell communication by delivering their molecular cargo. Another important function of ABs is the clearance of apoptotic cell residues without triggering inflammatory reactions. They have remodeled membrane structure where the phosphatidylserine lipid is exposed onto the outer leaflet, and this serves as an “eat me” signal for phagocytes. This leads to a rapid clearance of ABs and prevents secondary necrosis. Altered clearance of ABs has been found to contribute to autoimmune disorders [60, 61]. While ABs have important biological functions, we will not discuss their characterization in the context of this review article.

2.3.4 Exomeres

Recent studies reported the discovery of a new member of EVs termed exomeres [46]. Exomeres are nanosized EVs that are typically less than 50 nm in size and unlike other types of EVs do not have lipid membrane [62]. The biogenesis pathway of exomeres formation and molecular mechanisms of their secretion remains unclear. Proteomic analysis of exomeres showed the presence of proteins related to endoplasmic reticulum, extracellular matrix, mitochondria, cytoskeleton, and higher levels of metabolic proteins. On the contrary, proteins associated with the plasma membrane and exosomes biogenesis pathway were found to be depleted [46, 62]. Exomeres lipid content includes ceramide, diglyceride and triglyceride, and phospholipids such as phosphatidylcholine, phosphatidylethanolamine, and phosphatidylserine [46, 62]. Exomeres are found to carry a nucleic acid cargo of DNA, RNA, and miRNAs [46, 62]. The role of exomeres in cell-cell communication is yet to be determined. Initial studies suggest that they may have a role in the regulation of metabolic pathways of the recipient cells [46, 62]. Due to the lack of studies, in this review, we will not discuss characterization of exomeres *via* label-free optical methods.

2.3.5 MISEV2018 guidelines

The ISEV notes that the size and amount of EVs make them difficult to obtain as pure preparations or to characterize. Specifically, defining functions of specific types of EVs or EVs in general requires comprehensive reporting and testing of potentially confounding properties or variables that arise in impure and heterogeneous samples of EVs. For example, claiming pathophysiological roles of EVs or proposing clinically relevant biomarkers requires rigorous controls of experiments and characterization that are not universal for all EVs types or populations. The ISEV has noted that some articles propose conclusions that are not fully supported by the reported information or experimental design. To better inform researchers and reviewers on designing experiments and processing of EVs, as well as to ensure that reports are sufficiently thorough and repeatable, the ISEV has published the MISEV2018 guidelines, based on the consensus of ISEV scientists. The MISEV2018 guidelines include information related to nomenclature, collection and pre-processing, EVs separation and concentration, EVs characterization, functional studies, and reporting, and are presented in three subcategories: quantification, bulk characterization, and single EV characterization [14].

In terms of EV characterization, it is important to use multiple, complementary techniques to attest that investigated biomarkers are coming from EVs and not from other contaminants of the isolation process. Quantification of EVs requires some minimal information such as the total initial volume of biofluid, or the number of cells for conditioned medium, the particles number, the total protein, lipid, and RNA amount, or quantification of specific molecules such as tetraspanins CD9, CD63, and/or CD81 or disease-specific proteins. As for bulk characterization, it is recommended to determine expression of three classes of protein markers to prove the presence EVs and their purity: (i) transmembrane or GPI-anchored protein localized in cells at the plasma membrane or endosomes whose presence demonstrates the lipid-bilayer structure of EVs, (ii) the presence of cytosolic or periplasmic proteins able to bind to membranes, and (iii) the presence of protein constituents of non-EV structures often co-isolated with EVs which indicate the purity degree of EVs. Additionally, for small EVs subtypes, the presence of proteins localized in/on intracellular compartments of origin cells must be evaluated. Single EVs characterization on the other hand requires techniques that allow the visualization of single EVs, such as TEM by contrast with uranyl acetate, for example, cryo-EM, scanning electron microscopy (SEM),

scanning probe microscopy including AFM or super-resolution microscopy. Another approach for single particles analysis is based on measuring biophysical parameters of single EVs and quantification of large numbers of particles. For example, nanoparticle tracking analysis, high-resolution flow cytometry, multi-angle light scattering combined with asymmetric flow field-flow fractionation (AF4-MALS), fluorescence correlation spectroscopy (FCS), or Raman tweezers microscopy are capable to assess the chemical composition of EVs.

2.4 Particle counting, sizing, and morphology characterization

The morphology of EVs is determined by a variety of parameters, such as specific biogenesis pathways and disease states. To elucidate EV functions and roles in physiological and pathological processes such as cancer and neurodegenerative diseases, it is important to accurately measure and quantify morphological features.

Various techniques have been adapted to enable EV counting, sizing, and morphological characterization. A recent survey in 2016 showed that both single particle tracking methods (72% out of 196 samples) and flow cytometry (41%) are prevalent among studies, while 9% of the research employed AFM [13]. The majority of EV-related studies used several complementary techniques, with only 9% reporting the use of only one characterization method [13]. It is very difficult to acquire both reliable and multiplexed results when analyzing different types of EVs with a single analysis method, as no current technique can fulfill the complete spectrum of EV properties of all sizes in polydisperse samples. Despite the attempts for EV characterization, overlapping biophysical characteristics and variable compositions are still hindering the monitoring of EV dynamic processes, especially at single-particle level [63]. Thus, novel detection methods are required to study the physical characteristics of EVs. This section describes the general working principle of five commonly used characterization techniques: NTA, DLS, AFM, flow cytometry, and SP-IRIS (Table 1). Several examples of their implementations in studying label-free EVs are provided to further demonstrate their applications. Advantages and limitations are discussed as well.

2.4.1 Nanoparticle tracking analysis

NTA is a technique that can characterize the size distribution and concentration of various nanoparticles in solution or suspension, such as protein aggregates, liposomes, and other

nanosized colloidal particles, including EVs [69, 70] Although it is often compared to DLS, which was discovered first, NTA has become the most popular method in single particle tracking of EV studies [13] due to its ability to simultaneously characterize large particles numbers. The inherent measurement condition keeps EVs in their close-to-native environment, such that artefacts of particle shrinking can be avoided and the sample can be recovered after the experiment [70, 71]. NTA is based on light scattering and Brownian motion of particles in liquid suspensions. It takes advantage of the relationship between particle velocity and hydrodynamic radius to determine a particle's size through the Stokes–Einstein Eq. (1) [69]:

$$(1) \overline{(x, y)^2} = \frac{2k_B T}{3r_h \pi \eta}$$

where k_B is the Boltzmann constant, η is the medium viscosity, $\overline{(x, y)^2}$ is the mean-squared speed of a particle, r_h is the particle's hydrodynamic radius, and T is the absolute temperature. This relationship indicates that smaller particles move faster than larger ones.

During NTA, particles suspended in liquid are injected into the sample chamber. As seen in Figure 3A, a narrow laser beam is directed into the chamber in a dark field or total internal reflection configuration such that the background from the incident light is minimized. Particles within the laser beam's path scatter its light. The chamber is configured so that videos can be captured with an optical microscope linked to a 2D array camera. The video is generally 30–90 s in length with around 30 fps. The software identifies and then tracks individual particles frame-by-frame to determine their velocity. Using the Stokes–Einstein Eq. (1), the size of each particle can be determined and gathered to produce the overall size distribution of particles in the sample. Knowing the volume of the sample, the concentration of particles can be deduced. This sizing range happens to correspond to the known sizes for the majority of EVs.

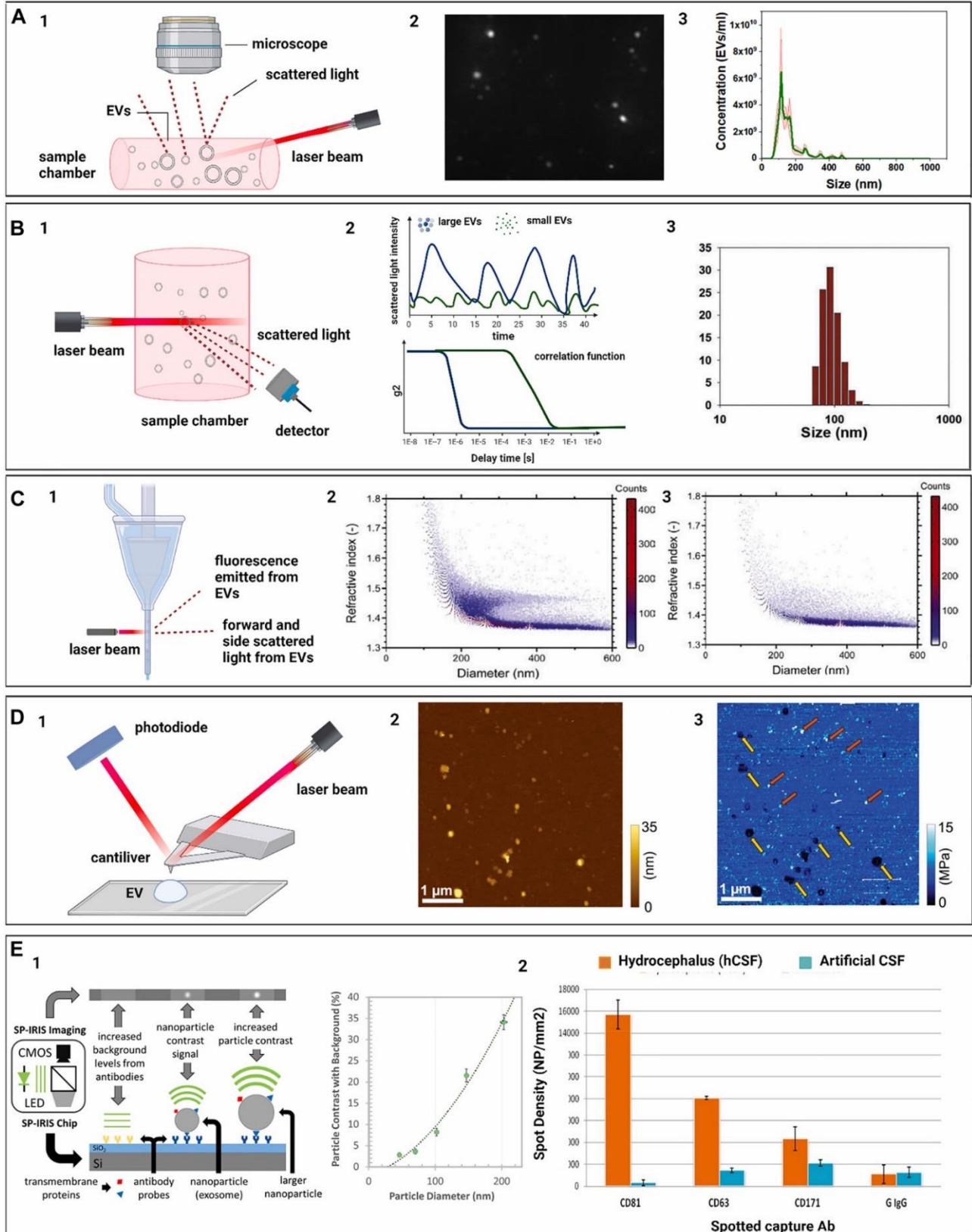


Figure 3: Label-free optical methods for EVs physical characterization. (A) Nanoparticle tracking analysis; (A1) basic setup of the NTA measurement system; (A2) typical micrograph of EVs in the imaging chamber; (A3) graphical representation of NTA histogram of neuronal EVs (adapted with permission from [64]). (B) Dynamic light scattering; (B1) schematic of the optical configuration; (B2) representation of DLS results of scattering of small and large EVs, and their correlation function; (B3) DLS histogram of particle size distribution (adapted with permission from [65]). (C) Flow cytometry; (C1) depiction of working principle; (C2) scatter plot of diameter versus refractive index of EVs and lipoproteins; (C3) scatter plot of all CD61 positive EVs from the same sample (adapted with permission from [66]). (D) Atomic force microscopy; (D1) AFM general components and operating principle; (D2) analysis of mesenchymal stem cells (MSCs) EVs. Topography image shows particles of various sizes. (D3) elasticity map of the same sample area depicted in (D2). Elastic modulus measurements revealed the presence of two types of particles EVs (yellow arrows) and nonvesicular particles (red arrows) (adapted with permission from [67]). (E) SP-IRIS; (E1) schematic illustration of SP-IRIS detection mechanism. The SP-IRIS signal is based on interference of light scattered from the Si-SiO₂ sensor surface and captured EVs. Graph shows size-dependent correlation of the contrast of particles; (E2) The expression of exosome surface proteins CD81, CD63, and neural adhesion protein CD171 quantified by SP-IRIS against the G IgG control (adapted with permission from [68]).

The lower size limit of NTA depends on the signal-to-noise ratio of the captured images [71]. Both the camera sensitivity and the amount of light scattered by the particles are thus potential limiting factors. At the lower size limit, which is much smaller than the wavelength of light, the particles exhibit Rayleigh scattering, which can be described by:

$$(2) \sigma_s = \frac{2\pi^5 d^6}{3 \lambda^4} \left(\frac{n^2-1}{n^2+2} \right)^2$$

where σ_s is the Rayleigh scattering cross-section, d is the particle diameter, λ is the wavelength of light, and n is the ratio of the particle refractive index to the solvent refractive index [71]. For particles with higher refractive index values, NTA's size limit can reach as low as 10 nm. EVs, however, have low refractive index values of approximately 1.37–1.59 [72, 73], limiting the minimum size that can be determined *via* NTA to around 30–50 nm [71]. As particle size increases to near or above the size of light wavelengths, Mie scattering is exhibited. Mie scattering calculations are more complex than Rayleigh scattering, but the key aspect is that the scattering cross-section drops rapidly as particles decrease in size. Mie scattering produces much more intense light scattering compared to Rayleigh scattering, due to the increasing size of the particle. It also distorts the scattering more towards the forward direction, compared to Rayleigh, whose scatter is relatively homogeneous around the particle. The upper size limitation arises

when particles are too large and their corresponding Brownian motion speeds are too slow to be accurately measured, which occurs around 1 μm [71].

Although the size range of NTA for EVs is 30–1000 nm, size heterogeneity in samples can further complicate the analysis of size distribution. First, an appropriate concentration of EVs must be present in the sample, otherwise, the particle density is too high and small EVs will not be discerned in a polydisperse sample. Prior to NTA measurements, samples must be diluted until particles can be observed individually, corresponding to approximately 10^7 to 10^9 particles/ml [69, 70]. However, as discussed before with Mie and Rayleigh scattering, larger particles scatter light more intensely than smaller particles, which can have an unintended masking effect over smaller particles and cause an underestimation of small particle concentration [69]. In order to properly characterize size distribution in highly polydisperse EV samples for their entire size range, the NTA analysis of a sample needs to be performed on multiple dilutions where the camera settings are adapted for the different light scattering behaviors of small and large EVs [70]. Moreover, in certain NTA setups, the suspension can be flown with a fixed flow rate through the chamber to increase the precision and repeatability of the results compared to a static suspension, since a greater number of particles are being analyzed. In this case, the flow settings must be carefully selected as it may impact the accuracy of the measurements [74].

Finally, there are several limitations of the NTA method that are important to consider for specific applications. First, one of the significant disadvantages of NTA is its lack of specificity. NTA cannot distinguish between contaminants, such as protein aggregates, or differentiate between EVs. Therefore, adequate isolation methodologies need to be used. Additionally, the precision and accuracy differences of various commercially available NTA machines have been compared, and it has been shown that EVs sized less than 60 nm cannot be accurately detected by several machines [75]. NTA also requires large sample volumes, which can limit its use for studies where a limited amount of sample is available, such as noninvasive clinical applications. It is worth noting that NTA is compatible with fluorescence detection if appropriate markers exist. Although this may increase the resolution and adds more specificity, details are out of the scope of this review. While being broadly applied in EVs sizing and counting, part of the focus for NTA studies has also been put into the optimization of imaging parameters and the

standardization between different systems. Comparative studies have been carried out between devices from either the same or different manufacturers, and the need for a standardized protocol still has to be fulfilled.

2.4.2 Dynamic light scattering

DLS is a technique that can characterize the size distribution of nanoparticles in solution or suspension [76]. The first device that used these principles to establish the diffusion coefficient of particles in suspension was developed in 1964 [77]. Given its simplicity in sample preparation and operation, accompanied by the need for small sample volumes and fast experiment results of only a few minutes, DLS has become a convenient method in the analysis of EV size [78].

Dynamic light scattering is similar to the NTA method as they both involve light scattering from particles in suspension. A laser is sent through a dark sample chamber with particles in suspension, as seen in Figure 3B. Particles within the path of the beam scatter the incident laser light. For DLS, this scattered light is often collected by a photon-counting detector [79]. Due to the Brownian motion, particles move in and out of the path of the laser beam and the number of scattered photons recorded by the detector fluctuates accordingly. Essentially, the intensity of light measured by the detector fluctuates as the particles undergo Brownian motion.

The diffusion behavior of nanoparticles is described by the translational diffusion coefficient D_τ , which will allow for the measurement of the hydrodynamic radius R_h :

$$(3) D_\tau = \frac{k_B T}{6\pi\eta R_h}$$

where k_B is the Boltzmann constant, T is an absolute temperature, η is the viscosity of medium, R_h is the hydrodynamic radius. This coefficient can be measured from the decay constant of the normalized correlation functions that describe how the scattering intensity patterns for one particle as well as for particles relative to each other are correlated [77]. For polydisperse particles, these correlation functions provide the link between the intensity decay constant Γ and the diffusion behavior D_τ of particles:

$$(4) \Gamma = -D_\tau \left(\frac{4\pi n}{\lambda} \sin\left(\frac{\theta}{2}\right) \right)^2$$

and where λ is the wavelength of incident light, n is the solvent refractive index, and θ is the detector angle. To fit the correlation function to polydisperse samples, a constrained regularization method for inverting data (CONTIN) method is commonly used.

DLS is capable of detecting particles in the range between 1 nm and 6000 nm range [80] and determining their size distributions. This wide detection range makes DLS an adequate fit for sizing EVs. In fact, various recent studies have adapted DLS for measuring the size distributions of the vesicles of interest [81–84].

However, this size range can be strongly affected by statistical errors from the experiments [85]. Particles in DLS analysis follow the same Rayleigh and Mie scattering behaviors as for NTA. Particles much smaller than the wavelength of light exhibit Rayleigh scattering, but as their size increases to the same regime as the wavelength of light, they can be described by Mie scattering [76]. With Rayleigh scattering, as shown in Eq. (2), the intensity distribution depends on the diameter of the particle to the sixth power, making DLS more sensitive to larger particles, as they have more intense light scattering behavior as their diameter increases. DLS is thus particularly vulnerable to potential contaminants and polydisperse solutions [78, 82, 86]. For example, when both DLS and NTA were used to characterize HTBE and Calu-3 vesicles from two airway cell culture systems, the latter technique indicated slightly smaller values for both groups. This further proves that the DLS results can be biased towards larger particles [87]. The same tendency for DLS was observed when assessing the size distribution of polystyrene beads with a range of known sizes, with the larger end of particle sizes being slightly larger than the NTA results [88]. Moreover, natural aqueous samples with a high polydispersity index can lead to misleading size distribution data in DLS [89]. This also implies that DLS has rather a low peak resolution compared to other techniques discussed in this section, given that it failed to produce bimodal distributions for a mixture of 20 and 100 nm particles [69, 90]. Lastly, being a low-resolution technique, DLS cannot further distinguish between similar-sized EVs, as it was unable to differentiate microvesicles apart from lipoprotein particles or small platelets when studying the selective release of circRNAs [91, 92].

Since DLS is inherently incompatible for more quantitative measurements, such limitation can be partially complemented with Bradford assay to recover sample concentration [82, 84], or size exclusion chromatography to perform sample fractioning first [93]. Other options of using DLS

to determine the presence of specific surfaces markers may include its combination with the immunoprecipitation approach [94].

Being a non-invasive and label-free technique with relatively high accuracy, DLS is often used along with flow cytometry as a complement for vesicle sizing or as validation for particles sizes acquired with NTA [69]. For instance, such complementary approaches were used to study human adipose-derived stem cell EVs on delaying cartilage degeneration, as well as examining the promotion of cancer lung metastasis upon treatment with indoor dust EVs [65, 95].

2.4.3 Atomic force microscopy

AFM is a technique that can characterize the topography, size, and a number of physical and mechanical properties of a material's surface [96]. AFM was developed in 1985 and in the past years has been widely applied in the biology research field.

AFM is a type of scanning probe microscopy technique with the probe that consists of a sharp tip attached to the end of a flexible cantilever [97, 98]. As the tip glides over the sample surface with or without contact, the distance between deposited samples and the tip is monitored based on the cantilever deflection or other feedback parameters (Figure 3D), depending on the selected mode. The recorded vertical positions can be later used to reconstruct the 3D topography of a sample or as a probe for other mechanical properties [99, 100]. AFM has great advantages over other morphology characterization techniques for being the only laser-based technique capable of identifying EV morphology and topography at nanometer-scale resolution [101]. Furthermore, AFM can be conducted under physiological conditions and is non-destructive (depending on the mode of operation). Despite the unsurpassed size resolution and level of morphological and physical detail, AFM's primary drawback is its low throughput. AFM requires extensive labor dedicated to only one particle at a time. AFM is therefore a useful technique for validation of other characterization methods but is not used in high-throughput applications.

AFM can be operated in various modes, depending on the specific scientific question that needs to be answered. The specific modes and their use for characterizing EVs are outlined below.

The *contact mode* through keeping a constant tip height or deflection can easily measure the mechanical properties of the surface with a force-distance curve, but it may bring irreversible deformations and damage to samples with the probing forces being hard to control [102].

Previous studies also found that mechanical stimulation of AFM could increase the release of exosomes as an important stress response [104]. There are several other AFM modes that are more suitable for soft biological samples and have been applied in various EV-related studies.

First is the *tapping mode* in which the cantilever vibrates near its resonance frequency and only encounters the surface intermittently. The tip-surface interactions are significantly reduced in the lateral direction and less perturbation is brought to the vesicles. It is now one of the most commonly seen modes in EV characterization and has been used to compare the size distribution of salivary and conditioned cell media EVs under aqueous conditions [104]. The same application in finding EV morphological properties of shape visualization and sizing can be seen elsewhere [101, 105, 106]. Although EV counting is more often carried out with light scattering techniques discussed in previous sections, AFM with an intrinsically high spatial resolution ($>0.5\text{--}1\text{ nm}$) is capable of collecting particle numbers as well. The result is presented as EV densities in the unit of number of particles per unit area [84, 88, 107].

A more advanced mode, *peak force tapping (PFT) mode*, also known as peak force QNM in quantitative mode, directly controls the deformation depth with the applied forces minimized to only a few piconewtons. With individual force curves being acquired with each tap, not only morphology, but also quantitative sample properties such as adhesion, deformation, and modulus can be mapped simultaneously. Sample stiffness, elasticity, and even energy dissipation can be calculated from the acquired data [107, 108]. However, this mode is still infrequently used for EVs characterization and only a few studies have employed it for quantifying EV rigidity or adhesive properties [94, 107, 109]. Another variation of this technique named *phase modulation AFM (PM-AFM)*, allows the mapping of compositional differences across the sample surface by recording the phase shift between the excitation force and the tip response. The phase shift values at a fixed feedback amplitude are converted into energy dissipation, which in turn can be used to characterize the adhesion and viscoelasticity of the sample surfaces [108]. Studies that utilize this mode for EV studies are not commonly seen, yet a recent study published in 2020 applied PM-AFM to quantify physical heterogeneity among several EV populations [110].

Nanoindentation is a technique related to AFM and its uniqueness lies in the ability of probing mechanical properties (stiffness) of submicrometer-sized vesicles ($>20\text{ nm}$) quantitatively. As the probing tip directly presses onto the surface of particles in the vertical direction, the indented

distance is recorded when a pre-set peak force value is reached. The sample rigidity can be later on calculated from the function that relates deformation to the applied force [111–115]. Raman techniques: fundamentals and frontiers Consequently, it is often used as a complement to AFM as the latter focuses more on the morphological properties [116]. By following well-established protocols, nanoindentation has been an effective method both in investigating the relationship between liquid composition with vesicle mechanics and their vesiculation pathways [102, 114, 117]. A recent study reported the use of AFM to distinguish EVs from non-EV particles within the same EVs isolate based on their mechanical properties, specifically Young's modulus (elasticity) [67]. The one subpopulation of the isolated MSC EVs showed a low Young's modulus value (4.5 ± 2.0 MPa) that corresponds to higher flexibility and has been reported previously for EVs (0.2–2.7 MPa). On the other hand, the second subpopulation showed a higher Young's modulus value (18.8 ± 10.8 MPa,) which relates to less elastic particles. It is important to note that morphological characterization of the isolated EVs by AFM was not able to distinguish EVs from non-EV particles due to their similar size and height. Aside from selecting the appropriate imaging mode, acquisition mode and surface immobilization are all important factors to be considered when studying EVs. AFM is compatible with both air [123] and liquid imaging environment [107, 118] in EVs studies, with the latter being more recommended. Although the air condition is more stable with immobilized EVs, it may cause an underestimation of sample sizes due to inevitable drying when the samples are exposed to the air, leading to mechanical artefacts. Indeed, the typical “cup shape” morphology resulting from EV dehydration can often be observed when imaged in the air [119]. Conversely, the liquid mode resembles more of the EV physiological conditions, and the native spherical shape can be preserved to allow more accurate size measurement. AFM imaging of dry samples is useful when it is needed to rapidly check the presence of the EVs. However, AFM characterization of EVs in the liquid will yield in more profound size distribution and mechanical properties assessment [120].

As a fairly new member in the field of EV characterization, this multiparameter technique does not come without limitations. It is highly labor-intensive and only analyzes one particle at a time, making it a low-throughput method. Moreover, aside from the mechanical stress caused by tip-surface interactions, the tip convolution effect often leads to lateral expansion of particle sizes, especially when the probed features are smaller than the cantilever tip size. Additionally, EV

binding to the flat immobilization surface also experience deformation and alter their geometry accordingly [118, 114, 121]. In a 2013 study that explored cell-to-cell communication *via* exosome-like particles, the observed widened vesicle dimensions were likely to be a combined effect of the factors stated above [122]. Nevertheless, a deconvolution algorithm has successfully reduced the widening error, and the tip geometry can possibly be addressed by depositing nanobeads with known dimensions during measurement [121, 123]. Moreover, innovative correlation techniques such as AFM combined with infrared spectroscopy (AFM-IR) or Raman spectroscopy may provide new insights into resolving heterogeneity among EV populations [96, 124].

Although primarily being a label-free method, both antibody surface immobilization or gold nanoparticle (AuNP) labelling methods enable AFM to locate and measure certain groups of EVs more precisely [106, 107, 121]. However, detailed discussions regarding labelling approaches are outside the scope of this review.

2.4.4 Flow cytometry

Flow cytometry (FC) is a well-established, high-throughput technique of particle analysis. It can capture a variety of chemical and morphological information. Specifically, for morphological characterization, FC can measure particle size and count using light-scattering principles [125]. Conventionally, FC requires larger sample volumes, but it has recently been shown to work for microvolume samples [126].

A typical FC instrument relies on three systems: the fluidics system, the optics system, and the electronics system. As seen in Figure 3C, the fluidics system collects the sample liquid and controls the flow of the stream so that the individual cells or particles are focused into a single-file path in the center of the stream. At the interrogation point, a laser light normal to the stream illuminates the individual particles, who scatter the light. The scattered light is filtered and collected by the optical system with sensors perpendicular to the stream path in the forward and side directions. Finally, the electronics system receives the signals collected by the optical system and processes them to output the collected data [125, 127, 128].

The fluidics system is responsible for organizing the flow of the particles such that they can individually be illuminated by a laser and their scattered light read by the sensors. To do this, the fluidics system uses an additional sheath fluid to hydrodynamically focus the sample fluid. The

sheath fluid is a simple saline solution that is pumped with constant pressure from a chamber through a narrow nozzle. The sample fluid is pumped through an inlet tube through the center of this chamber and meets the faster-moving sheath fluid as they both enter the same nozzle, causing the sample fluid to be forced into a smaller, central core stream that passes through the nozzle with the sheath fluid surrounding it. The drag that occurs at the boundaries of the sample stream as it enters the sheath fluid stream directs the particles in the sample fluid towards the middle of the stream, where is a faster and more stable flow. This central core containing the particles from the sample liquid will have laminar flow and the particles will travel at approximately the same speed through the same single axis. Without this focusing effect, the cells or particles in liquid would move in a disorganized and turbulent manner, introducing variability to the data. Furthermore, their proximity or overlap could cause two particles to be read at once by the optical system. The differential pressure between the sample and sheath fluid controls the width of the core stream. The lower the differential pressure, the narrower the core stream, which allows cells or particles to pass through the interrogation point single file on the same axis. Increasing the differential pressure by increasing the sample pressure will allow for a higher flow rate and faster processing times, but will cause widening of the core stream, which could cause multiple particles to line up beside each other and pass through the interrogation point at the same time [126, 126, 128].

To record an event, the signal received by the sensors must pass a specified “trigger” threshold, above background noise. This trigger can be based on three different modes: forward scatter, side scatter, or fluorescence. Often, particles are labeled with fluorophores, and multiple dedicated lasers within the instrument will excite them and the fluorescent light will be collected. The forward scatter light (FSC) (0.5–5.0) and the side scatter light (SSC) (15–150) are generally considered to be indications of the particle size and granularity, respectively [127]. However, light scattering depends heavily on a variety of other parameters, including the refractive indices of the sheath, sample media and particles, the laser wavelength, contact and collection angles [127]. It is important to consider that FSC signals are highly variable between different instruments [127].

Furthermore, SSC can also be correlated with size, especially for smaller particles. The Mie theory predicts a strong dependence of light-scatter intensity on the angle of measurement [128].

For EVs that are smaller than the wavelength of light, scattering is more isotropic. Thus, given a lower background in the SSC direction, it has been shown to be more effective at capturing the scattered light.

It is well known that size limitations for conventional flow cytometers render them insufficient for EV characterization, given that they were first designed for cell analysis. The lower detection limit is usually around 300 nm, meaning the majority of EVs ranging from 30 to 300 nm are undetectable. Nevertheless, instrument setups have been adapted to accommodate small particles and heterogeneous samples. Both high throughput and single particle analysis are attractive properties of flow cytometry in further understanding EV morphological and functional diversity. As discussed earlier, light scattering for smaller particles is less intense. Detection of such low intensity light scattering events is challenging due to low signal-to-noise ratios [125, 129].

For conventional flow cytometers that were developed for cells, the core stream and laser beam dimensions would allow hundreds of EVs to fit within the interrogation point instead of a single particle [130]. The combined signals of these particles reach the detection limit and trigger the event to be screened as a single particle. This phenomenon has been termed as “swarm detection” and leads to the underestimation of EV counting [131]. To validate single particle detection, researchers often use serial dilution to observe how the fluorescence or light intensity changes with controlled concentration changes [133, 132].

Adapting flow cytometers for EV characterization encompasses a variety of hardware modifications. Higher laser power and lower wavelength lasers have been used to produce more intense light scattering [66, 132]. Furthermore, narrowing the core stream and reducing the flow rate also benefit EV characterization [132]. Modifying the FSC and SSC angles used to collect larger angle scatter is also useful because smaller particles tend to scatter light at larger angles, proportional to their overall light scatter [68, 127, 134]. In a few studies that reported the detection limit of a commercial flow cytometer to be around 200 nm, the SSC detector was set to be a photomultiplier tube. When compared with the photodiode commonly used for FSC detectors, this approach is not only more sensitive, but also detects scattered light over a much broader angle, which allows capture scattering from multiple particles smaller than the wavelength of incident light [131, 135, 136]. Finally, using more sensitive detectors by, for

example, incorporating avalanche diodes, can also increase the signal-to-noise ratio of the setup [130].

Impedance-based FC is different from all the above. It is a non-optical, label-free technique based on the Coulter principle and can be used for the determination of both EV size distribution and concentration. As vesicles flow through the narrow sensing aperture under an electric field, a voltage pulse is generated across the aperture whose amplitude is proportional to the volume of the particle. Although it is only capable of resolving EVs above 300 nm, its unique compatibility with microfluidic devices among FC enhances the portability and further extends potential applications [137, 138]. So far, it has been applied to characterize EVs bound to extracellular matrix molecules [139], as well as the profiling of miRNA of exosomes from peripheral blood samples [140] (Table 1).

2.4.5 Single particle interferometric reflectance imaging sensor

SP-IRIS is an interferometric imaging-based technology for individual particle detection [143, 144]. The signal generated during the measurement is an interference between the scattering signal from the particle of interest and the signal reflected from the layered substrate [143], as shown in Figure 3E1. The typical SP-IRIS system consists of a monochromatic LED, Si-SiO₂ sensor chip, and CCD camera. The SP-IRIS signal is mainly affected by the polarizability of the particle, amplitude of the reference field, and the phase lag between them. The phase shift of the scattered and reflected light is regulated by the thickness of the SiO₂ layer of the sensor chip. The surface of the sensor chip is typically immobilized with capture antibodies of the proteins of interest. The technology has been used for quantification and size characterization of viruses in the serum or whole blood [145]. SP-IRIS shows great potential to be applied in the field of EV characterization due to its ability to detect surface molecules and to measure the size of single EVs [68, 144]. The method had been applied to measure the size of individual EVs derived from cerebral spinal fluid and their surface protein profile [68] (Figure 3E2). Moreover, a recent study employed SP-IRIS to explore tetraspanins expression profile across single EVs from cell culture media and ovarian cancer patients' serum [142]. The authors demonstrated the uneven distribution of CD9, CD63, and CD81 tetraspanins commonly used as EV capture markers. These results shine light on the heterogeneity of EVs and may impact the EV diagnostic application.

Current limitations of the SP-IRIS method are its inability to measure particle concentration [146] as well as the potential detection of several vesicles instead of single particles due to the diffraction limit of optical microscopy (lateral resolution approximately 200-400 nm).

Table 1: Summary of label-free optical particle counting, sizing, and morphology characterization methods.

Method	Morphological information	Data acquisition time	Sample type Liquid/dry	Advantages	Disadvantages	References
NTA	Size: 30-1000 nm Size distribution Refractive index Counting	Minutes	Liquid	Size distribution of individual EVs, high throughput	Bias towards overestimation of large particle concentration Requires large sample volumes	4-7
DLS	Size: 1-6000 nm Size distribution	Minutes	Liquid	High throughput analysis of EV size, concentration, and shape	Bias towards large particles Low resolution cannot distinguish small particles from each other	8-10
AFM	Morphology: nm Topography: nm EV density Size Adhesion, deformation, elastic modulus	~Hour per sample	Air (more stable, faster) Liquid (more accurate size)	Single EV analysis, enables measurements of mechanical properties of EVs with high resolution (lateral resolution 1-3 nm)	Mechanical stress Low throughput Labor intensive	11-14
FC	Size: >300 nm (conventional) 100 nm (high-	Minutes	Liquid	Single EV analysis, determinates	Variability between instruments and	15-18

	resolution fluorescent tagging) Counting			concentration, size distribution, and biochemical cargo characterization, high throughput	runs Few instruments can detect below 300 nm with the use of fluorescent labels only	
SRM	50-1000 nm	Seconds	Liquid	Single EV analysis, allows investigation of EVs functions <i>in vivo/in situ</i> with molecular resolution	Requires labels	19
SP-IRIS	Single EV size: 400 nm Counting	Minutes	Dry	Single EV analysis, allows simultaneous measurement of EVs size and surface markers	Bias towards large particles in highly concentrated EVs samples	20-22

2.4.6 Super resolution microscopy

Super resolution microscopy (SRM) offers a unique opportunity to characterize samples with a size that is below the light diffraction limit, reaching spatial resolution capabilities as low as tens of nanometers. The most popular SRM techniques are based on fluorescence signal detection [147]. However, these methods have several drawbacks including phototoxicity and photobleaching. Label-free SRM, on the other hand, is a more desirable option in the biomedical research field and has a wider range of applications compared to fluorescence-based techniques [148].

Currently, there is no reported research that employed label-free SRM techniques for EV characterization. Yet, several studies applied label-based SRM in EV research for EV tracking [149] and cancer diagnosis immunoassay [150]. Using SRM, specifically direct stochastic optical

reconstruction microscopy (with lipid dye), Nizamudeen et. al. detected 20-30 nm size EVs [141].

2.5 Characterization of EV molecular content

The molecular composition of EVs includes nucleic acids, lipids, proteins, and various other biomarkers. EVs released from healthy and diseased cells are known to carry a cargo with different molecular compositions. Therefore, the biochemical content of EVs circulating in body fluids is useful for the evaluation of a patient's health and early diagnosis of diseases. However, the concentration of EVs released by diseased cells that are present in body fluids is minimal compared to the concentration of EVs originating from normal cells. Therefore, it is crucial to translate and adapt innovative and accurate methods for the analysis of EVs. Traditional methods for EVs' molecular content characterization are mass spectrometry, Western blot, ELISA, and qPCR. However, these methods require large volumes and high concentrations of EVs, which is a major drawback for many applications. Recently, label-free optical methods are being employed for the analysis of EV molecular composition since they provide several advantages over the traditional methods. Raman spectroscopy, SERS, SPR, and IR spectroscopy are able to identify surface receptors and membrane proteins, in addition to EV internal molecular cargo (Table 2).

In the following sections, we will review some of the most recent studies reported on the EV molecular characterization using the aforementioned methods.

2.5.1 Raman spectroscopy

Raman spectroscopy is a label-free spectroscopy technique based on inelastic scattering of laser light that interacts with molecular vibrations. When incident photons interact with molecules, some of the photons are scattered with particular energy shifts, as a function of the structure and composition of the sample [151]. The frequency of scattered photons is recorded and translated into a Raman spectrum that contains the fingerprint of analyzed samples with information on their molecular composition [152]. Since it is a nondestructive and label-free technique, Raman spectroscopy is an ideal tool to investigate EVs. As we mentioned before, EVs are released by all mammalian cells and travel the entire body through the stream of body fluids. They are specific and resemble the cells of origin, carrying a molecular cargo that includes a variety of molecules,

proteins, and nucleic acids that may also potentially serve as disease biomarkers relevant for liquid biopsy [8]. With no need for selective antibodies or labels that can interfere with the sample signal, Raman spectroscopy could potentially record even small differences or alterations in the EVs membrane or molecular content. For the analysis of such subtle variations, Raman spectroscopy is often complemented and empowered by multivariate analysis techniques, such as PCA. These methods are able to analyze and interpret high-dimensional data sets to demonstrate spectral differences between different EV populations [153].

Since the first Raman spectrum of EVs was reported in 2009 [154], Raman spectroscopy has been extensively employed for the study of EVs. Next, we will review some of the most recent advances in the detection, analysis, and investigation of EV composition by Raman spectroscopy.

Raman spectroscopy has been employed to characterize EVs in bulk [158–160] as well as single EVs [155–166]. Bulk characterization of EVs *via* Raman spectroscopy showed differences in tissue specific biochemical composition of EVs and the ability to distinguish EVs based on their Raman spectra with high accuracy (>90%) [161, 159]. Moreover, Raman spectroscopy of EVs measured in bulk is a fast and sensitive method to assess EV purity after isolation [160]. On the other hand, Raman spectroscopy is a powerful tool to characterize the biochemical content of the membrane and cargo of single EVs, and therefore may unravel the heterogeneity of EVs [155, 162, 164, 165]. Such single-particle analysis techniques are essential in the field of biomarkers discovery due to their ability to provide information about the protein, lipid, and nucleic acid content of a single EV [161, 163, 165]. Moreover, the combination of single EV Raman spectroscopy with machine learning algorithms has great potential to be used as a rapid and sensitive diagnostic tool [155, 161, 164, 166].

Using Raman spectroscopy, our lab reported that EV subpopulations are shared among different cell types, based on their functionality [155]. This report revealed the heterogeneous chemical composition of single EVs isolated from both cancerous and noncancerous cells by employing laser tweezers Raman spectroscopy to trap individual EVs within the laser focus. While there are similarities among the recorded spectra, some major differences can be noticed between EVs derived from healthy and cancerous cell lines (Figure 4A1). These are the higher intensity of the peak centered at 700 cm^{-1} , in the case of EVs isolated from noncancerous cell lines, the shape of

the 1000–1100 and 1200–1300 cm^{-1} regions, and the 1600–1700 cm^{-1} region, which discriminates 3 cancer lines derived EVs from the others. The PCA spectral analysis of the averaged spectra revealed a significant variation in the chemical content of EVs which clusters into 4 distinct groups corresponding to 4 major EV subpopulations, unspecific to origin cell lines (Figure 4A2). Most of the 7 cell lines analyzed present multiple subpopulations of EVs and all subpopulations contain EVs from multiple cell lines. These differences are mainly due to the membrane content of the EVs. For example, noncancerous cells present mostly 2 subtypes of EVs that are enriched in cholesterol and relatively depleted in phospholipid, compared to EVs isolated from cancerous cell lines.

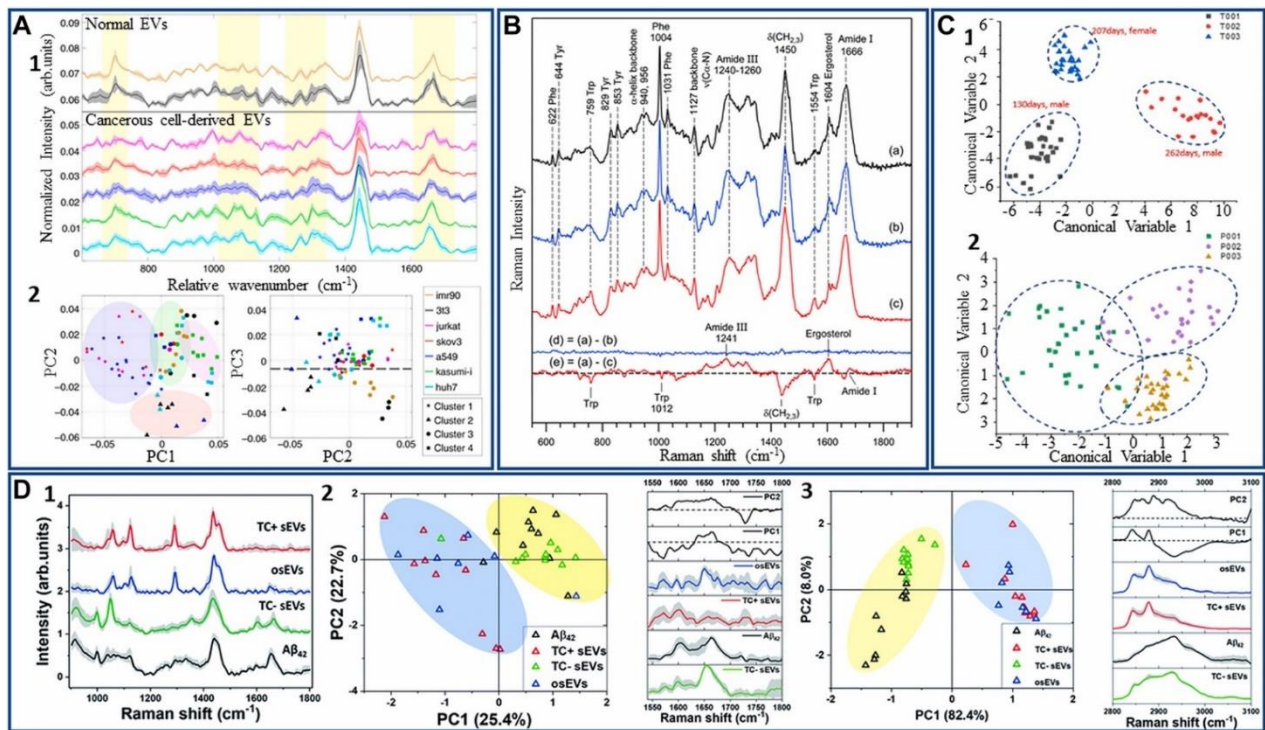


Figure 4: Label-free Raman characterization of EVs. (A) Differences between normal and cancer-cell derived single EVs obtained with Raman tweezer microspectroscopy; (A1) Raman spectra from single EVs derived from healthy and cancerous cell lines; (A2) Scatter plot of PC1 and PC2 obtained for principal component analysis for each cell line. Cell lines are represented with different colors and cluster membership is highlighted by different shapes as shown in the legend (adapted with permission from [156]). (B) Study of Raman tweezers microspectroscopy of EVs. Differences between EVs isolated from cells treated and untreated with hepatotoxin acetaminophen (treated cells - curve a and b, nontreated cells – curve c), as seen in the bottom spectra (reproduced with permission from [157]). (C) Principal component analysis (PCA) – linear discriminant analysis (LDA) of the EVs obtained from peripheral mononuclear blood cells (P001, P002, and P003) and trophoblast cells (T001, T002, and T003); (C1) Plots of trophoblast derived EVs from three different bovines; (C2) Plots of PBMC-derived EVs

from three different bovines (adapted with permission from [158]). (D) Investigation of A β ₄₂ presence in the molecular cargo of EVs isolated from AD cell culture model; (D1) average Raman spectra of TC-sEVs, TC + sEVs, osEVs, and A β ₄₂ pure protein in the fingerprint region; (D2) Analysis of the Raman spectra of the amide I region 1540–1800 cm⁻¹. The scatter plot of the first two principal components for each EVs group; (D3) Analysis of the “high-wavenumber region” 2800–3100 cm⁻¹ of normalized Raman spectra. The PCA scatter plot of the first two principal components (adapted with permission from [64]).

Also, with Raman tweezers microspectroscopy, the biomolecular content of a small number or even single EVs around 100 nm was characterized in colloidal suspensions. Besides the regular EV fingerprint biomolecular contributions from proteins, lipids, and nucleic acids, this technique discriminated different subpopulations present in a heterogeneous EV sample isolated from the same cell line. Using Raman tweezers microspectroscopy, Kruglik et. al. highlighted the differences in biochemical composition of EVs isolated from rat hepatocytes before and after the treatment with a hepatotoxin [156] (Figure 4B). The results showed some major changes in the biomolecular contents of the EVs, reflected in the Raman spectra by a decrease of the tryptophan content, an enhancement of the amide III band, and a shift of the amide I band to higher frequencies. In addition, the spectral changes included an enhancement of the 1602–1604 cm⁻¹ band, assigned to ergosterol, lipids that contribute to the regulation of membrane fluidity, plasma membrane biogenesis and function. Therefore, this technique showed high sensitivity for detection of the hepatotoxicity signatures in EVs and could potentially be applied for the diagnostic of liver damage.

Raman spectroscopy was also successfully employed to characterize and differentiate four types of EVs derived from healthy red blood cells and platelets, and two different prostate cancer cell lines PC3 and LNCaP, respectively [167]. The recorded spectra reveal the distinctive Raman signatures of EVs both in the fingerprint and high-frequency region, with characteristic lipid peaks at 2847 and 2876 cm⁻¹, protein contribution at 2932 cm⁻¹, CH₂ deformation in lipids at 1296 cm⁻¹, CH₂ and CH₃ deformation in proteins and lipids at 1440 cm⁻¹, phenylalanine at 1603 cm⁻¹, amide II at 1544 cm⁻¹ and C=C stretching in lipids 1650 cm⁻¹. However, the spectral differences across different EV subpopulations are subtle, and further PCA was required. PCA analysis was able to clearly separate the Raman spectra into four distinct groups specific to different EV subtypes. The best separation is obtained in the fingerprint region which provides

an obvious discrimination of the EV groups with 94.67% and 98% of the data being classified into two categories: healthy cell-derived EVs and prostate cancer-derived EVs.

Recently, Dash et al. used label-free Raman spectroscopy to analyze and compare the EVs isolated from conditioned media of two cancer cell lines (COLO 205 and MCF-7) by three different isolation techniques, namely total exosome isolation reagent, protein organic solvent precipitation, and differential ultracentrifugation [168]. Raman spectra were collected using a 532 nm laser line and then multivariate analysis was performed to study specific variations of the EVs spectra. This allowed the authors to differentiate the isolation techniques and classify them based on the quality of spectra.

Another study published in 2020 showed the potential application of placental EVs as non-invasive liquid markers for pregnancy complications prediction and monitoring. The results of the study determined certain peaks such as 728 cm^{-1} and 1573 cm^{-1} that attribute to collagen and purine/protein can only be found in EVs isolated from peripheral blood mononuclear cells (PBMC), whereas cholesterol and tryptophan peaks located at 702 cm^{-1} and 1553 cm^{-1} appear only in trophoblast EVs [157] (Figure 4C). Also, the 784 cm^{-1} peak (DNA/RNA) can be found in both EVs types, but it is significantly higher in the spectra of the PBMC derived EVs. The authors used PCA and LDA to analyze data collected from Raman spectroscopy characterization of EVs (Figure 4C1–2). Interestingly, they found no significant difference in Raman spectra of PBMC EVs of different bovines while EVs derived from trophoblast of three placental samples were clustered separately based on gestational age.

Additionally, using Raman spectroscopy, our group highlighted the presence of A β in the molecular cargo of EVs isolated from the AD cell culture model [63]. Specifically, we used EVs derived from MC65 human neuroblastoma cells with the secretion of A β regulated by tetracycline promoter. To investigate the presence of A β in EVs, we analyzed the EVs isolated from MC65 cells before and after treatment with tetracycline, denoted TC- and TC+EVs, respectively (Figure 4D1). This will ensure that the biochemical difference between the two EVs groups is due to the potential association of A β in TC-EVs. PCA analysis and the intense Raman peaks centered at 1650 cm^{-1} and 2930 cm^{-1} together with TC-EVs spectra similarity with the spectra of pure A β protein confirm the presence of the A β in TC-EVs (Figure 4D2–3). Also, we observed some differences in the lipid structure of EVs. For example, TC +EVs present lipids

with longer fatty acid chains while TC-EVs have shorter fatty acid chains, suggesting the association of A β protein with plasma membrane which alters the membrane fluidity. The results were validated by testing EVs isolated from 3D midbrain organoids as a healthy brain neurons control.

Collectively, Raman spectroscopy is a useful tool that can complement traditional EVs characterization methods and provide valuable information about the biochemical content of EVs. Yet, inherently weak Raman scattering limits the application of the technique. To overcome this challenge, plasmonic nanomaterials and coherent Raman techniques have been applied to enhance the intensity of the Raman signal.

2.5.2 Surface enhanced Raman spectroscopy

As we showed above, Raman spectroscopy is a highly useful method for EVs characterization. However, during Raman scattering, very few photons are scattered inelastically and as a result, the Raman signal is very weak. Consequently, this requires higher sample concentration, laser power, and a long integration time for the acquisition of quality spectra [170]. However, the Raman signal can be significantly enhanced up to $\sim 10^{14}$ times by a technique called SERS [170]. SERS technique is based on the phenomenon of surface plasmon resonance. Plasmon resonances from irregular substrates with gaps and junctions created between nanoparticles (NPs), form hot spots that enhance the signal from Raman active molecules located in these regions. This makes SERS spectroscopy a powerful technique with the capability to detect and analyze even single molecules [171].

In the field of EVs characterization, SERS is particularly important due to its label-free and nondestructive nature and ability to obtain information about the vibrational modes of molecules with high sensitivity [172]. Additionally, considering the low abundant populations of disease-related EVs compared with EVs from healthy cells in body fluids, SERS overcomes the aforementioned Raman limitations [173]. To date, different types of SERS substrates have been developed for the study and characterization of EVs. Stremersch et al. used an innovative method to characterize EVs *via* SERS. In this study, individual EVs were enveloped in gold shells [174]. In this way, due to the reduced size of the AuNPs, multiple hot spots were created, enabling the recording of an intense SERS signal. This signal is coming from the DMAP molecules that were functionalized on the gold surface, and from the biomolecular EVs components with peaks

located at 1123 cm^{-1} , (lipids and proteins), 1172 cm^{-1} (proteins), 1307 cm^{-1} (proteins and lipids), $1366\text{--}1370\text{ cm}^{-1}$ (phospholipids and carbohydrates), 1445 cm^{-1} (lipids and proteins), and $1572\text{--}1576\text{ cm}^{-1}$ (nucleic acids). The authors proved the diagnostic potential of this method by discriminating EVs isolated from B16F10 melanoma cells from the healthy red blood cell (RBC)-derived EVs. Later, this approach was improved by growing a silver layer directly on the surface of EVs coated AuNPs to form core-shell Au@AgNPs directly on the surface of EVs [185] (Figure 5A1). Thus, the interfering signal from DMAP stabilizing molecules is removed and an additional near-field enhancement is obtained from the core-shell structure (Figure 5A2). The spectra recorded using this system allowed a better separation of the cancerous and healthy EVs data points in the PCA analysis and quantification of the discriminative capability of the system with the partial least-squares discriminant analysis (PLS-DA) (Figure 5A3). The performance of this approach was proved by a higher than 90% specificity and sensitivity determined for both EVs types.

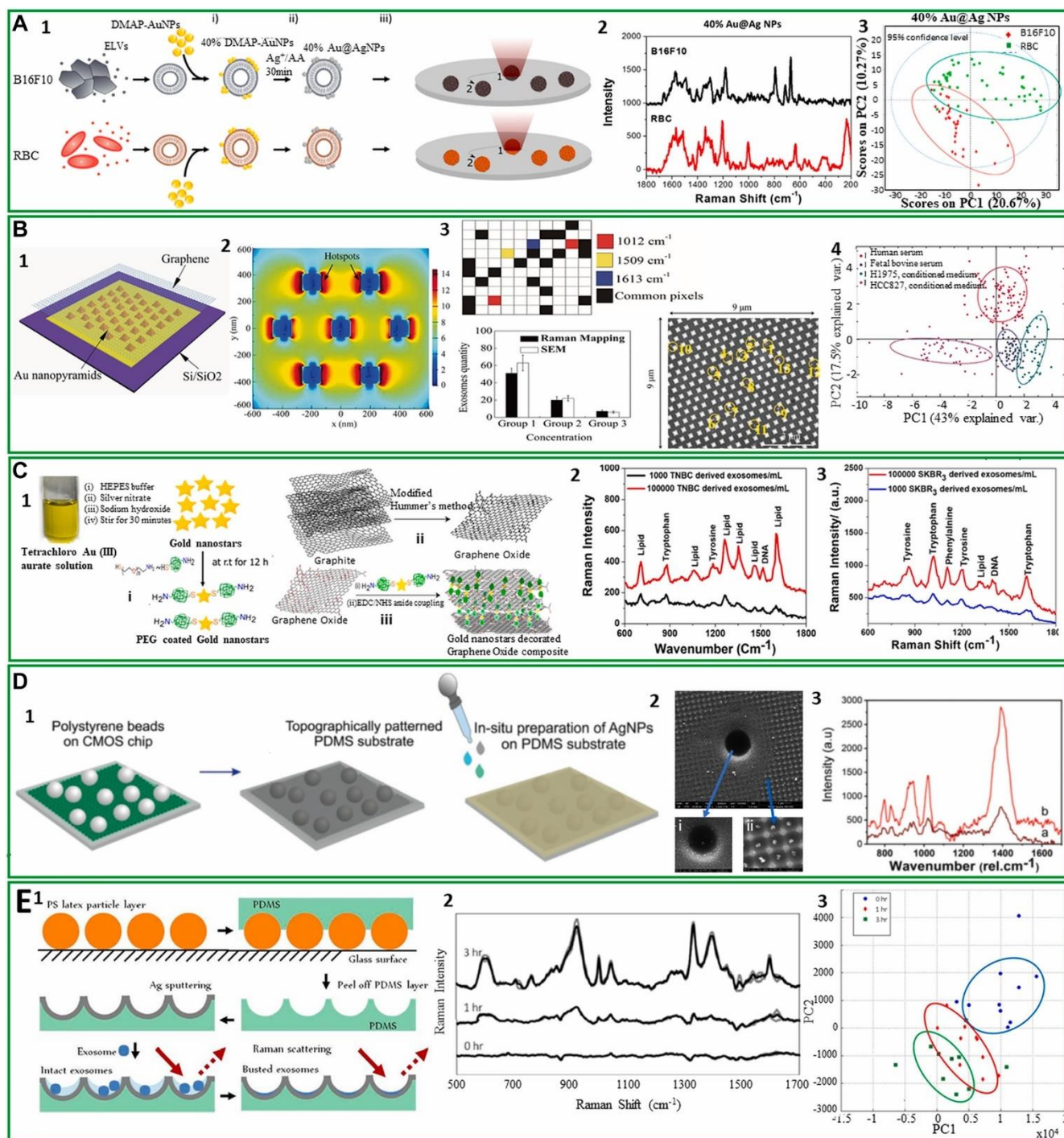


Figure 5: Label-free SERS characterization of EVs.

(A) Functionalization and SERS analysis of EVs isolated from two types of cells; (A1) Schematic representation of the procedure for EVs functionalization; (A2) SERS spectra of individual B16F10 melanoma- and RBC-derived EVs; (A3) The 2D PCA for B16F10 and RBC EVs Au@AgNPs (adapted with permission from [175]). (B) Fabrication of a hybrid platform for SERS investigation of EVs; (B1) Schematic diagram of the SERS hybrid

platform; (B2) Electromagnetic field distribution simulated by FDTD for 785 nm laser; B3. SERS and SEM mapping of EVs adsorbed on the hybrid substrate; the graph compares the EVs density obtained through Raman mapping and SEM at three different EVs concentrations. SEM micrograph of EVs attached to the graphene-covered surface, where the yellow circles mark the presence of EVs within this region. The colored pixels represent the presence of selected peaks in the Raman spectrum; B4. PCA analysis of EVs from different sources (adapted with permission from [177]). (C) Synthesis and analysis of EVs on a mixed metal–graphene substrate; (C1) Schematic representation of the synthesis of PEG-coated gold nanostars; (C2) SERS spectra of EVs isolated from TNBC cells (10^5 and 10^3 cell/ml) on the fabricated surface; (C3) SERS spectra of EVs obtained from SKBR3 cells (10^5 and 10^3 cell/ml) on the developed surface (adapted with permission from [180]). (D) Fabrication of a superhydrophobic substrate for EVs concentration and analysis; (D1) Schematic illustration of the substrate fabrication containing micro and nanobowls; (D2) SEM image of the AgNPs grown on the patterned PDMS substrate; insets show the AgNPs grown inside (i) microbowls and (ii) nanobowls; (D3) SERS spectra of EVs acquired with 633 nm laser excitation from inside of (a) nanobowls and (b) microbowls (adapted with permission from [179]). (E) Preparation of an SERS substrate and its use in analysis of intact and ruptured EVs; (E1) Schematic representation of the substrate preparation; (E2) SERS spectra of EVs isolated from SKOV3 cell line recorded at different time intervals; (E3) PCA of recorded SERS spectra (adapted with permission from [180]).

Yin and co-authors proposed a new isolation method for cancer cell-derived EVs and a new label-free SERS substrate [176]. Specifically, they used a PEG-based method to isolate the EVs by simply incubating a PEG solution with conditioned media for 24 h at 4°C and centrifuging the mixture for 15 min at 3000 g. Three types of male cancer cell lines COLO-205 (colorectal cancer), THP-1 (leukemia), and DU-145 (prostate cancer), and healthy male blood samples were selected for EVs isolation. The obtained EVs were placed on an amino molybdenum oxide (AMO) nanoflakes substrate to be detected by SERS under 532 nm laser irradiation and analyzed by PCA supported by vector machine (SVM), a machine learning method able to accurately recognize complex vibrational signals of EVs. This method provides close to 100% accuracy in differentiating the healthy and cancer EVs.

Recently, a new plasmonic hybrid platform based on periodically arranged Au nanopillars covered by a single layer of graphene was proposed [177] (Figure 5B1). In this setup, the metallic nanopillars generate hotspots with a high electromagnetic field on each side (Figure 5B2) for enhancement of the EV Raman signal, while the graphene layer provides a biocompatible and chemically stable surface for EVs detection. To test this label-free SERS substrate, EVs from four different sources were used. Their localization on the substrate was confirmed by three specific peaks with high signal-to-noise ratios in the Raman spectra.

In Figure 5B3 a pixel was assigned for each peak: 1012 cm^{-1} coming from the vibrational mode of phenylalanine is represented by red, 1509 cm^{-1} the ring-breathing mode in DNA bases is yellow, and the Raman mode of tyrosine peak at 1613 cm^{-1} is the blue pixel. The black pixels represent all three peaks and are considered to originate from EVs. To observe the 1613 cm^{-1} peak, the graphene G-peak was subtracted. SEM images confirmed the Raman mapping result of the EV location on the substrate at three different EV concentrations. Additionally, the PCA analysis proved that all different EVs detected by this platform clustered into distinguishable groups of EVs isolated from two lung cancer cell lines HCC827 and H1975 with <5% overlap and a sensitivity of >84% (Figure 5B4).

In 2020, Pramanik et. al. used a mixed graphene oxide (GO) gold nanostars (GNSs) substrate for ultrasensitive SERS detection of EVs derived from triple-negative breast cancer (TNBC) type MDA-MB-231 cells and HER2(+) type SKBR3 breast cancer cells *via* their specific fingerprint Raman bands [178] (Figure 5C1). Amino functionalized GNSs were covalently linked to GO nanosheets to obtain the mixed-dimensional heterostructure-based GO-GNS substrate. This substrate is capable to highly amplify ($\sim 10^{10}$) the Raman signal of EVs through a synergistic electromagnetic and chemical enhancement mechanism. The sensitivity of the platform is characterized by LOD of 3.8×10^2 EVs/mL and 4.4×10^2 EVs/mL for TNBC and HER2(+) breast cancer-derived EVs, respectively. The EVs spectra recorded using this hybrid material show that each type of EVs has a specific Raman fingerprint. The lipid bands centered at ~ 1605 , ~ 1260 , ~ 1056 , and ~ 970 cm^{-1} are unique for TNBC-derived EVs, while HER2(+) breast cancer cell-derived EVs shows unique protein bands at ~ 1634 , ~ 1198 , ~ 1101 , and ~ 1014 cm^{-1} (Figure 5C2). Also, DNA band of EVs isolated from TNBC cells appears at ~ 1510 cm^{-1} and DNA bands of HER2(+) breast cancer cell-derived EVs are at ~ 1388 cm^{-1} (Figure 5C3).

Also, our group developed a SERS platform for EV concentration and characterization [179]. The innovative superhydrophobic substrate was able to analyze ultralow sample volumes of EVs isolated from the MC65 neural cell line by concentrating EVs in bowl-like features (Figure 5D1). Specifically, a polystyrene bead-decorated CMOS sensor was used to create a template PDMS replica patterned with nano- and micro-bowls for EVs concentration (Figure 5D2). Next, these voids within PDMS replicas were decorated by AgNPs to generate local electromagnetic field enhancement (hot spots) and consequently increase EVs Raman signal (Figure 5D3).

Another study employed a similar concept of EVs concentration by developing nanobowl-like plasmonic substrate for EV capturing and SERS [180]. Specifically, the substrate was prepared by soft lithography on a flexible PDMS substrate using polystyrene beads. Obtained nanobowls were sputtered with a thin silver layer to act as SERS active surfaces (Figure 5E1). Initial SERS measurements are acquired from EVs captured in nanobowls in aqueous solution. Later during spectra acquisition, the water eventually evaporates which may affect the intactness of analyzed EVs which is reflected in the differences in SERS spectra (Figure 5E2). PCA analysis shows that spectra cluster into different groups based on the recording time, as can be seen in Figure 5E3.

Recently, Koster et.al. demonstrated the ability of SERS-based analysis combined with machine learning algorithms to detect cancer-derived sEVs despite contamination with lipoproteins [181]. These authors isolated sEVs by known isolation techniques including differential ultracentrifugation, size exclusion chromatography, and density gradient ultracentrifugation. All three methods showed different degrees of lipoprotein contamination, which, however, did not significantly affect the SERS results.

Altogether, these studies validate the use of SERS for label-free characterization of the biomolecular composition of single EVs or EVs in bulk. However, the phenomenon of SERS enhancement by plasmonic resonance depends on the distance between the molecule and nanoplasmonic substrate and decays exponentially with the distance such that it becomes insignificant at distances larger than 10s on nanometers [182]. This limits the applicability of SERS for the characterization of intraluminal content of EVs and makes it more suitable for probing EVs membrane and membrane-bounded molecules.

2.5.3 Surface plasmon resonance spectroscopy

Another label-free sensing method that has been introduced for EV characterization is surface plasmon resonance (SPR) spectroscopy. SPR is a physical phenomenon that occurs as a result of resonance between the incident light at certain angles of incidence and the collective oscillation of the metal electrons propagating along the metal surface [185]. The SPR measures changes in the refractive index of the material adjacent to the metal substrate surface. An example of such refractive index change is the binding of a macromolecule to the surface of the metal due to immunoreaction. Typical SPR systems include a prism connected to a glass sensor chip coated with a thin film of gold (~50 nm) (Kretschmann configuration). Biomolecular interactions

between an immobilized ligand and analyte from a sample result in changes in refractive index and change in the coupling angle with time. Injection of various concentrations of analyte allows the measurement of association rate constants (K_a) which represents the number of binding events per unit of time and describes ligand-analyte complex formation. Next, is the dissociation phase a change in the coupling angle can be measured in response to the release of the analyte after the sensor surface is washed with buffer. Afterward, the affinity binding constant can be determined using the signal obtained during both phase measurements. This allows SPR sensor to measure concentrations of the analytes including EVs in a sample of interest.

SPR sensors have been applied to detect and characterize biomarkers and hormones in the medical diagnostics field, pathogens, and toxins detection for food control purposes, and to detect pollutants in environmental monitoring. In the field of EV characterization SPR has been used to determine EV concentration [184, 185], biomarker detection [186–189], characterization of surface and intravesicular proteins [190, 191], determination of mechanical properties of EVs [192], and single EV detection [193]. While certainly SPR is a widely used technique in the EV field, for the purpose of illustrating the potential applications in the clinic, in this review we will specifically focus on articles that describe the use of SPR techniques for the analysis of clinically relevant samples. So far, several SPR biosensors have been developed to detect EVs containing clinically relevant biomarkers. First, the platform termed nPLEX is a nanoplasmonic assay based on periodic nanohole arrays functionalized with antibodies [190]. In this study, EVs were isolated from ascites of 20 ovarian cancer patients and 10 healthy individuals. Detection of EVs was based on the binding kinetics of EVs to CD63, EPCAM, and CD24 antibodies-functionalized nanoholes. The results of the study showed decreased levels of EPCAM and CD24 in patients-derived EVs. Another study reported the development of a nano-plasmon enhanced scattering (nPES) assay for the detection of ephrin type-A receptor 2 (EphA2) protein pancreatic cancer specific EV biomarker [194]. The nPES assay demonstrated the ability to distinguish pancreatic cancer patients ($n = 49$) from pancreatitis patients ($n = 48$) based on a level of EphA2-EVs. Moreover, the platform showed promising results in the staging of tumor progression and monitoring drug therapy response. Next, Liu and co-authors introduces a simple SPR sensing platform for lung cancer diagnosis and used exosomes associated EGFR and programmed death ligand-1 (PD-L1) as biomarkers of disease [195]. The SPR platform detected higher levels of EVs EGFR and PD-L1 in the serum of lung cancer patients compared to healthy

individuals isolated exosomes. Most recently, Thakur and co-authors reported the development and application of an SPR-based biosensor for glioblastoma diagnosis [196]. The progression of glioblastoma is characterized by enhanced expression of CD44 enriched EVs. The SPR substrate was fabricated using Titanium nitride nanoholes, and CD44 and CD133 capturing antibodies were immobilized onto the sensor surface. The study utilized EVs isolated from blood and CSF of a glioblastoma mouse model. The biosensor was capable to detect and quantify CD44 enriched EVs with $3.46 \times 10^{-3} \mu\text{g/mL}$ LOD. The described platform supports the potential application of SPR biosensors for EVs-based glioblastoma diagnosis.

Finally, SPR based immunosensors have a great potential as commercially available label-free optical biosensors for EV characterization due to their high sensitivity and ability to monitor binding events in real-time. However, there are drawbacks of the technique that needs to be addressed. For instance, detection of EVs in complex sample matrices including biological fluids without pre-treatment remains challenging. In addition, SPR sensors may provide false-positive or false-negative results as a consequence of artifactual changes in the refractive index. Also, EV heterogeneity is rarely addressed in the above-described sensors which may certainly affect the measurements.

Table 2: Summary of label-free optical methods for EV biochemical composition characterization

Method	Biochemical information	Data acquisition time	Sample type Liquid/ dry	Advantages	Disadvantages	References
Raman spectroscopy	Protein, lipid, nucleic acids, metabolites, and saccharides	Minutes	Liquid/ dry	Quantitative and qualitative characterization of surface and internal biochemical content of EVs, is able to reveal conformational form and structure of proteins and lipids, minimal preprocessing, small,	Weak Raman scattering, Low throughput	23,24

				sample size		
SERS	Protein, lipid, nucleic acids, metabolites, and saccharides	Minutes	Liquid/dry	Quantitative and qualitative characterization of surface biochemical content of EVs, is able to reveal conformational form and structure of proteins and lipids, minimal preprocessing, small sample size	Limited by the distance between biomolecule and the SERS substrate, suitable for characterization of membrane bounded molecules	25,26
SPR	Specific molecules (proteins and lipids) of interest	~Hour	Liquid	Real-time monitoring of EV-ligand binding kinetics, small sample size	Labor intensive, limited by use of capturing molecules	27
IR spectroscopy	Protein, lipid, nucleic acids, and saccharides	Seconds	Liquid/dry	Quantitative and qualitative characterization of EV biochemical content, minimal preprocessing, small sample size	Low throughput	28
Multiphoton microscopy	Metabolites	Seconds	Liquid/dry	Single EV analysis, allows investigation of EV functions <i>in vivo/in situ</i>	Limited by penetration depth (250-500 um), costly, phototoxicity	29

2.5.4 Infrared spectroscopy

FTIR spectroscopy is a vibrational spectroscopy technique that primarily uses the ability of chemical bonds within a biomolecule to absorb in the mid-infrared range of the electromagnetic spectrum.

The method describes specific absorption bands of proteins, lipids, and nucleic acids that may be found in the molecular cargo of EVs [197]. Moreover, FTIR provides quantitative spectral data and may highlight possible alterations in EV biochemical composition based on a clinical condition of a patient. Additionally, FTIR is sensitive to the conformation of the analyzed biomolecules that is not commonly described by conventional EV characterization techniques and may have valuable clinical information.

From the first study published in 2016 [198], FTIR spectroscopy has shown to be an effective method for EV characterization. Using FTIR, Mihaly et.al., analyzed EV subpopulations and found differences in protein secondary structure and lipid content among EV subpopulations [199]. These findings were further confirmed by analyzing EV subpopulations enriched from cancer cell lines highlighting FTIR as an effective tool for quick EV subpopulation characterization [200, 201]. Recent studies reported the use of FTIR to characterize changes in the biochemical composition of EVs released from cell cultures mimicking various pathological conditions such as septic shock [202], cancer [201, 203–206], AD [217] as well as the effect of cellular treatment on EV cargo [208]. In addition, IR of single microvesicles by coupling IR and AFM have been reported [209] (Table 2).

2.5.5 Multiphoton microscopy

MM is a powerful technique that allows imaging of cellular and subcellular processes *in vivo*. The method is based on the simultaneous absorption of two or more light photons by the molecule of interest [213]. It had been used to study cell–cell interactions, embryonic development, cancer, and neurology [214]. In the field of EV research, multiphoton microscopy may offer unique opportunities to explore EV dynamic (release and uptake) *in vivo*. Specifically, second and third harmonic generation in combination with autofluorescence imaging are suitable for label-free detection and characterization of EV molecular components including metabolites, structural proteins, and lipids. To our knowledge so far, a single study applied label-free multiphoton microscopy for EV characterization. You et al. studied EVs isolated from breast

cancer tissue using multiphoton microscopy [212]. They were able to visualize EVs, characterize their metabolic profile as well as track EV release, movement, and uptake. The main finding of the study indicates high enrichment of nicotinamide adenine dinucleotide phosphate (NADPH) in breast cancer patients' EVs. Finally, the authors reported the ability of the multiphoton microscopy to study EV release, movement, and uptake *in situ*. Indeed, as it is the case for all analytical techniques multiphoton microscopy has its own limitations such as relatively poor spatial resolution, limited penetration depth (250–500 μm), phototoxicity, and costly optical microscopy components.

2.6 Applications

Label-free optical methods have been used to detect and characterize EVs as potential biomarkers for the diagnosis of various diseases including neurological disorders and cancer [215]. Moreover, EVs exhibit great potential to be utilized as drug delivery vehicles for disease treatment. In this section, we will discuss applications of label-free optical methods for the diagnosis of neurodegenerative diseases and different cancer types.

2.6.1 Neurodegenerative diseases

The human central nervous system (CNS) is a complex organ where cell-cell communication is crucial for the processing and transmission of information. The main constituents of CNS are neurons and glial cells. The functions of these highly specialized cells are controlled and organized by the communication system of secreted molecules, and EVs have been suggested to play a role in it. EVs are found to be released by all types of CNS cells, including neurons, astrocytes, oligodendrocytes, microglia, and Schwann cells. Existing knowledge indicates the role of glial cells EVs in neuronal maintenance, trophic support, and homeostasis including neurite growth and axonal protection (synapsin I [216], neuroglobin [217], prion protein [218], HSPc70 [219] in EVs) [220–222], myelination [223] and stress response, oligodendrocyte-microglia communication [224–226], and synaptic plasticity [227–230] (Figure 6A). Moreover, EVs are also considered as important mediators of neuronal communication [231] and are able to bypass the blood-brain barrier [232]. In addition to their essential role in the normal physiology of CNS, it is hypothesized that EVs contribute to the pathogenesis of neurodegenerative diseases (ND) *via* the transport of misfolded proteins including prion [233], A β [234, 235], tau [236], and α -synuclein [237] as well as specific populations of nucleic acids [238]. More importantly, EVs

have the potential to be used as readily accessible liquid biomarkers for the detection of neurodegenerative diseases. Nowadays, identification and quantification of potential ND biomarkers require the use of invasive collection techniques, which therefore makes routine diagnosis and monitoring of diseases progression challenging. CSF is considered as a body fluid that reflects molecular processes in the brain. Currently, measurements of $A\beta_{1-42}$, total tau, p-tau, and α -synuclein concentration in CSF are used for the diagnosis of some types of neurological diseases. However, invasiveness and the relative high cost of the CSF collection procedure over blood collection are the main drawbacks of the method. In addition, extremely low concentrations of misfolded proteins in CSF and blood of patients limit their use as biomarkers [239]. Therefore, the use of brain-derived EVs carrying ND markers may potentially address aforementioned problems. EVs are found in CSF and blood of patients with various neurological disorders, yet purification of specific brain derived EV subpopulations remains challenging. Several studies proposed the affinity-immunocapture method to select EVs based on their surface markers. This method has been used to analyze EV-associated biomarkers of AD, Parkinson's disease (PD), and amyotrophic lateral sclerosis (ALS) isolated from patients' peripheral blood [240–246].

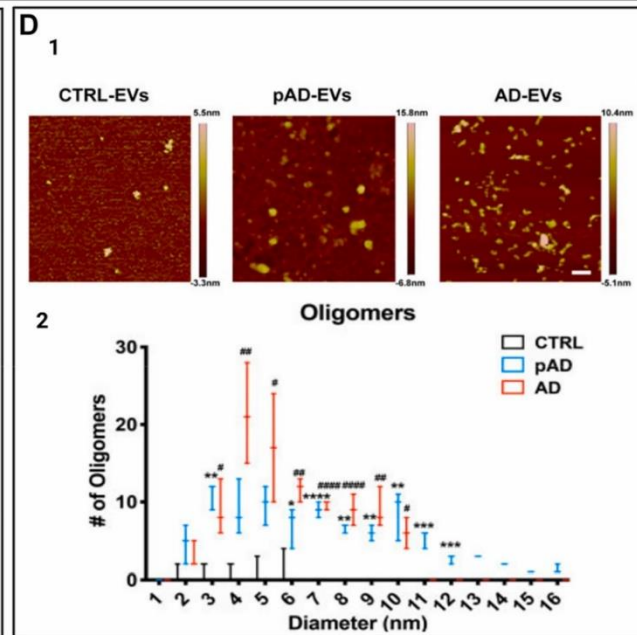
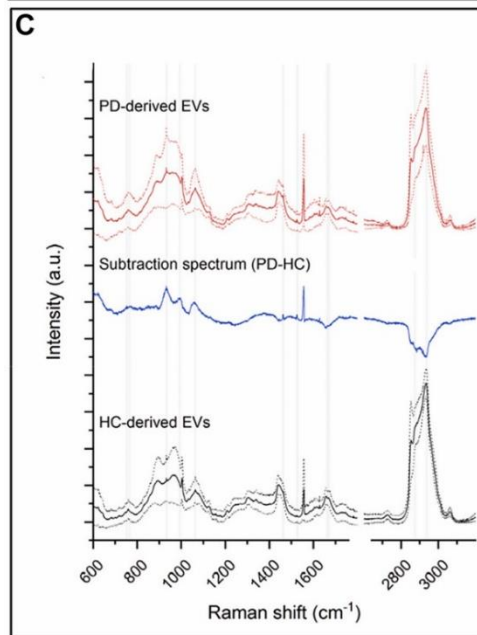
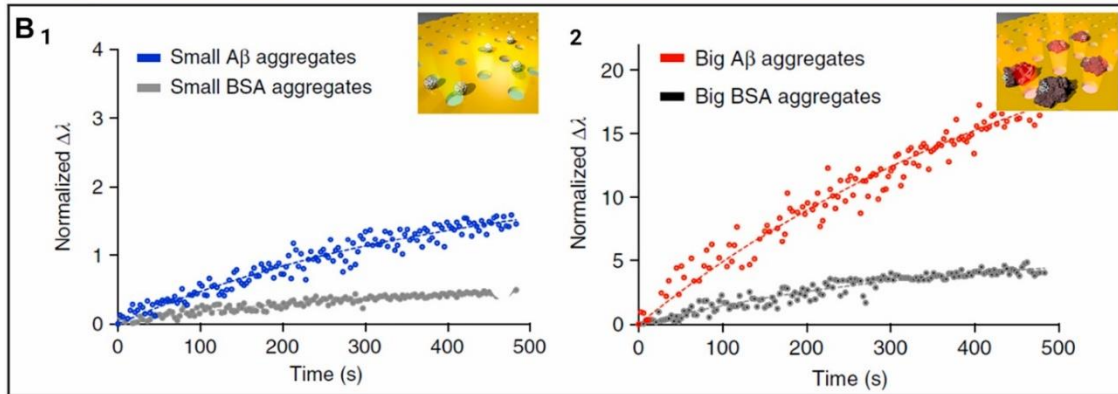
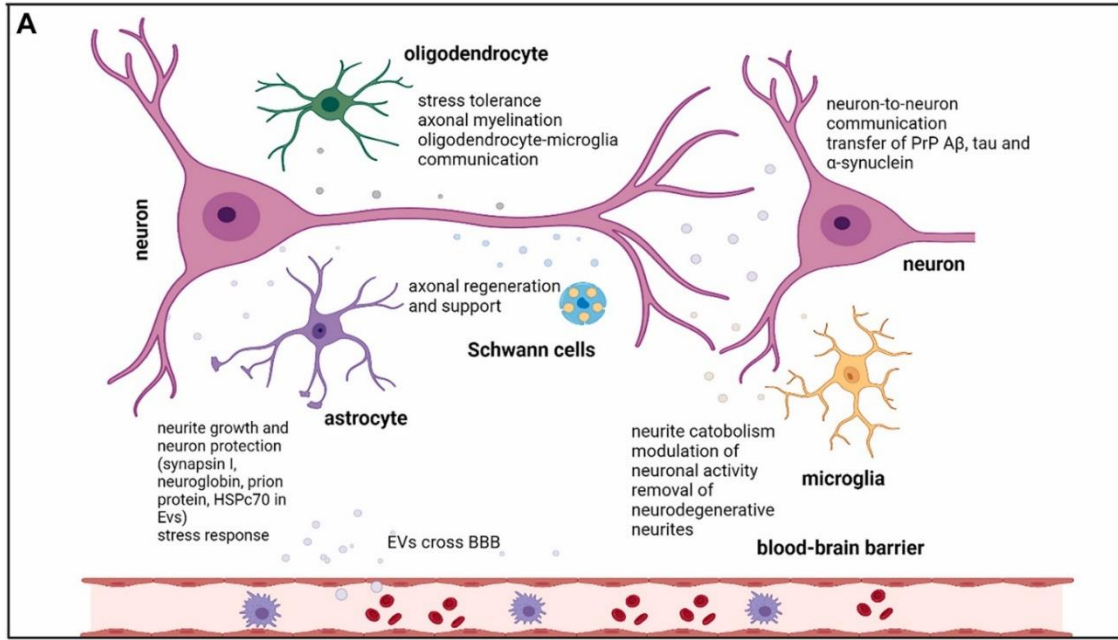


Figure 6: Application of label-free optical methods for characterization of EVs isolated from patients with neurological disorders. (A) Schematic of EVs based intercellular communication in CNS. (B) APEX platform for exosome associated A β detection. SPR sensograms showing exosome binding kinetics to (B1) small and (B2) large A β aggregates as well as to control bovine serum albumin (BSA) aggregates (adapted with permission from [250]). (C) Raman spectroscopy-based characterization of EVs for detection of patients with PD. Average Raman spectra of PD patients' serum derived EVs (red spectra) and EVs isolated from the serum of healthy individuals (black spectra). The main spectral differences between the two groups are depicted by blue Raman spectra that is obtained by subtraction between PD-derived EVs Raman spectra and healthy control group EVs Raman spectra (adapted with permission from [248]). (D) Characterization of brain-derived EVs tau oligomers by AFM; (D1) AFM images of EV-associated tau oligomers isolated from AD and prodromal AD (pAD) brains; (D2) graph shows size distribution of A β oligomers (adapted with permission from [251]).

Label-free optical methods have not been widely used for the detection and characterization of CNS-derived EVs. Indeed, NTA and DLS have been used commonly to characterize the size and concentration of EVs, yet these methods did not yield ND specific information through EV analysis. There are few reports in the literature that described the use of Raman spectroscopy for the identification of ND biomarkers in EVs derived from patients' blood [247, 248]. Gualerzi et al. demonstrated the use of Raman microspectroscopy to stratify PD patients from a healthy individual group based on their circulating EV biochemical profile [247] (Figure 6C). The main differences found in spectra of two groups attributed to protein and lipid content of analyzed EVs, where the spectra from healthy control-derived EVs showed higher relative intensities of the amide I protein band and 2800–3000 cm^{-1} lipid band compared to PD EVs spectra. On the other hand, some peaks corresponding to carbohydrates centered at 930, 960, 1370, and 1436 cm^{-1} and lipid peak centered at 1057 cm^{-1} showed higher intensities in spectra of PD derived EVs. Further, the authors applied PCA to discriminate the analyzed groups of patients based on their EVs profile.

Another study used a similar Raman spectroscopy-based approach to identify differences in biochemical content of ALS patients' EVs [248]. In this study authors isolated small and large EVs from plasma of age-match groups of ALS patients and healthy donors. The main findings indicate a difference in EV lipid and protein profile of ALS patients compared to healthy patients.

Taken together these studies validated the ability of Raman spectroscopy to identify differences in the EV biochemical content of PD patients compared to healthy individuals. However, the origin of the described differences in Raman spectra remains to be explored.

Next, there are several reports describing the application of SPR for CNS-derived EV analysis. Lim and co-authors developed a SPR-based platform termed APEX that was applied to measure exosome-bonded A β proteins directly from AD patients' blood (Figure 6B). Their findings indicated that exosomes preferentially bound to large prefibrillar A β aggregates [249] and better reflect neuroimaging results in comparison with total circulating A β . Further, the reported results are similar to PET tracers binding behavior that particularly binds to large A β aggregates and demonstrate a lower binding activity to smaller aggregates.

Another study utilized SPR to measure the concentration of A β , ganglioside M1 (GM1), and translocator protein (TSPO) in AD EVs [251]. In this pilot study, EVs were isolated from the plasma of AD patients ($n=10$) and healthy individuals ($n=10$) *via* size exclusion chromatography. Further NTA analysis revealed a higher concentration of EVs in AD patients in plasma (1.18×10^{11} particles/ml) compared to healthy subjects (2.34×10^{10} particles/ml). Moreover, SPR imaging showed a higher signal of activated microglia EVs in AD patients' plasma supporting the potential contribution of neuroinflammation to the pathogenesis of AD. Furthermore, SPR enabled simultaneous detection of potential AD biomarkers including A β , TSPO, and GM1. The results of these specific molecules associated with plasma EVs showed a higher amount of all markers of interest in AD EVs compared to healthy controls EVs.

Additionally, AFM has been employed to characterize EV-associated tau oligomers [250]. In this study results of AFM analysis showed the presence of 4–6 nm globular particles, tau oligomers, in fractions of AD and prodromal AD EVs (Figure 6D). In contrast, EVs isolated from control samples did not contain described oligomers. These data suggest enrichment of AD EVs with tau oligomers and their potential pathogenic functions as tau seeding vehicles.

Finally, label-free optical methods have a great potential to be used not only by complementing traditional label-based characterization techniques but to reveal new information about EV biology and potential application as a liquid biopsy for the diagnosis of ND. For instance, these methods may be used to discover disease-specific conformation of misfolded proteins associated

with EVs, where this information is lacking or difficult to explore using current label-based assays.

2.6.2 Cancer

The detection and characterization of EVs as cancer biomarkers is particularly useful for the noninvasive early diagnosis of various types of cancers. Label-free optical methods for EV analysis can provide valuable information about the EV structure and molecular content that cannot be achieved using other methods.

Multiple myeloma is an incurable type of bone marrow cancer formed by malignant plasma cells. Multiple myeloma is always preceded by monoclonal gammopathy of uncertain significance (MGUS), which later slowly progresses to asymptomatic multiple myeloma or symptomatic multiple myeloma. Since the molecular composition of the cargo transported by EVs is dependent on their cells of origin, EVs have been found to be particularly useful in cancer detection and evaluation of the disease progression and in providing clinical info for patient care. Raman spectroscopy is capable of characterizing circulating EVs from a liquid biopsy sample, being a robust technique used not only for cancer detection but also for its prognosis. The spectra of EVs extracted from the serum of multiple myeloma patients in different stages are analyzed by PCA, which effectively stratified these three different clinical conditions [252, 253]. As can be seen in Figure 7A, the EVs' Raman spectra recorded with an 830 nm laser source are very similar, exhibiting the major known peaks. The most intense peak is phenylalanine at 1003 cm^{-1} , amide III, nucleic acids, and fatty acids' signature are located between 1240 and 1340 cm^{-1} , CH deformations in lipids and proteins are at 1440 – 1450 cm^{-1} , while the amide I vibration of proteins band shows up at 1640 – 1700 cm^{-1} (Figure 7A1). Even though they present similar patterns, they can be clearly separated and stratified by multivariate analysis as shown in Figure 7A2 and 7A3. Although the collected SERS measurements show promising results, poor reproducibility of spectra collection is a major challenge. This is possibly due to the use of SERS substrate with random Au nanostructures. The acquisition of reproducible SERS spectra requires highly ordered SERS substrates, which in turn will increase the cost of the EVs testing due to a more expensive substrate fabrication process. Additionally, SPR biosensors have been used to detect multiple myeloma and stratify multiple myeloma patients from MGUS patients and healthy individuals [254]. These studies reported a 4-fold increase in sEV concentration in

serum of multiple myeloma patients ($n=10$) compared to healthy subjects ($n=10$) and MGUS patients ($n=5$).

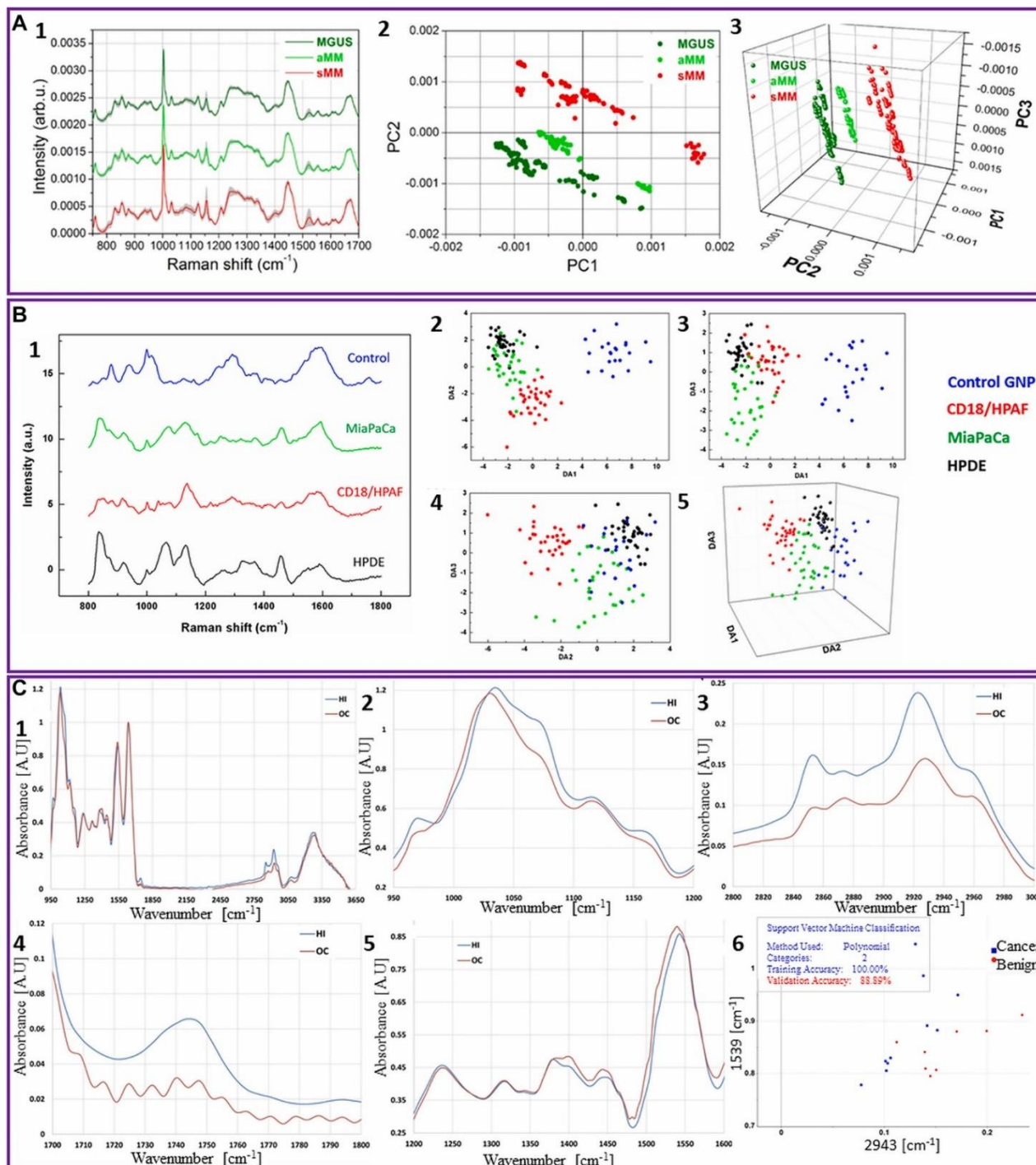


Figure 7: Application of label-free optical methods for characterization of EVs isolated from cancer patients.

(A) Raman spectra recorded from EVs isolated from multiple myeloma patients and their PCA analysis; (A1) Average Raman spectra collected from EVs isolated from patients with different stages of multiple myeloma; (A2)

PCA analysis shows the stratification of EVs based on the stage of multiple myeloma patients; (A3) 3D scatter plot of PCA analysis (adapted with permission from [254]). (B) SERS spectra of EVs and their PCA and DFA analysis used for the early detection of pancreatic cancer; (B1) SERS spectra of EVs from both normal human pancreatic ductal epithelial cell line (HPDE) and pancreatic cancer cell lines (CD18/HPAF, MiaPaCA); (B2)–(B5) Scatter plots of the discriminant function classifiers DAs showing the capability of the PC-DFA algorithm to differentiate different EVs subpopulations; (B2) Scatter plot of DA1 versus DA2; (B3) Scatter plot of DA1 versus DA3; (B4) Scatter plot of DA2 versus DA3; (B5) Scatter plot of DA1 versus DA2 versus DA3 (reproduced with permission [256]). (C) Label-free FTIR EVs analysis used in the diagnosis of oral cancer. Average IR absorbance spectra of the oral cancer patients and healthy individuals EVs in the range of: (C1) 950–3650 cm^{-1} ; (C2) 950–1200 cm^{-1} ; (C3) 1200–1600 cm^{-1} ; (C4) 1700–1800 cm^{-1} ; (C5) 2800–3000 cm^{-1} ; (C6) Support vector machine classification results clearly separate cancer and benign originating EVs (adapted with permission from [205]).

Pancreatic cancer is a highly lethal disease characterized by a relentless progression with a five-year survival rate of around 3% due to the late diagnosis when metastasis has already occurred. In an effort to address this issue, Carmicheal et. al. proposed a SERS detection platform combined with principal component discriminant function analysis (PC-DFA). In this study, EVs were collected from the supernatant of one healthy and two pancreatic cancer cell lines [255] (Figure 7B1). For detection, positively charged 10 nm AuNPs were used to bind to the surface of isolated EVs and to form a large number of hotspots that highly amplify the Raman signal. As we mentioned before, the EVs surface composition is highly variable between cancer and healthy EVs. The label-free SERS identifies the molecular signature of isolated EVs and the PC-DFA analysis separates them based on spectral differences. To determine the diagnostic accuracy of the method, EVs collected from serum samples of 10 benign control patients and 10 pancreatic cancer patients with early-stage disease were analyzed (Figure 7B2–5). The predictive capabilities still need to be improved, which is not surprising considering the diverse origin of EVs in patient serum, especially in the case of early-stage cancer patients which usually have a large percentage of EVs arising from the normal epithelium. This study demonstrates the potential of SERS combined with PC-DFA analysis for the detection of pancreatic cancer. A recent study by Rasuleva et. al. applied FTIR to the study of tumor-derived sEVs as potential diagnostic biomarkers for pancreatic cancer detection [256]. FTIR revealed enrichment of beta-sheet proteins in tumor derived sEVs ($n=15$) compared to control sEVs ($n=15$).

Oral cancer is another type of cancer that can be diagnosed using EVs. Oral cancer has a high global incidence with more than 657,000 new cases and 330,000 deaths annually, being the 8th

most common cancer in the world [257]. Even if the oral cavity has an easy access for examination, usually this type of cancer is diagnosed in the late stages due to subtle mucosal lesions that appear in the early stages of the disease. By the time of concluding diagnosis, the 5-year survival rate decreases considerably to less than 50%. Therefore, screening and early detection of oral cancer are critical for improving survival rates and monitoring its progression. A recent study used FTIR in Attenuated Total Reflection (ATR) mode combined with machine learning methods to study and differentiate EVs isolated from the saliva of 21 oral cancer diagnosed patients and 13 healthy individuals [204] (Figure 7C). FTIR spectra highlighted the differences in the EV content and structure of nucleic acids, lipids, and proteins. These differences can be described mainly by a lower intensity of the oral cancer EV peaks at 1072 cm^{-1} , 2924 cm^{-1} , and 2854 cm^{-1} corresponding to nucleic acids and lipids, respectively, compared with healthy EV spectra (Figure 7C1–5). Also, the relative intensity ratio of peaks centered at 1033 cm^{-1} and 1072 cm^{-1} (I_{1033}/I_{1072}) and attributed to glycogen/carbohydrates and nucleic acids ratio, is higher in oral cancer-derived EV spectra compared to control EV spectra. The PCA–LDA and SVM methods used for the analysis and classification of EVs showed a 100% sensitivity, 89% specificity, and 95% accuracy (Figure 7C6). This clearly proves the potential of this method to be further implemented in clinical facilities for the early diagnosis of oral cancer from liquid biopsy samples.

Finally, using SERS, Ma et. al. were able to detect exosomal miRNA-21 as a potential cancer biomarker [259]. The results of the study showed an increased concentration of sEV miRNA-21 (6.59×10^{-3} molecules/EV) in lung cancer patient samples compared to healthy subjects (1.26×10^{-3} molecules/EV). Another study reports the application of SERS as a tool for cancer diagnosis [259]. Rojalín et. al. used SERS to stratify ovarian cancer and endometrial patients. The authors developed a nanoplasmonic substrate that was chemically pretreated for nonspecific capturing of sEVs. The SERS platform allowed the separation of cancerous sEVs and their differentiation from healthy control derived sEVs. Importantly, this study suggested a critical role of protein corona and glycocalyx in sEV functions.

Overall, label-free methods for EVs analysis show the potential to differentiate between healthy and cancerous cell-derived EVs, justifying future clinical studies for early diagnosis of various types of cancer using liquid biopsy samples.

2.6.3 Data analysis

Analysis of large data sets is important for providing valuable predictive information. One of the promising, emerging approaches to handle large data sets and discriminate subpopulations of EVs is machine learning (ML). ML algorithms are well equipped to deal with segmentation of large and complex datasets that are typically encountered in heterogenous EVs samples. For example, microscopy images and spectral data from Raman spectroscopy and SERS can be analyzed and processed into various clusters and subpopulations.

ML algorithms can be supervised, meaning that the algorithms are trained on datasets where each training example is explicitly labeled with its corresponding desired output value. This is specifically useful in clinical cases, where diagnostic criteria or biomarkers are known, and the objective is to have a predictive model. Supervised ML models for EVs analysis has been used for the detection of cancers [176, 204, 255, 259] and neurodegenerative diseases [248].

Unsupervised ML algorithms are not trained on pre-labeled datasets and therefore must interpret data patterns on their own. Clustering and PCA are examples of unsupervised ML that are used in EVs research [156, 64, 157, 168, 176, 204]. The interesting aspect of unsupervised learning is the potential to discover previously unknown underlying patterns within datasets that the algorithms have identified without human input. For classification problems, an ML model's performance is evaluated based on the AUC (area under the curve) ROC (receiver operating characteristic) curve. The ROC curve plots the true positive rate (sensitivity) against the false-positive rate for different classification threshold values. The AUC can be calculated as the area under the plotted ROC, and it determines the model's ability to separate the classes, or the performance of the model through the various classification thresholds. ML models that maximize this metric are very well suited for classification of EVs into healthy or diseased groups. In further studies it is essential to incorporate ML methods to assess different populations of EVs and determine clinically viable diagnostic methods based on optical label-free techniques.

Deep learning (DL) is a subset of ML that uses neural networks to create layers of algorithms to process large-scale datasets. The neural network structure to some extent mimics the interconnection of neurons in the human brain. Predictive classification models have been developed using DL approaches and they can achieve more "human-like" decision-making. EV

research using DL is less common. Shin et al., applied DL approach to classify cancer EVs from healthy patients derived EVs [260]. The DL model was trained using SERS spectra of lung cancer cell lines EVs and human pulmonary alveolar epithelial cell line EVs as healthy control EVs and was able to stratify them with 95% accuracy. Furthermore, the developed DL model was tested using EVs isolated clinical samples. It was able to predict lung cancer for all patients (stages 1A, 1B, and 2B) with an AUC of 0.912 and for stage 1 patients specifically, the model predicted lung cancer with an AUC of 0.910, demonstrating potential for noninvasive, early-stage diagnostics.

2.7 Conclusions and perspectives

As shown in this review, optical label-free methods are currently used as complementary to conventional EV characterization methods. We anticipate the coexistence of label-free and conventional technologies when the users need to analyze complex analytes such as EVs.

Label-free optical methods enhance the growing field of EV research by providing effective tools for disease specific biomarkers discovery and simultaneous detection of multiple markers of disease specific molecular fingerprints in small volumes of samples. Among optical label-free technologies described in this review NTA, SPR, and FC gained the most popularity in the EV research field. To date, label-free optical technologies have been most successfully applied for the characterization of EV morphological features such as size, shape, and concentration as well as characterizing the biochemical content of EVs. Furthermore, they have been mostly applied for the detection of EV-associated markers of various cancer types but have been less commonly used for the diagnosis of other diseases.

Classification of EVs into subpopulations of interest has generally been difficult, due to complex heterogeneity and limited characterization capabilities. Variations between these subpopulations are important to be analyzed to better understand their role in the normal physiology and pathology of the disease. To better quantify these variations, comprehensive and accurate methodologies for the characterization of subpopulations are required. Furthermore, introducing standardized isolation, processing, and analysis methods for different subpopulations of EVs would be a significant benefit to the field, allowing for more consistent and accurate results. In addition, quantitative methods of analysis are critical for establishing EVs as clinical biomarkers and for the development of clinical guidelines.

One of the major current challenges for new technologies to provide accurate diagnosis *via* EVs is the fact that the accuracy of EVs as biomarkers of disease is not always known. It is not always possible to differentiate between the accuracy of a specific biosensing technique and the accuracy of the EVs themselves as biomarkers of pathology. This ambiguity is a key impediment to establishing EVs for clinical use. Biomarkers can be established directly through clinical data or indirectly through a gold-standard methodology. When new biosensors or biosensing methodologies are designed, they are generally developed based on and compared to established biomarkers and their gold-standard detection. In the case of EVs, biosensor development may become problematic, because the accuracy of EVs as biomarkers to diagnose specific diseases is not always established. Consequently, the performance metrics of biosensors tested on unestablished biomarkers is ambiguous, as both the biosensor and the biomarker influence the overall performance.

Within EV research, ML is an emerging technique used for classifying and clustering samples within large datasets. Various ML algorithms have been employed for classifying clinical samples as well as for investigating underlying patterns within complex, heterogeneous EVs samples to elucidate new subpopulation criteria. Numerous current reports focus on developing predictive models using ML algorithms. Notably, cancers and neurodegenerative diseases have shown to be well classified by predictive models. Integrating ML and including DL into further studies on EVs and their subpopulations or pathology is an important avenue to develop diagnostic criteria, especially combined with high-throughput optical label-free characterization techniques.

Overall, despite many challenges, we expect the field to grow in significance in the near future for liquid biopsy applications, driven by biomarker discovery, standardized sample handling and isolation, technological improvements for characterization, and advanced data analysis methodologies.

Funding source: Natural Sciences and Engineering Research Council of Canada

Award Identifier / Grant number: Discovery RGPIN-2018-05675

Funding source: Faculty of Engineering, McGill University

Funding source: Fonds de Recherche du Québec - Nature et Technologies

Author contributions: SWH and MI conceived the idea and defined the structure and content of the manuscript, MI wrote most of the manuscript, SS, YL, and SJ contributed to parts of the manuscript. SWH supervised the project. All authors reviewed and approved the manuscript in current form.

Research funding: This work was financially supported by the Natural Sciences and Engineering Research Council of Canada (NSERC), Discovery Grant RGPIN-2018-05675 (to S.W.-H.); M.I. acknowledges the FRQNT award for PhD studies; YL was financially supported by the McGill SURE undergraduate internship.

Conflict of interest statement: The authors declare that the research was conducted in the absence of any commercial or financial relationships that could be construed as a potential conflict of interest.

References

1. G. van Niel, G. D'Angelo, and G. Raposo, "Shedding light on the cell biology of extracellular vesicles," *Nat. Rev. Mol. Cell Biol.*, vol. 19, pp. 213–228, 2018.
2. E. R. Abels and X. O. Breakefield, "Introduction to extracellular vesicles: biogenesis, RNA cargo selection, content, release, and uptake," *Cell. Mol. Neurobiol.*, vol. 36, pp. 301–312, 2016.
- 105 M. Mathieu, L. Martin-Jaular, G. Lavieu, and C. Théry, "Specificities of secretion and uptake of exosomes and other extracellular vesicles for cell-to-cell communication," *Nat. Cell Biol.*, vol. 21, pp. 9–17, 2019.
4. S. Caruso and I. K. H. Poon, "Apoptotic cell-derived extracellular vesicles: more than just debris," *Front. Immunol.*, vol. 9, p. 1486, 2018.
5. H. Hirata, A. Takahashi, S. Kobayashi, et al., "Caspases are activated in a branched protease cascade and control distinct downstream processes in fas-induced apoptosis," *J. Exp. Med.*, vol. 187, pp. 587–600, 1998.
6. M. P. Zaborowski, L. Balaj, X. O. Breakefield, and C. P. Lai, "Extracellular vesicles: composition, biological relevance, and methods of study," *Bioscience*, vol. 65, pp. 783–797, 2015.
7. E. Willms, C. Cabañas, I. Mäger, M. J. A. Wood, and P. Vader, "Extracellular vesicle heterogeneity: subpopulations, isolation techniques, and diverse functions in cancer progression," *Front. Immunol.*, vol. 9, p. 738, 2018.
8. L. M. Doyle and M. Z. Wang, "Overview of extracellular vesicles, their origin, composition, purpose, and methods for exosome isolation and analysis," *Cells*, vol. 8, p. 727, 2019.
9. J. Conde-Vancells, E. Rodriguez-Suarez, N. Embade, et al., "Characterization and comprehensive proteome profiling of exosomes secreted by hepatocytes," *J. Proteome Res.*, vol. 7, pp. 5157–5166, 2008.
10. T. Skotland, K. Sagini, K. Sandvig, and A. Llorente, "An emerging focus on lipids in extracellular vesicles," *Adv. Drug Deliv. Rev.*, vol. 159, pp. 308–321, 2020.

11. H. Valadi, K. Ekström, A. Bossios, M. Sjöstrand, J. J. Lee, and J. O. Lötvall, “Exosome-mediated transfer of mRNAs and microRNAs is a novel mechanism of genetic exchange between cells,” *Nat. Cell Biol.*, vol. 9, pp. 654–659, 2007.
12. E. Z. Malkin and S. V. Bratman, “Bioactive DNA from extracellular vesicles and particles,” *Cell Death Dis.*, vol. 11, p. 584, 2020.
13. C. Gardiner, D. D. Vizio, S. Sahoo, et al., “Techniques used for the isolation and characterization of extracellular vesicles: results of a worldwide survey,” *J. Extracell. Vesicles*, vol. 5, p. 32945, 2016.
14. C. Théry, K. W. Witwer, E. Aikawa, et al., “Minimal information for studies of extracellular vesicles 2018 (MISEV2018): a position statement of the international society for extracellular vesicles and update of the MISEV2014 guidelines,” *J. Extracell. Vesicles*, vol. 7, p. 1535750, 2018.
15. F. J. Verweij, L. Balaj, C. M. Boulanger, et al., “The power of imaging to understand extracellular vesicle biology in vivo,” *Nat. Methods*, vol. 18, pp. 1013–1026, 2021.
16. M. S. T. Gonçalves, “Fluorescent labeling of biomolecules with organic probes,” *Chem. Rev.*, vol. 109, pp. 190–212, 2009.
17. S. Vallabhajosula, D. Lyden, H. P. Selgas, and A. Nikolopoulou, *Radiolabeled Exosomes for the Early Detection of Metastases and to Predict Breast Cancer Premetastatic Niche*, NEW YORK, Cornell Univ Medical Coll (WEILL), 2015.
18. P. P. Dominkuš, M. Stenovec, S. Sitar, et al., “PKH26 labeling of extracellular vesicles: Characterization and cellular internalization of contaminating PKH26 nanoparticles,” *Biochim. Biophys. Acta Biomembr.*, vol. 1860, pp. 1350–1361, 2018.
19. V. Hyenne, S. Ghoroghi, M. Collot, et al., “Studying the fate of tumor extracellular vesicles at high spatiotemporal resolution using the zebrafish embryo,” *Dev. Cell*, vol. 48, pp. 554–572, 2019.
20. F. J. Verweij, C. Revenu, G. Arras, et al., “Live tracking of inter-organ communication by endogenous exosomes in vivo,” *Dev. Cell*, vol. 48, pp. 573–589, 2019.
21. K. E. van der Vos, E. R. Abels, X. Zhang, et al., “Directly visualized glioblastoma-derived extracellular vesicles transfer RNA to microglia/macrophages in the brain,” *Neuro Oncol.*, vol. 18, pp. 58–69, 2015.
22. A. Y. T. Wu, Y. C. Sung, Y. J. Chen, et al., “Multiresolution imaging using bioluminescence resonance energy transfer identifies distinct biodistribution profiles of extracellular vesicles and exomeres with redirected tropism,” *Adv. Sci.*, vol. 7, p. 2001467, 2020.
23. M. Dehghani, S. M. Gulvin, J. Flax, and T. R. Gaborski, “Systematic evaluation of PKH labelling on extracellular vesicle size by nanoparticle tracking analysis,” *Sci. Rep.*, vol. 10, p. 9533, 2020.
24. K. Rautaniemi, J. Zini, E. Löfman, et al., “Addressing challenges in the removal of unbound dye from passively labelled extracellular vesicles,” *Nanoscale Adv.*, vol. 4, pp. 226–240, 2022.
25. J. B. Simonsen, “Pitfalls associated with lipophilic fluorophore staining of extracellular vesicles for uptake studies,” *J. Extracell. Vesicles*, vol. 8, p. 1582237, 2019.
26. J. Icha, M. Weber, J. C. Waters, and C. Norden, “Phototoxicity in live fluorescence microscopy, and how to avoid it,” *Bioessays*, vol. 39, p. 1700003, 2017.

27. M. Yáñez-Mó, P. R. M. Siljander, Z. Andreu, et al., “Biological properties of extracellular vesicles and their physiological functions,” *J. Extracell. Vesicles*, vol. 4, p. 27066, 2015.
28. R. Kalluri and S. LeBleu Valerie, “The biology, function, and biomedical applications of exosomes,” *Science*, vol. 367, p. eaau6977, 2020.
29. C. Théry, L. Zitvogel, and S. Amigorena, “Exosomes: composition, biogenesis and function,” *Nat. Rev. Immunol.*, vol. 2, pp. 569–579, 2002.
30. G. Raposo and W. Stoorvogel, “Extracellular vesicles: exosomes, microvesicles, and friends,” *JCB (J. Cell Biol.)*, vol. 200, pp. 373–383, 2013.
31. C. Raiborg and H. Stenmark, “The ESCRT machinery in endosomal sorting of ubiquitylated membrane proteins,” *Nature*, vol. 458, pp. 445–452, 2009.
32. J. Huotari and A. Helenius, “Endosome maturation,” *EMBO J.*, vol. 30, pp. 3481–3500, 2011.
33. E. Nielsen, F. Severin, J. M. Backer, A. A. Hyman, and M. Zerial, “Rab5 regulates motility of early endosomes on microtubules,” *Nat. Cell Biol.*, vol. 1, pp. 376–382, 1999.
34. G. Li and M. C. Marlin, “Rab family of GTPases,” *Methods Mol. Biol.*, vol. 1298, pp. 1–15, 2015.
35. R. L. Williams and S. Urbé, “The emerging shape of the ESCRT machinery,” *Nat. Rev. Mol. Cell Biol.*, vol. 8, pp. 355–368, 2007.
36. S. Stuffers, C. Sem Wegner, H. Stenmark, and A. Brech, “Multivesicular endosome biogenesis in the absence of ESCRTs,” *Traffic*, vol. 10, pp. 925–937, 2009.
37. K. Trajkovic, C. Hsu, S. Chiantia, et al., “Ceramide triggers budding of exosome vesicles into multivesicular endosomes,” *Science*, vol. 319, pp. 1244–1247, 2008.
38. G. Van Niel, S. Charrin, S. Simoes, et al., “The tetraspanin CD63 regulates ESCRT-independent and-dependent endosomal sorting during melanogenesis,” *Dev. Cell*, vol. 21, pp. 708–721, 2011.
39. Z. Andreu and M. Yáñez-Mó, “Tetraspanins in extracellular vesicle formation and function,” *Front. Immunol.*, vol. 5, p. 442, 2014.
40. Y. Feng, B. Press, and A. Wandinger-Ness, “Rab 7: an important regulator of late endocytic membrane traffic,” *JCB (J. Cell Biol.)*, vol. 131, pp. 1435–1452, 1995.
41. M. Ostrowski, N. B. Carmo, S. Krumeich, et al., “Rab27a and Rab27b control different steps of the exosome secretion pathway,” *Nat. Cell Biol.*, vol. 12, pp. 19–30, 2010.
42. G. Raposo, D. Tenza, S. Mecheri, R. Peronet, C. Bonnerot, and C. Desaymard, “Accumulation of major histocompatibility complex class II molecules in mast cell secretory granules and their release upon degranulation,” *Mol. Biol. Cell*, vol. 8, pp. 2631–2645, 1997.
43. A. Savina, C. M. Fader, M. T. Damiani, and M. I. Colombo, “Rab11 promotes docking and fusion of multivesicular bodies in a calcium-dependent manner,” *Traffic*, vol. 6, pp. 131–143, 2005.
44. P. D. Stahl and G. Raposo, “Vesicles: exosomes and microvesicles, integrators of homeostasis,” *Physiology*, vol. 34, pp. 169–177, 2019.

45. J. Kowal, G. Arras, M. Colombo, et al., “Proteomic comparison defines novel markers to characterize heterogeneous populations of extracellular vesicle subtypes,” *Proc. Natl. Acad. Sci. U. S. A.*, vol. 113, pp. E968–E977, 2016.
46. H. Zhang, D. Freitas, H. S. Kim, et al., “Identification of distinct nanoparticles and subsets of extracellular vesicles by asymmetric flow field-flow fractionation,” *Nat. Cell Biol.*, vol. 20, pp. 332–343, 2018.
47. F. G. Kugeratski, K. Hodge, S. Lilla, et al., “Quantitative proteomics identifies the core proteome of exosomes with syntenin-1 as the highest abundant protein and a putative universal biomarker,” *Nat. Cell Biol.*, vol. 23, pp. 631–641, 2021.
48. J. Skog, T. Würdinger, S. van Rijn, et al., “Glioblastoma microvesicles transport RNA and proteins that promote tumour growth and provide diagnostic biomarkers,” *Nat. Cell Biol.*, vol. 10, pp. 1470–1476, 2008.
49. D. K. Jeppesen, A. M. Fenix, J. L. Franklin, et al., “Reassessment of exosome composition,” *Cell*, vol. 177, pp. 428–445, 2019.
50. C. Tricarico, J. Clancy, and C. D’Souza-Schorey, “Biology and biogenesis of shed microvesicles,” *Small GTPases*, vol. 8, pp. 220–232, 2017.
51. E. Cocucci, G. Racchetti, and J. Meldolesi, “Shedding microvesicles: artefacts no more,” *Trends Cell Biol.*, vol. 19, pp. 43–51, 2009.
52. H. T. McMahon and J. L. Gallop, “Membrane curvature and mechanisms of dynamic cell membrane remodelling,” *Nature*, vol. 438, pp. 590–596, 2005.
53. I. Del Conde, C. N. Shrimpton, P. Thiagarajan, and J. A. López, “Tissue-factor-bearing microvesicles arise from lipid rafts and fuse with activated platelets to initiate coagulation,” *Blood*, vol. 106, pp. 1604–1611, 2005.
54. J. F. Nabhan, R. Hu, R. S. Oh, S. N. Cohen, and Q. Lu, “Formation and release of arrestin domain-containing protein 1-mediated microvesicles (ARMMs) at plasma membrane by recruitment of TSG101 protein,” *Proc. Natl. Acad. Sci. U. S. A.*, vol. 109, p. 4146, 2012.
55. V. Muralidharan-Chari, J. W. Clancy, A. Sedgwick, and C. D’Souza-Schorey, “Microvesicles: mediators of extracellular communication during cancer progression,” *J. Cell Sci.*, vol. 123, pp. 1603–1611, 2010.
56. F. Jansen, G. Nickenig, and N. Werner, “Extracellular vesicles in cardiovascular disease: potential applications in diagnosis, prognosis, and epidemiology,” *Circ. Res.*, vol. 120, pp. 1649–1657, 2017.
57. S. Dujardin, S. Bégard, R. Caillierez, et al., “Ectosomes: a new mechanism for non-exosomal secretion of tau protein,” *PLoS One*, vol. 9, p. e100760, 2014.
58. P. Joshi, E. Turola, A. Ruiz, et al., “Microglia convert aggregated amyloid- β into neurotoxic forms through the shedding of microvesicles,” *Cell Death Differ.*, vol. 21, pp. 582–593, 2014.
59. M. Battistelli and E. Falcieri, “Apoptotic bodies: particular extracellular vesicles involved in intercellular communication,” *Biology*, vol. 9, p. 21, 2020.
60. M. Schiller, M. Parcina, P. Heyder, et al., “Induction of type I IFN is a physiological immune reaction to apoptotic cell-derived membrane microparticles,” *J. Immunol.*, vol. 189, pp. 1747–1756, 2012.

61. M. Schiller, I. Bekeredjian-Ding, P. Heyder, N. Blank, A. D. Ho, and H. M. Lorenz, "Autoantigens are translocated into small apoptotic bodies during early stages of apoptosis," *Cell Death Differ.*, vol. 15, pp. 183–191, 2008.
62. Q. Zhang, J. N. Higginbotham, D. K. Jeppesen, et al., "Transfer of functional cargo in exomeres," *Cell Rep.*, vol. 27, pp. 940–954, 2019.
63. G. Bordanaba-Florit, F. Royo, S. G. Kruglik, and J. M. Falcón-Pérez, "Using single-vesicle technologies to unravel the heterogeneity of extracellular vesicles," *Nat. Protoc.*, vol. 16, pp. 3163–3185, 2021.
64. M. Imanbekova, S. Suarasan, T. Rojalin, et al., "Identification of amyloid beta in small extracellular vesicles via Raman spectroscopy," *Nanoscale Adv.*, vol. 3, pp. 4119–4132, 2021.
65. C. H. Woo, H. K. Kim, G. Y. Jung, et al., "Small extracellular vesicles from human adipose-derived stem cells attenuate cartilage degeneration," *J. Extracell. Vesicles*, vol. 9, p. 1735249, 2020.
66. E. van der Pol, L. de Rond, F. A. W. Coumans, et al., "Absolute sizing and label-free identification of extracellular vesicles by flow cytometry," *Nanomed. Nanotechnol. Biol. Med.*, vol. 14, pp. 801–810, 2018.
67. E. Priglinger, J. Strasser, B. Buchroithner, et al., "Label-free characterization of an extracellular vesicle-based therapeutic," *J. Extracell. Vesicles*, vol. 10, p. e12156, 2021.
68. G. G. Daaboul, P. Gagni, L. Benussi, et al., "Digital detection of exosomes by interferometric imaging," *Sci. Rep.*, vol. 6, p. 37246, 2016.
69. V. Filipe, A. Hawe, and W. Jiskoot, "Critical evaluation of nanoparticle tracking analysis (NTA) by nanosight for the measurement of nanoparticles and protein aggregates," *Pharm. Res. (N. Y.)*, vol. 27, pp. 796–810, 2010.
70. C. Gardiner, Y. J. Ferreira, R. A. Dragovic, C. W. G. Redman, and I. L. Sargent, "Extracellular vesicle sizing and enumeration by nanoparticle tracking analysis," *J. Extracell. Vesicles*, vol. 2, p. 19671, 2013.
71. R. A. Dragovic, C. Gardiner, A. S. Brooks, et al., "Sizing and phenotyping of cellular vesicles using Nanoparticle Tracking Analysis," *Nanomed. Nanotechnol. Biol. Med.*, vol. 7, pp. 780–788, 2011.
72. E. van der Pol, F. A. W. Coumans, A. Sturk, R. Nieuwland, and T. G. van Leeuwen, "Refractive index determination of nanoparticles in suspension using nanoparticle tracking analysis," *Nano Lett.*, vol. 14, pp. 6195–6201, 2014.
73. C. Gardiner, M. Shaw, P. Hole, et al., "Measurement of refractive index by nanoparticle tracking analysis reveals heterogeneity in extracellular vesicles," *J. Extracell. Vesicles*, vol. 3, p. 25361, 2014.
74. M. Tong, O. Brown, P. Stone, L. Cree, and L. Chamley, "Flow speed alters the apparent size and concentration of particles measured using NanoSight nanoparticle tracking analysis," *Placenta*, vol. 38, pp. 29–32, 2016.
75. D. Bachurski, M. Schuldner, P. H. Nguyen, et al., "Extracellular vesicle measurements with nanoparticle tracking analysis - an accuracy and repeatability comparison between NanoSight NS300 and ZetaView," *J. Extracell. Vesicles*, vol. 8, p. 1596016, 2019.
76. J. Stetefeld, S. A. McKenna, and T. R. Patel, "Dynamic light scattering: a practical guide and applications in biomedical sciences," *Biophys. Rev.*, vol. 8, pp. 409–427, 2016.
77. R. d. Pecora, "Doppler shifts in light scattering from pure liquids and polymer solutions," *J. Chem. Phys.*, vol. 40, pp. 1604–1614, 1964.

78. T. S. Lyu, Y. Ahn, Y.-J. Im, et al., “The characterization of exosomes from fibrosarcoma cell and the useful usage of Dynamic Light Scattering (DLS) for their evaluation,” *PLoS One*, vol. 16, p. e0231994, 2021.
79. S. Falke and C. Betzel, “Dynamic Light Scattering (DLS),” *Radiation Bioanal.*, vol. 8, pp. 173–193, 2019.
80. M. Kaszuba, D. McKnight, M. T. Connah, F. K. McNeil-Watson, and U. Nobbmann, “Measuring sub nanometre sizes using dynamic light scattering,” *J. Nanoparticle Res.*, vol. 10, pp. 823–829, 2008.
81. T. Kahraman, G. Gucluler, I. Simsek, et al., “Circulating LL37 targets plasma extracellular vesicles to immune cells and intensifies Behçet’s disease severity,” *J. Extracell. Vesicles*, vol. 6, p. 1284449, 2017.
82. A. Mallardi, N. Nuzziello, M. Liguori, C. Avolio, and G. Palazzo, “Counting of peripheral extracellular vesicles in Multiple Sclerosis patients by an improved nanoplasmonic assay and dynamic light scattering,” *Colloids Surf. B Biointerfaces*, vol. 168, pp. 134–142, 2018.
83. A. Lawrie, A. Albanyan, R. Cardigan, I. Mackie, and P. Harrison, “Microparticle sizing by dynamic light scattering in fresh-frozen plasma,” *Vox Sang.*, vol. 96, pp. 206–212, 2009.
84. V. Palmieri, D. Lucchetti, I. Gatto, et al., “Dynamic light scattering for the characterization and counting of extracellular vesicles: a powerful noninvasive tool,” *J. Nanoparticle Res.*, vol. 16, p. 2583, 2014.
85. B. Giebel and C. Helmbrecht, “Methods to analyze EVs,” in *Exosomes and Microvesicles: Methods and Protocols*, A. F. Hill, Ed., New York, NY, Springer, 2017, pp. 1–20.
86. K. Fischer and M. Schmidt, “M. Pitfalls and novel applications of particle sizing by dynamic light scattering,” *Biomaterials*, vol. 98, pp. 79–91, 2016.
87. M. Kesimer and R. Gupta, “Physical characterization and profiling of airway epithelial derived exosomes using light scattering,” *Methods*, vol. 87, pp. 59–63, 2015.
88. U. Erdbrügger and J. Lannigan, “Analytical challenges of extracellular vesicle detection: a comparison of different techniques,” *Cytometry*, vol. 89, pp. 123–134, 2016.
89. T. Z. Tegegn, S. H. De Paoli, M. Orecna, et al., “Characterization of procoagulant extracellular vesicles and platelet membrane disintegration in DMSO-cryopreserved platelets,” *J. Extracell. Vesicles*, vol. 5, p. 30422, 2016.
90. C. M. Hoo, N. Starostin, P. West, and M. L. Mecartney, “A comparison of atomic force microscopy (AFM) and dynamic light scattering (DLS) methods to characterize nanoparticle size distributions,” *J. Nanoparticle Res.*, vol. 10, pp. 89–96, 2008.
91. Á. M. Lőrincz, C. I. Timár, K. A. Marosvári, et al., “Effect of storage on physical and functional properties of extracellular vesicles derived from neutrophilic granulocytes,” *J. Extracell. Vesicles*, vol. 3, p. 25465, 2014.
92. C. Preußer, L.-H. Hung, T. Schneider, et al., “Selective release of circRNAs in platelet-derived extracellular vesicles,” *J. Extracell. Vesicles*, vol. 7, p. 1424473, 2018.
93. Z. Varga, Y. Yuana, A. E. Grootemaat, et al., “Towards traceable size determination of extracellular vesicles,” *J. Extracell. Vesicles*, vol. 3, p. 23298, 2014.
94. V. Bairamukov, A. Bukatin, S. Landa, et al., “Biomechanical properties of blood plasma extracellular vesicles revealed by atomic force microscopy,” *Biology*, vol. 10, p. 4, 2020.
95. N. T. H. Dinh, J. Lee, J. Lee, et al., “Indoor dust extracellular vesicles promote cancer lung metastasis by inducing tumour necrosis factor- α ,” *J. Extracell. Vesicles*, vol. 9, p. 1766821, 2020.

96. A. Ridolfi, M. Brucale, C. Montis, et al., “AFM-based high-throughput nanomechanical screening of single extracellular vesicles,” *Anal. Chem.*, vol. 92, pp. 10274–10282, 2020.
97. M. Krieg, G. Fläschner, D. Alsteens, et al., “Atomic force microscopy-based mechanobiology,” *Nat. Rev. Phys.*, vol. 1, pp. 41–57, 2019.
98. E. U. Azeloglu and K. D. Costa, “Atomic force microscopy in mechanobiology: measuring microelastic heterogeneity of living cells,” *Methods Mol. Biol.*, vol. 736, pp. 303–329, 2011.
99. Y. F. Dufrière, “Atomic force microscopy, a powerful tool in microbiology,” *J. Bacteriol.*, vol. 184, pp. 5205–5213, 2002.
100. H.-J. Butt, B. Cappella, and M. Kappl, “Force measurements with the atomic force microscope: Technique, interpretation and applications,” *Surf. Sci. Rep.*, vol. 59, pp. 1–152, 2005.
101. Y. Yuana, T. H. Oosterkamp, S. Bahatyrova, et al., “Atomic force microscopy: a novel approach to the detection of nanosized blood microparticles,” *J. Thromb. Haemostasis*, vol. 8, pp. 315–323, 2010.
102. D. Vorselen, M. C. Piontek, W. H. Roos, and G. J. L. Wuite, “Mechanical characterization of liposomes and extracellular vesicles, a protocol,” *Front. Mol. Biosci.*, vol. 7, p. 139, 2020.
103. K. Wang, L. Zhou, J. Li, et al., “Label-free and three-dimensional visualization reveals the dynamics of plasma membrane-derived extracellular vesicles,” *Nano Lett.*, vol. 20, pp. 6313–6319, 2020.
104. K. Iwai, T. Minamisawa, K. Suga, Y. Yajima, and K. Shiba, “Isolation of human salivary extracellular vesicles by iodixanol density gradient ultracentrifugation and their characterizations,” *J. Extracell. Vesicles*, vol. 5, p. 30829, 2016.
105. R. S. Dagur, K. Liao, S. Sil, et al., “Neuronal-derived extracellular vesicles are enriched in the brain and serum of HIV-1 transgenic rats,” *J. Extracell. Vesicles*, vol. 9, p. 1703249, 2019.
106. S. Matsumura, T. Minamisawa, K. Suga, et al., “Subtypes of tumour cell-derived small extracellular vesicles having differently externalized phosphatidylserine,” *J. Extracell. Vesicles*, vol. 8, p. 1579541, 2019.
107. J. Hardij, F. Cecchet, A. Berquand, et al., “Characterisation of tissue factor-bearing extracellular vesicles with AFM: comparison of air-tapping-mode AFM and liquid Peak Force AFM,” *J. Extracell. Vesicles*, vol. 2, p. 21045, 2013.
108. S. Sharma, M. LeClaire, and J. K. Gimzewski, “Ascent of atomic force microscopy as a nanoanalytical tool for exosomes and other extracellular vesicles,” *Nanotechnology*, vol. 29, p. 132001, 2018.
109. S. Sharma, K. Das, J. Woo, and J. K. Gimzewski, “Nanofilaments on glioblastoma exosomes revealed by peak force microscopy,” *J. R. Soc. Interface*, vol. 11, p. 20131150, 2014.
110. Y. Kikuchi, N. Obana, M. Toyofuku, et al., “Diversity of physical properties of bacterial extracellular membrane vesicles revealed through atomic force microscopy phase imaging,” *Nanoscale*, vol. 12, pp. 7950–7959, 2020.
111. D. Vorselen, M. Marchetti, C. López-Iglesias, P. J. Peters, W. H. Roos, and G. J. L. Wuite, “Multilamellar nanovesicles show distinct mechanical properties depending on their degree of lamellarity,” *Nanoscale*, vol. 10, pp. 5318–5324, 2018.

112. M. LeClaire, J. Gimzewski, and S. Sharma, “A review of the biomechanical properties of single extracellular vesicles,” *Nano Select*, vol. 2, pp. 1–15, 2021.
113. D. Vorselen, S. M. van Dommelen, R. Sorkin, et al., “The fluid membrane determines mechanics of erythrocyte extracellular vesicles and is softened in hereditary spherocytosis,” *Nat. Commun.*, vol. 9, p. 4960, 2018.
114. F. Royo, D. Gil-Carton, E. Gonzalez, et al., “Differences in the metabolite composition and mechanical properties of extracellular vesicles secreted by hepatic cellular models,” *J. Extracell. Vesicles*, vol. 8, p. 1575678, 2019.
115. M. C. Piontek, R. B. Lira, and W. H. Roos, “Active probing of the mechanical properties of biological and synthetic vesicles,” *Biochim. Biophys. Acta Gen. Subj.*, vol. 1865, p. 129486, 2021.
116. A. Ridolfi, M. Bruciale, C. Montis, et al., “AFM-based high-throughput nanomechanical screening of single extracellular vesicles,” *Anal. Chem.*, vol. 92, pp. 10274–10282, 2020.
117. R. Sorkin, R. Huisjes, F. Bošković, et al., “Nanomechanics of extracellular vesicles reveals vesiculation pathways,” *Small*, vol. 14, p. 1801650, 2018.
118. B. Whitehead, L. Wu, M. L. Hvam, et al., “Tumour exosomes display differential mechanical and complement activation properties dependent on malignant state: implications in endothelial leakiness,” *J. Extracell. Vesicles*, vol. 4, p. 29685, 2015.
119. S. Sharma, H. I. Rasool, V. Palanisamy, et al., “Structural-mechanical characterization of nanoparticle exosomes in human saliva, using correlative AFM, FESEM, and force spectroscopy,” *ACS Nano*, vol. 4, pp. 1921–1926, 2010.
120. P. Parisse, I. Rago, L. Ulloa Severino, et al., “Atomic force microscopy analysis of extracellular vesicles,” *Eur. Biophys. J.*, vol. 46, pp. 813–820, 2017.
121. N. Sebaihi, B. D. Boeck, Y. Yuana, R. Nieuwland, and J. Pétry, “Dimensional characterization of extracellular vesicles using atomic force microscopy,” *Meas. Sci. Technol.*, vol. 28, p. 034006, 2017.
122. N. Regev-Rudzki, D. W. Wilson, T. G. Carvalho, et al., “Cell-cell communication between malaria-infected red blood cells via exosome-like vesicles,” *Cell*, vol. 153, pp. 1120–1133, 2013.
123. J. Canet-Ferrer, E. Coronado, A. Forment-Aliaga, and E. Pinilla-Cienfuegos, “Correction of the tip convolution effects in the imaging of nanostructures studied through scanning force microscopy,” *Nanotechnology*, vol. 25, p. 395703, 2014.
124. S. Y. Kim, D. Khanal, B. Kalionis, and W. Chrzanowski, “High-fidelity probing of the structure and heterogeneity of extracellular vesicles by resonance-enhanced atomic force microscopy infrared spectroscopy,” *Nat. Protoc.*, vol. 14, pp. 576–593, 2019.
125. M. G. Macey and M. G. Macey, *Flow Cytometry*, Totowa, NJ, Springer, 2007.
126. J. Maia, S. Batista, N. Couto, et al., “Employing flow cytometry to extracellular vesicles sample microvolume analysis and quality control,” *Front. Cell Dev. Biol.*, vol. 8, p. 1165, 2020.
127. H. M. Shapiro, *Practical Flow Cytometry*, Hoboken, New Jersey, John Wiley & Sons, 2005.
128. M. J. Wilkerson, “Principles and applications of flow cytometry and cell sorting in companion animal medicine,” *Vet. Clin. North Am. Small Anim. Pract.*, vol. 42, pp. 53–71, 2012.

129. H. M. Shapiro and W. G. Telford, "Lasers for flow cytometry," *Curr. Protoc. Cytom.*, vol. 49, pp. 1–9, 2009.
130. J. A. Welsh, J. A. Holloway, J. S. Wilkinson, and N. A. Englyst, "Extracellular vesicle flow cytometry analysis and standardization," *Front. Cell Dev. Biol.*, vol. 5, p. 78, 2017.
131. E. V. D. Pol, M. J. C. V. Gemert, A. Sturk, R. Nieuwland, and T. G. V. Leeuwen, "Single vs. swarm detection of microparticles and exosomes by flow cytometry," *J. Thromb. Haemostasis*, vol. 10, pp. 919–930, 2012.
132. A. Görgens, M. Bremer, R. Ferrer-Tur, et al., "Optimisation of imaging flow cytometry for the analysis of single extracellular vesicles by using fluorescence-tagged vesicles as biological reference material," *J. Extracell. Vesicles*, vol. 8, p. 1587567, 2019.
133. G. Marcoux, A.-C. Ducheze, N. Cloutier, P. Provost, P. A. Nigrovic, and E. Boilard, "Revealing the diversity of extracellular vesicles using high-dimensional flow cytometry analyses," *Sci. Rep.*, vol. 6, p. 35928, 2016.
134. E. N. Nolte-'t Hoen, E. J. van der Vlist, M. Aalberts, et al., "Quantitative and qualitative flow cytometric analysis of nanosized cell-derived membrane vesicles," *Nanomedicine*, vol. 8, pp. 712–720, 2012.
135. J. P. Nolan, "Flow cytometry of extracellular vesicles: potential, pitfalls, and prospects," *Curr. Protoc. Cytom.*, vol. 73, p. 13, 2015.
136. R. Lacroix, S. Robert, P. Poncelet, R. S. Kasthuri, N. S. Key, and F. Dignat-George, "Standardization of platelet-derived microparticle enumeration by flow cytometry with calibrated beads: results of the International Society on Thrombosis and Haemostasis SSC Collaborative workshop," *J. Thromb. Haemostasis*, vol. 8, pp. 2571–2574, 2010.
137. S. Roy, H.-Y. Lin, C.-Y. Chou, et al., "Navigating the landscape of tumor extracellular vesicle heterogeneity," *Int. J. Mol. Sci.*, vol. 20, p. 1349, 2019.
138. W. L. Chandler, W. Yeung, and J. F. Tait, "A new microparticle size calibration standard for use in measuring smaller microparticles using a new flow cytometer," *J. Thromb. Haemostasis*, vol. 9, pp. 1216–1224, 2011.
139. D. Patko, B. Gyorgy, A. Nemeth, et al., "Label-free optical monitoring of surface adhesion of extracellular vesicles by grating coupled interferometry," *Sensor. Actuator. B Chem.*, vol. 188, pp. 697–701, 2013.
140. L. Cheng, R. A. Sharples, B. J. Scicluna, and A. F. Hill, "Exosomes provide a protective and enriched source of miRNA for biomarker profiling compared to intracellular and cell-free blood," *J. Extracell. Vesicles*, vol. 3, p. 23743, 2014.
141. Z. Nizamudeen, R. Markus, R. Lodge, et al., "Rapid and accurate analysis of stem cell-derived extracellular vesicles with super resolution microscopy and live imaging," *Biochim. Biophys. Acta Mol. Cell Res.*, vol. 1865, pp. 1891–1900, 2018.
142. R. R. Mizenko, T. Brostoff, T. Rojalin, et al., "Tetraspanins are unevenly distributed across single extracellular vesicles and bias sensitivity to multiplexed cancer biomarkers," *J. Nanobiotechnol.*, vol. 19, p. 250, 2021.
143. E. Özkumur, J. W. Needham, D. A. Bergstein, et al., "Label-free and dynamic detection of biomolecular interactions for high-throughput microarray applications," *Proc. Natl. Acad. Sci. U. S. A.*, vol. 105, p. 7988, 2008.
144. O. Avci, N. L. Ünlü, A. Y. Özkumur, and M. S. Ünlü, "Interferometric Reflectance Imaging Sensor (IRIS)—a platform technology for multiplexed diagnostics and digital detection," *Sensors*, vol. 15, pp. 17649–17665, 2015.

145. G. G. Daaboul, C. A. Lopez, J. Chinnala, B. B. Goldberg, J. H. Connor, and M. S. Ünlü, “Digital sensing and sizing of vesicular stomatitis virus pseudotypes in complex media: a model for ebola and marburg detection,” *ACS Nano*, vol. 8, pp. 6047–6055, 2014.
146. T. Arab, E. R. Mallick, Y. Huang, et al., “Characterization of extracellular vesicles and synthetic nanoparticles with four orthogonal single-particle analysis platforms,” *J. Extracell. Vesicles*, vol. 10, 2021, Art no. e12079.
147. B. O. Leung and K. C. Chou, “Review of super-resolution fluorescence microscopy for biology,” *Appl. Spectrosc.*, vol. 65, pp. 967–980, 2011.
148. V. Astratov, *Label-Free Super-Resolution Microscopy*, Cham, Springer, 2019.
149. C. Chen, S. Zong, Z. Wang, et al., “Imaging and intracellular tracking of cancer-derived exosomes using single-molecule localization-based super-resolution microscope,” *ACS Appl. Mater. Interfaces*, vol. 8, pp. 25825–25833, 2016.
150. C. Liu, X. Xu, B. Li, et al., “Single-exosome-counting immunoassays for cancer diagnostics,” *Nano Lett.*, vol. 18, pp. 4226–4232, 2018.
151. Y. Kumamoto, Y. Harada, T. Takamatsu, and H. Tanaka, “Label-free molecular imaging and analysis by Raman spectroscopy,” *Acta Histochem. Cytoc.*, vol. 51, pp. 101–110, 2018.
152. J. Liu, M. Jalali, S. Mahshid, and S. Wachsmann-Hogiu, “Are plasmonic optical biosensors ready for use in point-of-need applications?” *Analyst*, vol. 145, pp. 364–384, 2020.
153. H. Shin, H. Jeong, J. Park, S. Hong, and Y. Choi, “Correlation between cancerous exosomes and Protein Markers Based on Surface-Enhanced Raman Spectroscopy (SERS) and Principal Component Analysis (PCA),” *ACS Sens.*, vol. 3, pp. 2637–2643, 2018.
154. F. Laviolle, S. Deshayes, F. Gonnet, et al., “Nanovesicles released by dictyostelium cells: a potential carrier for drug delivery,” *Int. J. Pharm.*, vol. 380, pp. 206–215, 2009.
155. Z. J. Smith, C. Lee, T. Rojalin, et al., “Single exosome study reveals subpopulations distributed among cell lines with variability related to membrane content,” *J. Extracell. Vesicles*, vol. 4, p. 28533, 2015.
156. S. G. Kruglik, F. Royo, J.-M. Guigner, et al., “Raman tweezers microspectroscopy of circa 100 nm extracellular vesicles,” *Nanoscale*, vol. 11, pp. 1661–1679, 2019.
157. H. Zhang, A. C. Silva, W. Zhang, H. Rutigliano, and A. Zhou, “Raman spectroscopy characterization extracellular vesicles from bovine placenta and peripheral blood mononuclear cells,” *PLoS One*, vol. 15, p. e0235214, 2020.
158. A. Gualerzi, S. Niada, C. Giannasi, et al., “Raman spectroscopy uncovers biochemical tissue-related features of extracellular vesicles from mesenchymal stromal cells,” *Sci. Rep.*, vol. 7, p. 9820, 2017.
159. W. Lee, A. T. M. Lenferink, C. Otto, and H. L. Offerhaus, “Classifying Raman spectra of extracellular vesicles based on convolutional neural networks for prostate cancer detection,” *J. Raman Spectrosc.*, vol. 51, pp. 293–300, 2020.
160. A. Gualerzi, S. A. A. Kooijmans, S. Niada, et al., “Raman spectroscopy as a quick tool to assess purity of extracellular vesicle preparations and predict their functionality,” *J. Extracell. Vesicles*, vol. 8, p. 1568780, 2019.

161. Y. Dai, S. Bai, C. Hu, K. Chu, B. Shen, and Z. J. Smith, "Combined morpho-chemical profiling of individual extracellular vesicles and functional nanoparticles without labels," *Anal. Chem.*, vol. 92, pp. 5585–5594, 2020.
162. I. Tatischeff, E. Larquet, J. M. Falcón-Pérez, P.-Y. Turpin, and S. G. Kruglik, "Fast characterisation of cell-derived extracellular vesicles by nanoparticles tracking analysis, cryo-electron microscopy, and Raman tweezers microspectroscopy," *J. Extracell. Vesicles*, vol. 1, p. 19179, 2012.
163. A. Enciso-Martinez, E. van der Pol, A. T. M. Lenferink, L. W. M. M. Terstappen, T. G. van Leeuwen, and C. Otto, "Synchronized Rayleigh and Raman scattering for the characterization of single optically trapped extracellular vesicles," *Nanomed. Nanotechnol. Biol. Med.*, vol. 24, p. 102109, 2020.
164. A. Enciso-Martinez, E. Van Der Pol, C. M. Hau, et al., "Label-free identification and chemical characterisation of single extracellular vesicles and lipoproteins by synchronous Rayleigh and Raman scattering," *J. Extracell. Vesicles*, vol. 9, p. 1730134, 2020.
165. R. P. Carney, S. Hazari, M. Colquhoun, et al., "Multispectral optical tweezers for biochemical fingerprinting of CD9-positive exosome subpopulations," *Anal. Chem.*, vol. 89, pp. 5357–5363, 2017.
166. J. Penders, A. Nagelkerke, E. M. Cunnane, et al., "Single particle automated Raman trapping analysis of breast cancer cell-derived extracellular vesicles as cancer biomarkers," *ACS Nano*, vol. 15, pp. 18192–18205, 2021.
167. W. Lee, A. Nanou, L. Rikkert, et al., "Label-free prostate cancer detection by characterization of extracellular vesicles using Raman spectroscopy," *Anal. Chem.*, vol. 90, pp. 11290–11296, 2018.
168. M. Dash, K. Palaniyandi, S. Ramalingam, S. Sahabudeen, and N. S. Raja, "Exosomes isolated from two different cell lines using three different isolation techniques show variation in physical and molecular characteristics," *Biochim. Biophys. Acta Biomembr.*, vol. 1863, p. 183490, 2021.
169. R. R. Jones, D. C. Hooper, L. Zhang, D. Wolverson, and V. K. Valev, "Raman techniques: fundamentals and frontiers," *Nanoscale Res. Lett.*, vol. 14, pp. 1–34, 2019.
170. C. Chen, W. Liu, S. Tian, and T. Hong, "Novel surface-enhanced Raman spectroscopy techniques for DNA, protein and drug detection," *Sensors*, vol. 19, p. 1712, 2019.
171. L. M. Almealmadi, S. M. Curley, N. A. Tokranova, S. A. Tenenbaum, and I. K. Lednev, "Surface enhanced Raman spectroscopy for single molecule protein detection," *Sci. Rep.*, vol. 9, p. 12356, 2019.
172. L. Guerrini, E. Garcia-Rico, A. O'Loghlen, V. Giannini, and R. A. Alvarez-Puebla, "Surface-Enhanced Raman Scattering (SERS) Spectroscopy for sensing and characterization of exosomes in cancer diagnosis," *Cancers*, vol. 13, p. 2179, 2021.
173. T. Rojalín, B. Phong, H. J. Koster, and R.P. Carney, "Nanoplasmonic approaches for sensitive detection and molecular characterization of extracellular vesicles," *Front. Chem.*, vol. 7, no. 279, p. 279, 2019.
174. S. Stremersch, M. Marro, B. E. Pinchasik, et al., "Identification of individual exosome-like vesicles by surface enhanced Raman spectroscopy," *Small*, vol. 12, pp. 3292–3301, 2016.
175. J. C. Fraire, S. Stremersch, D. Bouckaert, et al., "Improved label-free identification of individual exosome-like vesicles with Au@Ag nanoparticles as SERS substrate," *ACS Appl. Mater. Interfaces*, vol. 11, pp. 39424–39435, 2019.

176. P. Yin, G. Li, B. Zhang, et al., “Facile PEG-based isolation and classification of cancer extracellular vesicles and particles with label-free surface-enhanced Raman scattering and pattern recognition algorithm,” *Analyst*, vol. 146, pp. 1949–1955, 2021.
177. Z. Yan, S. Dutta, Z. Liu, et al., “A label-free platform for identification of exosomes from different sources,” *ACS Sens.*, vol. 4, pp. 488–497, 2019.
178. A. Pramanik, J. Mayer, S. Patibandla, et al., “Mixed-dimensional heterostructure material-based SERS for trace level identification of breast cancer-derived exosomes,” *ACS Omega*, vol. 5, pp. 16602–16611, 2020.
179. S. Suarasan, J. Liu, M. Imanbekova, and S. Wachsmann-Hogiu, “Superhydrophobic bowl-like SERS substrates patterned from CMOS sensors for extracellular vesicle characterization,” *J. Mater. Chem. B*, vol. 8, pp. 8845–8852, 2020.
180. C. Lee, R. P. Carney, S. Hazari, et al., “3D plasmonic nanobowl platform for the study of exosomes in solution,” *Nanoscale*, vol. 7, pp. 9290–9297, 2015.
181. H. J. Koster, T. Rojalín, A. Powell, et al., “Surface enhanced Raman scattering of extracellular vesicles for cancer diagnostics despite isolation dependent lipoprotein contamination,” *Nanoscale*, vol. 13, pp. 14760–14776, 2021.
182. G. Kumari, J. Kandula, and C. Narayana, “How far can we probe by SERS?” *J. Phys. Chem. C*, vol. 119, pp. 20057–20064, 2015.
183. B. Liedberg, C. Nylander, and I. Lundström, “Biosensing with surface plasmon resonance—how it all started,” *Biosens. Bioelectron.*, vol. 10, pp. i–ix, 1995.
184. D. L. Rupert, C. Lässer, M. Eldh, et al., “Determination of exosome concentration in solution using surface plasmon resonance spectroscopy,” *Anal. Chem.*, vol. 86, pp. 5929–5936, 2014.
185. D. L. M. Rupert, G. V. Shelke, G. Emilsson, et al., “Dual-Wavelength surface plasmon resonance for determining the size and concentration of sub-populations of extracellular vesicles,” *Anal. Chem.*, vol. 88, pp. 9980–9988, 2016.
186. B. Hosseinkhani, N. van den Akker, J. D’Haen, et al., “Direct detection of nano-scale extracellular vesicles derived from inflammation-triggered endothelial cells using surface plasmon resonance,” *Nanomedicine*, vol. 13, pp. 1663–1671, 2017.
187. L. Grasso, R. Wyss, L. Weidenauer, et al., “Molecular screening of cancer-derived exosomes by surface plasmon resonance spectroscopy,” *Anal. Bioanal. Chem.*, vol. 407, pp. 5425–5432, 2015.
188. A. A. I. Sina, R. Vaidyanathan, S. Dey, L. G. Carrascosa, M. J. A. Shiddiky, and M. Trau, “Real time and label free profiling of clinically relevant exosomes,” *Sci. Rep.*, vol. 6, p. 30460, 2016.
189. H. Im, H. Shao, Y. I. Park, et al., “Label-free detection and molecular profiling of exosomes with a nano-plasmonic sensor,” *Nat. Biotechnol.*, vol. 32, pp. 490–495, 2014.
190. J. Park, H. Im, S. Hong, C. M. Castro, R. Weissleder, and H. Lee, “Analyses of intravesicular exosomal proteins using a nano-plasmonic system,” *ACS Photonics*, vol. 5, pp. 487–494, 2018.
191. K. S. Yang, H. Im, S. Hong, et al., “Multiparametric plasma EV profiling facilitates diagnosis of pancreatic malignancy,” *Sci. Transl. Med.*, vol. 9, p. 3226, 2017.

192. L. Caselli, A. Ridolfi, J. Cardellini, et al., “A plasmon-based nanoruler to probe the mechanical properties of synthetic and biogenic nanosized lipid vesicles,” *Nanoscale Horizons*, vol. 6, pp. 543–550, 2021.
193. D. Raghu, J. A. Christodoulides, M. Christophersen, et al., “Nanoplasmonic pillars engineered for single exosome detection,” *PLoS One*, vol. 13, p. e0202773, 2018.
194. K. Liang, F. Liu, J. Fan, et al., “Nanoplasmonic quantification of tumor-derived extracellular vesicles in plasma microsamples for diagnosis and treatment monitoring,” *Nat. Biomed. Eng.*, vol. 1, p. 0021, 2017.
195. C. Liu, X. Zeng, Z. An, et al., “Sensitive detection of exosomal proteins via a compact surface plasmon resonance biosensor for cancer diagnosis,” *ACS Sens.*, vol. 3, pp. 1471–1479, 2018.
196. A. Thakur, C. Xu, W. K. Li, et al., “In vivo liquid biopsy for glioblastoma malignancy by the AFM and LSPR based sensing of exosomal CD44 and CD133 in a mouse model,” *Biosens. Bioelectron.*, vol. 191, p. 113476, 2021.
197. V. Ramos-Garcia, I. Ten-Doménech, A. Moreno-Giménez, et al., “ATR-FTIR spectroscopy for the routine quality control of exosome isolations,” *Chemometr. Intell. Lab. Syst.*, vol. 217, p. 104401, 2021.
198. V. S. Baddela, V. Nayan, P. Rani, S. K. Onteru, and D. Singh, “Physicochemical biomolecular insights into buffalo milk-derived nanovesicles,” *Appl. Biochem. Biotechnol.*, vol. 178, pp. 544–557, 2016.
199. J. Mihály, R. Deák, I. C. Szigyártó, A. Bóta, T. Beke-Somfai, and Z. Varga, “Characterization of extracellular vesicles by IR spectroscopy: fast and simple classification based on amide and CH stretching vibrations,” *Biochim. Biophys. Acta Biomembr.*, vol. 1859, pp. 459–466, 2017.
200. L. Paolini, S. Federici, G. Consoli, et al., “Fourier-transform Infrared (FT-IR) spectroscopy fingerprints subpopulations of extracellular vesicles of different sizes and cellular origin,” *J. Extracell. Vesicles*, vol. 9, p. 1741174, 2020.
201. E. Ł. Stępień, A. Kamińska, M. Surman, D. Karbowska, A. Wróbel, and M. Przybyło, “Fourier-Transform InfraRed (FT-IR) spectroscopy to show alterations in molecular composition of EV subpopulations from melanoma cell lines in different malignancy,” *Biochem. Biophys. Rep.*, vol. 25, p. 100888, 2021.
202. J. Lee, B. Wen, E. A. Carter, V. Combes, G. E. R. Grau, and P. A. Lay, “Infrared spectroscopic characterization of monocytic microvesicles (microparticles) released upon lipopolysaccharide stimulation,” *Faseb. J.*, vol. 31, pp. 2817–2827, 2017.
203. C. Krafft, K. Wilhelm, A. Eremin, et al., “A specific spectral signature of serum and plasma-derived extracellular vesicles for cancer screening,” *Nanomed. Nanotechnol. Biol. Med.*, vol. 13, pp. 835–841, 2017.
204. A. Zlotogorski-Hurvitz, B. Z. Dekel, D. Malonek, R. Yahalom, and M. Vered, “FTIR-based spectrum of salivary exosomes coupled with computational-aided discriminating analysis in the diagnosis of oral cancer,” *J. Cancer Res. Clin. Oncol.*, vol. 145, pp. 685–694, 2019.
205. X. L. Yap, B. Wood, T. A. Ong, J. Lim, B. H. Goh, and W. L. Lee, “Detection of prostate cancer via IR spectroscopic analysis of urinary extracellular vesicles: a pilot study,” *Membranes*, vol. 11, p. 591, 2021.
206. S. Romanò, F. Di Giacinto, A. Primiano, et al., “Label-free spectroscopic characterization of exosomes reveals cancer cell differentiation,” *Anal. Chim. Acta*, vol. 1192, p. 339359, 2022.
2017. T. Soares Martins, S. Magalhães, I. M. Rosa, et al., “Potential of FTIR spectroscopy applied to exosomes for Alzheimer’s disease discrimination: a pilot study,” *J. Alzheimer. Dis.*, vol. 74, pp. 391–405, 2020.

208. S. Romanò, F. Di Giacinto, A. Primiano, et al., “Fourier Transform Infrared Spectroscopy as a useful tool for the automated classification of cancer cell-derived exosomes obtained under different culture conditions,” *Anal. Chim. Acta*, vol. 1140, pp. 219–227, 2020.
209. R. Polito, M. Musto, M. E. Temperini, et al., “Infrared nanospectroscopy of individual extracellular microvesicles,” *Molecules*, vol. 26, p. 887, 2021.
210. D. Cialla, S. Pollok, C. Steinbrücker, K. Weber, and J. Popp, “SERS-based detection of biomolecules,” *Nanophotonics*, vol. 3, pp. 383–411, 2014.
211. S. Suarasan, J. Liu, M. Imanbekova, et al., “Superhydrophobic bowl-like SERS substrates patterned from CMOS sensors for extracellular vesicle characterization,” *J. Mater. Chem. B*, vol. 8, pp. 8845–8852, 2020.
212. S. You, R. Barkalifa, E. J. Chaney, et al., “Label-free visualization and characterization of extracellular vesicles in breast cancer,” *Proc. Natl. Acad. Sci. U. S. A.*, vol. 116, pp. 24012–24018, 2019.
215. A. M. Larson, “Multiphoton microscopy,” *Nat. Photonics*, vol. 5, p. 1, 2011.
214. G. Borile, D. Sandrin, A. Filippi, K. I. Anderson, and F. Romanato, “Label-free multiphoton microscopy: much more than fancy images,” *Int. J. Mol. Sci.*, vol. 22, p. 2657, 2021.
215. G. Alice, P. Silvia, C. Cristiano, R. Francesca, and B. Marzia, “Biophotonics for diagnostic detection of extracellular vesicles,” *Adv. Drug Deliv. Rev.*, vol. 174, pp. 229–249, 2021.
216. S. Wang, F. Cesca, G. Loers, et al., “Synapsin I is an oligomannose-carrying glycoprotein, acts as an oligomannose-binding lectin, and promotes neurite outgrowth and neuronal survival when released via glia-derived exosomes,” *J. Neurosci.*, vol. 31, pp. 7275–7290, 2011.
217. A. Venturini, M. Passalacqua, S. Pelassa, et al., “Exosomes from astrocyte processes: signaling to neurons,” *Front. Pharmacol.*, vol. 10, p. 1452, 2019.
218. K. Guitart, G. Loers, F. Buck, U. Bork, M. Schachner, and R. Kleene, “Improvement of neuronal cell survival by astrocyte-derived exosomes under hypoxic and ischemic conditions depends on prion protein,” *Glia*, vol. 64, pp. 896–910, 2016.
219. A. R. Taylor, M. B. Robinson, D. J. Gifondorwa, M. Tytell, and C. E. Milligan, “Regulation of heat shock protein 70 release in astrocytes: role of signaling kinases,” *Dev. Neurobiol.*, vol. 67, pp. 1815–1829, 2007.
220. M. A. Lopez-Verrilli, F. Picou, and F. A. Court, “Schwann cell-derived exosomes enhance axonal regeneration in the peripheral nervous system,” *Glia*, vol. 61, pp. 1795–1806, 2013.
221. L.-W. Chang, A. Viader, N. Varghese, J. E. Payton, J. Milbrandt, and R. Nagarajan, “An integrated approach to characterize transcription factor and microRNA regulatory networks involved in Schwann cell response to peripheral nerve injury,” *BMC Genom.*, vol. 14, pp. 1–20, 2013.
222. R. C. Ching, M. Wiberg, and P. J. Kingham, “Schwann cell-like differentiated adipose stem cells promote neurite outgrowth via secreted exosomes and RNA transfer,” *Stem Cell Res. Ther.*, vol. 9, pp. 1–12, 2018.
223. E.-M. Krämer-Albers and R. White, “From axon–glial signalling to myelination: the integrating role of oligodendroglial Fyn kinase,” *Cell. Mol. Life Sci.*, vol. 68, pp. 2003–2012, 2011.
224. C. Fruhbeis and D. Frohlich, “Neurotransmitter-triggered transfer of exosomes mediates oligodendrocyte–neuron communication,” *PLoS Biol.*, vol. 11, 2013, Art no. e1001604.

225. D. Fröhlich, W. P. Kuo, C. Frühbeis, et al., “Multifaceted effects of oligodendroglial exosomes on neurons: impact on neuronal firing rate, signal transduction and gene regulation,” *Phil. Trans. Biol. Sci.*, vol. 369, p. 20130510, 2014.
226. D. Fitzner, M. Schnaars, D. Van Rossum, et al., “Selective transfer of exosomes from oligodendrocytes to microglia by macropinocytosis,” *J. Cell Sci.*, vol. 124, pp. 447–458, 2011.
227. I. Potolicchio, G. J. Carven, X. Xu, et al., “Proteomic analysis of microglia-derived exosomes: metabolic role of the aminopeptidase CD13 in neuropeptide catabolism,” *J. Immunol.*, vol. 175, pp. 2237–2243, 2005.
- [228] F. Antonucci, E. Turola, L. Riganti, et al., “Microvesicles released from microglia stimulate synaptic activity via enhanced sphingolipid metabolism,” *EMBO J.*, vol. 31, pp. 1231–1240, 2012.
229. I. Bahrini, J.-h. Song, D. Diez, and R. Hanayama, “Neuronal exosomes facilitate synaptic pruning by up-regulating complement factors in microglia,” *Sci. Rep.*, vol. 5, pp. 1–8, 2015.
230. M. C. Morton, V. N. Neckles, C. M. Seluzicki, J. C. Holmberg, and D. M. Feliciano, “Neonatal subventricular zone neural stem cells release extracellular vesicles that act as a microglial morphogen,” *Cell Rep.*, vol. 23, pp. 78–89, 2018.
231. J. C. Polanco, C. Li, N. Durisic, R. Sullivan, and J. Götz, “Exosomes taken up by neurons hijack the endosomal pathway to spread to interconnected neurons,” *Acta Neuropathol. Commun.*, vol. 6, pp. 1–14, 2018.
232. X. Zhuang, X. Xiang, W. Grizzle, et al., “Treatment of brain inflammatory diseases by delivering exosome encapsulated anti-inflammatory drugs from the nasal region to the brain,” *Mol. Ther.*, vol. 19, pp. 1769–1779, 2011.
233. L. J. Vella, R. A. Sharples, V. A. Lawson, C. L. Masters, R. Cappai, and A. F. Hill, “Packaging of prions into exosomes is associated with a novel pathway of PrP processing,” *J. Pathol.*, vol. 211, pp. 582–590, 2007.
234. L. Rajendran, M. Honsho, T. R. Zahn, et al., “Alzheimer’s disease β -amyloid peptides are released in association with exosomes,” *Proc Natl Acad Sci U S A*, vol. 103, pp. 11172–11177, 2006.
235. E. Eitan, E. R. Hutchison, K. Marosi, et al., “Extracellular vesicle-associated A β mediates trans-neuronal bioenergetic and Ca (2+)-handling deficits in Alzheimer’s disease models,” *NPJ Aging Mech. Dis.*, vol. 2, p. 16019, 2016.
236. S. Saman, W. Kim, M. Raya, et al., “Exosome-associated tau is secreted in tauopathy models and is selectively phosphorylated in cerebrospinal fluid in early Alzheimer disease,” *J Biol Chem*, vol. 287, pp. 3842–3849, 2012.
237. K. M. Danzer, L. R. Kranich, W. P. Ruf, et al., “Exosomal cell-to-cell transmission of alpha synuclein oligomers,” *Mol. Neurodegener.*, vol. 7, p. 42, 2012.
238. J. P. Cogswell, J. Ward, I. A. Taylor, et al., “Identification of miRNA changes in Alzheimer’s disease brain and CSF yields putative biomarkers and insights into disease pathways,” *J. Alzheimers Dis.*, vol. 14, pp. 27–41, 2008.
239. K. Blennow and H. Zetterberg, “Understanding biomarkers of neurodegeneration: ultrasensitive detection techniques pave the way for mechanistic understanding,” *Nat. Med.*, vol. 21, pp. 217–219, 2015.
240. M. S. Fiandaca, D. Kapogiannis, M. Mapstone, et al., “Identification of preclinical Alzheimer’s disease by a profile of pathogenic proteins in neurally derived blood exosomes: A case-control study,” *Alzheimers Dement*, vol. 11, pp. 600–607, 2015.

241. E. J. Goetzl, A. Boxer, J. B. Schwartz, et al., “Altered lysosomal proteins in neural-derived plasma exosomes in preclinical Alzheimer disease,” *Neurology*, vol. 85, pp. 40–47, 2015.
242. E. J. Goetzl, M. Mustapic, D. Kapogiannis, et al., “Cargo proteins of plasma astrocyte-derived exosomes in Alzheimer’s disease,” *Faseb. J.*, vol. 30, pp. 3853–3859, 2016.
243. E. J. Goetzl, E. L. Abner, G. A. Jicha, D. Kapogiannis, and J. B. Schwartz, “Declining levels of functionally specialized synaptic proteins in plasma neuronal exosomes with progression of Alzheimer’s disease,” *Faseb. J.*, vol. 32, pp. 888–893, 2018.
244. D. Kapogiannis, M. Mustapic, M. D. Shardell, et al., “Association of extracellular vesicle biomarkers with Alzheimer disease in the Baltimore longitudinal study of aging,” *JAMA Neurol.*, vol. 76, pp. 1340–1351, 2019.
245. E. J. Goetzl, C. Noguera-Ortiz, M. Mustapic, et al., “Deficient neurotrophic factors of CSPG4-type neural cell exosomes in Alzheimer disease,” *FASEB J.*, vol. 33, pp. 231–238, 2019.
246. E. D. Hamlett, E. J. Goetzl, A. Ledreux, et al., “Neuronal exosomes reveal Alzheimer’s disease biomarkers in Down syndrome,” *Alzheimers Dement.*, vol. 13, pp. 541–549, 2017.
247. A. Gualerzi, S. Picciolini, C. Carlomagno, et al., “Raman profiling of circulating extracellular vesicles for the stratification of Parkinson’s patients,” *Nanomed. Nanotechnol. Biol. Med.*, vol. 22, p. 102097, 2019.
248. C. F. Morasso, D. Sproviero, M. C. Mimmi, et al., “Raman spectroscopy reveals biochemical differences in plasma derived extracellular vesicles from sporadic Amyotrophic Lateral Sclerosis patients,” *Nanomed. Nanotechnol. Biol. Med.*, vol. 29, p. 102249, 2020.
249. C. Z. J. Lim, Y. Zhang, Y. Chen, et al., “Subtyping of circulating exosome-bound amyloid β reflects brain plaque deposition,” *Nat. Commun.*, vol. 10, p. 1144, 2019.
250. Z. Ruan, D. Pathak, S. Venkatesan Kalavai, et al., “Alzheimer’s disease brain-derived extracellular vesicles spread tau pathology in interneurons,” *Brain*, vol. 144, pp. 288–309, 2021.
251. S. Picciolini, A. Gualerzi, C. Carlomagno, et al., “An SPRi-based biosensor pilot study: Analysis of multiple circulating extracellular vesicles and hippocampal volume in Alzheimer’s disease,” *J. Pharmaceut. Biomed. Anal.*, vol. 192, p. 113649, 2021.
252. J. Wang, Y.-C. Kao, Q. Zhou, et al., “An integrated microfluidic-SERS platform enables sensitive phenotyping of serum extracellular vesicles in early-stage melanomas,” *Adv. Funct. Mater.*, vol. 32, p. 2010296, 2022.
253. M. Russo, L. Tirinato, F. Scionti, et al., “Raman spectroscopic stratification of multiple myeloma patients based on exosome profiling,” *ACS Omega*, vol. 5, pp. 30436–30443, 2020.
254. G. Di Noto, A. Bugatti, A. Zandrini, et al., “Merging colloidal nanoplasmonics and surface plasmon resonance spectroscopy for enhanced profiling of multiple myeloma-derived exosomes,” *Biosens. Bioelectron.*, vol. 77, pp. 518–524, 2016.
255. J. Carmichael, C. Hayashi, X. Huang, et al., “Label-free characterization of exosome via surface enhanced Raman spectroscopy for the early detection of pancreatic cancer,” *Nanomedicine*, vol. 16, pp. 88–96, 2019.
256. K. Rasuleva, S. Elamurugan, A. Bauer, et al., “ β -Sheet richness of the circulating tumor-derived extracellular vesicles for noninvasive pancreatic cancer screening,” *ACS Sens.*, vol. 6, pp. 4489–4498, 2021.

257. R. Wang and Y. Wang, “Fourier transform Infrared spectroscopy in oral cancer diagnosis,” *Int. J. Mol. Sci.*, vol. 22, p. 1206, 2021.
258. D. Ma, C. Huang, J. Zheng, et al., “Quantitative detection of exosomal microRNA extracted from human blood based on surface-enhanced Raman scattering,” *Biosens. Bioelectron.*, vol. 101, pp. 167–173, 2018.
259. T. Rojalin, H. J. Koster, J. Liu, et al., “Hybrid nanoplasmonic porous biomaterial scaffold for liquid biopsy diagnostics using extracellular vesicles,” *ACS Sens.*, vol. 5, pp. 2820–2833, 2020.
260. H. Shin, S. Oh, S. Hong, et al., “Early-stage lung cancer diagnosis by deep learning-based spectroscopic analysis of circulating exosomes,” *ACS Nano*, vol. 14, pp. 5435–5444, 2020.

Transition to chapter III

The previous chapter presented a recent review of existing optical label-free methodologies used for EV characterization. The specifics of each technique and the challenges for EV analysis application were discussed. The existing literature shows that label-free optical methods are used as complementary techniques to conventional EV characterization methods and can provide additional valuable information about EV characteristics.

Among many methodologies of EV characterization imaging of EVs is important for revealing their spatiotemporal properties and further understanding of their functions. This analysis is often performed to determine the morphological features of EVs such as size and shape and to demonstrate the quality of EV purification. Researchers often use EM and AFM to characterize morphological features of EVs. While both techniques provide nanometer resolution and can distinguish EVs from non-EV particles, they are labor-intensive, time-consuming, and require costly equipment. Therefore, the research field needs alternative methods that will allow rapid morphology analysis and particle sizing. The growing field of lensless microscopy has great potential to address this demand, especially because the pixel size of imaging sensors is in the nanometer scale range and will continue to decrease.

In this chapter, to implement of aim II of the thesis, we present a new technology for the morphological characterization of EVs. The technology enables lensless, dark-field microscopy directly on a CMOS imaging sensor. It consists of two imaging modalities for particle visualization and size measurement: direct on-chip dark-field microscopy and shadow-based object height measurements. The dark-field modality results from contrast reversal observed at oblique illumination angles when most of the incident light is reflected from the surface of the sensor. This phenomenon can be explained through Fresnel equations. When objects are illuminated at angles between 0 and 85 degrees, they cast shadows that can be used to calculate their height.

Using this technique, we were able to detect and characterize unstained biological and non-biological samples including polystyrene nanospheres, single microorganisms, and clusters of microorganisms. While the technology has not been used for EVs characterization we believe it can be applied for the morphological analysis of EVs. The resolution of the system is determined by the pixel size of the CMOS imaging sensor and currently is 1.4 μm . At this point, large EVs

and clusters of sEVs can be visualized and characterized. However, we believe that with advancements in optical instrumentation, it will be feasible to characterize small EVs. Moreover, the approach does not require staining, labeling or large volumes of a sample, which makes it appealing for the EV research field. Other advantages of the technology are its straightforward sample preparation, and its low cost mainly due to the inexpensive CMOS imaging sensor and custom-built multi-angle illumination stage.

This chapter is based on the second of four first-author publications. The contributions of each author are as below:

SWH and ASP conceived the study concept. SWH, ASP, and MI designed the experiments. MI and ASP conducted the experiments and analysed the results. MI wrote the main text of the manuscript with input from all co-authors. SK drafted and revised the article. SWH supervised the project. All authors reviewed and approved the manuscript in its current form.

Chapter III. Lensless, reflection-based dark-field microscopy (RDFM) on a CMOS chip

Meruyert Imanbekova^{1,2}, Ayyappasamy Sudalaiyadum Perumal^{1,2}, Sara Kheireddine¹, Dan V. Nicolau¹, and Sebastian Wachsmann-Hogiu^{1,*}

¹Department of Bioengineering, McGill University, Montreal, Quebec, H3A 0E9, Canada

²Equal contributions

*sebastian.wachsmannhogiu@mcgill.ca

3.1 Abstract: We present for the first time a lens-free, oblique illumination imaging platform for on-sensor dark-field microscopy and shadow-based 3D object measurements. It consists of an LED point source that illuminates a 5-megapixel, 1.4 μm pixel size, back-illuminated CMOS sensor at angles between 0° and 90° . Analytes (polystyrene beads, microorganisms, and cells) were placed and imaged directly onto the sensor. The spatial resolution of this imaging system is limited by the pixel size ($\sim 1.4 \mu\text{m}$) over the whole area of the sensor ($3.6 \times 2.73 \text{ mm}$). We demonstrated two imaging modalities: (i) shadow imaging for estimation of 3D object dimensions (on polystyrene beads and microorganisms) when the illumination angle is between 0° and 85° , and (ii) dark-field imaging, at $>85^\circ$ illumination angles. In dark-field mode, 3-4 times drop in background intensity and contrast reversal similar to traditional dark-field imaging was observed, due to larger reflection intensities at those angles. With this modality, we were able to detect and analyze morphological features of bacteria and single-celled algae clusters.

© 2020 Optical Society of America under the terms of the OSA Open Access Publishing Agreement

3.2. Introduction

Light microscopy is one of the oldest scientific techniques and a key instrument in modern research. Lens-based microscopes are the most broadly used light microscopy systems. Yet, the ability to perform high spatial resolution imaging at enhanced magnification leads to limited field-of-view (FOV) and optical aberrations that distort the resulting image. To overcome the limitations of lens-based approaches, image stitching can be implemented to form mosaics with a large overall FOV of high-resolution images. However, such techniques require long acquisition times and can result in artifacts that are especially apparent at the overlap regions between the

individual tiles [1]. Mobile phones can serve as a practical, portable imaging platform, where a suitable compromise between spatial resolution and FOV can be found based on the camera specifications. There are many reports describing mobile phones as biomedical imaging devices that can be used for health-related imaging [2-4] and environmental applications [5, 6].

Lens-free approaches that typically use CMOS cameras found in mobile phones further simplify the hardware of imaging systems, whereby the sample is placed between the image sensor and the illumination source. One example is in-line holography, where the sensor detects shadows and diffraction interference patterns generated by the object, and the final image is reconstructed using computational algorithms. Whereas the FOV is limited by the sensor area, the spatial resolution can reach sub-pixel proportions using ptychographic imaging, where multiple images of the sample are taken at different illumination angles followed by image reconstruction [7, 8]. Such approaches can also be used for imaging biological samples [9-15], nanoparticles [16, 17] and can serve as portable and adaptable devices with minimal hardware requirements. However, these advantages come at a cost, which in this case is the computationally heavy holographic reconstruction, that eventually makes the system more complex.

Lens-free shadow imaging technologies have been successfully applied for various in vitro cellular applications [18-22]. However, the determination of micrometer-scale object size by existing systems without performing computing-intensive image reconstruction is an ongoing challenge. Cell size and volume are crucial parameters that have a significant impact on cell proliferation [23], response to environmental triggers [24], cellular homeostasis [25], and synaptic transmission [26]. The traditional techniques for micrometer-scale object size measurements such as flow cytometry and coulter counter are able to accurately detect the cell size in the range of tens of micrometers. However, the high cost of these methods limits their application to point-of-need applications. In addition to biological objects, the size of the particles within powders [27], emulsions [28], and aerosols [29] can influence the properties of these materials.

Non-holographic on-chip imaging, on the other hand, combines the conventional hardware design of lens-free imaging with ease of image acquisition since complicated image reconstruction is not required in this case [30]. In terms of biological applications, direct on-chip sensing has been used to characterize individual cell types on microscope slides [31], and within

microfluidic devices [32], study the behavior of *C. elegans* [33], detect cells that exhibit chemiluminescence [34] and have been adapted for sub-pixel resolution imaging [35, 36].

While lens-based, and to some degree lens-free holographic technologies, can be implemented in numerous different or combined modalities, direct on-chip lens-free microscopy is still limited to transmission-based imaging. One of the potential new modalities that will expand the existing range is dark-field microscopy.

Dark-field microscopy is an elegant optical technique, that allows extremely sensitive imaging due to its very low background and enhanced contrast of unstained objects. From the time of Van Leeuwenhoek, microscopists noted that some objects were more readily seen by applying oblique illumination that caused the darkening of the background while the object was visible due to the scattering of the oblique light. Since then, dark-field microscopy has been widely applied to image unstained biological samples [37-39] and nanoparticles [40, 41]. In the last decade, several groups of researchers reported dark-field microscopy using a CMOS sensor for imaging mainly metal nanoparticles. Z. Li et al., reported a miniaturized dark-field microscope based on a CMOS sensor and microfluidic chip [42]. Further work by Grishin et al. showed the 3D-nanoparticle and microparticle tracking technique based on dark-field microscopy [43]. Previously we reported a dual- phone illumination-imaging microscope that is able to perform various modalities of traditional microscopes, including dark-field [44] and phase contrast [45]. However, while these systems are potentially simpler and less expensive than dark-field microscopes, they still use lenses to achieve oblique illumination or for imaging.

Here we present for the first time a reflection-based lens-free directly on the sensor imaging system with oblique illumination for dark-field imaging and object height measurement of non-biological and biological objects of micrometer size. We show that by measuring the shadow length of the object, we can calculate the approximate height of the objects such as polystyrene microspheres and bacteria. Moreover, by illuminating the sensor surface at large angles, we observed a significant reduction of the background intensity and reversal of the contrast for the objects of interest. This is due to higher reflection intensities at those large angles (in accordance with Fresnel equations of reflection) and is the equivalent to the dark-field illumination mode normally seen in lens-based microscopes.

In our platform, the light beam from an incoherent illumination source is situated at a distance much larger than the size of the CMOS sensor or the LED such that it can be considered a point source. This beam is partially reflected, refracted, or scattered at the interface between the two different optical media. When the sample of interest placed on the CMOS sensor is illuminated from the top (0° angle), most of the light is transmitted and reaches the photosensitive area of the photodiode. As a result, the resulting image has a typical bright field appearance. On the other hand, when the angle of the incident light is close to 90° , most of the light is reflected and only a small amount of light is refracted, which, together with the scattered light from the sample, reach the photosensitive area of the detector. Subsequently, the background intensity of the images drops significantly, which leads to a better contrast of the object.

3.3 Experimental methods

5.3.1 Chemicals

Phosphate buffer saline (PBS) and ethanol were purchased from Sigma-Aldrich (USA). Sulfate latex particles (8% w/v) size of $1.6\ \mu\text{m}$ were purchased from Invitrogen (USA). Polystyrene microspheres (50 mg/ml) size $7\ \mu\text{m}$ were purchased from Microspheres-Nanospheres (USA).

3.3.2 Lensless imaging platform

The imaging sensor is a back-illuminated 5-megapixel (MP) sensor module (OV5647, OmniVision technologies) with a 2592×1944 active array, and 8-/10-/24-bit RGB/RAW image output. The original lens and IR filter were removed in this set-up to achieve lensless imaging, and the sensor surface was thoroughly characterized via SEM and AFM (Fig. 1). Next, we applied a thin layer of a polymer (polydimethylsiloxane) onto the edges of the sensor in order to protect the electrical circuitry surrounding the immediate sensor area.

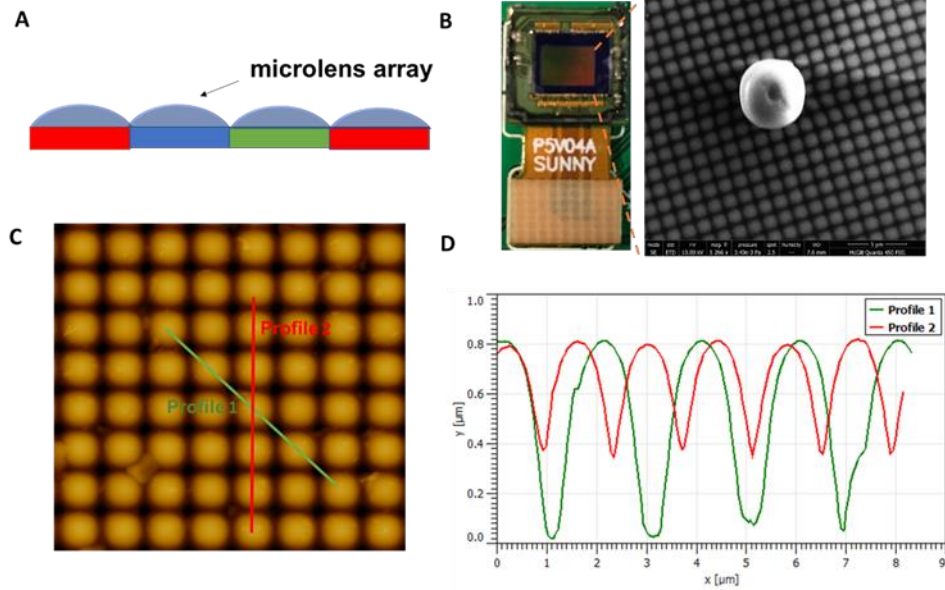


Fig. 1. CMOS sensor surface characterization. (A) Schematic illustration of the image sensor surface. (B) Photographic image of the CMOS sensor (left) and Scanning Electron Microscopy (SEM) image of a 7 μm bead on the sensor surface (right). (C) AFM image of the CMOS sensor surface. (D) AFM profile of the sensor surface and measurement of the height of the microlenses array.

Image acquisition and image processing were performed by via Raspberry Pi 3 Model B board using the Python programming language. Note that the FOV of the image sensor is the same as the active area and is 3.67×2.73 mm. The spatial resolution of the system is limited by the pixel size and is $1.4 \mu\text{m}$.

We designed a multi-angle illumination platform that consists of three rulers set perpendicular to each other in XYZ directions. The X axis ruler provides the horizontal support and has a digital angle finder that allows precise measurement of the incident angle (Fig. 2). The Y axis ruler provides adjustment for the height of the light source to achieve certain angles of illumination. As a source of incoherent light, we used a single cool white light LED with the wavelength range approximately 420-700 nm, diameter less than 1 mm and a remote controller for intensity modulation (SUSAY Electronics technology, China, model number NI-TL). The LED is mounted onto the Z axis holder that travels in a semi-circular path above the CMOS sensor, thereby creating a radius of 270 mm from the center of the sensor to the light source. Since the distance between the LED and the CMOS sensor is much larger than their physical dimensions, the illumination can be considered as a point source. The CMOS sensor was placed on a Z-adjustable stage and illuminated from various angles from 90° (oblique angle) up to 0° (top

illumination). A droplet of polystyrene beads (5 μL) of different sizes 1.6 μm and 7 μm was added directly onto the sensor surface and allowed to dry. We then imaged the beads under multiple angles, ranging from 0° (top) angle to 90° (oblique) angle.

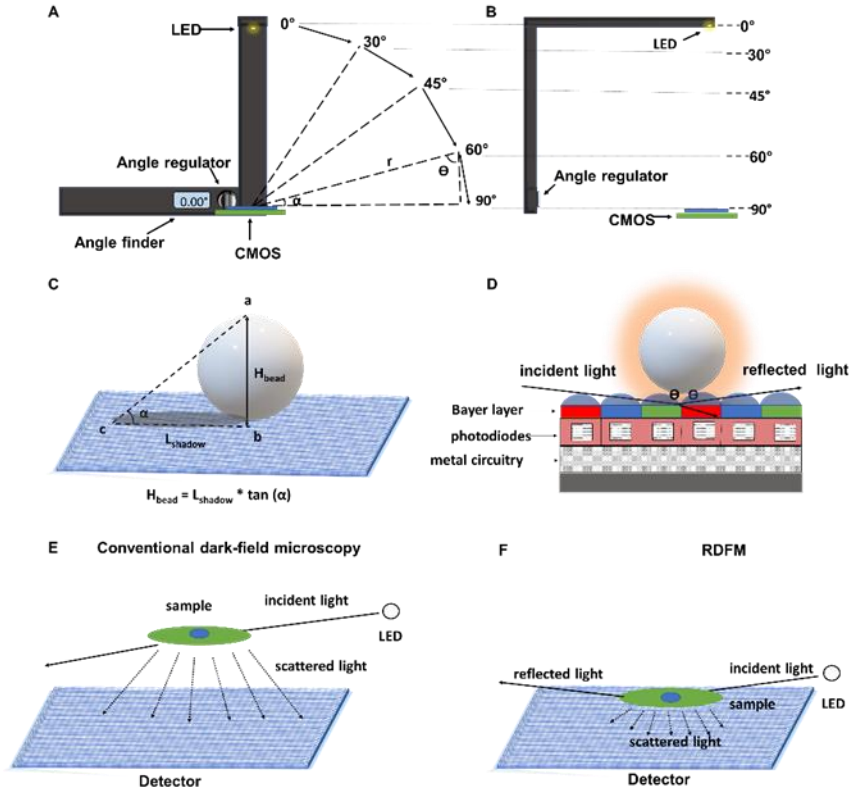


Fig. 2. Schematic of on-sensor dark-field microscopy via oblique angle illumination. (A) Diagram of the illumination set-up (front view) that allows for multi-angle illumination ranging from 0° to 90° by rotating the point-like illumination source along a semicircle with radius r with the CMOS sensor placed in the center of the circle. (B) The side view diagram of the illumination set-up (C) Representation of a bead on the CMOS sensor. The shadow cast by the point source illumination is measured experimentally and the height of the object can be calculated based on a length of the shadow and known angle of incidence. (D) Schematic representation of the CMOS sensor and light illumination at a large angle. Microlenses are at the top layer, with the Bayer layer, photodiodes, and metal circuitry underneath. Microlenses focus the light onto the photodiodes such that a high fill factor can be achieved. The light beam travelling at a large angle reaches the sensor surface and gets reflected with the intensity of the reflected light obeying the Fresnel equations. The pixel fill factor also changes (is reduced) at shallow illumination angles. These two phenomena lead to a change in the contrast and background intensities. (E) In conventional oblique illumination dark-field microscopy the sample of interest is placed in a distance from the sensor surface and

illuminated at an oblique angle. The incident light rays will illuminate the sample, and the photons that are not scattered are either blocked or propagate next to the detector without being detected. Only scattered photons will be collected by the detector. (F) In RDFM, dark-field microscopy is achieved through Fresnel reflection of the incident light at the interface between air and the CMOS surface.

To capture the image, we used a custom Python code to acquire standard JPEG images and raw Bayer data. The raw Bayer data is the data from the camera sensor prior to GPU processing such as demosaicing, auto white balance, smoothing etc. This data output is important in this work in order to be able to quantify the change in the image background. The raw Bayer image has a green and dark output appearance due to the BGGR pattern that has twice as many green pixels as red and blue. The raw images were saved to the camera as 6 MB data files, followed by extracting the PNG images that allow lossless compression of files. Afterwards, images were further analysed by additional software packages as described in the following section.

After imaging, the sensor can be effectively cleaned by pipetting a few microliters of 70% ethanol onto the sensor surface and gently wiping with lens tissue. The sensor can then be reused without any noticeable alterations in image quality.

3.3.3 Bead-size quantification based on shadow images

ImageJ (NIH), GraphPad Prism 6, and MATLAB (MathWorks) were utilized to process and analyse all captured bead shadow images. In Fig. 2C, the height of the objects H was calculated from geometrical considerations from the measurement of the length of the shadow casted by the object at an angle α . The length of the shadow was measured by using averaged gray scale intensity values of the indicated area measured from the image. The angle α is equal $(90^\circ - \Theta)$, where Θ is the incidence angle (Fig. 2A). The height of the object is determined from the tangent of the angle α , for known shadow length and incidence angle.

3.3.4 Characterization via Scanning Electron Microscopy

The structural properties of the surface of the sensor were characterized by SEM microscopy. All SEM images were obtained using FEI NanoSEM instrument with accelerating voltage of 10 kV under high vacuum mode.

3.3.5 Characterization via Atomic Force Microscopy

The sensor surface was analyzed by an AFM (Multi Mode 8, Bruker) contact mode using triangular cantilevers (Hi'Res-C, MicroMasch, Estonia) with a radius of curvature of 1 nm. The obtained images were analyzed by Gwydion software.

3.3.6 Preparation of Microorganisms

Euglena gracilis and *Staphylococcus epidermidis* were purchased from Carolina Biological supply Company (USA). The chosen biological sample, *E. gracilis*, has pigmented organelles, chloroplasts, and hence a strong ability to scatter light effectively, which makes it an ideal sample for testing the dark-field illumination mode. *E. gracilis* cells range from 8-20 μm in length, are oval in shape cells and are much larger than the previously tested 7 μm beads. On the other hand, *S. epidermidis* is a spherical bacterium with the body size ranging from 0.5-1.5 μm , whose dimensions are close to the resolving power of the pixels of this CMOS sensor. We grow *E. gracilis* at room temperature in a liquid Provasoli's enriched seawater (PES) medium that was prepared following the protocol in a Handbook of Culture Media for Food and Water Microbiology [46]. The liquid PES culture was added directly onto the sensor surface, dried, and imaged. *S. epidermidis* colonies were cultured in a Nutrient broth (NB) medium at 30° overnight. Prior to incubation, a single colony of *S. epidermidis* was inoculated in 6 ml of NB medium. During the experiment, the liquid culture was added by pipetting directly onto the sensor surface or diluted beforehand if necessary.

3.4 Results and discussions

3.4.1 3D geometrical measurements from shadow imaging

In order to demonstrate 3D geometrical measurements a droplet of microspheres of 7 μm and 1.6 μm in size was pipetted onto the sensor surface, dried and imaged at four angles of illumination. Fig. 3A shows the shadow images of the 7 μm and 1.6 μm beads acquired at four different illumination angles. When the particle is illuminated by a source located above the sensor (0°), a shadow is cast right below the microsphere. The resulting images are used to evaluate the lateral dimensions of the object. Changing the angle of illumination will affect the projection of the shadow and increase the shadow length for larger angles, which in turn can be used for determination of the height of the object. Whereas shadow-based height estimation can be

theoretically performed using multiple illumination angles, the choice of angle is important to be able to accurately delineate object-shadow boundaries. At small illumination angles (close to bright-field mode) as seen in Figure 3A it is difficult to accurately determine the object-shadow boundaries especially in the cases where the size of the object is similar to the pixel size of the sensor. In addition, at small angles the shadow cast by the object lies beneath the object itself. Conversely, at large illumination angles, the object casts large shadows that can be measured as intensity drop. This makes the object-shadow boundaries discernable and measurable (Fig.3A). Therefore, for the measurement of the height of micrometer-sized samples, the ideal illumination angle that provides the aforementioned conditions was found to be 84° . Next, using the images of the beads at 84° angle, we first obtained the plots of the grayscale intensity values across the background-bead-shadow-background region (blue rectangle), as shown in Fig. 3B. The highest point in the plot (global maximum) represents the maximum scattering intensity generated by the bead. We then measured the cast shadow length starting from the global maximum marked in the graph, since part of the bead cast shadow lies under the object itself. Note, that this criterion of the shadow beginning is applicable for objects that are measured at 84° angle. The end of the cast shadow is identified by the point where the grayscale intensity values reach those of the background (plateau region). Since the best shadow measurements are obtained at large angles, one may think that further increasing the angle will provide better results. However, at the larger illumination angles (87° - 90°) scattering of the particles becomes predominant. This mode, which we call dark field mode, will be described in the following section (section 3.2). The distance between the photosensitive area of the pixels and the sample is relatively small and was not considered in the measurements of the shadow. However, the subtraction of the microlens array height (~ 440 800 nm) could possibly reduce the potential error in the object height measurements. Yet, the subtraction of the full microlens array height depends on the particles size and their distribution on the sensor surface, meaning that some particles will dry on top of the highest points of the microlens array, while others will fall into the gaps between adjacent microlenses (Figure 1D). In the first scenario, the subtraction of the full size of the microlens array is more meaningful. On the other hand, the particles that are smaller than the gap between top ends of the adjacent microlenses (~ 1.93 μm along Profile 1, and ~ 1.4 μm along Profile 2, Figure 1D) will more likely lie at shorter distances from the sensor surface, which would warrant the subtraction of a reduced microlens height. Then, knowing the size of the pixels, we were able

to calculate the shadow length in μm . Next, the height of microparticles of various sizes was measured by using the right triangle that is formed as depicted in Fig. 2C, where H is the height of the microparticle, L is the shadow length, and α is the angle ($90^\circ - \Theta$), where Θ is the illumination angle. The estimated values of the height of the microparticles are presented in Table 1.

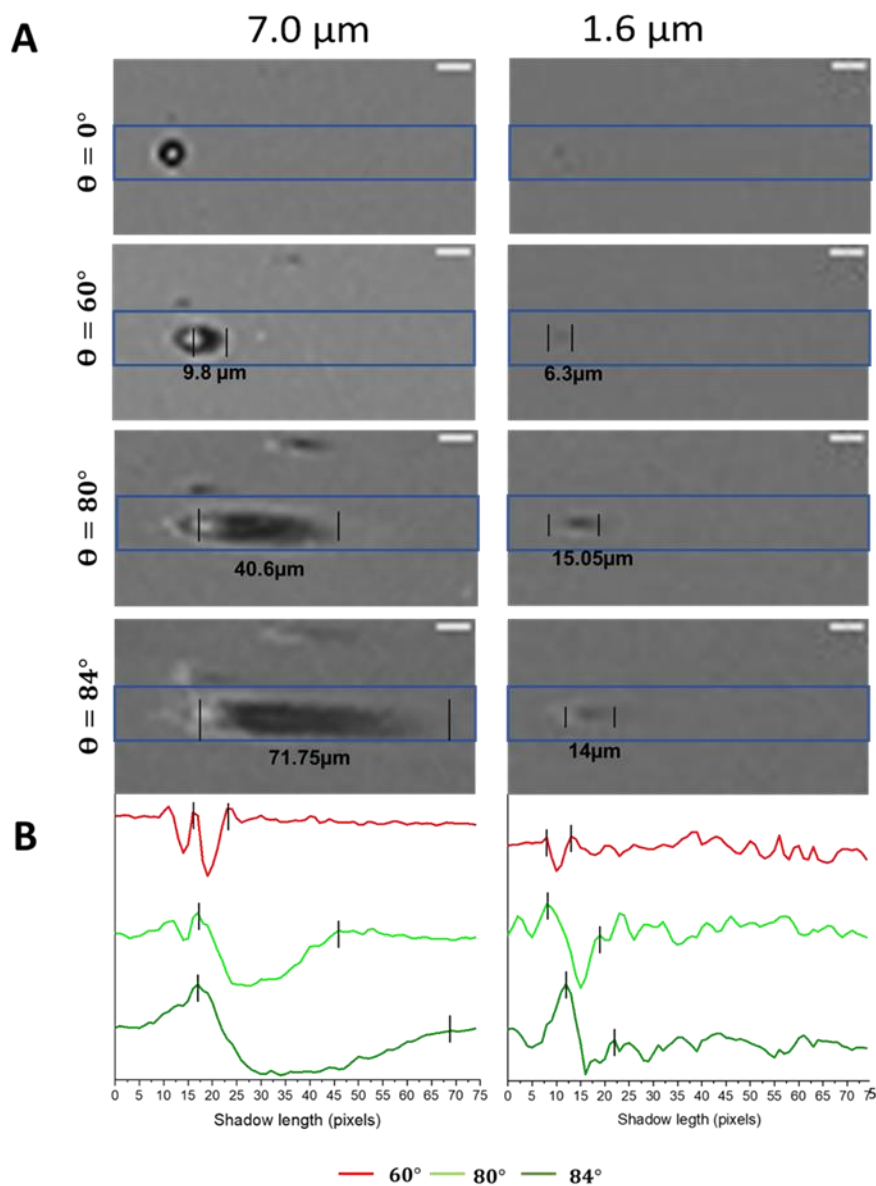


Fig. 3. Shadow measurements for estimation of object dimensions. (A) The length of the shadow increases as the illumination angle is increased from 0° to 84° for both 7 μm and 1.6 μm beads. (B) Plot of gray scale intensities measured within the blue rectangle. The length of the shadow changes can be measured for various angles of illumination and bead size. The scale bar in the inset corresponds to 10 μm .

Table 1. Shadow-based object height estimation

Polystyrene bead size (μm)	The length of the shadow cast (pixels and μm)			The length of the shadow cast at 84° (pixels and μm)	Estimated height (μm)
	(0°)	(60°)	(80°)		
7 μm	(0°)	(60°)	(80°)	51.25 pixels/ 71.75 μm	~7.4 μm
	5 pixels/7 μm	7 pixels/9.8 μm	29 pixels/40.6 μm		
1.6 μm	1-2pixels/ 1.4-2.8 μm	4.5 pixels/ 6.3 μm	10.75 pixels/ 15.05 μm	10 pixels/ 14 μm	~1.5 μm

The results show a good correlation between the estimated height and the original size of the microspheres. Yet it is important to note that the microspheres were dispersed over the whole area of the CMOS sensor in order to achieve accurate height estimation. Estimation of the height of a denser sample will be more challenging as sample entities may have shadow regions nested within one another. For the reported range of angles, even with improved shadow contrast, the minimal distance between adjacent objects has to be large enough to completely cover the full length of the cast shadow, excluding the penumbra for simplicity. Recently, several groups have presented CMOS-based lens-free platforms for particle size and height measurements [20, 21]. With respect to these measurements, the main difference between our platform and existing systems is the inherent simplicity. For example, while other methods for height measurements (such as those based on in line holography) require advanced computation techniques, in our platform the sample is placed onto the sensor surface and the shadow is directly measured from the resulting image. Moreover, the accuracy of the height estimate could be further improved by placing the sample even closer to the sensor surface by removing the microlenses and/or by using a CMOS chip with a smaller pixel size.

3.4.2 Dark-field microscopy on the CMOS sensor

In traditional microscopes, dark-field imaging is typically achieved by oblique illumination where the direct light is blocked from passing through the objective. The sample is placed at a

certain distance from the sensor and the microscope objective collects only light that is scattered from the sample with minimal background or unscattered light, thus enhancing the contrast between the sample and the relatively dark background (Fig. 2E).

On the other hand, in a lens-free platform, the light beam reaches the sensor surface, and the sensor collects both scattered and unscattered light from the sample. At large angles of incidence, according to the Fresnel equations of reflection, almost all the light is reflected leaving a small number of photons to be transmitted which leads to the darkening of the background. However, scattered light is mostly isotropic, and it will be collected by the detector. This leads to a microscopy mode where the scattering objects appear brighter than the background, similar to the dark-field microscopy mode (Fig. 2F).

In order to achieve dark-field illumination mode, we designed a configuration where the light is incident at large angles (close to 90° vs. the normal incidence to the surface of the sensor). This will make dark-field imaging possible even when blocking of the incident light is not possible such as for samples that are very close to the detector. The intensity of the reflected light at the interface between air (refractive index of 1) and the surface of the sensor (plastic, with a refractive index approximately 1.5) obeys the Fresnel equations such that at large angles of incidence, almost total reflection at this interface is expected. We explored this phenomenon as a modality of reducing the background in our images and recording scattered light similar to dark-field microscopy. In order to characterize the performance of this technique, we scanned across a sequence of incident angles starting from 84° up to 90° . For this, a droplet of microspheres of $7\ \mu\text{m}$ and $1.6\ \mu\text{m}$ in size was pipetted onto the sensor surface, dried, and imaged at various angles of illumination. The blue lines on the image correspond to the ones depicted in the graph and aimed to highlight the analysed objects. As shown in Fig. 4, we observed a gradual change in background intensity starting from 84° of incidence angle and reaching a maximum darkening at 90° in processed as well as in raw images. We were still able to observe long shadows of the $7\ \mu\text{m}$ microspheres at angles between 84° up until 89° (Fig. 4A). On the other hand, at the 90° angle, the shadows disappeared and only scattering of the object was observed. The analysis of $1.6\ \mu\text{m}$ (Fig. 4B) showed similar trend in background intensity drop, yet the scattering intensity of the microspheres differed and was reduced due to the smaller size of the object. The raw images of the beads at top illumination angle show different patterns of coloration that could be

explained by false coloration artifact of processing generated by color filter array. However, the observed coloration of the images did not affect further analysis of the background intensity reduction. The graphs in Fig. 4C and 4D represent gray scale intensities of the raw and processed images of 7 μm and 1.6 μm microspheres. In order to calculate the decrease in background intensity, we also acquired an image without any incident light to be used as a baseline intensity (shown as a black dotted line in Fig. 4C and 4D). The graphs reveal a three to four times drop of the background intensity in the dark-field mode of the system in comparison with top illumination at 0° . This is at least three times lower than the expected drop that can be calculated from Fresnel equations, mainly due to the low flatness of the CMOS sensor (see Fig. 1) that leads to additional scattering. The calculated contrast values for the dark-field (90°) images of 7 μm and 1.6 μm beads are 0.3 for both, compared to 0.07 and 0.04, respectively, for the bright-field (0°) images.

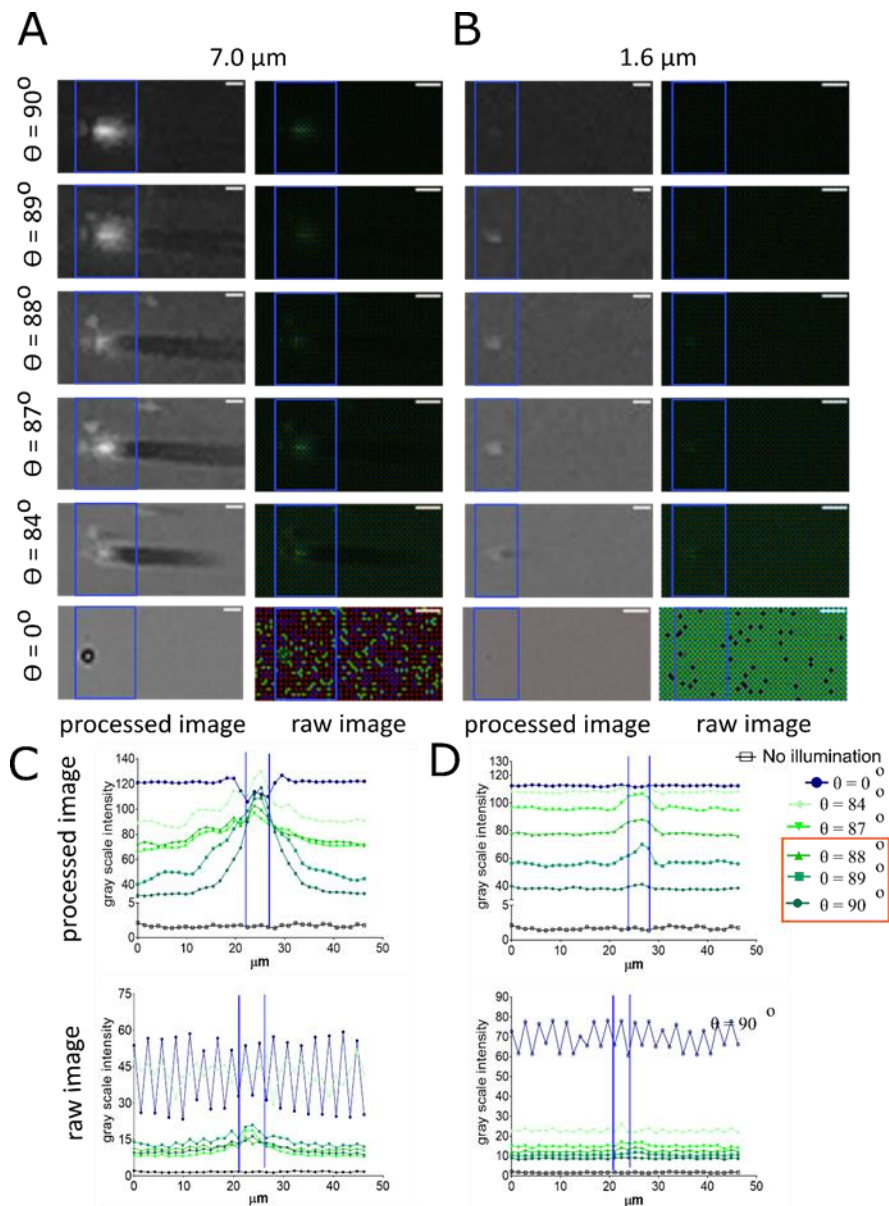


Fig. 4. Dark-field illumination mode. As the angle of incidence approaches 90° a gradual change in image contrast due to the decrease in background intensity for $7\ \mu\text{m}$ (A) and $1.6\ \mu\text{m}$ (B) beads. Panels A and B contain two sub-columns with processed images (left) and raw images (right) acquired from the Raspberry Pi. (C) and (D) represents two rows of graphs corresponding to processed (top) and raw (image) gray scale intensities. The background intensity drops three to four times at large angles. The drastic drop in background was more prominent in a narrow angle range, i.e., for illumination angles between 87° - 90° (red box). The black dotted line corresponds to baseline intensities from a control image acquired in a completely dark room. The blue lines running vertically represent the borders for the areas used for plotting the graphs here and throughout this work. The scale bar corresponds to $10\ \mu\text{m}$.

Furthermore, the dark-field imaging set-up described here has been used for the detection of two or more clustered objects that are close to each other. (Figure 5)

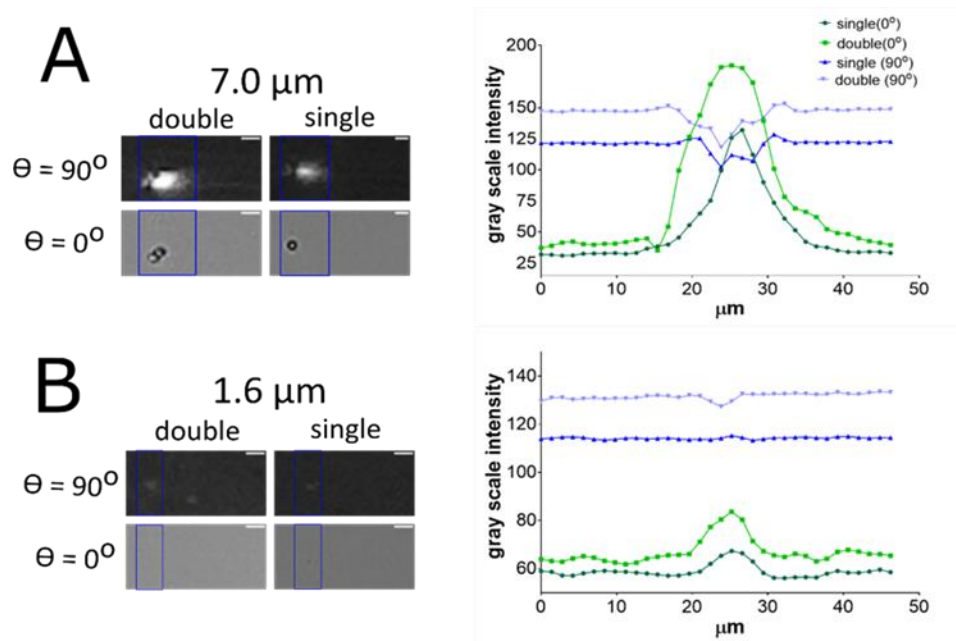


Fig. 5. Detection of clustered beads using the intensity of the reflected light at Fresnel reflection angles.

Intensity difference for a single particle and two particles in close proximity for 7 μm sized (A) and also 1.6 μm sized beads (B). The graph at the right for the corresponding bead size illuminated at two different incident angles ($\theta = 90^\circ$ and $\theta = 0^\circ$) shows the variation of scattered light intensity depending on the number of clustered particles. The blue lines represent the borders used for plotting the graphs.

When several objects are close to each other, the scattering intensity is proportional to the number of objects. According to the Mie scattering theory, the intensity of light scattered by micrometer-sized objects also depends on the object size angle of incidence, and wavelength of light. While we cannot distinguish between these phenomena, we observed and were able to detect clustered polystyrene beads of various sizes (7 μm and 1.6 μm) based on gray scale intensities (Figure 5). A similar effect of detection using intensity differences has been further demonstrated using biological samples in the following sections.

3.4.3 Imaging of biological samples on the CMOS sensor

3.4.3.1 Reflection-based dark-field microscopy of biological objects and geometrical shadow- based height measurements

A 5 μl droplet of *E. gracilis* liquid culture was pipetted onto the sensor surface that was previously hydrophilized with poly-l-lysine, followed by heat fixing. Two types of imaging were performed with *E. gracilis*, namely the shadow-based object height measurements as well as

RFDM at large angles of illumination, i.e., $> 84^\circ$. Fig. 6A represents the single *E. gracilis* cell at various angles of illumination. Here, we were able to observe the same gradual background drop as in previous experiments with polystyrene microspheres. Single *E. gracilis* cells were observed as bright shining objects on a dark background at illumination angles close to 90° . In Fig. 6B, the depicted graph shows a gradual drop in the background intensity starting from 0° to an angle close to 90° , in agreement with Fresnel equations of reflection. The contrast values changed from 0.2 in the bright-field images to 0.6 in the dark field images. Next, we measured the height of *E. gracilis* based on a cast shadow length and the angle of incidence. Fig. 6C depicts elongation of the *E. gracilis* shadows with a decrease of an incident angle. This effectively verifies the experimental results performed with polystyrene beads, showing the versatility of this system for fixed biological samples. Afterward, using the gray scale intensity plots, we measured the lengths of the cast shadows. The limits of the shadow were determined with the same method used for microspheres described above. The calculation of the height of the *E. gracilis* cells using determined shadow length and known incidence angle resulted to be $\sim 5 \mu\text{m}$. The result is consistent with *E. gracilis* dimensions previously reported in the literature, while taking into consideration the potential size reduction of the sample as a result of fixation. [47]. The measurement of the single *E. gracilis* length at a top angle is found to be between 10-11 μm for Fig. 6A and close to 15 μm for Fig. 6C.

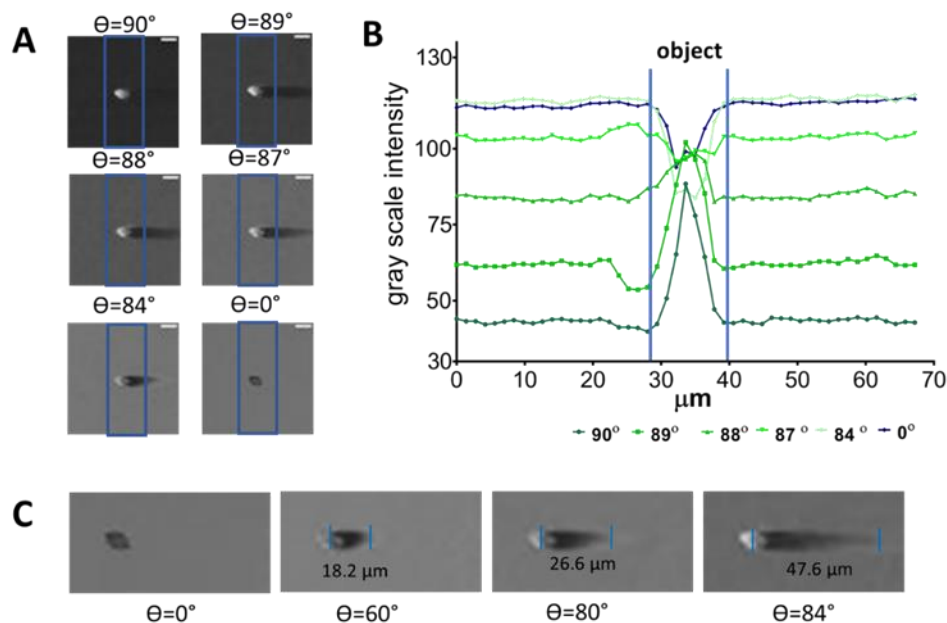


Fig. 6. Imaging *E. gracilis*. (A) *E. gracilis* at different illumination angles ranging from 0° to 90° . A gradual reduction in the background intensity is observed when the illumination angle is increased. (B) Graphical representation of the intensity profiles measured within the blue rectangle shown in panel (A). A 3-times drop of the background intensity with the increase of the incident angle reaching the maximum dark-field mode at 90° is observed. (C) Determination of the shadow length for the subsequent height calculation. (scale bars – $10\mu\text{m}$).

Following experiments with *E. gracilis*, *S. epidermidis* was used as a biological sample to demonstrate close-to-pixel resolution/visualization. A $5\mu\text{L}$ droplet of the bacterial culture was mixed with 3% glutaraldehyde solution (1:1 vol by vol) and pipetted onto the poly-l-lysine treated sensor surface. The droplet was then dried and imaged at various illumination angles. Fig. 7 shows the representative results of the experiment. The sample, which was not visible under top illumination, becomes distinguishable at higher incidence angles starting from 84° up to 90° due to changes in contrast between the shadow and the background intensity. The cells appear bright at higher incidence angles between 90° to 87° , while a faint shadow was visible at lower angles starting from 87° . These observations demonstrate the visualization of the bacterial samples with dimensions close to the pixel size of the sensor. In addition, the gray scale intensity-based quantification (Fig. 7B) shows a gradual decrease of the background brightness (y-axis, Fig. 7B) with an increase of the incidence angles from 90° to 84° (shades of green). The scattering images show approximately 2-3 μm object width (across x-axis), that corresponds to

the width of either a single bacterium or a doublet of bacteria (represented as short peaks) that is commonly known to form a doublet or clusters.

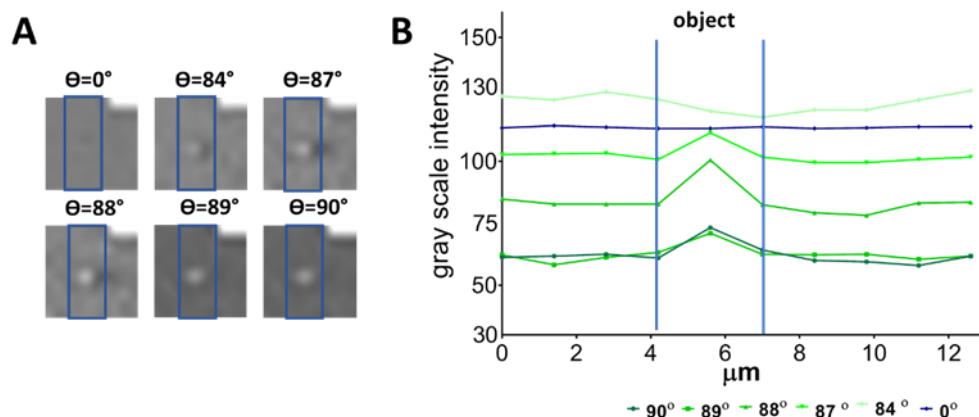


Fig. 7. Imaging of the fixed *S. epidermidis* under various angles of illumination. (A) The bacteria, which is of a size similar to the size of a pixel of the CMOS sensor, becomes visible under the large angles starting at 70° up to 90° angles. (B) Graphical representation of the data shows two times drop in the background intensity at larger illumination angles due to Fresnel reflection and lower fill factor, which leads to better contrast (scale bar $5\mu\text{m}$).

In summary, the results demonstrate the ability of the presented platform to perform dark-field imaging of biological and non-biological objects over the full field-of view of an inexpensive CMOS sensor, as well as straightforward measurements of the height of micrometer-sized objects. The platform configuration allows us to perform experiments rapidly. However, the method has several limitations that could be improved by applying further engineering approaches. One such limitation is the increase of the sensor surface temperature during imaging, which restricts the use of this method for live biological samples. However, this issue could be potentially resolved by the addition of a heat sink that can reduce the temperature of the sensor. Another limitation of the system is that, at this point of development, it allows measurements of only fixed/dry samples. In order to perform dark field imaging of liquid samples, further improvements to the system are necessary for refractive index matching.

3.4.3.2 Resolving features in a 3D cluster of single-celled algae (*E. gracilis*)

We imaged the cluster of *E. gracilis* using a multiangle illumination platform. Fig. 8 represents the results of the pixel-by-pixel mapping of the *E. gracilis* cluster. The imaging and following analysis consider four different angles of illumination, such as scattering angle (90°), near scattering angles (84° and 80°) and top angle (0°). Fig. 8A illustrates that, at scattering angles, the

cluster of *E. gracilis* cells produces varying intensities of bright and dark spots, while in near scattering angles, the image appears as an overlap of bright field and dark-field images, with a unique observation of the dark pixels from dark-field imaging subsequently showing features of varying brightness intensity from near scattering illumination. The bright field illumination at top angle, showed no major variation of intensity although the cells appeared greenish, due to the chloroplast pigments. The gray scale intensities of the selective illumination angles, here 90° (Fig. 8C -left), 10° (Fig. 8C – middle) and 0° (Fig. 8C - right), shows a systematic pixel by pixel mapping of information that can be extracted from images using the presented set-up (shown as white arrows, labelled as numbers). This is performed by comparing the quantification graph for three representative angles (Fig. 8B) to the corresponding images of the *E. gracilis* cluster (Fig. 8C – scattering, near-scattering and top images). The peaks marked as numbers in the graph could be mapped from the x-axis scale values of the graph to that of the x-axis scale of the image. Each number in the graph for a different illumination set-up maps to the corresponding gray scale intensity line in the graph with the same numbers marked for mapping either as pixel by pixel or as μm by μm across the x-axis of the graph and the image.

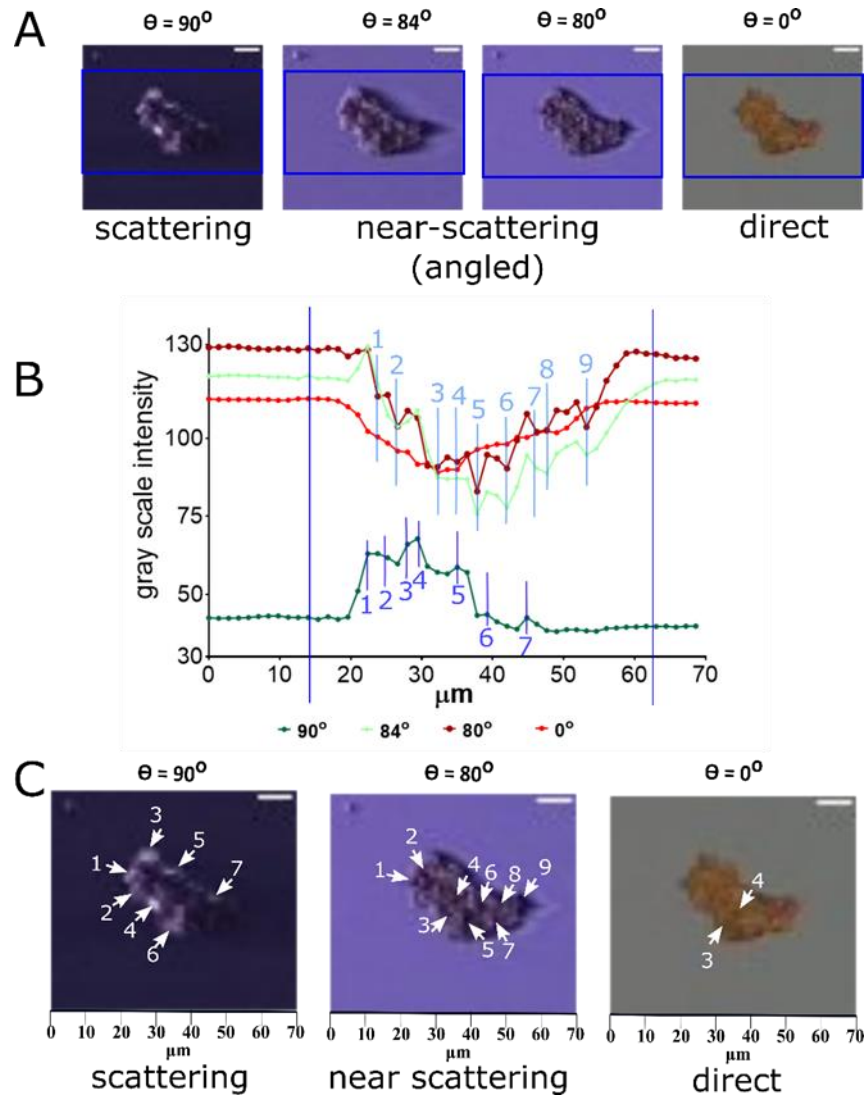


Fig. 8. Mapping pixel by pixel details of the biological samples at different angles. (A) *E. gracilis* cluster imaged under various angles of illumination. (B) Graph with pixel-by-pixel mapping based on the gray scale intensities calculated for the images, observed as peaks, labelled with numbers which are marked in the respective cluster of *E. gracilis* image at three different illumination angles (C).

These mapping can be used for further elucidating the morphological differences within the cluster. Under the top illumination, the morphological characteristics of the cluster are not clear (only two discernible peaks). In contrast, changing the angle of incidence to 90° (7 discernible bright spots in image and peak in graph) and 84° to 80° (9 discernible bright and dark spots for both the graph and image) leads to the observation of distinguishable morphological features of the *E. gracilis* cluster (Fig. 8B and 8C). This analysis led to the prediction of a total of 7-9 *E. gracilis* cells in the cluster. Such measurements and a combinatorial superimposition were

demonstrated here without any post processing but by changing the angle of illumination only, makes this set-up promising for analysis of microbial consortia. Furthermore, we were able to observe shadows cast by the microspheres of different sizes as well as single protist/bacterial samples at near scattering angles, which combines both bright field and scattering characteristics within one image.

3.5 Conclusion

In this article, we demonstrated, for the first-time, dark-field microscopy directly on a CMOS sensor without the use of any lenses. This novel technique takes advantage of the fact that for incident light propagating from a medium with a lower refractive index (such as air) to a higher refractive index (such as plastic) at angles of illumination close to 90° , a larger fraction of light intensity is reflected, in accordance with the Fresnel equations of reflection. The larger the intensity of reflected light, the lower the background recorded by the CMOS sensor, leading to a reversal of the contrast of the object in dark-field mode vs. the bright field illumination mode, similar to that observed in lens-based dark-field microscopy modes. Individual objects and clusters of objects could be observed, for objects both larger and similar to the pixel size, highlighting the strength and robustness of the technique. In addition, using oblique illumination at angles between 0° and 85° we observed and quantified geometrical shadows of objects ranging in sizes from few micrometers to tens of micrometers. From simple geometrical considerations, we were able to calculate the height of these objects, in addition to their lateral dimensions that were determined from the bright field images.

The capabilities of the new imaging modality were tested on polystyrene beads of sizes ranging from $1.6\ \mu\text{m}$ to $7\ \mu\text{m}$, where a three- to four-fold reduction of the background was observed for illumination at angles close to 90° vs. 0° . This is short of the expected $>$ ten-fold background reduction (from Fresnel equations), largely due to the fact that the surface of the sensor is not flat. Improvements in the background reduction factor are expected if the surface flatness is increased by physical or chemical methods. For the 84° angle of illumination, shadow measurements of these polystyrene beads allowed for accurate height measurements, indicating the possibility of this technique to be used for 3D measurements of biological objects.

Next, we used these modalities for the imaging and quantification of biological samples that were fixed on the surface of the CMOS sensor. Single *E. gracilis* cells were imaged in both

shadow and RDFM modes, which allowed for the calculation of height (~5 μm) and length (10-11 μm). Fixed bacteria (*S. epidermidis*) were also imaged under various angles of illumination, demonstrating the ability of resolving and quantifying small, micrometer-sized biological objects. In addition, large clusters of *E. gracilis* algae were imaged to demonstrate the capability of the technique for quantifying 3D morphological features within colonies of microorganisms.

Overall, we demonstrated here a new platform for cost-effective, reflection-based dark-field microscopy modality (RDFM) directly on a CMOS sensor that allows for high spatial resolution (limited to the pixel size) and large field-of-view imaging of unstained, dried, or fixed biological and non-biological objects. In addition, this platform allows estimation of the height of micrometer-sized particles (via geometrical shadow measurements at oblique illumination) for the characterization of 3D morphological features. From a practical viewpoint, such measurements can be useful to understand different states of the cancerous cells, particularly during the metastatic cancer cells studies, the tissue generation, studying the effects of drug molecules on the cell membranes of the cancerous cells [48] and the effects on extracellular matrix materials [49]. The cancerous cells produce different levels of extracellular matrix, leading to variability in cellular thickness, cytoplasm to nucleus ratios and as a result to differences in morphology and cell mechanics [50]. These effects are challenging to be axially resolved for large FOV using a conventional microscopy technique without fluorescence or even with fluorescence requires confocal microscopy with extensive image post-processing and sample labeling [51]. In addition, quantitative phase imaging (QPI) has been applied to characterize morphological alterations of the cancer cells and has several advantages over conventional techniques, such as ability to analyse live and unlabeled cells [52]. However, QPI method requires extensive image acquisition process with image-post processing and expensive equipment. Recently, 3D- on-chip imaging has been discussed widely for such applications [53], and the RDFM platform would fall in line with similar applications. Due to the low cost and simplicity, this technique can also be implemented for use in low resource environments for biological, medical, food safety, or environmental monitoring applications. Applications to the pathology field for the imaging of large, fixed (stained or unstained) thin tissue sections or blood or cell culture smears are also possible, where the large field-of-view, coupled with the high spatial resolution and improved contrast, would provide an advantage over existing methods.

3.6 Author contributions

All authors made substantial intellectual contributions to the manuscript and approved it for publication.

3.7 Conflict of interest

The authors declare that the research was conducted in the absence of any commercial or financial relationships that could be construed as a potential conflict of interest.

3.8 Acknowledgements

This work was financially supported by the National Sciences and Engineering Research Council of Canada (NSERC), Discovery Grant RGPIN-2018-05675 (to S.W.-H.), Natural Sciences and Engineering Research Council (NSERC) Discovery Project No 238925 (to D.V.N.); M.I. acknowledges the Bolashak International Scholarship for PhD studies.

References

1. J. Chalfoun, M. Majurski, T. Blattner, K. Bhadriraju, W. Keyrouz, P. Bajcsy, and M. Brady, "MIST: Accurate and Scalable Microscopy Image Stitching Tool with Stage Modeling and Error Minimization," *Scientific Reports* 7, 4988 (2017).
2. Z. J. Smith, K. Chu, A. R. Espenson, M. Rahimzadeh, A. Gryshuk, M. Molinaro, D. M. Dwyre, S. Lane, D. Matthews, and S. Wachsmann-Hogiu, "Cell-Phone-Based Platform for Biomedical Device Development and Education Applications," *PLOS ONE* 6, e17150 (2011).
3. T. Gao, Z. J. Smith, T.-y. Lin, D. Carrade Holt, S. M. Lane, D. L. Matthews, D. M. Dwyre, J. Hood, and S. Wachsmann-Hogiu, "Smart and Fast Blood Counting of Trace Volumes of Body Fluids from Various Mammalian Species Using a Compact, Custom-Built Microscope Cytometer," *Anal Chem* 87, 11854-11862 (2015).
4. C. W. Pirnstill and G. L. Coté, "Malaria Diagnosis Using a Mobile Phone Polarized Microscope," *Scientific Reports* 5, 13368 (2015).
5. Q. Wei, R. Nagi, K. Sadeghi, S. Feng, E. Yan, S. J. Ki, R. Caire, D. Tseng, and A. Ozcan, "Detection and Spatial Mapping of Mercury Contamination in Water Samples Using a Smart-Phone," *ACS Nano* 8, 1121-1129 (2014).
6. T. S. Park, W. Li, K. E. McCracken, and J.-Y. Yoon, "Smartphone quantifies Salmonella from paper microfluidics," *Lab on a Chip* 13, 4832-4840 (2013).
7. W. Bishara, T.-W. Su, A. F. Coskun, and A. Ozcan, "Lensfree on-chip microscopy over a wide field-of-view using pixel super-resolution," *Opt. Express* 18, 11181-11191 (2010).

8. Y. Wu, Y. Luo, G. Chaudhari, Y. Rivenson, A. Calis, K. de Haan, and A. Ozcan, "Bright-field holography: cross-modality deep learning enables snapshot 3D imaging with bright-field contrast using a single hologram," *Light: Science & Applications* 8, 25 (2019).
9. A. Ozcan and U. Demirci, "Ultra wide-field lens-free monitoring of cells on-chip," *Lab on a Chip* 8, 98-106 (2008).
10. G. Stybayeva, O. Mudanyali, S. Seo, J. Silangcruz, M. Macal, E. Ramanculov, S. Dandekar, A. Erlinger, A. Ozcan, and A. Revzin, "Lensfree Holographic Imaging of Antibody Microarrays for High-Throughput Detection of Leukocyte Numbers and Function," *Anal Chem* 82, 3736-3744 (2010).
11. Y. Zhang, H. Ceylan Koydemir, M. M. Shimogawa, S. Yalcin, A. Guziak, T. Liu, I. Oguz, Y. Huang, B. Bai, Y. Luo, Y. Luo, Z. Wei, H. Wang, V. Bianco, B. Zhang, R. Nadkarni, K. Hill, and A. Ozcan, "Motility-based label-free detection of parasites in bodily fluids using holographic speckle analysis and deep learning," *Light: Science & Applications* 7, 108 (2018).
12. A. F. Coskun, T.-W. Su, and A. Ozcan, "Wide field-of-view lens-free fluorescent imaging on a chip," *Lab on a Chip* 10, 824-827 (2010).
13. T.-W. Su, A. Erlinger, D. Tseng, and A. Ozcan, "Compact and Light-Weight Automated Semen Analysis Platform Using Lensfree on-Chip Microscopy," *Anal Chem* 82, 8307-8312 (2010).
14. R. Delacroix, S. N. A. Morel, L. Hervé, T. Bordy, J.-M. Dinten, M. Drancourt, and C. Allier, "Cerebrospinal fluid lens-free microscopy: a new tool for the laboratory diagnosis of meningitis," *Scientific Reports* 7, 39893 (2017).
15. W. Xu, M. H. Jericho, I. A. Meinertzhagen, and H. J. Kreuzer, "Digital in-line holography for biological applications," *Proceedings of the National Academy of Sciences* 98, 11301 (2001).
16. O. Mudanyali, E. McLeod, W. Luo, A. Greenbaum, A. F. Coskun, Y. Hennequin, C. P. Allier, and A. Ozcan, "Wide-field optical detection of nanoparticles using on-chip microscopy and self-assembled nanolenses," *Nature Photonics* 7, 247-254 (2013).
17. F. Kazemzadeh and A. Wong, "Laser Light-field Fusion for Wide-field Lensfree On-chip Phase Contrast Microscopy of Nanoparticles," *Scientific Reports* 6, 38981 (2016).
18. T. Aidukas, R. Eckert, A. R. Harvey, L. Waller, and P. C. Konda, "Low-cost, sub-micron resolution, wide-field computational microscopy using opensource hardware," *Scientific Reports* 9, 7457 (2019).
19. G. Jin, I.-H. Yoo, S. P. Pack, J.-W. Yang, U.-H. Ha, S.-H. Paek, and S. Seo, "Lens-free shadow image based high-throughput continuous cell monitoring technique," *Biosensors and Bioelectronics* 38, 126-131 (2012).
20. A. Greenbaum, Y. Zhang, A. Feizi, P.-L. Chung, W. Luo, S. Kandukuri, and A. Ozcan, "Wide-field computational imaging of pathology slides using lens-free on-chip microscopy," *Science translational medicine* 6, 267ra175 (2014).
21. M. Roy, D. Seo, C.-H. Oh, M.-H. Nam, Y. J. Kim, and S. Seo, "Low-cost telemedicine device performing cell and particle size measurement based on lens-free shadow imaging technology," *Biosensors and Bioelectronics* 67, 715-723 (2015).

22. A. Shanmugam and C. Salthouse, "Lensless fluorescence imaging with height calculation," *Journal of Biomedical Optics* 19, 016002 (2014).
23. F. Lang, M. Ritter, N. Gamper, S. Huber, S. Fillon, V. Tanneur, A. Lepple-Wienhues, I. Szabo, and E. Bulbins, "Cell Volume in the Regulation of Cell Proliferation and Apoptotic Cell Death," *Cellular Physiology and Biochemistry* 10, 417-428 (2000).
24. T. Key, A. McCarthy, D. A. Campbell, C. Six, S. Roy, and Z. V. Finkel, "Cell size trade-offs govern light exploitation strategies in marine phytoplankton," *Environmental Microbiology* 12, 95-104 (2010).
25. S. Taheri-Araghi, S. Bradde, J. T. Sauls, N. S. Hill, P. A. Levin, J. Paulsson, M. Vergassola, and S. Jun, "Cell-size control and homeostasis in bacteria," *Curr Biol* 25, 385-391 (2015).
26. E. Henneman, G. Somjen, and D. O. Carpenter, "FUNCTIONAL SIGNIFICANCE OF CELL SIZE IN SPINAL MOTONEURONS," *Journal of Neurophysiology* 28, 560-580 (1965).
27. X. Fu, D. Huck, L. Makein, B. Armstrong, U. Willen, and T. Freeman, "Effect of particle shape and size on flow properties of lactose powders," *Particuology* 10, 203-208 (2012).
28. R. Pal, "Effect of droplet size on the rheology of emulsions," *AIChE Journal* 42, 3181-3190 (1996).
29. U. Dusek, G. P. Frank, L. Hildebrandt, J. Curtius, J. Schneider, S. Walter, D. Chand, F. Drewnick, S. Hings, D. Jung, S. Borrmann, and M. O. Andreae, "Size Matters More Than Chemistry for Cloud-Nucleating Ability of Aerosol Particles," *Science* 312, 1375 (2006).
30. Z. Göröcs and A. Ozcan, "On-chip biomedical imaging," *IEEE Rev Biomed Eng* 6, 29-46 (2013).
31. T.-W. Su, S. O. Isikman, W. Bishara, D. Tseng, A. Erlinger, and A. Ozcan, "Multi-angle lensless digital holography for depth resolved imaging on a chip," *Opt. Express* 18, 9690-9711 (2010).
32. J. Kun, M. Smieja, B. Xiong, L. Soleymani, and Q. Fang, "The Use of Motion Analysis as Particle Biomarkers in Lensless Optofluidic Projection Imaging for Point of Care Urine Analysis," *Scientific Reports* 9, 17255 (2019).
33. X. Cui, L. M. Lee, X. Heng, W. Zhong, P. W. Sternberg, D. Psaltis, and C. Yang, "Lensless high-resolution on-chip optofluidic microscopes for *Caenorhabditis elegans* and cell imaging," *Proceedings of the National Academy of Sciences* 105, 10670 (2008).
34. T. Tanaka, T. Saeki, Y. Sunaga, and T. Matsunaga, "High-content analysis of single cells directly assembled on CMOS sensor based on color imaging," *Biosensors and Bioelectronics* 26, 1460-1465 (2010).
35. G. Zheng, S. A. Lee, Y. Antebi, M. B. Elowitz, and C. Yang, "The ePetri dish, an on-chip cell imaging platform based on subpixel perspective sweeping microscopy (SPSM)," *Proceedings of the National Academy of Sciences* 108, 16889 (2011).
36. A. C. Sobieranski, F. Inci, H. C. Tekin, M. Yuksekkaya, E. Comunello, D. Cobra, A. von Wangenheim, and U. Demirci, "Portable lensless wide-field microscopy imaging platform based on digital inline holography and multi-frame pixel super-resolution," *Light: Science & Applications* 4, e346-e346 (2015).
37. G. S. Verebes, M. Melchiorre, A. Garcia-Leis, C. Ferreri, C. Marzetti, and A. Torreggiani, "Hyperspectral enhanced dark field microscopy for imaging blood cells," *Journal of Biophotonics* 6, 960-967 (2013).

38. R. M. Macnab, "Examination of bacterial flagellation by dark-field microscopy," *J Clin Microbiol* 4, 258-265 (1976).
39. S. Enoki, R. Iino, N. Morone, K. Kaihatsu, S. Sakakihara, N. Kato, and H. Noji, "Label-Free Single-Particle Imaging of the Influenza Virus by Objective-Type Total Internal Reflection Dark-Field Microscopy," *PLOS ONE* 7, e49208 (2012).
40. T. Wagner, H.-G. Lipinski, and M. Wiemann, "Dark field nanoparticle tracking analysis for size characterization of plasmonic and non-plasmonic particles," *J Nanopart Res* 16, 2419-2419 (2014).
41. T. Wagner, A. Kroll, C. R. Haramagatti, H.-G. Lipinski, and M. Wiemann, "Classification and Segmentation of Nanoparticle Diffusion Trajectories in Cellular Micro Environments," *PLOS ONE* 12, e0170165 (2017).
42. Z. Li, "Miniature optofluidic darkfield microscope for biosensing," in *Ultrafast Nonlinear Imaging and Spectroscopy II*, (International Society for Optics and Photonics, 2014), 91980G.
43. O. V. Grishin, I. V. Fedosov, and V. V. Tuchin, "Lens-free dark-field digital holographic microscopy for 3D tracking of microparticles," in *Saratov Fall Meeting 2014: Optical Technologies in Biophysics and Medicine XVI; Laser Physics and Photonics XVI; and Computational Biophysics*, (International Society for Optics and Photonics, 2015), 944816.
44. S. Kheireddine, A. Sudalaiyadum Perumal, Z. J. Smith, D. V. Nicolau, and S. Wachsmann-Hogiu, "Dual-phone illumination-imaging system for high resolution and large field of view multi-modal microscopy," *Lab on a Chip* 19, 825-836 (2019).
45. S. Kheireddine, Z. J. Smith, D. V. Nicolau, and S. Wachsmann-Hogiu, "Simple adaptive mobile phone screen illumination for dual phone differential phase contrast (DPDPC) microscopy," *Biomed Opt Express* 10, 4369-4380 (2019).
46. J. E. Corry, G. D. Curtis, and R. M. Baird, *Handbook of culture media for food and water microbiology* (Royal Society of Chemistry, 2011).
47. R. Pal and A. K. Choudhury, *An introduction to phytoplanktons: diversity and ecology* (Springer, 2014).
48. R. Domura, R. Sasaki, Y. Ishikawa, and M. Okamoto, "Cellular Morphology-Mediated Proliferation and Drug Sensitivity of Breast Cancer Cells," *J Funct Biomater* 8, 18 (2017).
49. C. Walker, E. Mojares, and A. Del Río Hernández, "Role of Extracellular Matrix in Development and Cancer Progression," *Int J Mol Sci* 19, 3028 (2018).
50. A. Pathak and S. Kumar, "Independent regulation of tumor cell migration by matrix stiffness and confinement," *Proc Natl Acad Sci U S A* 109, 10334-10339 (2012).
51. F. Pampaloni, E. G. Reynaud, and E. H. K. Stelzer, "The third dimension bridges the gap between cell culture and live tissue," *Nature Reviews Molecular Cell Biology* 8, 839-845 (2007).
52. Y. Park, C. Depeursinge, and G. Popescu, "Quantitative phase imaging in biomedicine," *Nature Photonics* 12, 578-589 (2018).

53. Y. Zhang, Y. Shin, K. Sung, S. Yang, H. Chen, H. Wang, D. Teng, Y. Rivenson, R. P. Kulkarni, and A. Ozcan, "3D imaging of optically cleared tissue using a simplified CLARITY method and on-chip microscopy," *Science Advances* 3, e1700553 (2017).

Transition to chapter IV

In the previous chapter, we demonstrated the fabrication, characterization, and application of the RDFM technique. These modalities have numerous advantages including high spatial resolution (limited to the pixel size) and large FOV imaging of unstained, dried, or fixed biological and non-biological objects, low cost of the platform and ease of operation. The RDFM has been applied to visualize and characterize morphological features of micrometer-sized objects. While the detection and visualization of EVs have not been demonstrated, it is assumed that given the size range of EVs (30 nm – 2000 nm) the platform is applicable for the analysis of large EVs or clustered sEVs. Moreover, considering advancements in optical sensors leading to a reduction of the pixel size of an imaging sensor (currently the smallest pixel size is 560 nm), analysis of small EVs could be possible in due course.

In this chapter, according to Aim III of the thesis, we expand the use of the CMOS imaging sensor beyond the detection of EVs to the characterization of their biochemical cargo *via* SERS.

SERS is an optical label-free technology that allows detection and characterization of molecules that are carried by EVs with high sensitivity in a non-destructive manner. SERS has been applied to characterize EV molecular content (see Section 3 of the comprehensive literature review). Moreover, the SERS substrate may be used to concentrate and trap EVs in strong plasmonic enhancement areas known as hot spots. The following study describes the CMOS-based sensing platform for trapping, imaging, and chemical characterization (CMOS TrICC) of biological samples, including EVs. We performed a thorough characterization of the morphological features of the surface of SERS substrate and identified crevices between adjacent microlenses that concentrate electromagnetic fields and at the same time trap EVs. Evaluation of the performance of the technology using 4-ATP and R6G molecules yielded results comparable to what was previously reported.

Additionally, 100 nm size polystyrene nanospheres and EVs were analysed. The results show two orders of magnitude higher SERS intensities in the intracavity areas compared to SERS intensities on top of the microlenses. The collected SERS spectra exhibit characteristic peaks of each aforementioned analytes.

Overall, integration of SERS modality within a lens-free imaging platform enables optical imaging and spectroscopic analysis of EVs in one analytical system. This unique combination of

modalities is promising in regard to the rapid and sensitive assessment of EV sample purity and heterogeneity analysis.

This work has been done within a framework of an international collaboration with researchers from Gaziantep University, Turkey, and Tampere University, Finland.

This chapter is based on my third first-author article. The contributions of each author are as below:

SWH conceived the idea. MI and SWH designed experiments. MI and JL performed the substrate fabrication and hot spots localization characterization. MK and AMS performed the substrate morphology characterization and EF calculation experiments. HC conducted simulations. MI conducted experiments for the application of the SERS substrate for nanospheres and EVs characterization. MI wrote the main body of the manuscript with input from all the co-authors. SWH supervised the project. All authors reviewed and approved the manuscript in its current form.

Chapter IV. Complementary Metal-Oxide-Semiconductor - Based Sensing Platform for Trapping, Imaging, and Chemical Characterization of Biological Samples

Meruyert Imanbekova^a, Ayse Mine Saridag^b, Mehmet Kahraman^b, Juanjuan Liu^a, Humeyra Caglayan^c, and Sebastian Wachsmann-Hogiu^{a,*}

^a Department of Bioengineering, McGill University, Montreal, QC, H3A 0E9, Canada

^b Department of Chemistry, Gaziantep University, Sehitkamil/Gaziantep, 27310, Turkey

^c Faculty of Engineering and Natural Sciences, Tampere University, Tampere, 33720, Finland

* Corresponding author: sebastian.wachsmannhogiu@mcgill.ca

Keywords: CMOS imaging sensor, particle trapping, optical imaging, SERS substrate, extracellular vesicles, label-free

Abstract

CMOS imaging sensors provide the unique opportunity for combining lensless imaging with new modalities that enable sample handling and chemical characterization. In this study, we present a new CMOS-based sensing platform for trapping, imaging, and chemical characterization of samples via SERS (CMOS-TrICC). The SERS substrate is fabricated directly on a CMOS imaging sensor by depositing a thin metallic layer on top of the CMOS microlenses. SERS activity is based on square unite cell patterned, closely spaced, micrometer-sized microlenses on the surface of the imaging sensor. Morphological analysis of the surface revealed an intracavity depth of approximately 700 nm and height-dependent width ranging from a minimum of just a few nm between two lenses to a maximum of 1,400 nm, with a flat valley exhibiting approximately 300 nm width at the bottom between four lenses. These morphological features concentrate electromagnetic fields into SERS hot spots and at the same time help trap nanometer-sized particles in the wells created by microlenses. Strongest plasmonic effect is expected in the gaps between microlenses. Simulations were used to map the distribution of electromagnetic field enhancement on the SERS substrate surface and at a distance above it. The performance of the SERS substrate and its dependence on the silver layer thickness was examined using 4-aminotheophenol and rhodamine 6G with the experimental enhancement

factor measured to be 5.0×10^4 . We demonstrated the use of this substrate for parallel trapping of 100 nm nanospheres and EVs in the gaps between microlenses and SERS characterization of these particles in the hot spots. SERS intensities are two orders of magnitude higher in the nanogaps between microlenses (intracavity area) than on top of the microlenses and for polystyrene they exhibited signature peaks centered at 1000 cm^{-1} and 1600 cm^{-1} . SERS spectra of small EVs collected from intracavity areas where EVs were trapped show peaks known to arise from their main biochemical constituents, such as lipids, proteins, and nucleic acids. While the surface of the CMOS imaging sensor became SERS active by the addition of the metallic layer, the imaging capability is maintained and provides the opportunity for direct on-chip lensless imaging with spatial resolution limited by the pixel size, opening new directions for integrated (bio)sensing devices.

Introduction

CMOS imaging sensors provide the unique opportunity for lensless imaging. Digital holography is one example of such lensfree approach, where the imaging sensor detects shadows and diffraction interference patterns caused by sample placed in a certain distance from a sensor and computation algorithms are applied to generate final image. Recent advances in lensless imaging technologies enabled sub-pixel spatial resolution by employing ptychography¹, coded aperture correlation holography² and noniterative super-pixel shifting holography³. While such approaches have been successfully applied for imaging of biological samples^{4, 5} and nanoparticles⁶, they require the use of complex image reconstruction algorithms. On the other hand, direct on-chip imaging enables high resolution microscopy with ease of image acquisition and does not require complicated image reconstruction step^{7,8}. Previously, our group reported a direct on-chip dark-field microscopy as a new modality in addition to conventional transmission-based imaging modality⁹. Development of a new imaging mode to direct on-chip imaging platforms expands existing range of their functionality and opens new ways for their applications. One of such potential modalities is SERS. Combination of SERS with lensfree on-chip microscopy enables both high spatial resolution over the wide field of view imaging and chemical content characterization.

SERS is a powerful technique that allows detection and chemical characterization of low concentration analytes^{10,11}. The technique employs an enhancement mechanism (electromagnetic

and chemical) to amplify weak yet structurally rich Raman signals to detectable levels¹². Such amplification is the result of the excitation of the localized surface plasmons that often occurs in between gaps of nanostructures and crevices (so-called hot spots) of noble metals such as gold and silver¹². The enhancement of SERS is found to reach factors as high as 10^{14} and depends on the plasmonic material and its structure, as well as the source of excitation¹³. Plasmonic nanostructures are commonly made of silver (Ag), gold (Au), or copper (Cu), and have been developed in a wide variety of shapes and configurations to reach maximum SERS enhancement¹⁴⁻¹⁶. It is important to note that SERS enhancement strongly depends on the distance between the surface of the substrate and the molecule of interest and reaches its highest values within a few nanometers (1-4 nm) distance¹⁷. SERS has been used to study chemical dynamics¹⁸ and single molecules detection¹⁹, protein conformational changes²⁰, and biological samples including bacteria^{21, 22} and viruses²³, nucleic acids²⁴, and disease markers²⁵.

In the field of EVs, SERS has been used to detect EVs and characterize mainly their membrane composition and less often their molecular cargo^{26, 27}. EVs are lipid membrane enclosed particles that carry proteins, lipids, nucleic acids and found to function as mediators of cell-cell communications²⁸. EVs are secreted by all cells in human body and are found in variety of biological fluids. Consequently, they may be used as a liquid biopsy source for diagnosis and monitoring of diseases. Currently isolation and purification of EVs remains challenging and rely on a laborious multi-step process such as differential centrifugation and/or size exclusion chromatography that often leads to low EVs yield and may generate, in addition to the desired EVs, isolation co-contaminants. Therefore, assessment of the purity of isolated EVs is essential to compare cross-study results and their therapeutic application. Moreover, considering EV diagnostic and therapeutic value, rigorous analysis of their molecular cargo is essential.

While the desirable purity of EV preparation mainly depends on scientific question, increasing concentration of EVs is often required for downstream analysis in both basic and clinical research. The choice of the concentration methods varies between studies and most of them report use of additional techniques to complement primary technique such as variety of affinity isolation methods and filtration techniques, variations of chromatography methods and microfluidics-based approaches. In SERS-based studies, the role of such enrichment technique may be fulfilled by the SERS substrate with unique specifications that allow in situ concentration

of EVs. This approach has been applied by using superhydrophobic plasmonic materials²⁹ and substrates with complex geometries that can concentrate, capture or trap EVs within the area of plasmonic enhancement. Researchers developed SERS substrates with vast variety of surface geometries including micropillars³⁰, nanopillars³¹, microbowls²⁹ and nanobowls³², nano-porous films³³, perforated pyramidal structures³⁴ that allowed trapping of EVs in hot spot locations. In some cases, preparation of such substrates requires the use of laborious lithography methods, clean room, or expensive equipment. There are other shortcomings of existing SERS substrates for EV characterization. One important disadvantage is that hot spots are usually not uniform across the substrate, leading to large variations in the SERS intensities and inability of making accurate comparisons between molecules or particles trapped in different regions, and therefore making it difficult to apply meaningful classification methodologies. In addition, common SERS substrates are able to enhance Raman signals of molecules located only in close proximity to the plasmonic structures, limiting the analysis of EVs to mostly EV membranes but not the intraluminal cargo. Moreover, SERS measurements of EVs in liquid media remains difficult to perform. Most studies that use SERS for EV biochemical characterization require drying of EVs on the surface of a substrate, which may introduce artifacts related to drying. While the choice of sample handling depends on specific research goal, in studies with a clear clinical end goal or functional studies it is desired to keep EVs in conditions as close to physiological as possible³.

To address some of these shortcomings, in this study, we introduce a new platform that can be used to record optical images, capture, and analyze the biochemical content of EVs by SERS. The active surface of the substrate is fabricated by sputtering a thin layer of silver onto a CMOS imaging sensor surface. The microlenses on the CMOS sensor in this lensless microscopy platform play the role of enhancing the fill factor of photodiodes and do not contribute to image formation. The SERS substrate poses various advantages when compared to substrates fabricated using traditional photolithography or soft lithography techniques, such as simple preparation that does not require nanofabrication, low cost, and most importantly uniform distribution of hot spots. The ability to generate even distributions of hot spots with large SERS active area results in consistent SERS intensity enhancement factors and, due to the distribution of the field enhancement, the ability to probe both EV membrane and intraluminal cargo. This important feature has the potential to help identify subpopulations of EVs spread over large areas by recording SERS chemical maps and perform classification of spectra from many different hot

spots. Next important characteristic of this SERS substrate is its ability to capture EVs in the nanometer sized gaps located between microlenses allowing analysis of a few EVs at a time. Finally, CMOS-TrICC enables recording optical images of the analytes placed directly on its surface. This unique function paves the way for direct lens free chemical imaging of biological analytes of interest.

Materials and Methods

Materials

4-ATP (97%), Rh6G, ethanol (70%), phosphate buffer saline, and polystyrene nanospheres of 100 nm diameter were purchased from Sigma Aldrich.

Fabrication of the CMOS-SERS substrates

To fabricate the SERS substrate, we removed the original lens and IR filter from the CMOS sensor (OV5647, OmniVision technologies) revealing a layer of uniformly distributed and a closely packed microlens array (3670 μm \times 2740 μm) arranged in a square unit pattern. Next, a silver layer of various thicknesses (20 nm, 40 nm, 60 nm, and 80 nm) was deposited onto the sensor surface via electron beam evaporation (BJD1800 EBeam Evaporator).

Structural characterization of the uncoated CMOS imaging sensors and SERS substrates

SEM and AFM were used for the structural characterization of silver-coated CMOS sensors. SEM images were obtained by using a Carl Zeiss FE-SEM instrument at a high vacuum with the acceleration voltage of 3 kV. EDX analysis was also used to determine the concentration of the silver (Ag) on the Ag-coated CMOS sensors. EDX spot analysis was performed for the CMOS sensors having different Ag thicknesses using three different points on the surface: top of the lens, between two lenses and between four lenses. AFM images of uncoated CMOS sensors and CMOS sensors coated with various Ag thicknesses were obtained by Park Systems XE-100 instrument using non-contact mode.

SERS Measurements

4-ATP and Rh6G were used to evaluate SERS performance of the developed SERS substrates. For this purpose, the coated SERS substrates were first treated with 4-ATP (1 mM) dissolved in ethanol for an hour, and then they were washed with ethanol and water. 1 mM Rh6G was also prepared in ethanol and 5 μl of Rh6G was dropped onto the SERS substrates with different Ag

thicknesses (20 nm, 40 nm, 60 nm, and 80 nm) and air-dried. The SERS measurements were performed with a Renishaw InVia Reflex Raman Microscopy System (Renishaw Plc., UK) equipped with a 785 nm laser and 50× magnification objective (NA 0.75) with laser power of 0.3 mW was used for 4-ATP and 3 mW for Rh6G. The exposure time and accumulation were 1 s and 1, respectively. Spectra of 4-ATP and R6G were obtained from the three different samples and at least ten randomly chosen points on each sample. The obtained 10 spectra were averaged to assess the SERS performance of the SERS substrates with different Ag thicknesses.

SERS enhancement factor (EF) was also calculated for SERS substrates with 40 nm Ag layer. Two spectra were obtained to calculate the SERS EF. First, we obtained the Raman spectrum of 5 μ l of R6G (0.1 M) solution dropped on a CaF₂ slide. Then, 5 μ l of R6G (1.0×10^{-4} M) was dropped on SERS substrate, and SERS spectra were recorded from 10 different (randomly selected) spots on the SERS surface using 3 mW excitation from a 785 nm laser (50×, NA 0.75) with 1 s acquisition time.

SERS hot spot characterization

The SERS substrate coated with 40 nm layer of Ag was immersed for 1 hour in 1 mM 4-ATP that was prepared in ethanol. To remove the unbound 4-ATP molecules the surface of the SERS substrate was washed with ethanol. For SERS mapping, a WITec Confocal Raman microscopy system (WITec Alpha300R) with 633 nm HeNe laser was used (100×, NA: 0.9). An area of 10 μ m by 10 μ m was mapped with a step size 250 nm in X -axis and 500 nm in Y-axis (40×20 data points). The spectra were collected in 1 accumulation during 1 s. The laser power was ~0.3 mW at the sample.

EV isolation and characterization

To isolate EVs we collected cell culture media (50 ml) from midbrain organoids cultured as described previously³⁵. Briefly, midbrain organoids were formed from induced pluripotent stem cell line (iPSCs) derived from peripheral blood mononuclear cells of a healthy individual.

Next, we centrifuged cell culture media at low speed 300 g for 10 min. The supernatant was then centrifuged at 2,000 g for 15 min to remove cell fragments and debris. The collected supernatant was further centrifuged at 10,000 g for 30 min. This step is aimed to pellet large vesicles, protein aggregates, and microvesicles. All the above-mentioned steps were performed at 4°C using Beckman Culture Microfuge 20R centrifuge with a FA361.5 Biosafe rotor. To pellet EVs,

collected supernatant was ultracentrifuged at 120,000 g for 90 min at 4°C using Beckman Optima TLX Ultracentrifuge with SW 28 swinging bucket rotor. Finally, collected pellet was resuspended, aliquoted (50 ml) to reduce freeze-thaw cycles, and stored at -80°C. NTA was performed to analyse EVs concentration and size distribution using NanoSight model LM10 (Malvern Panalytical Ltd, UK) as described previously³⁵. Briefly, the isolated EVs were diluted in ultrapure water 100 – fold. Next, 1 ml of the sample was injected into the NTA machine. After, three 30 s videos of the sample in flow conditions were recorded. The acquired data was then analyzed using a NanoSight NTA 3.1. software. We employed TEM to characterize morphological features of isolated EVs. For this, we incubated EVs on the carbon-film coated glow discharged TEM grids for 5 min at room temperature. Then, a solution of 1% uranyl acetate (8 ml) was dropped onto the surface of the grid and incubated for 1 min. This step was followed by the removal of the excess uranyl acetate and grids were dried at room temperature for 30 min. TEM was performed using FEI Tecnai G2F20 transmission microscope operating at 120 kV. For SERS characterization, 5 µl droplet containing EVs was put onto the SERS substrate surface and let air-dry. SERS maps were recorded over are 5 µm ×5 µm under 100X objective (NA 0.9, WD 0.31 mm) and integration time 1 s.

Simulations

The numerical simulations were performed using Ansys Lumerical FDTD Solutions which is based on the finite-difference time-domain (FDTD) method. In the simulation, the symmetric and antisymmetric boundary conditions were applied in the X and Y directions to minimize the simulation time, while PML (perfectly matched layer) was used along the Z-axis (propagation direction) to remove the unwanted reflections. A plane wave was launched from the Z-axis to excite the resonance cavity mode. The complex refractive index of the Ag layer (40 nm) was assigned from the “Johnson and Christy” data set which was inbuilt in the software material library³⁶. The microlens array was modeled as a dielectric with a refractive index $n = 1.5$.

The electric field profiles are obtained using a field monitor at different z values (0.15 and 0.30 micron) for 2 different wavelengths 785 nm and 633 nm.

Data pre-processing and analysis

WITec Project 5.1. build-in software (ImageLab) and OriginPro (OriginLab, Northampton, MA) were used to perform pre-processing and analysis of the data. Pre-processing step included fifth

polynomial correction of the baseline and Savitzky-Golay smoothing. Peak deconvolution was achieved by built-in multiple peak fit analysis using Voigt peak shape function.

Results and discussion

Results

The simple, robust, and low-cost CMOS-based SERS active platform (CMOS-TrICC) was fabricated by coating a thin Ag layer on commercially available CMOS imaging sensors. Figure 1 describes the workflow of the study including the Raman microscopy system, fabrication of SERS substrate, trapping of biological particles in SERS hot spots, optical and SERS imaging, and chemical characterization via SERS.

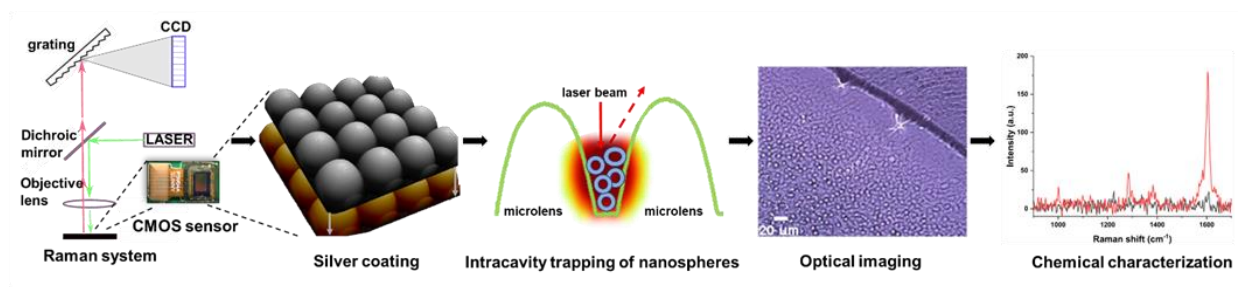


Figure 1. Schematic representation of CMOS-TrICC, including Raman microscopy system, CMOS coating, trapping of small particles and biological samples of interest, optical imaging with the CMOS sensor, and chemical characterization of analytes of interest trapped in hot spots via SERS.

Electron beam evaporation technique was used to coat the CMOS sensors with various thicknesses of silver (20 nm, 40 nm, 60 nm, and 80 nm) to tune the plasmonic properties of the SERS-active surfaces.

Structural characterization of fabricated SERS substrates was performed using SEM and AFM. SEM was used for 2-dimensional (2D) morphology and elemental analysis of the surfaces. AFM was used for the 3D structural morphology and line analysis of the surfaces. Figure 2A shows the SEM image of SERS substrate.

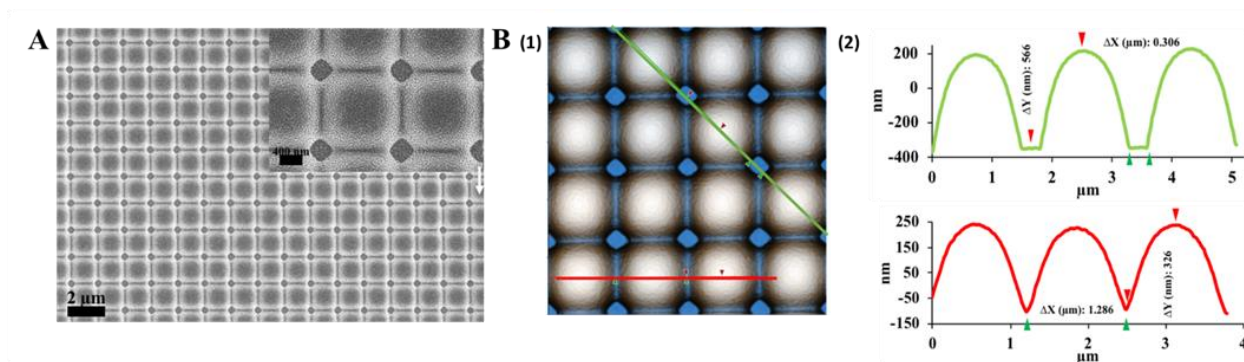


Figure 2. SERS substrate surface morphology characterization. A) SEM image of SERS substrate surface reveals highly uniform distribution of microlenses with hot spot forming crevices between four microlenses. B) 2D AFM images of the surface with line analysis of the surfaces (B1); AFM profile (B2) describes the size of the gap between 4 microlenses (hot spot) in the bottom of the well that is 306 nm (green line) and confirm the size of microlenses (approximately 1.3 μm , red line).

The surface of the SERS substrate has a uniformly distributed microlens array with individual size of 1.4 μm as seen in Figure 2A. The inset of Figure 2A shows the higher magnification of the surface. EDX analysis was performed to determine the presence of Ag on the CMOS sensor. The most dominant peaks on the EDX spectrum were C, Si and O due to the main components of the CMOS sensors. We obtained similar Ag concentrations for each spot used for the EDX analysis. When the thickness of Ag on the CMOS sensors is increased, the measured concentration of Ag increased.

Second technique for the structural characterization of the fabricated surface is AFM. The line analysis from the AFM images was performed to demonstrate the uniformity of the surface and structural information (height and size of lenses). Figure 2B shows the AFM image obtained from the 80 nm Ag coated surface and line analysis of the image. One can clearly see in the Figure 2B1 that the surface of the substrate has regular and uniform array of microlenses with nanometer sized gaps in between. Horizontal and crossline analysis are performed on the AFM image of SERS substrates to measure heights between two and four lenses and size of lenses (Figure 2B1). The size of lens was measured as about 1.3 μm which is smaller (1.4 μm) compared to the SEM images. This mismatch is due to an inability of the AFM cantilever to reach the gap between the microlenses. The height between the two microlenses is about 300 nm from the AFM line analysis (Figure 2B2). On the other hand, the height between the four

microlenses is about 600 nm from the AFM line analysis (Figure 2B2). As seen in Figure 2B2 the bottom of the gap between the four microlenses is flat and is around 250 nm.

SERS spectra were obtained as described earlier using 4-ATP and Rh6G as test molecules (Figure 3).

Figure 3A shows SERS spectra of 4-ATP and Rh6G on the 40 nm Ag-coated SERS substrates that was obtained from ten arbitrarily chosen spots and confirms reproducibility of the results. The percent coefficient variation of the obtained spectra was calculated and found to be about 10% for both probe molecules which is proper for SERS application. The observed background correlates with the SERS enhancement, as previously reported by Mahajan et al³⁷. Thus, we obtained spectra with and without probe molecules from the surfaces to see the contribution of SERS substrate spectra to the analyte spectrum. Figure 3B illustrates the comparison of SERS spectra obtained from the bare SERS substrate surface coated with 40 nm layer of silver and with dried probe molecules (4-ATP and Rh6G). It is clearly seen in the Figure 3B that the SERS signal from the probe molecules has no or minimal interfering signal from the materials constituting the SERS substrate. The calculated percent relative standard deviation (RSD) or coefficient of variation (CV) for the spectra of 4-ATP and Rh6G are found to be 8% and 7%, respectively. Next, we evaluated the effect of the silver thickness on the SERS intensities. For this experiment, CMOS sensors were coated with various layers of silver thickness: 20 nm, 40 nm, 60 nm, and 80 nm. Different SERS intensities were obtained from both 4-ATP and Rh6G on the SERS substrate depending on the Ag layer thickness (see Figure 3C). The SERS intensity for both probe molecules is very low for the 60 nm and 80 nm Ag coated CMOS sensors. However, SERS intensity is higher when thinner coating is performed. The maximum SERS intensity was measured for 40 nm Ag layer coated CMOS sensors. This observation is consistent with previous reports showing that the thickness of the metallic layer plays an important role in Raman enhancement³⁸ and can be explained by the fact that transversal modes are not allowed at optical wavelengths for very thin or very thick layers which lead to reduction of the overall SERS enhancement factor.

Finally, we calculated the SERS enhancement factor (EF) using Rh6G. Figure 3D shows the comparison of Raman spectrum and SERS spectrum of Rh6G dropped on CMOS sensor and SERS substrate coated with 40 nm Ag, respectively. The peak at 1512 cm^{-1} was used to estimate

the analytical enhancement factor (AEF) of the surface. Solution (0.1 M and 1.0×10^{-4} M) of Rh6G was used to obtain bulk Raman and SERS spectra, respectively.

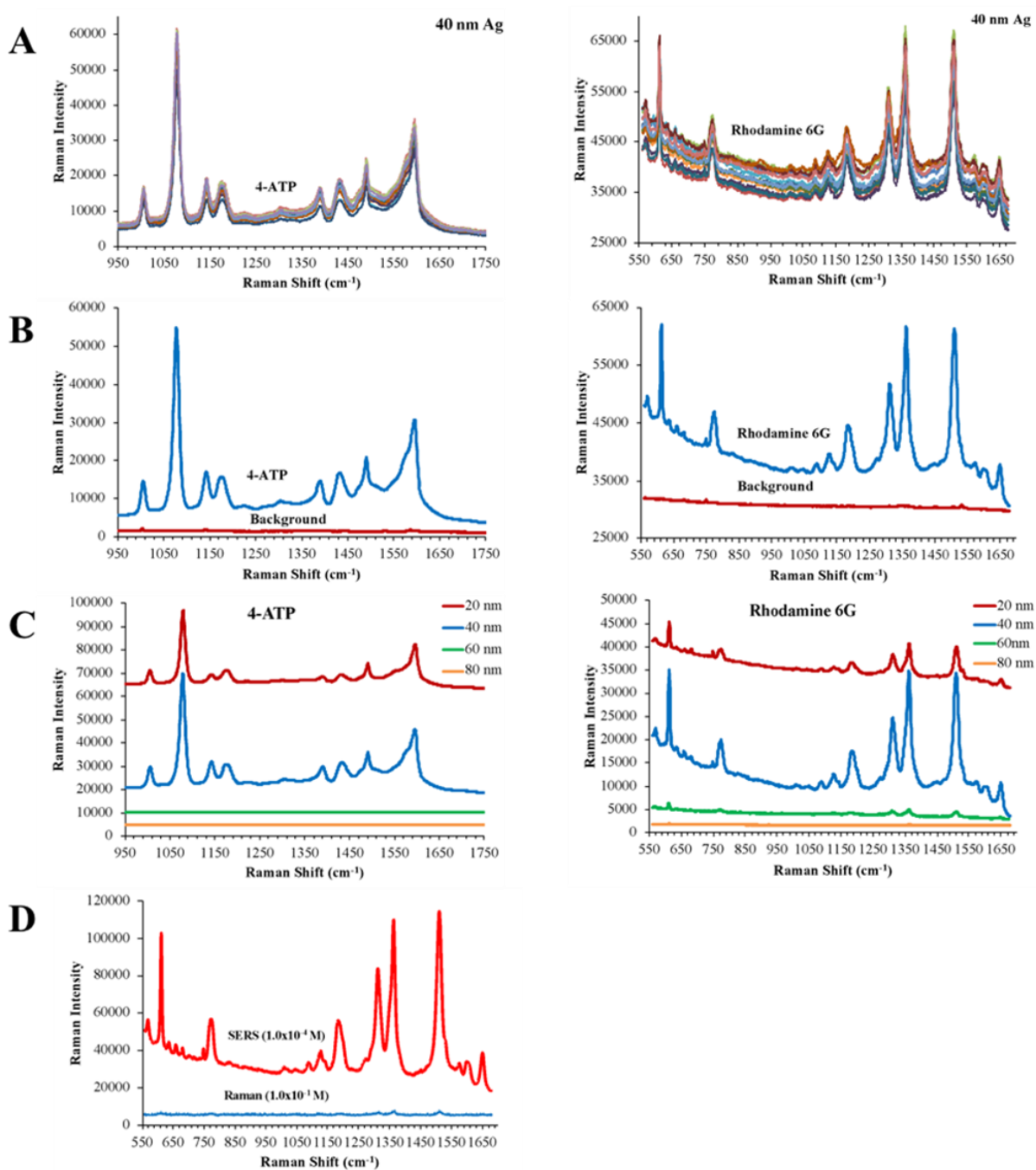


Figure 3. Reproducibility of SERS spectra of 4-ATP and Rh6G on the 40 nm Ag-coated CMOS sensors obtained from arbitrarily chosen ten spots (A); comparison of SERS spectra obtained from the background and probe molecules (B); intensity changes of SERS spectra of 4-ATP and Rh6G obtained from CMOS sensors having

different thicknesses of Ag layers (C); and comparison of Raman and SERS spectrum of Rh6G for the calculation of EF (D).

The AEF was calculated by using following equation:

$$AEF = (I_{SERS} \times C_{RS}) / (I_{RS} \times C_{SERS}) \quad (1)$$

where I_{SERS} and I_{RS} are intensity of the average SERS and Raman signal, respectively, and C_{SERS} and C_{RS} are concentrations of the analyte in SERS and Raman measurements respectively.

The SERS spectra intensity ratio and the concentration factor are 50 and 1.0×10^3 , respectively. The calculated AEF is found to be 5.0×10^4 from equation (1).

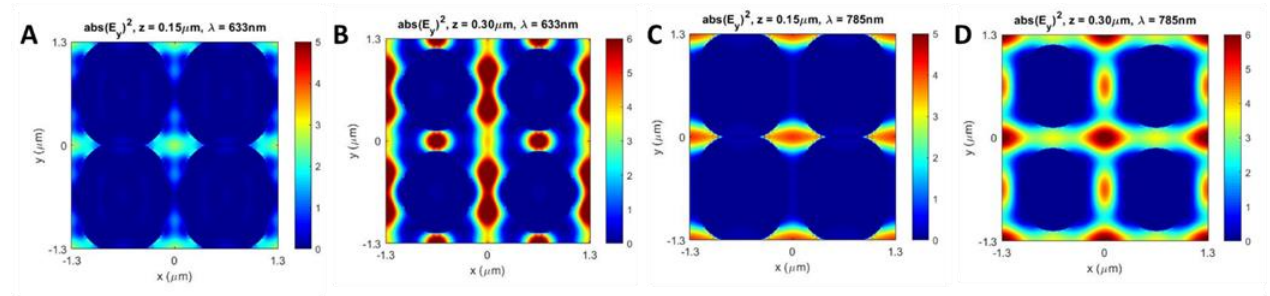


Figure 4. Distribution of hot spots on SERS substrate. FDTD simulations show the electromagnetic field intensity $z=0.15$ mm (A and C) and 0.30 mm (B and D) above the deepest point on the SERS substrate coated with 40 nm silver layer at 633 nm (A and B) and 785 nm (C and D) excitation wavelengths.

Figure 4 represents results of FDTD simulations indicating average SERS enhancement on the SERS substrates coated with 40 nm silver layer at two different wavelengths and positions along the z -axis. One can observe strong electromagnetic (EM) field enhancement areas (hot spots) between adjacent microlenses at 300 nm distance from the bottom of the SERS substrate illuminated by a Gaussian beam centered at 633 nm wavelength (Figure 4B). Electromagnetic field intensity drops in the area at 150 nm below described region and lower enhancement spot is observed in the area between four microlenses (Figure 4A). When the source of illumination was changed to 785 nm excitation wavelength, hot spots were found to be located mainly between four microlenses (Figure 4C and D). Finally, these results support experimental data that for 633 nm excitation the hot spot distribution (presented below) where higher SERS intensities are detected in between adjacent microlenses and not exactly in the gap between four microlenses.

To characterize the spatial distribution of hot spots on the fabricated SERS substrate we used 4-ATP as reporter molecule, since 4-ATP can self-assemble as a monolayer onto the surface of the substrate. SERS substrates were immersed in 10^{-4} M solution of 4-ATP in ethanol and incubated for 1 hour. Then, the surface of the substrate was thoroughly washed with ethanol to eliminate unbonded 4-ATP molecules.

Large area scan of $10\ \mu\text{m} \times 10\ \mu\text{m}$ area was performed with 1 s integration time. Figure 5A1 shows optical image of the SERS substrate surface, while Figure 5A2 represents the SERS map of the same area resulted after plotting the intensity of a peak at $1075\ \text{cm}^{-1}$ of 4-ATP. To compare the distribution of the hot spots on the microlens array, the SERS map is overlaid with the optical image. As shown in Figure 5A3, the intensity within the cavities between microlenses is higher, while the intensity on top of the lenses is lower, indicating that the hot spots with significant enhancement of Raman signal are distributed within the cavities. The average SERS spectra collected from 20 hot spots (Figure 5A4 red spectra) clearly indicate typical SERS spectra of 4-ATP molecule with characteristic peaks centered at $1075\ \text{cm}^{-1}$, $1140\ \text{cm}^{-1}$, $1190\ \text{cm}^{-1}$, $1303\ \text{cm}^{-1}$, $1390\ \text{cm}^{-1}$, $1440\ \text{cm}^{-1}$, and $1575\ \text{cm}^{-1}$. The calculated RSM of the 4-ATP average SERS spectra is found to be 11.86%. Black SERS spectra were collected from the top of the microlens and show an extremely weak signal compared to the intensity of the spectra from the hot spot regions.

Next, to demonstrate the ability of the substrate for size-based capturing and detection of nanoparticles we focused on the characterization of 100 nm polystyrene nanospheres. For this, we placed a droplet of 100 nm polystyrene beads dispersed in deionized water onto the SERS substrate and allow it to dry in the air. Then, we collected SERS spectra under a confocal scanning mode (633 nm laser excitation) and high magnification (100X objective, NA 0.9). To generate SERS images the intensities of the most prominent peak centered at $1600\ \text{cm}^{-1}$ were plotted over the scanned area (Figure 5B2). The reconstructed SERS map exhibits a uniform pattern of lateral periodicity that correlates with the optical image of the same area depicted in Figure 5B1. It is worth noting that the represented SERS map is reproducible, as we recorded many SERS maps with same SERS intensity pattern from various areas on the substrate.

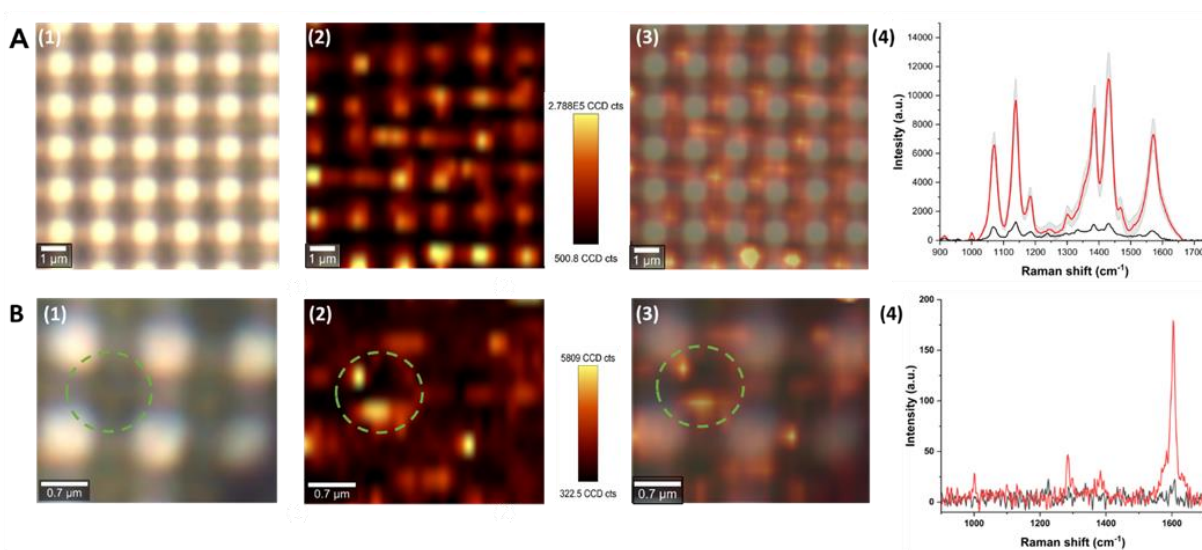


Figure 5. Analysis of 4-ATP and intracavity trapping, and detection of 100 nm polystyrene nanospheres. A) Optical image of the surface (A1); SERS map obtained plotting the intensities of the Raman peak at 1075 cm^{-1} of air-dried 4-ATP on top of the substrate (A2); overlay image of the SERS map with the optical image of the same region (A3); Average SERS spectra collected from hot spots ($n=20$) (red) and top of the microlens (black) (A4). Shaded areas represent ± 1 standard deviation. B) Optical image of substrate surface (B1); SERS map generated by plotting 1600 cm^{-1} peak over the scanned area (B2); overlay image of the SERS map with optical image of the same region (B3); SERS spectra of the “fingerprint region” $800\text{--}1800\text{ cm}^{-1}$ of normalized Raman spectra of polystyrene nanospheres captured in the hot spot area (red) and spectra collected from the top of the microlenses (black).

The SERS map in Figure 5B3 shows a distribution of high intensity spots that appear bright and located in between adjacent microlenses in the described hot spot area, and not on top of them. The red-colored SERS spectra shown in Figure 5B4 that are collected from the intracavity area of the SERS substrate are almost two orders of magnitude higher than the spectra recorded from the top of the microlenses (black spectra). The red spectra exhibit specific polystyrene peaks located at 1000 cm^{-1} and 1600 cm^{-1} , which are attributed to the ring breathing mode and vibration of the benzene ring, respectively. The black spectra that were collected from top of the microlens structure do not show presence of the above-mentioned peaks.

Finally, to demonstrate the usability of the SERS substrate for a biological application, we detected and characterized EVs isolated from brain organoids. For this purpose, we first extracted EVs by ultrafiltration and differential ultracentrifugation from brain organoids cell culture media that is free of fetal bovine serum. Then we characterized EV morphology and concentration using TEM and NTA. Electron microscopy revealed the presence of EVs with

typical cup-shaped morphology (Figure 6A) with clear inner and outer barriers of EV lipid membrane. Figure 6B shows the NTA size distribution plot for the analysed EVs. The mean concentration and particle size are 2×10^8 particles/ml and 160 nm, respectively, and correspond to small EVs³⁹.

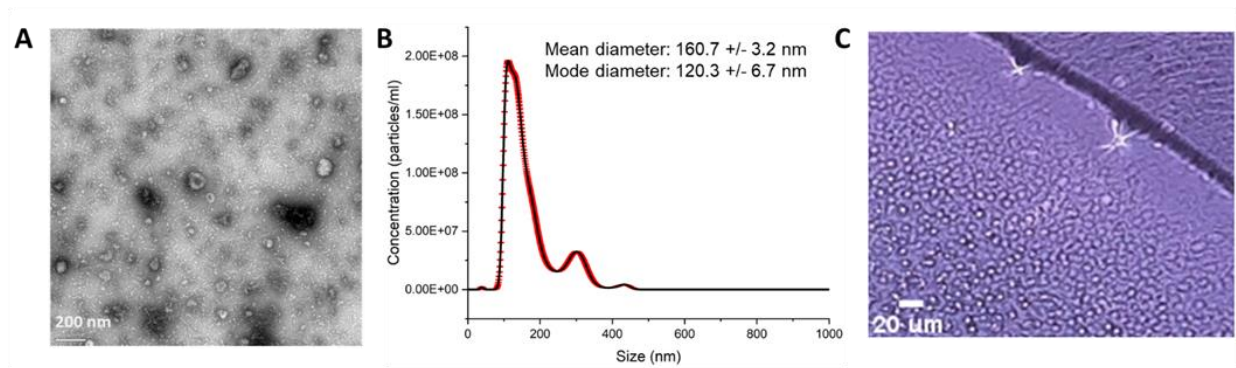


Figure 6. EVs characterization. A) Transmission electron microscopy image of EVs. Scale bar – 200 nm B) Nanoparticle tracking analysis of EVs. C) Image of the EVs containing droplet dried on the SERS substrate recorded by the CMOS imaging sensor. Scale bar – 20 μm .

Next, to demonstrate the CMOS SERS imaging mode we recorded images of the EVs containing droplet dried directly on the surface of the substrate (Figure 6C). One can clearly discern part of the ring formed by resuspended and dried particles and other circular features formed by aggregated particles located in close proximity to the ring. Another observation is that the size of these features gradually increases towards the center of the dried droplet. This phenomenon has been previously well described for EVs dried on the surface of the glass⁴⁰. Overall, coating of the CMOS sensor with thin layer of silver did not alter transmission of the light and consequently its function as an imaging sensor.

For SERS measurements we placed a droplet containing resuspended EVs onto the SERS substrate and let it air-dry (Figure 7A1). Then we scanned $5 \mu\text{m} \times 5 \mu\text{m}$ areas on the SERS substrate and plotted SERS maps of the peak centered at 2930 cm^{-1} (Figure 7A2).

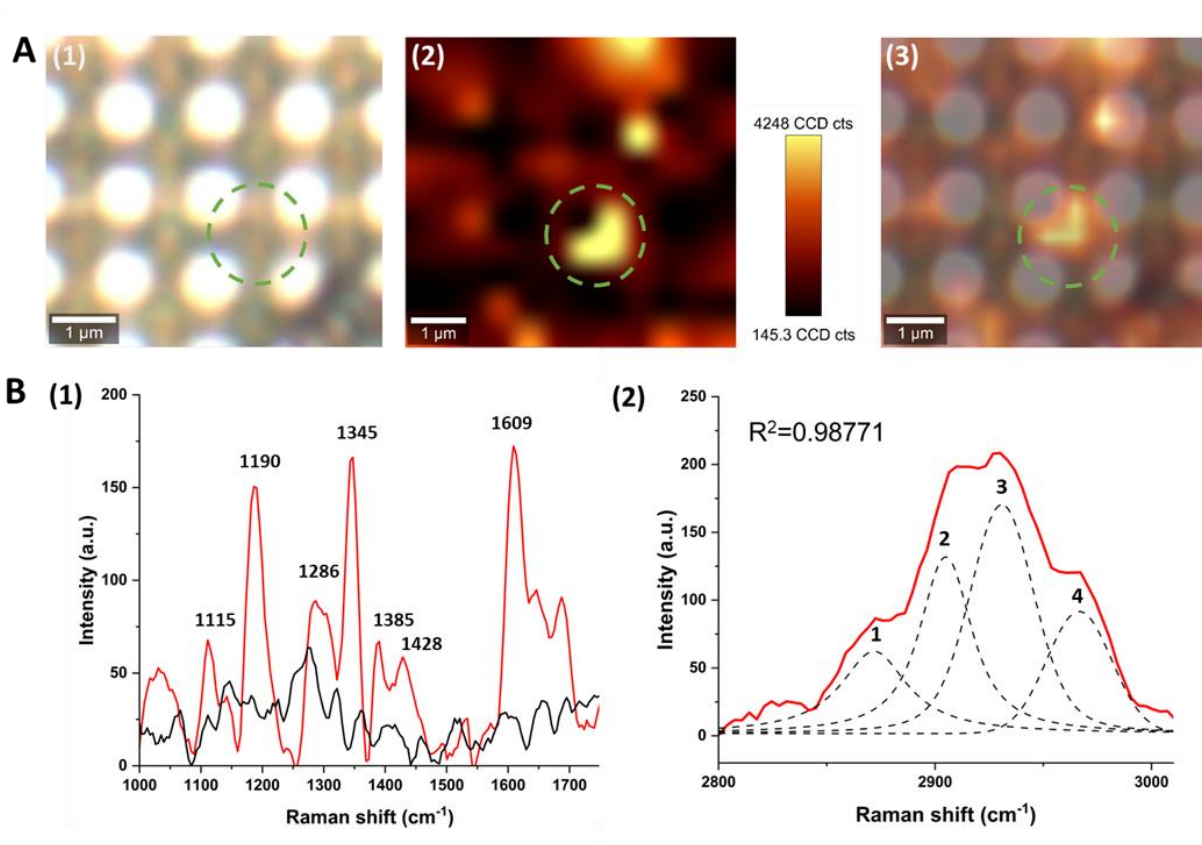


Figure 7. Analysis of EVs via SERS. A) Optical image of the surface (A1); SERS map generated by plotting of the peak centered at 2930 cm^{-1} (A2); overlay image of SERS map with optical image of the same area (A3). B) SERS spectra of the “fingerprint” region $900 - 1800\text{ cm}^{-1}$ of EVs collected from hot spot (red) and top of the microlenses (black) (B1); SERS spectra and peak deconvolution of the “high-wavenumber region” $2800-3100\text{ cm}^{-1}$ (B2). Dotted lines represent 4 peaks analyzed and labeled with numbers as follows: peak 1 – 2870 cm^{-1} , peak 2 – 2900 cm^{-1} , peak 3 – 2930 cm^{-1} , peak 4 – 2960 cm^{-1} .

When the optical image was overlaid with the SERS map of the same area (Figure 7A3), we identified that the location of the highest intensity signal is in intracavity area where EVs were trapped. SERS spectra of EVs (Figure 7B1 red spectra) collected from hot spot area within green circle indicated in Figure 7A show peaks that are known to arise from main biochemical constituents of EVs, such as lipids, proteins, and nucleic acids. Specifically, peaks centered at 1190 cm^{-1} , 1609 cm^{-1} and 1645 cm^{-1} correspond to proteins chemical bonds vibrations⁴¹⁻⁴⁴, 1115 cm^{-1} and 1280 cm^{-1} correspond to lipid content of EVs⁴⁵. Additionally, the peak located at 1345 cm^{-1} has contribution from nucleic acids of EVs⁴⁶. The detailed assignment of Raman peaks is given in Table 1. On the other hand, the SERS signal collected from top of the microlens

structures remains low and does not show any signature peaks that indicate presence of EVs (Figure 7B black spectra).

Table 1. Raman peak assignments for EVs measured on the SERS substrate.

Peak assignment	Peak position (rel. cm^{-1})
Proteins and lipids	1115 ⁴¹
Amide III	1190 ⁴¹
Amide III and fatty acids	1280 ^{41, 42, 47}
Amide III, nucleic acids, and fatty acids	1345 ⁴⁶
Amide I	1645-1678 ⁴⁸
Phenylalanine	1609 ⁴⁸
Lipids (CH ₂ asymmetric stretching)	2870 ⁴⁵
Lipids (CH ₂ asymmetric stretching)	2900 ⁴⁵
Proteins (CH ₃ symmetric stretching)	2930 ⁴⁴
Proteins (CH ₃ symmetric stretching)	2960 ⁴⁴

Additionally, SERS spectra in the “high-wavenumber” region has been analysed. Figure 7B2 shows deconvolution of the broad peak in this area that revealed presence of 4 hidden peaks from which peaks centered at 2870 cm^{-1} and 2900 cm^{-1} correspond to CH₂ asymmetric stretching of lipids⁴². We observed these peaks previously when analyzed EVs isolated from AD cell culture model and brain organoids³⁵ and in line with previously reported studies^{47, 49}. Peaks located at 2930 cm^{-1} and 2960 cm^{-1} correspond to proteins CH₃ bond symmetric stretch⁴⁴. The intensities ratios of these peaks are similar to previously reported EVs spectra and reflect protein and lipid contents^{35, 50}. Moreover, these results serve as evidence of EV purification and show that the analyte is neither protein aggregates nor lipoproteins or lipids from which higher intensity of corresponding peaks are expected^{43, 50, 51}.

Discussion

Theoretical and experimental results presented above demonstrate the presence of hot spots localized in the confined spaces between interconnected microlenses. Our findings are supported by previously reported studies showing that SERS substrates with periodic arrays of closely spaced nanostructures exhibit overall higher uniform SERS enhancement compared to SERS substrates with randomly structured surfaces⁵². In addition, the lighting rod effect in the funnel-

like structure may contribute to the overall observed Raman enhancement⁵³. Moreover, retardation or damping effects are minimized for EM fields created in nanogaps within quasistatic limit, which again results in higher SERS enhancement^{54, 55}. Finally, it is important to note that the hot spots created between adjacent microlenses exhibit larger volumes (extend in the z dimension) and may potentially allow for probing of molecules that are located at longer distance from the SERS substrate surface, for example enabling probing of the EV intraluminal cargo. In our measurements this is supported by the detection of specific peaks centered at 1345 cm⁻¹ that indicate the presence of nucleic acids⁴⁶ which are mainly part of the intraluminal cargo of EVs⁵⁶.

The ability to trap small nanometer-sized biological objects is another important feature of the CMOS-TrICC. In this study, the size of the nanogaps in between microlenses is approximately 300 nm, as seen in the AFM measurements. Therefore, only a few EVs could fit in this region that is otherwise also the volume with the highest SERS enhancement. One may argue that bigger particles may concentrate and cover the nanogaps containing EVs such that the signal represents the biochemical content of larger particles as well. However, due to the nature of SERS enhancement that occurs in close proximity to the plasmonic material, particles that are larger than the size of nanogaps have minimal or no interference to EV SERS signal¹⁷. Previous studies have applied similar concepts of SERS characterization of EVs using nanoplasmonic materials that allow SERS characterization of EVs that fall in the nanogaps between gold nanorods³¹, porous nanoplasmonic scaffolds^{33, 57}, array of gold covered graphene pyramids⁵⁸.

Finally, attempts to combine SERS and optical microscopy in one platform have been reported previously, mostly by utilizing research-grade microscopes, which operate on a trade-off mode between spatial resolution and FOV⁹. One recent example is of simultaneous SERS measurements and Stochastic Optical Reconstruction Microscopy (STORM) of biological structures and microorganisms⁵⁹⁻⁶¹, which reports high spatial resolution (<50 nm) and chemical information of the analyte but is limited in terms of FOV. The technique is also complex, require acquisition of multiple images and uses computing-intensive image reconstruction algorithms. On the other hand, our approach based on lensless imaging has a spatial resolution limited by the pixel size (imaging sensors with pixels as small as 800 nm are commercially available) and a

FOV limited only by the size of the sensor (as high as 1 cm). In addition, as this device does not need external lenses, can be miniaturized, and designed to operate in point of need applications.

Conclusions

This study reports for the first time the design and fabrication of substrates with triple function: trapping of analytes, optical imaging with high spatial resolution and large FOV, and molecular characterization of analytes (including small particles such as polystyrene nanospheres and EVs). We demonstrated that coating of a CMOS imaging sensor surface with a thin layer of silver (40 nm) creates plasmonic hot spots between microlenses and allows high amplification of Raman scattering signal of the analyte, while trapping analytes and maintaining optical imaging capability.

The surface of the SERS substrate mimics the uniform, closely packed layer of microlenses coated with a thin layer of evenly distributed silver. We used 4-ATP as a reporter molecule to assess the effect of the silver layer thickness on the performance of the SERS substrate and spatial distribution of hot spots. R6G was used to calculate the enhancement factor (5.0×10^4). The gaps between microlenses serve both for capturing and biochemical characterization of samples of interest. Simulations supported experimental data and showed that for experimental conditions used in our study hot spots are expected to be distributed between adjacent microlenses.

Ultimately, the substrate was used to analyse small volumes of EVs isolated from brain organoids. Analysis of SERS peaks in the “fingerprint region” and “high-wavenumber region” of the recorded spectra validated the presence of EVs trapped within nanocavities and reveals chemical constituents typical for both membrane and intraluminal content (proteins, lipids, and nucleic acids). Specifically, peaks centered at 1190 cm^{-1} , 1609 cm^{-1} , 1645 cm^{-1} , 2930 cm^{-1} and 2960 cm^{-1} correspond to proteins, 1115 cm^{-1} , 1280 cm^{-1} and 28700 cm^{-1} , 2900 cm^{-1} correspond to lipid content of EVs, and peak located at 1345 cm^{-1} has contribution from nucleic acids enclosed in EV intraluminal cargo.

Going beyond EV analysis, combining imaging with SERS on the same platform may enable recording optical microscopy and chemical images of analytes of interest (such as molecules

related to infectious diseases, pathogens, food safety, and other applications) placed directly on its surface, opening-up new directions towards biosensor development.

Author contributions

MI and SWH designed the experiments and wrote the manuscript, MI prepared the CMOS-SERS chips and performed optical and SERS imaging, AMS and MK performed morphological and SERS characterization, HC provided the simulations of electric field enhancement, JL contributed to SERS imaging, all authors interpreted the data, reviewed the manuscript, and provided input for the discussion and conclusions. SWH supervised the project.

Acknowledgments

This work was financially supported by the Natural Sciences and Engineering Research Council of Canada (NSERC), Discovery Grant RGPIN-2018-05675, and McGill Faculty of Engineering Louis Ho Scholarship in Technological Innovation (to S.W.-H.); M.I. acknowledges the FRQNT award for PhD studies and Bolashak International Scholarship. We acknowledge Prof. Thomas Durcan and Dr. Maria LaCalle from The Early Drug Discovery Unit (EDDU), Montreal Neurological Institute and Hospital for kindly providing cell culture media from neuronal cell line.

References

1. Bishara, W.; Su, T.-W.; Coskun, A. F.; Ozcan, A., Lensfree on-chip microscopy over a wide field-of-view using pixel super-resolution. *Opt. Express* 2010, 18 (11), 11181-11191.
2. Rai, M. R.; Rosen, J., Resolution-enhanced imaging using interferenceless coded aperture correlation holography with sparse point response. *Scientific Reports* 2020, 10 (1), 5033.
3. Lee, H.; Kim, J.; Kim, J.; Jeon, P.; Lee, S. A.; Kim, D., Noniterative sub-pixel shifting super-resolution lensless digital holography. *Opt. Express* 2021, 29 (19), 29996-30006.
4. Delacroix, R.; Morel, S. N. A.; Hervé, L.; Bordy, T.; Dinten, J.-M.; Drancourt, M.; Allier, C., Cerebrospinal fluid lens-free microscopy: a new tool for the laboratory diagnosis of meningitis. *Scientific Reports* 2017, 7 (1), 39893.
5. Xu, W.; Jericho, M. H.; Meinertzhagen, I. A.; Kreuzer, H. J., Digital in-line holography for biological applications. *Opt. Express* 2001, 9 (20), 11301-11305.
6. Kazemzadeh, F.; Wong, A., Laser Light-field Fusion for Wide-field Lensfree On-chip Phase Contrast Microscopy of Nanoparticles. *Scientific Reports* 2016, 6 (1), 38981.
7. Göröcs, Z.; Ozcan, A., On-chip biomedical imaging. *IEEE Rev Biomed Eng* 2013, 6, 29-46.
8. Kun, J.; Smieja, M.; Xiong, B.; Soleymani, L.; Fang, Q., The Use of Motion Analysis as Particle Biomarkers in Lensless Optofluidic Projection Imaging for Point of Care Urine Analysis. *Scientific Reports* 2019, 9 (1), 17255.

9. Imanbekova, M.; Perumal, A. S.; Kheireddine, S.; Nicolau, D. V.; Wachsmann-Hogiu, S., Lensless, reflection-based dark-field microscopy (RDFM) on a CMOS chip. *Biomed Opt Express* 2020, 11 (9), 4942-4959.
10. Zhang, C.; Man, B. Y.; Jiang, S. Z.; Yang, C.; Liu, M.; Chen, C. S.; Xu, S. C.; Qiu, H. W.; Li, Z., SERS detection of low-concentration adenosine by silver nanoparticles on silicon nanoporous pyramid arrays structure. *Applied Surface Science* 2015, 347, 668-672.
11. Wang, C.; Madiyar, F.; Yu, C.; Li, J., Detection of extremely low concentration waterborne pathogen using a multiplexing self-referencing SERS microfluidic biosensor. *Journal of Biological Engineering* 2017, 11 (1), 9.
12. Hering, K.; Cialla, D.; Ackermann, K.; Dörfer, T.; Möller, R.; Schneidewind, H.; Mattheis, R.; Fritzsche, W.; Rösch, P.; Popp, J., SERS: a versatile tool in chemical and biochemical diagnostics. *Analytical and bioanalytical chemistry* 2008, 390 (1), 113-124.
13. Michaels, A. M.; Jiang; Brus, L., Ag Nanocrystal Junctions as the Site for Surface-Enhanced Raman Scattering of Single Rhodamine 6G Molecules. *The Journal of Physical Chemistry B* 2000, 104 (50), 11965-11971.
14. Kosuda, K.; Bingham, J.; Wustholz, K.; Van Duyne, R., Nanostructures and surfaceenhanced Raman spectroscopy. *Handbook of Nanoscale Optics and Electronics* 2010, 309.
15. Mosier-Boss, P. A., Review of SERS Substrates for Chemical Sensing. *Nanomaterials* 2017, 7 (6), 142.
16. Kahraman, M.; Mullen, E. R.; Korkmaz, A.; Wachsmann-Hogiu, S., Fundamentals and applications of SERS-based bioanalytical sensing. *Nanophotonics* 2017, 6 (5), 831-852.
17. Kumari, G.; Kandula, J.; Narayana, C., How Far Can We Probe by SERS? *The Journal of Physical Chemistry C* 2015, 119 (34), 20057-20064.
18. Zou, S.; Hou, M.; Li, J.; Ma, L.; Zhang, Z., Semi-quantitative analysis of multiple chemical mixtures in solution at trace level by surface-enhanced Raman Scattering. *Scientific Reports* 2017, 7 (1), 6186.
19. Almejadi, L. M.; Curley, S. M.; Tokranova, N. A.; Tenenbaum, S. A.; Lednev, I. K., Surface Enhanced Raman Spectroscopy for Single Molecule Protein Detection. *Scientific Reports* 2019, 9 (1), 12356.
20. Feliu, N.; Hassan, M.; Garcia Rico, E.; Cui, D.; Parak, W.; Alvarez-Puebla, R., SERS Quantification and Characterization of Proteins and Other Biomolecules. *Langmuir* 2017, 33 (38), 9711-9730.
21. Ciloglu, F. U.; Hora, M.; Gundogdu, A.; Kahraman, M.; Tokmakci, M.; Aydin, O., SERS-based sensor with a machine learning based effective feature extraction technique for fast detection of colistin-resistant *Klebsiella pneumoniae*. *Analytica Chimica Acta* 2022, 1221, 340094.
22. Ciloglu, F. U.; Caliskan, A.; Saridag, A. M.; Kilic, I. H.; Tokmakci, M.; Kahraman, M.; Aydin, O., Drug-resistant *Staphylococcus aureus* bacteria detection by combining surface-enhanced Raman spectroscopy (SERS) and deep learning techniques. *Scientific Reports* 2021, 11 (1), 18444.
23. Saviñon-Flores, F.; Méndez, E.; López-Castaños, M.; Carabarin-Lima, A.; López-Castaños, K. A.; González-Fuentes, M. A.; Méndez-Albores, A., A Review on SERS-Based Detection of Human Virus Infections: Influenza and Coronavirus. *Biosensors (Basel)* 2021, 11 (3).
24. Garcia-Rico, E.; Alvarez-Puebla, R. A.; Guerrini, L., Direct surface-enhanced Raman scattering (SERS) spectroscopy of nucleic acids: from fundamental studies to real-life applications. *Chemical Society Reviews* 2018, 47 (13), 4909-4923.

25. Zhang, Y.; Mi, X.; Tan, X.; Xiang, R., Recent Progress on Liquid Biopsy Analysis using Surface-Enhanced Raman Spectroscopy. *Theranostics* 2019, 9 (2), 491-525.
26. Rojalin, T.; Phong, B.; Koster, H. J.; Carney, R. P., Nanoplasmonic Approaches for Sensitive Detection and Molecular Characterization of Extracellular Vesicles. 2019, 7 (279).
27. Imanbekova, M.; Suarasan, S.; Lu, Y.; Jurchuk, S.; Wachsmann-Hogiu, S., Recent advances in optical label-free characterization of extracellular vesicles. *Nanophotonics* 2022.
28. van Niel, G.; Carter, D. R. F.; Clayton, A.; Lambert, D. W.; Raposo, G.; Vader, P., Challenges and directions in studying cell–cell communication by extracellular vesicles. *Nature Reviews Molecular Cell Biology* 2022, 23 (5), 369-382.
29. Suarasan, S.; Liu, J.; Imanbekova, M.; Rojalin, T.; Hilt, S.; Voss, J. C.; Wachsmann-Hogiu, S. J. J. o. M. C. B., Superhydrophobic bowl-like SERS substrates patterned from CMOS sensors for extracellular vesicle characterization. 2020.
30. Tirinato, L.; Gentile, F.; Di Mascolo, D.; Coluccio, M.; Das, G.; Liberale, C.; Pullano, S.; Perozziello, G.; Francardi, M.; Accardo, A., SERS analysis on exosomes using super-hydrophobic surfaces. *Microelectronic Engineering* 2012, 97, 337-340.
31. Sivashanmugan, K.; Huang, W.-L.; Lin, C.-H.; Liao, J.-D.; Lin, C.-C.; Su, W.-C.; Wen, T.-C., Bimetallic nanoplasmonic gap-mode SERS substrate for lung normal and cancer-derived exosomes detection. *Journal of the Taiwan Institute of Chemical Engineers* 2017, 80, 149-155.
32. Lee, C.; Carney, R. P.; Hazari, S.; Smith, Z. J.; Knudson, A.; Robertson, C. S.; Lam, K. S.; Wachsmann-Hogiu, S., 3D plasmonic nanobowl platform for the study of exosomes in solution. *Nanoscale* 2015, 7 (20), 9290-9297.
33. Rojalin, T.; Koster, H. J.; Liu, J.; Mizenko, R. R.; Tran, D.; Wachsmann-Hogiu, S.; Carney, R. P., Hybrid Nanoplasmonic Porous Biomaterial Scaffold for Liquid Biopsy Diagnostics Using Extracellular Vesicles. *ACS Sensors* 2020, 5 (9), 2820-2833.
34. Rigó, I.; Veres, M.; Váczi, T.; Holczer, E.; Hakkel, O.; Deák, A.; Fürjes, P., Preparation and Characterization of Perforated SERS Active Array for Particle Trapping and Sensitive Molecular Analysis. *Biosensors (Basel)* 2019, 9 (3).
35. Imanbekova, M.; Suarasan, S.; Rojalin, T.; Mizenko, R. R.; Hilt, S.; Mathur, M.; Lepine, P.; Nicouveau, M.; Mohamed, N.-V.; Durcan, T. M.; Carney, R. P.; Voss, J. C.; Wachsmann-Hogiu, S., Identification of amyloid beta in small extracellular vesicles via Raman spectroscopy. *Nanoscale Advances* 2021, 3 (14), 4119-4132.
36. Johnson, P. B.; Christy, R.-W., Optical constants of the noble metals. *Physical review B* 1972, 6 (12), 4370.
37. Mahajan, S.; Cole, R. M.; Speed, J. D.; Pelfrey, S. H.; Russell, A. E.; Bartlett, P. N.; Barnett, S. M.; Baumberg, J. J., Understanding the Surface-Enhanced Raman Spectroscopy “Background”. *The Journal of Physical Chemistry C* 2010, 114 (16), 7242-7250.
38. Lee, C.; Robertson, C. S.; Nguyen, A. H.; Kahraman, M.; Wachsmann-Hogiu, S., Thickness of a metallic film, in addition to its roughness, plays a significant role in SERS activity. *Scientific Reports* 2015, 5 (1), 11644.39.
39. Théry, C.; Witwer, K. W.; Aikawa, E.; Alcaraz, M. J.; Anderson, J. D.; Andriantsitohaina, R.; Antoniou, A.; Arab, T.; Archer, F.; Atkin-Smith, G. K.; Ayre, D. C.; Bach, J.-M.; Bachurski, D.; Baharvand, H.; Balaj, L.;

Baldacchino, S.; Bauer, N. N.; Baxter, A. A.; Bebawy, M.; Beckham, C.; Zavec, A. B.; Benmoussa, A.; Berardi, A. C.; Bergese, P.; Bielska, E.; Blenkiron, C.; Bobis-Wozowicz, S.; Boilard, E.; Boireau, W.; Bongiovanni, A.; Borràs, F. E.; Bosch, S.; Boulanger, C. M.; Breakefield, X.; Breglio, A. M.; Brennan, M. Á.; Brigstock, D. R.; Brisson, A.; Broekman, M. L. D.; Bromberg, J. F.; Bryl-Górecka, P.; Buch, S.; Buck, A. H.; Burger, D.; Busatto, S.; Buschmann, D.; Bussolati, B.; Buzás, E. I.; Byrd, J. B.; Camussi, G.; Carter, D. R. F.; Caruso, S.; Chamley, L. W.; Chang, Y.-T.; Chen, C.; Chen, S.; Cheng, L.; Chin, A. R.; Clayton, A.; Clerici, S. P.; Cocks, A.; Cocucci, E.; Coffey, R. J.; Cordeiro-da-Silva, A.; Couch, Y.; Coumans, F. A. W.; Coyle, B.; Crescitelli, R.; Criado, M. F.; D'Souza-Schorey, C.; Das, S.; Chaudhuri, A. D.; Candia, P. d.; Junior, E. F. D. S.; Wever, O. D.; Portillo, H. A. d.; Demaret, T.; Deville, S.; Devitt, A.; Dhondt, B.; Vizio, D. D.; Dieterich, L. C.; Dolo, V.; Rubio, A. P. D.; Dominici, M.; Dourado, M. R.; Driedonks, T. A. P.; Duarte, F. V.; Duncan, H. M.; Eichenberger, R. M.; Ekström, K.; Andaloussi, S. E. L.; Elie-Caille, C.; Erdbrügger, U.; Falcón-Pérez, J. M.; Fatima, F.; Fish, J. E.; Flores-Bellver, M.; Försonits, A.; Frelet-Barrand, A.; Fricke, F.; Fuhrmann, G.; Gabrielsson, S.; Gámez-Valero, A.; Gardiner, C.; Gärtner, K.; Gaudin, R.; Gho, Y. S.; Giebel, B.; Gilbert, C.; Gimona, M.; Giusti, I.; Goberdhan, D. C. I.; Görgens, A.; Gorski, S. M.; Greening, D. W.; Gross, J. C.; Gualerzi, A.; Gupta, G. N.; Gustafson, D.; Handberg, A.; Haraszti, R. A.; Harrison, P.; Hegyesi, H.; Hendrix, A.; Hill, A. F.; Hochberg, F. H.; Hoffmann, K. F.; Holder, B.; Holthofer, H.; Hosseinkhani, B.; Hu, G.; Huang, Y.; Huber, V.; Hunt, S.; Ibrahim, A. G.-E.; Ikezu, T.; Inal, J. M.; Isin, M.; Ivanova, A.; Jackson, H. K.; Jacobsen, S.; Jay, S. M.; Jayachandran, M.; Jenster, G.; Jiang, L.; Johnson, S. M.; Jones, J. C.; Jong, A.; Jovanovic-Talisman, T.; Jung, S.; Kalluri, R.; Kano, S.-i.; Kaur, S.; Kawamura, Y.; Keller, E. T.; Khamari, D.; Khomyakova, E.; Khvorova, A.; Kierulf, P.; Kim, K. P.; Kislinger, T.; Klingeborn, M.; Ii, D. J. K.; Kornek, M.; Kosanović, M. M.; Kovács, Á. F.; Krämer-Albers, E.-M.; Krasemann, S.; Krause, M.; Kurochkin, I. V.; Kusuma, G. D.; Kuypers, S.; Laitinen, S.; Langevin, S. M.; Languino, L. R.; Lannigan, J.; Lässer, C.; Laurent, L. C.; Lavieu, G.; Lázaro-Ibáñez, E.; Lay, S. L.; Lee, M.-S.; Lee, Y. X. F.; Lemos, D. S.; Lenassi, M.; Leszczynska, A.; Li, I. T. S.; Liao, K.; Libregts, S. F.; Ligeti, E.; Lim, R.; Lim, S. K.; Linē, A.; Linnemannstöns, K.; Llorente, A.; Lombard, C. A.; Lorenowicz, M. J.; Lörinč, Á. M.; Lötval, J.; Lovett, J.; Lowry, M. C.; Loyer, X.; Lu, Q.; Lukomska, B.; Lunavat, T. R.; Maas, S. L. N.; Malhi, H.; Marcilla, A.; Mariani, J.; Mariscal, J.; Martens-Uzunova, E. S.; Martin-Jaular, L.; Martinez, M. C.; Martins, V. R.; Mathieu, M.; Mathivanan, S.; Mageri, M.; McGinnis, L. K.; McVey, M. J.; Jr, D. G. M.; Meehan, K. L.; Mertens, I.; Minciacchi, V. R.; Möller, A.; Jørgensen, M. M.; Morales-Kastresana, A.; Morhayim, J.; Mullier, F.; Muraca, M.; Musante, L.; Mussack, V.; Muth, D. C.; Myburgh, K. H.; Najrana, T.; Nawaz, M.; Nazarenko, I.; Nejsun, P.; Neri, C.; Neri, T.; Nieuwland, R.; Nimrichter, L.; Nolan, J. P.; Hoen, E. N. M. N.-t.; Hooten, N. N.; O'Driscoll, L.; O'Grady, T.; O'Loughlen, A.; Ochiya, T.; Olivier, M.; Ortiz, A.; Ortiz, L. A.; Osteikoetxea, X.; Østergaard, O.; Ostrowski, M.; Park, J.; Pegtel, D. M.; Peinado, H.; Perut, F.; Pfaffl, M. W.; Phinney, D. G.; Pieters, B. C. H.; Pink, R. C.; Pisetsky, D. S.; Strandmann, E. P. v.; Polakovicova, I.; Poon, I. K. H.; Powell, B. H.; Prada, I.; Pulliam, L.; Quesenberry, P.; Radeghieri, A.; Raffai, R. L.; Raimondo, S.; Rak, J.; Ramirez, M. I.; Raposo, G.; Rayyan, M. S.; Regev-Rudzki, N.; Ricklefs, F. L.; Robbins, P. D.; Roberts, D. D.; Rodrigues, S. C.; Rohde, E.; Rome, S.; Rouschop, K. M. A.; Rugghetti, A.; Russell, A. E.; Saá, P.; Sahoo, S.; Salas-Huenuleo, E.;

Sánchez, C.; Saugstad, J. A.; Saul, M. J.; Schiffelers, R. M.; Schneider, R.; Schøyen, T. H.; Scott, A.; Shahaj, E.; Sharma, S.; Shatnyeva, O.; Shekari, F.; Shelke, G. V.; Shetty, A. K.; Shiba, K.; Siljander, P. R. M.; Silva, A. M.; Skowronek, A.; Ii, O. L. S.; Soares, R. P.; Sódar, B. W.; Soekmadji, C.; Sotillo, J.; Stahl, P. D.; Stoorvogel, W.; Stott, S. L.; Strasser, E. F.; Swift, S.; Tahara, H.; Tewari, M.; Timms, K.; Tiwari, S.; Tixeira, R.; Tkach, M.; Toh, W. S.; Tomasini, R.; Torrecilhas, A. C.; Tosar, J. P.; Toxavidis, V.; Urbanelli, L.; Vader, P.; Balkom, B. W. M. v.; Grein, S. G. v. d.; Deun, J. V.; Herwijnen, M. J. C. v.; Keuren-Jensen, K. V.; Niel, G. v.; Royen, M. E. v.; Wijnen, A. J. v.; Vasconcelos, M. H.; Jr, I. J. V.; Veit, T. D.; Vella, L. J.; Velot, É.; Verweij, F. J.; Vestad, B.; Viñas, J. L.; Visnovitz, T.; Vukman, K. V.; Wahlgren, J.; Watson, D. C.; Wauben, M. H. M.; Weaver, A.; Webber, J. P.; Weber, V.; Wehman, A. M.; Weiss, D. J.; Welsh, J. A.; Wendt, S.; Wheelock, A. M.; Wiener, Z.; Witte, L.; Wolfram, J.; Xagorari, A.; Xander, P.; Xu, J.; Yan, X.; Yáñez-Mó, M.; Yin, H.; Yuana, Y.; Zappulli, V.; Zarubova, J.; Žekas, V.; Zhang, J.-y.; Zhao, Z.; Zheng, L.; Zheutlin, A. R.; Zickler, A. M.; Zimmermann, P.; Zivkovic, A. M.; Zocco, D.; Zuba-Surma, E. K., Minimal information for studies of extracellular vesicles 2018 (MISEV2018): a position statement of the International Society for Extracellular Vesicles and update of the MISEV2014 guidelines. *J Extracell Vesicles* 2018, 7 (1), 1535750.

40. Jeong, H.; Shin, H.; Yi, J.; Park, Y.; Lee, J.; Gianchandani, Y.; Park, J., Size-based analysis of extracellular vesicles using sequential transfer of an evaporating droplet. *Lab on a Chip* 2019, 19 (19), 3326-3336.

41. Kamińska, A.; Roman, M.; Wróbel, A.; Gala-Błądzińska, A.; Małecki, M. T.; Paluszkiwicz, C.; Stepień, E. Ł., Raman spectroscopy of urinary extracellular vesicles to stratify patients with chronic kidney disease in type 2 diabetes. *Nanomedicine: Nanotechnology, Biology and Medicine* 2022, 39, 102468.

42. Czamara, K.; Majzner, K.; Pacia, M. Z.; Kochan, K.; Kaczor, A.; Baranska, M., Raman spectroscopy of lipids: a review. *Journal of Raman Spectroscopy* 2015, 46 (1), 4-20.

43. Gualerzi, A.; Kooijmans, S. A. A.; Niada, S.; Picciolini, S.; Brini, A. T.; Camussi, G.; Bedoni, M., Raman spectroscopy as a quick tool to assess purity of extracellular vesicle preparations and predict their functionality. *J Extracell Vesicles* 2019, 8 (1), 1568780.

44. Rygula, A.; Majzner, K.; Marzec, K. M.; Kaczor, A.; Pilarczyk, M.; Baranska, M., Raman spectroscopy of proteins: a review. *Journal of Raman Spectroscopy* 2013, 44 (8), 1061-1076.

45. Short, K. W.; Carpenter, S.; Freyer, J. P.; Mourant, J. R., Raman Spectroscopy Detects Biochemical Changes Due to Proliferation in Mammalian Cell Cultures. *Biophysical Journal* 2005, 88 (6), 4274-4288.

46. Russo, M.; Tirinato, L.; Scionti, F.; Coluccio, M. L.; Perozziello, G.; Riillo, C.; Mollace, V.; Gratteri, S.; Malara, N.; Di Martino, M. T.; Viglietto, G.; Tagliaferri, P.; Tassone, P.; Rossi, M.; Candeloro, P., Raman Spectroscopic Stratification of Multiple Myeloma Patients Based on Exosome Profiling. *ACS Omega* 2020, 5 (47), 30436-30443.

47. Gualerzi, A.; Niada, S.; Giannasi, C.; Picciolini, S.; Morasso, C.; Vanna, R.; Rossella, V.; Masserini, M.; Bedoni, M.; Ciceri, F.; Bernardo, M. E.; Brini, A. T.; Gramatica, F., Raman spectroscopy uncovers biochemical tissue-related features of extracellular vesicles from mesenchymal stromal cells. *Scientific Reports* 2017, 7 (1), 9820.

48. Dong, J.; Wan, Z.; Popov, M.; Carey, P. R.; Weiss, M. A., Insulin Assembly Damps Conformational Fluctuations: Raman Analysis of Amide I Linewidths in Native States and Fibrils. *Journal of Molecular Biology* 2003, 330 (2), 431-442.
49. Smith, Z. J.; Lee, C.; Rojalin, T.; Carney, R. P.; Hazari, S.; Knudson, A.; Lam, K.; Saari, H.; Ibañez, E. L.; Viitala, T.; Laaksonen, T.; Yliperttula, M.; Wachsmann-Hogiu, S., Single exosome study reveals subpopulations distributed among cell lines with variability related to membrane content. *J Extracell Vesicles* 2015, 4, 28533-28533.
50. Zini, J.; Saari, H.; Ciana, P.; Viitala, T.; Lõhmus, A.; Saarinen, J.; Yliperttula, M., Infrared and Raman spectroscopy for purity assessment of extracellular vesicles. *European Journal of Pharmaceutical Sciences* 2022, 172, 106135.
51. Ricciardi, A.; Piuri, G.; Porta, M. D.; Mazzucchelli, S.; Bonizzi, A.; Truffi, M.; Sevieri, M.; Allevi, R.; Corsi, F.; Cazzola, R.; Morasso, C., Raman spectroscopy characterization of the major classes of plasma lipoproteins. *Vibrational Spectroscopy* 2020, 109, 103073.
52. Gunnarsson, L.; Bjerneld, E.; Xu, H.; Petronis, S.; Kasemo, B.; Käll, M., Interparticle coupling effects in nanofabricated substrates for surface-enhanced Raman scattering. *Applied Physics Letters* 2001, 78 (6), 802-804.
53. Jones, R. R.; Hooper, D. C.; Zhang, L.; Wolverson, D.; Valev, V. K., Raman Techniques: Fundamentals and Frontiers. *Nanoscale Research Letters* 2019, 14 (1), 231.
54. Genov, D. A.; Sarychev, A. K.; Shalaev, V. M.; Wei, A., Resonant Field Enhancements from Metal Nanoparticle Arrays. *Nano Letters* 2004, 4 (1), 153-158.
55. Farcau, C.; Astilean, S., Mapping the SERS Efficiency and Hot-Spots Localization on Gold Film over Nanospheres Substrates. *The Journal of Physical Chemistry C* 2010, 114 (27), 11717-11722.
56. Anand, S.; Samuel, M.; Kumar, S.; Mathivanan, S., Ticket to a bubble ride: Cargo sorting into exosomes and extracellular vesicles. *Biochimica et Biophysica Acta (BBA) - Proteins and Proteomics* 2019, 1867 (12), 140203.
57. Dong, S.; Wang, Y.; Liu, Z.; Zhang, W.; Yi, K.; Zhang, X.; Zhang, X.; Jiang, C.; Yang, S.; Wang, F., Beehive-inspired macroporous SERS probe for cancer detection through capturing and analyzing exosomes in plasma. *ACS applied materials & interfaces* 2020, 12 (4), 5136-5146.
58. Yan, Z.; Dutta, S.; Liu, Z.; Yu, X.; Mesgarzadeh, N.; Ji, F.; Bitan, G.; Xie, Y.-H., A Label-Free Platform for Identification of Exosomes from Different Sources. *ACS Sensors* 2019, 4 (2), 488-497.
59. Olson, A. P.; Spies, K. B.; Browning, A. C.; Soneral, P. A. G.; Lindquist, N. C., Chemically imaging bacteria with super-resolution SERS on ultra-thin silver substrates. *Scientific Reports* 2017, 7 (1), 9135.
60. Ertsgaard, C. T.; McKoskey, R. M.; Rich, I. S.; Lindquist, N. C., Dynamic placement of plasmonic hotspots for super-resolution surface-enhanced Raman scattering. *ACS Nano* 2014, 8 (10), 10941-10946.
61. Olson, A. P.; Ertsgaard, C. T.; Elliott, S. N.; Lindquist, N. C., Super-resolution chemical imaging with plasmonic substrates. *ACS Photonics* 2016, 3 (3), 329-336.

Transition to chapter V

Chapters III and IV introduce new tools and used traditional technologies for EV characterization. Next, we aim to use label-free optical methodology Raman spectroscopy to identify AD biomarker A β associated with small EVs and to characterize its structure. A large body of literature outlines the role of EVs in the function of CNS as well as their contribution to the development of pathological conditions such as AD, PD, ALS, and other diseases (see Section 5 of the comprehensive literature review).

In this chapter, in line with Aim IV of the thesis, we employed Raman spectroscopy to identify A β , a misfolded protein that is a main component of the amyloid plaques in the brains of AD patients. The molecular mechanisms that lead to pathological changes in the brains of AD patients remain unclear. Researchers have hypothesized that the alterations in the APP metabolism could potentially relate to AD progression. The amyloidogenic pathway is initiated by the cleavage of the APP by β -secretase generating a C-terminal fragment with 99 amino acids. The C-terminal fragment is then cut by γ -secretase which subsequently results in the generation of A β_{40} and A β_{42} peptides. Previous studies have shown that A β_{42} peptides are found in multivesicular bodies of neurons and could potentially be enveloped in small EVs – exosomes. Existing literature associates misfolded proteins such as A β , tau, and α -synuclein with EVs, and proposes that EVs may play a role in the pathogenesis of neurodegenerative diseases, while serving as a potential biomarker for diagnosis. Therefore, we aimed to employ the power of Raman spectroscopy to characterize EVs isolated from the AD cell culture model and to identify EV-associated A β . To reach this goal, we first isolated small EVs from the AD cell culture model that mimics the overexpression of A β that is observed during AD pathogenesis. Then EVs were isolated and characterized using NTA, TEM, SP-IRIS, and Raman spectroscopy. The results show for the first time the Raman spectroscopic fingerprint of the A β present in the molecular cargo of small EVs and they reveal the size of the peptide, its structure, and potential impact on the EV membrane. These findings should be further explored using clinical samples and expanded to address questions of specificity to the AD stage.

Ultimately, the findings of the study pave the way for use of Raman spectroscopy as a method of choice for label-free non-invasive analysis of EV biochemical content and contribute to a general understanding of AD.

The described work has been conducted in the frame of international collaboration with researchers from the University of California, Davis, and the Early Drug Discovery Unit of Montreal Neurological Institute and Hospital

This chapter is based on my fourth first-author article. The contributions of each author are as follows:

MI and SWH conceived the idea and outlined the experimental design. SH, MM, PL, MN, NM, TD, and JV provide cell culture media for EVs isolation. MI and TR performed EVs isolation. MI, TR, RM, and RC conducted EVs characterization. MI, SS, and SWH performed analysis of the data. MI wrote the main text of the manuscript with contributions from all the co-authors. SWH supervised the project. All authors reviewed and approved the manuscript in its current form.

Chapter V. Identification of amyloid beta in small extracellular vesicles *via* Raman spectroscopy.

Meruyert Imanbekova¹, Sorina Suarasan¹, Tatu Rojalin², Rachel R. Mizenko², Silvia Hilt³, Meghna Mathur⁴, Paula Lepine⁴, Michael Nicouleau⁴, Nguyen-Vi Mohamed⁴, Thomas M. Durcan⁴, Randy P. Carney², John C. Voss³, and Sebastian Wachsmann-Hogiu^{1*}

¹ Department of Bioengineering, McGill University, Montreal, QC, H3A 0E9, Canada

² Department of Biomedical Engineering, University of California, Davis, CA 95616, USA

³ Department of Biochemistry & Molecular Medicine, University of California, Davis, CA 95616, USA

⁴ The Early Drug Discovery Unit (EDDU), Montreal Neurological Institute and Hospital, McGill University, Montreal, QC, H3A 2B4, Canada

* Corresponding author: sebastian.wachsmannhogiu@mcgill.ca

5.1 Abstract. A hallmark of AD pathogenesis is believed to be the production and deposition of A β peptide into extracellular plaques. Existing research indicates that EVs can carry A β associated with AD. However, characterization of the EV-associated A β and its conformational variants has yet to be realized. Raman spectroscopy is a label-free and non-destructive method that is able to assess the biochemical composition of EVs. This study reports for the first time the Raman spectroscopic fingerprint of the A β present in the molecular cargo of sEVs. Raman spectra were measured from sEVs isolated from AD cell culture model, where secretion of A β is regulated by tetracycline promoter, and from midbrain organoids. The averaged spectra of each sEV group showed considerable variation as a reflection of the biochemical content of sEVs. Spectral analysis identified more intense Raman peaks at 1650 cm⁻¹ and 2930 cm⁻¹ attributable to the A β peptide incorporated in sEVs produced by the AD cell culture model. Subsequent analysis of the spectra by principal component analysis differentiated the sEVs of the AD cell culture model from the control groups of sEVs. Moreover, the results indicate that A β associated with secreted sEVs has a α -helical secondary structure and the size of a monomer or small oligomer. Furthermore, by analyzing the lipid content of sEVs we identified altered fatty acid chain lengths in sEVs that carry A β that may affect the fluidity of the EV membrane. Overall,

our findings provide evidence supporting the use of Raman spectroscopy for the identification and characterization of sEVs associated with potential biomarkers of neurological disorders such as toxic proteins.

Keywords: small extracellular vesicles, amyloid beta, Raman spectroscopy, Alzheimer's disease

5.2 Introduction

AD is the most common form of dementia and has an overwhelming impact on patients' lives and their families. The formation of A β senile plaques and tau tangles are the hallmark of AD. A β is a 36-43 amino acid peptide that is derived from proteolysis of APP. Understanding the role of A β in the molecular pathways that lead to pathological changes in the brain of patients with AD is a long-standing goal in the AD research field. While the mechanisms of age-related accumulation of A β in the AD patients' brain remains unclear, it has been hypothesized that the alterations in the metabolism of APP could be related to AD progression. The non-amyloidogenic pathway, which prevents the formation of the toxic A β forms, proceeds from the proteolysis of APP on the cell surface by α -secretase followed by γ -secretase. On the other hand, the amyloidogenic pathway includes cleavage of APP by β -secretase generating 99 amino acid C-terminal fragment that is then cut by γ -secretase, leading to generation of the neurotoxic A β_{40} and A β_{42} peptides [1,2]. The A β_{42} peptide is shown to be more hydrophobic and prone to form fibrils compared to A β_{40} peptide and is found to be highly prevalent in senile plaques ¹⁰⁵. Moreover, several studies showed that intracellular A β_{42} can be located in multivesicular bodies of neurons and further enveloped into sEVs – exosomes [4,5].

Exosomes are nanometer-sized sEVs derived from the endocytic pathway and released from the cells upon diffusion of cytosolic multivesicular bodies with the plasma membrane. Exosomes have been detected in different fluids of the human body including serum, plasma, saliva, breast milk, amniotic fluid, semen, and urine [6]. Their molecular cargo reflects the state of the releasing cells and contains membrane proteins, endosome-associated proteins, cytosolic proteins, lipids, and nucleic acids. Functions of sEVs in normal physiology and in a variety of pathological processes are under extensive study. They are known to facilitate intercellular communication between neighboring cells or distant cells and to play a role in cardiovascular diseases [7], cancer [8], metabolic [9] and neurological disorders [10,11], and autoimmune

diseases [12,13]. Due to the lack of explicit consensus in the field of EVs on the appropriate nomenclature, and to adhere to the MISEV2018 guidelines [14] we chose to use the term “small EVs” or “sEVs” for the purpose of this study to refer to EVs in the approximate size range of 50-200 nm. In more broader contexts we used a collective term “extracellular vesicle” or “EVs”.

With relevance to neurodegenerative diseases, it has been proposed that the generation and progression of many neurodegenerative disorders are associated with exosome-mediated transport of misfolded proteins [15-17] and specific RNA species in exosomes [18-20]. Furthermore, recent clinical studies showed elevated levels of AD-associated proteins, tau, and A β , in exosomes isolated from plasma, serum, and cerebrospinal fluid (CSF) of AD patients [21-25]. These findings stimulate further exploration of the sEVs as potential biomarkers of neurodegenerative diseases.

EVs are characterized by a wide variety of methods. Morphological features of EVs are described by nanoparticle tracking analysis (NTA) [26], electron microscopy (EM) [27], and atomic force microscopy techniques (AFM) [28]. Their molecular cargo is characterized mainly by flow cytometry, Western blot, immunoprecipitation, and immunohistochemistry methods [29] as well as by mass spectrometry, and quantitative polymerase chain reaction. In addition, there are several emerging techniques that complement traditional methods for EV characterization by their ability to reveal new information about the EV molecular cargo or to characterize the composition of individual EVs. These methods include fluorescence-based techniques [30,31], AFM [32], SPR [34], Raman spectroscopy [34, 35], and electrochemical sensing methods [36]. Among these novel approaches, Raman spectroscopy enables sensitive label-free detection and analysis of EVs protein content.

Raman spectroscopy is an optical method where a laser beam is used to irradiate a sample resulting in inelastic scattering of photons. The difference in energy of these photons corresponds to the chemical bonds that are present in the sample [37]. Due to its label-free and non-destructive nature with high chemical specificity, Raman spectroscopy has great application potential in the characterization of EVs. Several studies have been published in the past decade using Raman spectroscopy as a tool to analyze the biochemical content of EVs. The pioneering work reporting the first Raman spectrum of sEVs was published in 2009 [38]. Later studies

demonstrated the use of Raman spectroscopy for characterization of single EVs [39], as well as clusters of EVs trapped in the laser focus [40]. In addition, recent studies have indicated that Raman spectroscopy can be used for tissue characterization by analyzing the spectral signature of cancer EVs for prostate cancer diagnosis [41,42], as well as tissue specific EVs derived from mesenchymal stromal cells [43] and peripheral blood mononuclear cells [44]. Furthermore, urinary EVs from diabetic patients and hyperglycemic endothelial cells [45] have been successfully characterized by Raman spectroscopy. Immune capture based single EV Raman spectroscopy [46] has also been reported as a promising approach.

In the research field of neurological disorders, Raman spectroscopy has been used to investigate structural features and changes of toxic proteins such as A β [47-49], α -synuclein [50,51], and tau [52] by analyzing the amide bands in the protein spectrum that is particularly sensitive to the protein's conformational state and environment. Moreover, differences in the Raman fingerprint of blood samples of patients compared to a healthy control have been reported for a variety of neurological conditions such as AD [53], PD [54,55], dementia with Lewy bodies [56], and Huntington disease [57]. Recent reports have demonstrated the ability of Raman spectroscopy to accurately distinguish PD [58] and ALS [59] patients from healthy control group based on their EVs profile. Our group previously demonstrated the application of laser tweezers Raman spectroscopy for exosomes heterogeneity analysis [39] and SERS for biochemical analysis of EVs [60-64].

However, to our knowledge, specific Raman studies indicating A β association within sEVs have not been reported. Here we report for the first time the use of Raman spectroscopy for the identification and characterization of A β associated with sEVs, as well as the structural and dynamical effects of A β on the membrane of sEVs.

5.3 Materials and methods

5.3.1 A β ₁₋₄₂ pure protein preparation

A β ₁₋₄₂ protein samples were prepared by resuspension of the stock A β ₁₋₄₂ protein (Stock number: A9810, Sigma-Aldrich, USA) in DMSO to a final concentration of 10⁻⁶ M and vortexed prior usage.

5.3.2 Cell culture models

In this work, we used sEVs derived from the MC65 cell culture model and midbrain organoids, as described next.

5.3.2.1 MC65 AD cell culture model

We used MC65 cells derived from human neuroblastoma SK-N-MC cell line with conditional expression of transfected APP-derived construct, consisting of carboxyl-terminal 99 residues of APP (APP-C99), under negative regulation of tetracycline (TC) sensitive promoter [65]. Upon withdrawal of TC from the cell culture media, the cells express C99 which is then converted to A β by cleavage with intramembrane proteases γ -secretase and β -secretase. A β remains inside the cell and forms aggregates within 3-4 h after removal of TC with complete apoptotic death of cells in 72 h.

MC65 cells were cultured in a 75 ml flask in Dulbecco's Modified Eagle Medium supplemented with 4.5 mg/ml D-glucose, non-essential amino acids, 1 mM sodium pyruvate, and 10% (v/v) heat-inactivated fetal bovine serum (FBS), supplemented with 0.1 mg/ml tetracycline, 50 IU/ml penicillin, and 50 g/ml streptomycin. In order to prevent the addition of nonspecific FBS EVs, we cultured the cells with an EV-depleted FBS (Life Technologies®). This ensures that the resulting sEVs in the cell culture medium supernatant only originate from the plated cells. The MC65 cells were cultured in the presence of TC for 24 h and the growth media was then collected MC65(TC+) for further isolation of sEVs. Expression of APPC99 in MC65 cells was induced by removing TC from the cell culture medium and cells cultured for another 16 h. At this point, the cell culture media MC65(TC-) was harvested and centrifuged at 2000 g for 30 min to remove any cells and debris.

5.3.2.2 Midbrain organoids 3D cell culture

The midbrain organoids were developed in the Early Drug Discovery Unit at McGill University [66]. Briefly, PBMCs were isolated from the blood of healthy individuals and reprogrammed into an induced pluripotent stem cell line (iPSCs). The use of iPSCs and stem cells in this research is approved by the McGill University Health Centre Research Ethics Board (DURCAN_IPSC/2019-5374). The iPSC used for Midbrain organoids generation was AIW002-02, a healthy male control line derived reprogrammed from PBMCs and obtained from the

MNI's Open biorepository (C-BIG). After the formation of embryoid bodies (EBs), they were patterned into neuronal midbrains by inductive signals. To promote tissue growth, EBs were embedded in Matrigel scaffold and cultured in a six-well plate or orbital shaker. Cell culture media for sEVs isolation was collected after 120-day old maturation of the MBOs. The media was collected after a 7-day period, before the weekly media change.

5.3.3 Isolation of sEVs from cell culture media

sEVs were isolated by differential ultracentrifugation with two rounds of spinning. First, we employed a low-speed centrifugation of the sEVs containing media to remove the cell portions, cell debris, apoptotic bodies, or large biopolymers, and microvesicles. For this, 34 ml of the cell culture media from MC65 cells and midbrain organoids were centrifuged at 300 g for 10 min, followed by 2000 g for 10 min centrifugation and a final step centrifugation at 10000 g for 30 min. All low-speed centrifugations (300-10000 g) were performed using a Beckman Coulter Microfuge 20R centrifuge with a FA361.5 Biosafe rotor. The second round is a high-speed centrifugation which has the following steps: 120000 g for 90 min, collected supernatant was discarded, and the pellet was dispersed in ultrapure water and centrifugated one more time at 120000 g for 90 min to pellet the sEVs. UC was performed using Beckman Optima TLX Ultracentrifuge with an SW 28 swinging bucket rotor. The resulting pellets were finally resuspended in up to 100 μ l of ultrapure water and stored at -80°C until use. The samples were aliquoted (50 μ l) to reduce freeze-thaw cycling which may otherwise damage the sEVs. In this way, only one freeze-thaw cycle is used, which has been shown previously to not have a significant effect on the integrity of sEVs [67,68]. Moreover, dispersion and aliquoting of the resulting pellet allows characterization of the same isolated sEVs sample by complementary characterization methods to meet MISEV guidelines (e.g., electron microscopy, SP-IRIS, NTA, etc.).

5.3.4 sEV characterization

5.3.4.1 Nanoparticle tracking analysis

NTA was carried out using a NanoSight model LM10 (Malvern Panalytical Ltd, UK), equipped with a blue (405 nm) laser and a sCMOS camera. The isolated sEVs were thawed to room temperature and diluted 500-fold in filtered ultrapure water. Filtered ultrapure water (~2 ml) was

also used to thoroughly flush the NTA tubing to confirm the background to be free of any nanoparticle contamination prior to the next sample addition. Next, 1 ml of each diluted sample was loaded into a single-use syringe and the syringe was placed to an automated syringe pump (Harvard Bioscience, MA, USA) for injection. Three consecutive 30 s videos of each sample in flow conditions with at least 130 particles per frame during each run were recorded at camera level 12. The data was analyzed using a NanoSight NTA 3.1. software with the detection threshold set to 5 and screen gain 10 to track the statistically relevant number of particles, concurrently minimizing the distorting background artefacts.

5.3.4.2 Transmission electron microscopy

sEVs were deposited on glow discharged carbon film-coated copper TEM grids and incubated at room temperature for 5 min. Next, 8 μ l of filtered 1% uranyl acetate (UA) solution was dropped on the surface of TEM grids and incubated for 1 min for staining. After, excess UA was removed by contacting the filter paper with the edge of the TEM grids. The grids were then dried at room temperature for 30 min. Transmission electron microscopy was performed using a FEI Tecnai G2F20 transmission microscope operating at 80 kV.

5.3.4.4 SP-IRIS. Tetraspanin kits, as well as the buffer and blocking solutions, were purchased, and used as-is from NanoView Biosciences. The following detection antibodies were used: anti-CD9 AF488, anti-CD63 CF647, and anti-CD81 CF555. sEVs were diluted in Solution A at 10x, 100x, or 1000x, and 35 μ L of each dilution was incubated on a chip for 6 h at room temperature in a 24 well plate. 1 ml of Solution A was added to each well and the plate was shaken at 500 rpm for 3 min 750 μ l of the solution was removed from each well and replaced with 750 μ l of Solution A then shaken at 500 rpm for 3 min. This step was repeated twice more for a total of 4 shaking steps. During these steps, a blocking mixture was prepared, combining 1:1 Solution A and blocking solution. Antibodies were diluted 1:600 in a blocking mixture. After the final mix, 750 μ l of the solution was taken out of each well and 250 μ l of antibody mixture was added. Chips were then incubated at room temperature for 1 h. After incubation, 500 μ l of Solution A was added to each well. 750 μ l of the solution was then immediately taken out and replaced by 750 μ l of new Solution A. This was shaken at 500 rpm for 3 min followed by removing 750 μ l of solution from each well. 750 μ l of Solution B was then added to each well and the plate was

shaken at 500 rpm for 3 min followed by removing 750 μ l of solution. This was repeated 3 times. 750 μ l of MilliQ water was then added to each well and shaken at 500 rpm for 3 min for a total of 5 shaking steps after antibody incubation. Each chip was washed in two successive dishes of MilliQ water, taking care to avoid drying of the chip between dishes. In the final dish, the chip was tipped at a 45-degree angle and slowly pulled out of the water. These were then dried on absorbent paper and added to the chuck. Chips were scanned by SP-IRIS and all three fluorescent channels. Data were analyzed with fluorescence cut-offs of 600, 400, and 400 arbitrary units for the blue, green, and red channels, which were chosen by limiting the number of particles on the negative control MIgG spot to less than 10 for all chips.

5.3.4.5 Raman spectroscopy setup and data acquisition

A WITec Confocal Raman microscopy system (WITec Alpha300R) with a 633 nm HeNe laser, maximum power of 5 mW at the sample, coupled into a microscope equipped with a 50x objective (NA 0.8, WD 0.58 mm), a spectrometer (spectral resolution 0.1 cm^{-1} at 633nm) and a CCD camera was used for these experiments. The acquisition time for sEVs characterization was 60 s. The spectra were collected after air-drying 5 μ l of isolated sEVs solutions on a glass cover slip from multiple points within the droplet fingerprint focusing on small aggregates of sEVs and in the rim area of the droplet. This approach allows size-based separation of sEVs from possible contaminants such as large EVs or protein aggregates, *via* convection currents that drive smaller particles to the outside of the ring. This is not possible if the spectra are measured from pellets where the EVs are clumped together, making the separation of larger aggregates (including protein aggregates) from the actual sEVs more challenging. Moreover, measuring Raman spectra of sEVs in liquid pellets presents difficulties due to their intrinsic Brownian motion, which will cause particles to move in and out of the laser beam. In addition, the momentum of the photons in the laser beam may push particles out of the focal region and, if not controlled properly, may make the measurements less accurate.

5.3.4.6 Data pre-processing and statistical analysis

The statistical analysis and data processing were performed using WITec Project Five build-in software (ImageLab) and OriginPro (OriginLab, Northampton, MA). Prior analysis the quality of Raman spectra was assessed, and data pre-processing was performed in order to minimize

insignificant variability. Pre-processing of the data included correction of baseline by subtraction of the spectral background from glass, cosmic rays, and other background deviations. Next, in order to enhance the spectral quality, we reduced the noise by applying Savitzky-Golay smoothing and then the data were normalized. PCA was performed using OriginPro PCA for spectroscopy app. PCA was performed on a range of 900-1800 cm^{-1} , 1540-1800 cm^{-1} , and 2800-3100 cm^{-1} . The variance-covariance matrix was utilized for further analysis and the reduction of initially complex data was achieved by PCA. Next, to build the PCA score plot we used the first two principal components (PCs). Peak deconvolution was achieved by using the OriginPro built-in Multiple Peak Fit tool. The peak positions were chosen based on existing literature and further deconvolved using Voigt peak shape function.

5.4 Results

The workflow of the study is represented in Figure 1, which describes schematically the steps followed to isolate, characterize, and analyze the sEVs. Specifically, in this study, we employed three different sEVs groups, isolated from two types of cell cultures: 2D MC65 neuroblastoma cell line and 3D midbrain organoids. The MC65 cell line is an *in vitro* AD model that provides a neuronal source of sEVs containing A β . We believe that it is important to fully investigate and understand the signatures of sEV-associated A β in simulated conditions before examining human samples. The study of an *in vitro* model of AD allows the investigation of possible roles A β protein has in neurons [69-71], and subsequently in neuronal sEVs, and may provide valuable insights into the pathogenesis of AD. Future work building on this data will apply Raman-based detection of AD in clinical settings. sEVs isolated from 3D midbrain organoids serve as an additional negative control in this study and represent healthy brain neurons. As described in the Methods section, sEVs isolation was achieved by first centrifuging the cell culture media several times at low speed to remove the remaining cell fragments, debris, and microvesicles, followed by two cycles of high-speed centrifugation. We expect that, in accordance with previous reports, the remaining pellet contains the small sEVs of interest. We will further denote the sEVs isolated from untreated and tetracycline treated MC65 cells line as TC- sEVs and TC+ sEVs, respectively. The sEVs isolated from organoids culture media are labeled as osEVs. The sEVs were characterized by established methodologies such as NTA and TEM and were further

studied by Raman spectroscopy to reveal their biochemical content. Subsequently, the recorded spectra were analyzed by PCA to identify the A β content of each sEVs group.

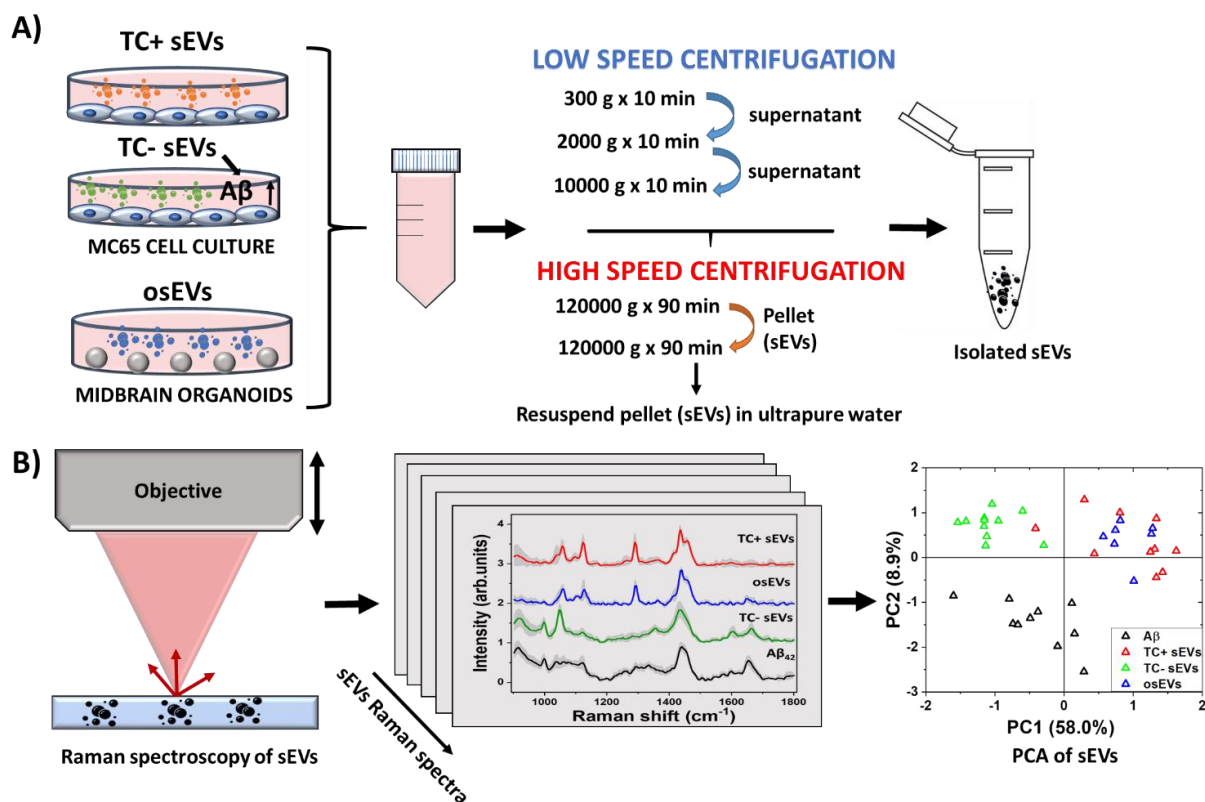


Figure 1. Schematic illustration of sEVs isolation and characterization by Raman spectroscopy. A) sEVs were isolated by differential ultracentrifugation from the MC65 AD cell culture model, which is under tetracycline promoter regulation, and midbrain organoids developed from PBMCs of healthy donors. B) The biochemical content of the isolated sEVs was characterized by Raman spectroscopy. The collected spectra were further analyzed by PCA.

5.4.1 sEVs characterization by NTA and TEM

First, we characterized the size and concentration of the isolated sEVs *via* NTA. Figure 2A shows the size distribution plots for all analyzed sEVs groups. The mean concentration of TC- sEVs, as measured by NTA, 6.5×10^9 EVs/ml, was higher than the mean concentration of TC+ and osEVs samples, which was 4.2×10^9 EVs/ml and 4.5×10^7 EVs/ml, respectively. Additionally, the mean particle size as measured by NTA was $157.3 \text{ nm} \pm 3.8 \text{ nm}$, $164.1 \text{ nm} \pm 11.2 \text{ nm}$, and $293.5 \pm 2.7 \text{ nm}$ for TC- sEVs, TC+ sEVs, and osEVs, respectively. One can see that the mean particle size of TC- sEVs was comparable with the one that is recorded for TC+ sEVs. On the

other hand, we observed a slightly larger particle size for osEVs. TEM images, presented in Figure 2B confirm this result, showing an increased size for organoids sEVs. Moreover, TEM images revealed the sEVs cup-shaped morphology, which is a typical experimental artefact related to deflation of EV structure during the sample preparation.

To confirm that sEVs were enriched during ultracentrifugation, expression of sEVs associated tetraspanins, CD9, CD63, and CD81, were tested by immuno-capture and immuno-fluorescence, using the SP-IRIS method implemented into the ExoView R100 instrument. This equipment utilizes a micropatterned chip with an array of spatially distinct antibody spots. During incubation, sEVs are captured by these antibodies and subsequently labeled with fluorescent detection antibodies. By directly imaging these antibody arrays, up to four co-expressed surface proteins (capture antibody and three fluorescent detection channels) can be detected on a single sEV.

For both sEV populations, all three tetraspanins were expressed with both capture and fluorescence detection of each tetraspanin. Furthermore, the tetraspanin profile of each sEVs population was very similar with most CD9 positive sEVs detected on the CD81 capture spot, the most CD63 positive sEVs detected on the CD63 capture spot, and similar amounts of CD81 positive sEVs captured on each spot. These results show that the co-expression of these tetraspanins is highly consistent between these sEV populations.

In addition, we note that the resuspension of sEVs in ultrapure water did not notably change the characteristics of analyzed sEVs. Their size, morphology, and surface protein expression (Figure 2) is comparable to the ones reported for sEVs resuspended in PBS or commercially available EVs resuspension buffers that maintain osmotic pressure. We believe that the ability of EVs to withstand the isotonic solution pressure can be explained by the higher rigidity of the EVs lipid bilayer that is enriched with cholesterol, sphingomyelin, and gangliosides compared to the membranes of their cells of origin [72,73]. Moreover, we experimentally determined that the composition of the resuspension buffer did not majorly impact the physical or chemical nature of sEVs (data not shown). To do this, we isolated sEVs by differential centrifugation from cell culture media and resuspended them using either 0.1 % filtered PBS or ultrapure water, both as the final buffer as well as during intermediate steps of processing. Then, we characterized sEVs

by NTA, resistive pulse sensing (RPS), and SP-IRIS methods. The results of concentration and size distribution analysis did not show a major difference between the two groups of sEVs. We found that the sEVs resuspended in water had a similar concentration (8.8×10^{11} particles/ml) compared to sEVs resuspended in PBS (2.4×10^{11} particles/ml), indicating similar yield for particles. Finally, we determined that both sEVs groups had similar CD9, CD63, and CD81 tetraspanins profiles, which further suggests that the chemical nature of sEVs remains generally similar regardless of the choice of resuspension buffer.

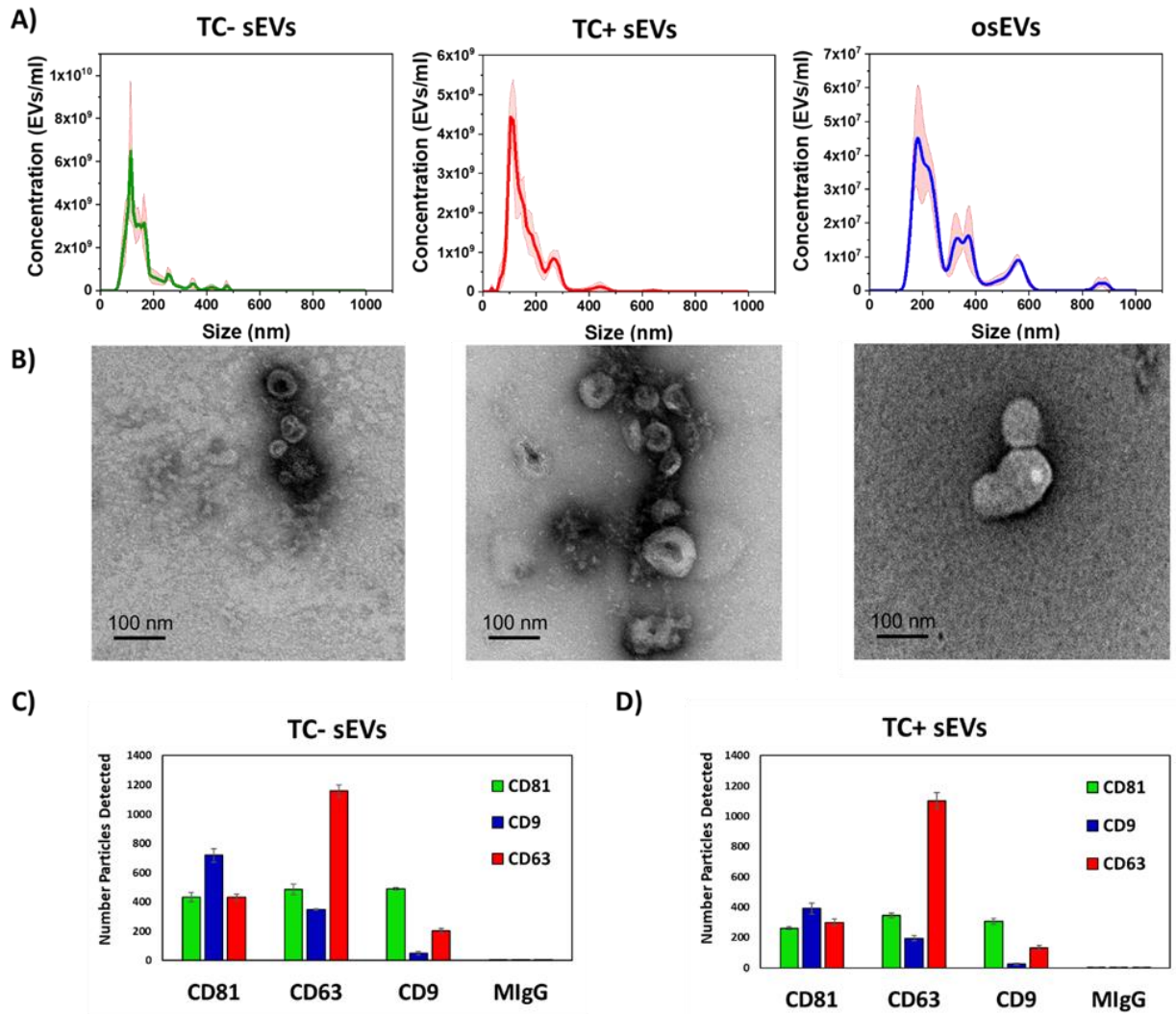


Figure 2. Characterization of sEVs by transmission electron microscopy, nanoparticle tracking analysis, and SP-IRIS. A) Graphs show the concentration of sEVs as a function of particle size for TC- sEVs, TC+ sEVs, and osEVs. Shaded areas represent error bars. B) Electron micrographs of TC- sEVs, TC+ sEVs, and osEVs showing the

cup-shaped morphology. Scale bar is 100 nm. Expression of typical EVs surface proteins CD81, CD63, and CD9 as well as the negative control MIgG in the C) TC- sEVs and D) TC+ sEVs samples.

5.4.2 Raman spectroscopy analysis of sEVs isolated from MC65 (TC -/+) cells and midbrain organoids cell culture media

The MC65 AD cell culture model used in this study overexpresses 99-aminoacid carboxyl-terminal fragments (β CTF) of APP under tetracycline promoter regulation. This model is designed to mimic the pathological pathway of APP that leads to amyloidogenesis. This pathway involves cleavage of mature APP by β - and γ -secretases, where β -secretase cleaves the amino terminus of A β , and membrane-associated β CTF. Further, β CTF is cleaved by γ -secretase resulting in the release of A β_{40} or A β_{42} peptides and APP intracellular domains (AICDs) [65]. As β CTF undergoes endocytosis, it can be trafficked to endosomal compartments such as MVBs and possibly enveloped in sEVs or exosomes [74]. It has been shown previously that APP CTFs are overabundant in CSF of AD patients and suggested to be potential diagnostic biomarkers of AD [75]. The control samples of sEVs are isolated from the same cell culture model in the presence of tetracycline (TC+) and midbrain organoids sEVs (osEVs). The midbrain organoids were developed from PBMCs of healthy individuals and were used in this study because they are biochemically and biophysically more similar to tissues due to their ability to mimic cell-matrix and cell-cell interactions. Therefore, they are representative of healthy brain neurons.

For the Raman spectroscopy analysis, the isolated sEVs were resuspended in ultrapure water and placed on a clean glass microscope slide to allow air-drying. Spectra were mostly recorded from the small aggregates of sEVs and from the edge of the dried sample, where sEVs accumulate preferentially due to the “coffee-ring effect”. This effect is observed upon the evaporation of water from droplet samples that contain small-sized particles. Explicitly, in a sample with a heterogeneous particle size distribution, the smallest particles flow radially toward the contact line during the drying process. The angle between the surface of the drying EVs sample and the microscope slide decreases progressively during water evaporation which limits the size of the particles that can approach the edge of the droplet. Therefore, after drying, the particles will be separated based on their size due to convective currents inside the droplet, as reported by Jeong et al. [76]. As the droplet dries, the smaller (lighter) particles such as sEVs are deposited and concentrated at the outer edge of the dried sample, and the bigger (heavier) particles, such as

large EVs or protein aggregates that could be co-isolated during differential ultracentrifugation, are concentrated closer to the center region. By positioning the laser spot in the ring and adjacent to the ring area we ensure that we measure particle sizes in the typical sEVs range according to MISEV 2018 nomenclature and as measured here by NTA and TEM (Figure 2). This is particularly important for the acquisition of reliable Raman spectra. In our case, we were able to record high-quality spectra with 633 nm continuum laser excitation at relatively low power of few mW and acquisition times on the order of one minute.

Next, we analyzed the collected Raman spectra from TC- sEVs (n=11), TC+ sEVs (n=10), and osEVs (n=7) samples and compared them with spectra recorded from pure A β ₄₂ protein (n=10). The Raman spectra of the “fingerprint region” 900-1800 cm⁻¹ from all sEVs groups and A β ₄₂ pure protein represent a complex set of peaks with shared features among all sEVs samples and some variations (Figure 3A). The Raman peak assignments are given in Table 1. All sEVs groups shared the same peak positions at 1123 cm⁻¹ and 1290 cm⁻¹ assigned to C-N vibration and Amide III α -helix protein structure, respectively. Peaks at 1436 cm⁻¹ and 1453 cm⁻¹ are assigned to the lipid content, specifically to the CH₂ and CH₃ deformation in lipids and triglycerides. Additionally, A β ₄₂ pure protein spectra presented two distinct peaks at 1000 cm⁻¹ and 1600 cm⁻¹, assigned to the breathing of the benzene ring and C=C vibration corresponding to phenylalanine, respectively. These peaks can be also observed in the TC- sEVs spectra, suggesting that these sEVs could potentially carry A β protein. Amide I region was also located at similar positions for TC-sEVs, osEVs, and A β ₄₂ pure protein covering the area 1650-1668 cm⁻¹. In the osEVs spectra, these peaks can be observed, while they are missing in the TC+ sEVs spectra.

Then, we performed PCA of the collected data and the results are shown in Figure 3B. The first two principal components represented 58.0% and 8.9% variability of the total variance, respectively. It is important to note that these scores may be influenced by both spectrum intensity and spectrum shape [77,78]. The samples are spread along the PC1 axis with TC- sEVs located on the negative side, while TC+ sEVs and osEVs are distributed loosely on the positive side of the axis. A β ₄₂ pure protein spectra form an elongated cluster between PC1 and PC2. By this, it is clear that the different sample groups can be distinguished from each other based on their Raman spectra, which also serves as a valuable starting point for further analyses.

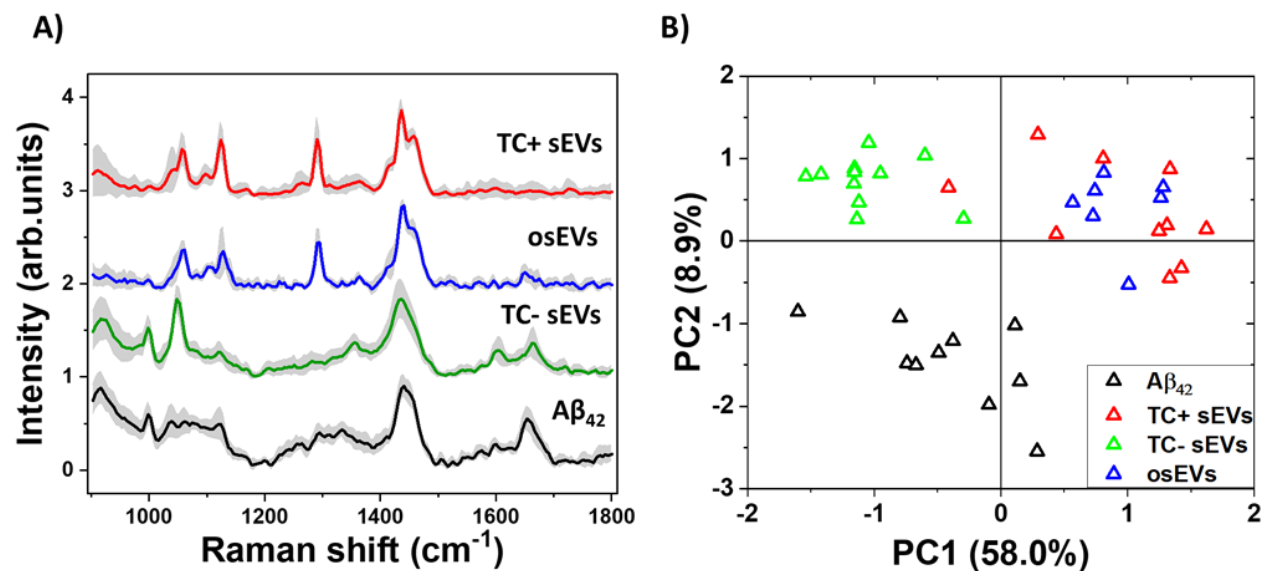


Figure 3. Characterization and analysis of the “fingerprint region” 900-1800 cm^{-1} of TC- sEVs, TC+ sEVs, osEVs, and $\text{A}\beta_{42}$ pure protein. A) Average Raman spectra of fingerprint region 900-1800 cm^{-1} of TC- sEVs, TC+ sEVs, osEVs, and $\text{A}\beta_{42}$ pure protein. Spectra are offset for clarity. Shaded areas represent ± 1 standard deviation. B) The score plot of the first two principal components for each sEVs group. Colors represent each sEVs group as shown in the legend.

Table 1. Assignments of the Raman spectra vibrational bands

Position (cm^{-1})	Peak assignment	Reference
1000	Phenylalanine ring breathing of protein	Hernandez et.al., 2013 [79]
1123	C-N of proteins	Teh et.al., 2009 [80]
1290	Amide III	Bandekar et.al., 1992 [81]
1436	Fatty acids, triglycerides, CH_2 or CH_3 deformations	Verma et.al., 1977 [82]
1453	Proteins, CH, CH_2 or CH_3 deformations of long chain fatty acids, phospholipids	Notiger et.al., 2009 [83]
1600	C=C of phenylalanine	Hernandez et.al., 2013 [79]
1650-1660	Unsaturated fatty acids cis form, Amide I α -helix	Bandekar et.al., 1992 [81]
1667-1668	Amide I β -sheet	Bandekar et.al., 1992 [81]

2845	CH ₂ symmetrical stretching of fatty acids, triglycerides	Song et.al., 2020 [84]
2878	CH ₂ asymmetric stretching (lipids)	Song et.al., 2020 [84]
2900	CH ₂ asymmetric stretching (lipids)	Song et.al., 2020 [84]
2930	CH ₃ symmetric stretching of proteins/lipids (cholesterol)	Rygula et.al., 2013 [85]
2960	CH ₃ symmetric stretching of proteins	Lis et.al., 1976 [86]
3060	Proteins aromatic CH stretching mode/nucleic acids	Rygula et.al., 2013 [85]

Raman spectroscopy can effectively determine the secondary structure of proteins [81]. The peaks centered at 1667-1668 cm⁻¹ assigned to C=O and a small contribution of C-N stretch corresponds to β -sheet protein conformation. The peaks located at 1650-1660 cm⁻¹ region arising from the coupling of C-N stretching vibration and N-H bending vibrations correspond to an α -helix structure. Therefore, our attention was further focused on the Amide I region which is mostly affected by the secondary structure of the proteins. The α -helix rich structure might originate from A β peptide bonded to a plasma membrane. In an attempt to identify specific peaks within the Amide I region, we performed peak deconvolution analysis. Figure 4 depicts the deconvolution of the Amide I region in TC- sEVs and A β ₄₂ pure protein spectra. For this, the most intense peaks at 1600 cm⁻¹ and 1650 cm⁻¹ in the spectra were centered, fixed, and fitted until high values of R² were obtained. The recorded Raman spectra are shown as solid lines and deconvolved peaks are marked as dashed lines.

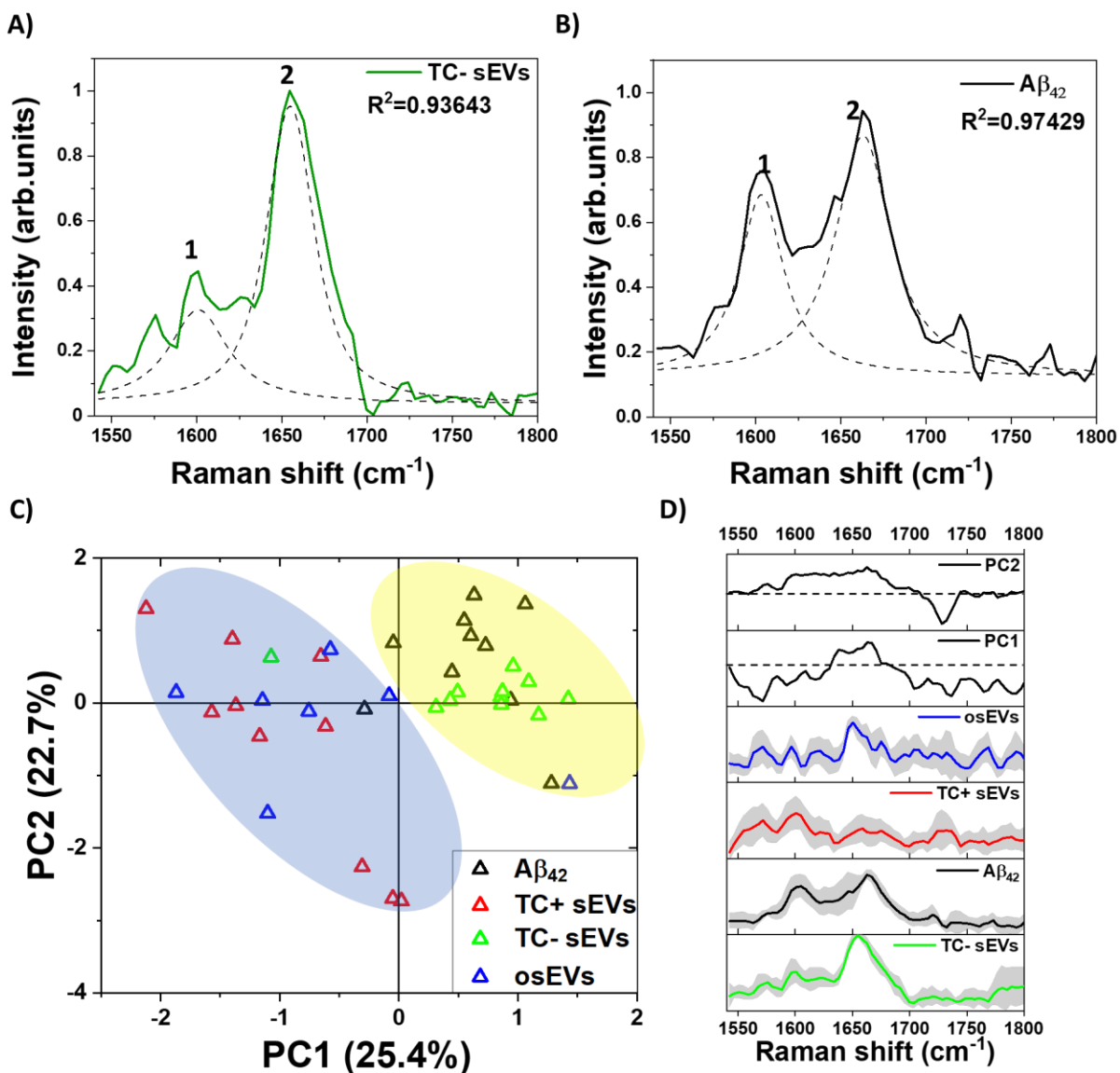


Figure 4. Analysis of the Raman spectra of the Amide I region 1540-1800 cm^{-1} . A) Deconvolution of Amide I region of averaged spectra of TC- sEVs and B) $\text{A}\beta_{42}$ pure protein indicated the presence of two peaks at 1600 cm^{-1} (labeled as peak 1) and 1650 cm^{-1} in TC-sEVs spectra and 1663 cm^{-1} for $\text{A}\beta_{42}$ pure protein spectra (labeled as peak 2). Deconvolved spectra are shown as dotted lines. C) The score plot of the first two principal components for each sEVs group. Colors represent each sEVs group as shown in the legend. Colored regions are to provide visual aids. D) Comparison of the PC1 and PC2 loadings with $\text{A}\beta_{42}$ pure protein spectrum and with average spectra of each sEVs group. Dotted lines represent zero-axes of the PCA loadings. Shaded areas represent ± 1 standard deviation. Spectra are offset for clarity.

The Amide I region deconvolution clearly identifies the presence of a peak at 1650 cm^{-1} in the spectra of TC- sEVs (Figure 4A) that corresponds to an α -helical conformation of the protein. The peak at 1663 cm^{-1} in the spectra of $A\beta_{42}$ pure protein is assigned to an α -helical conformation with a potential contribution from “disordered structures” (Figure 4B). On the other hand, the Amide I region of TC+ sEVs and osEVs is too weak to provide a reliable fit and to obtain information. In addition, the presence of only α -helical structure of the proteins in the spectra of TC- sEVs confirms that the collected spectra represent the proteins within sEVs and not insoluble protein or peptide deposits, which typically adopt an enriched β -sheet conformation [87].

The deconvolution of the $A\beta_{42}$ pure protein spectra identified strong peaks centered at 1600 cm^{-1} and 1663 cm^{-1} . The broad peaks in the Amide I region of TC- sEVs spectra indicated the presence of mainly monomeric form or small oligomers of $A\beta$. A previous NMR study characterized $A\beta$ associated with a phospholipid bilayer-mimicking environment as a monomeric amphipathic α -helix conformer [88]. Next, the Raman spectra region between $1540\text{--}1800\text{ cm}^{-1}$ that includes the Amide I region was analyzed by PCA. Figure 4C depicts the score plot of the first two principal components that cumulatively represent 48.1% variability of the total variance. In order to highlight different cluster regions, shaded ellipse areas are shown in the plot. One can observe that TC- sEVs and $A\beta_{42}$ pure protein are closely clustered in the positive side of the PC1 axis. In contrast, TC+ sEVs and osEVs spectra are dispersed along the PC1-PC2 plane. Next, the analysis of PC loadings showed the contribution of the individual wavenumber to PC1 and PC2 (Figure 4D). While the PC1 loading resembles the spectra of $A\beta_{42}$ pure protein, the biochemical meaning of the second PC is more difficult to interpret. Taken together, these data revealed that the major secondary structure of the proteins and potentially $A\beta$ within the analyzed sEVs is typical to the α -helix form of proteins.

Additionally, Raman spectra in the “high-wavenumber region” can provide valuable information about the biochemical composition of the sEVs. Figure 5 compares the experimentally recorded and deconvolved Raman bands that were obtained under the same experimental conditions as for the Amide I region. Two major peaks were present within all sEV spectra in this region at 2845 cm^{-1} and 2878 cm^{-1} . These peaks are characteristic vibrational features of lipids and correspond to symmetrical and asymmetrical CH_2 vibrations, respectively. The analysis of $A\beta_{42}$ pure protein

did not show the presence of the 2845 cm^{-1} peak and only showed weak intensity of the 2878 cm^{-1} peak. Specifically, these peaks can be attributed to the presence of long acyl chain lipids such as fatty acids and ceramides. In addition, there was a small contribution of cholesterol to these peaks. On the other hand, the characteristic peak of the proteins is located at 2930 cm^{-1} . Figure 5A and 5B depicts stronger intensities at 2930 cm^{-1} in deconvolved peaks of the TC- sEVs and $A\beta_{42}$ pure protein compared to TC+ sEVs (Figure 5C) and osEVs (Figure 5D).

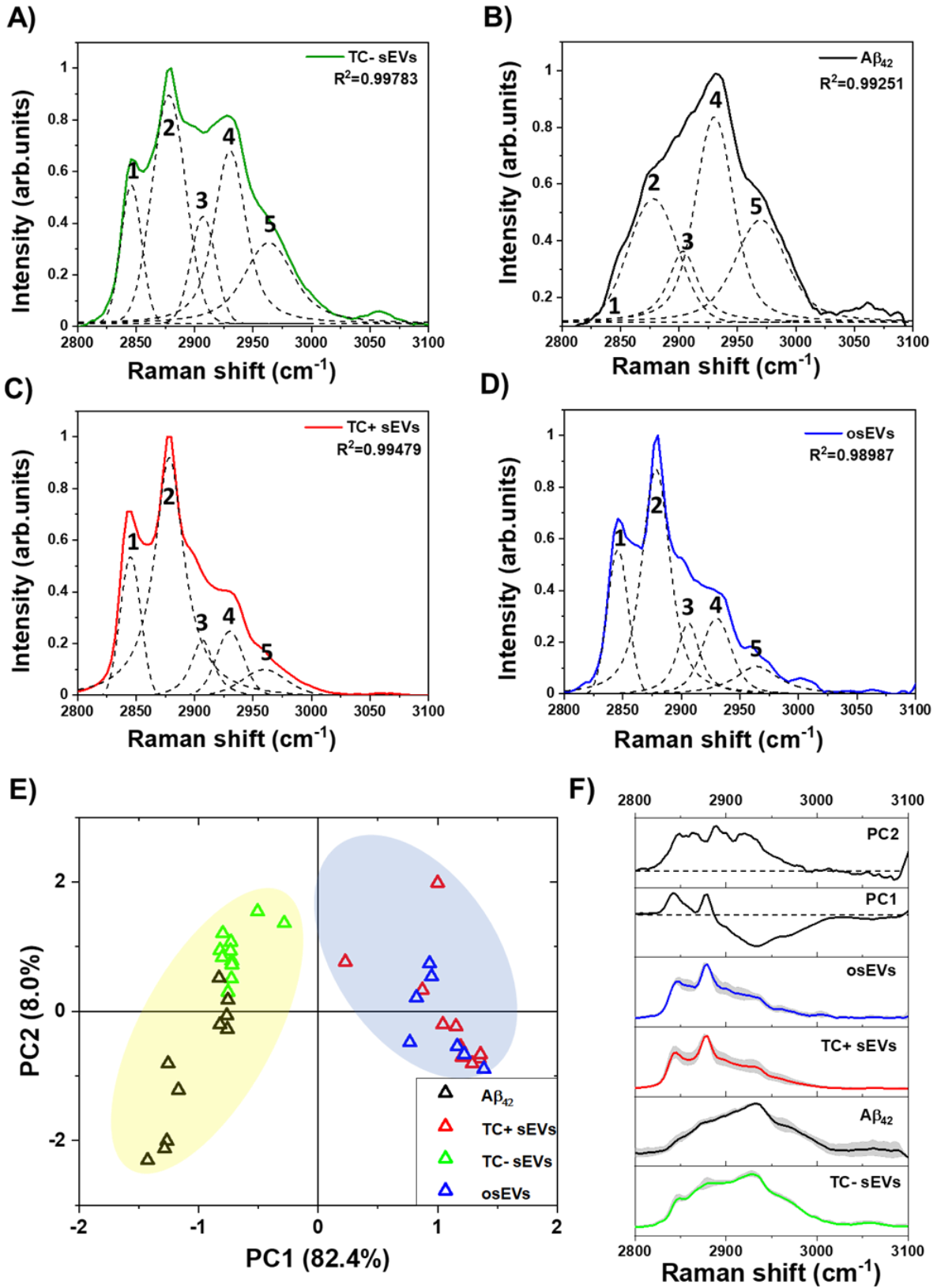


Figure 5. Analysis of the “high-wavenumber region” 2800-3100 cm^{-1} of normalized Raman spectra. Raman spectra and peak deconvolution for A) TC- sEVs, B) $\text{A}\beta_{42}$ pure protein, C) TC+ sEVs, and D) osEVs. Dotted lines represent five peaks that were analyzed in this region, labeled with numbers as follows: 1 – 2845 cm^{-1} , 2 – 2878 cm^{-1} , 3 – 2900 cm^{-1} , 4 – 2930 cm^{-1} , and 5 – 2960 cm^{-1} . E) The PCA score plot of the first two principal components. Colors represent each sEVs group as shown in the legend. Colored regions are to provide visual aids. F) Comparison of the PC1 and PC2 loadings and average spectra of sEVs groups. Shaded areas represent ± 1 standard deviation. Dotted lines represent zero-axes of the PCA loadings. Spectra are offset for clarity.

It has been shown previously that the ratio of Raman intensities at 2930 cm^{-1} and 2845 cm^{-1} ($I_{2930}/I_{2845} \text{ cm}^{-1}$) reflects the ratio of the protein and lipid content [89, 90]. Table 2 shows the calculated Raman intensity ratios for all analyzed sEV groups. The intensity values are calculated for the area under the curve for each peak.

Table 2. Raman intensity ratios at 2930/2845 cm^{-1}

sEVs group	$I_{2930} \text{ cm}^{-1}$	$I_{2845} \text{ cm}^{-1}$	Ratio $I_{2930}/I_{2845} \text{ cm}^{-1}$
TC- sEVs	29.16947	11.97269	2.43633
TC+ sEVs	8.97397	12.17685	0.73696
osEVs	11.55123	12.63436	0.91427

One can see that TC- sEVs had a higher $I_{2930}/I_{2845} \text{ cm}^{-1}$ intensity ratio compared to the TC+ sEVs and osEVs, indicating a higher concentration of proteins within TC- sEVs. These results indicate that $\text{A}\beta$ protein could be present in the TC- sEVs and could be at higher concentrations than in TC+ sEVs and osEVs. To complement these findings, we performed PCA of the peaks in the “high-wavenumber region” between 2800-3100 cm^{-1} of Raman spectra of all sEVs groups and $\text{A}\beta_{42}$ pure protein. Figure 5E represents the score plot in the PC1-PC2 plane where the first PC was responsible for 82.4% of the variability and PC2 carried 8.0% of variability of the total variance. It can be clearly seen that TC- sEVs and $\text{A}\beta_{42}$ pure protein spectra were clustered on the negative side of the PC1 axis while the TC+ sEVs and osEVs were clustered on the positive side of the PC1 axis. Figure 5F shows the loading plots of PC1 and PC2 and the average spectra of the sEVs analytes and $\text{A}\beta_{42}$ pure protein control protein. The loading spectrum for PC1 had several peaks at both positive and negative sides where the most significant wavenumbers are 2930 cm^{-1} , 2845 cm^{-1} , and 2878 cm^{-1} and resembled the spectra of $\text{A}\beta_{42}$ pure protein and sEVs

groups spectra. In contrast, the chemical meaning of the second principal component was not clear from the shape of the loading. Finally, PCA was able to successfully cluster similar spectra and segregate different ones.

Next, we evaluated the effect of A β on sEVs lipid membrane composition and structure. For this, we used the ratios of Raman peaks at 2845 cm⁻¹ (CH_{2 sym}) to 2878 cm⁻¹ (CH_{2 asym}) that describe an estimated lipid fluidity or degree of unsaturation [91, 92] (Table 3). The higher the I_{2845}/I_{2878} cm⁻¹ ratio is, the more unsaturated lipids are present, and the higher is the fluidity of the EV membrane. The results show that all three groups of sEVs had the same degree of saturation. Furthermore, in order to analyze the structure of lipids, we calculated the ratio of Raman peak intensities at 2845 cm⁻¹ (C-H stretch of CH₂) to 2930 cm⁻¹ (C-H stretch of CH₃) that has been shown to correlate with the number of C atoms in the fatty acid chain [92, 93]. We observed a slight change in the lipids structure, with the higher prevalence of unsaturated lipids with a longer chain in the TC+ sEVs and osEVs, and prevalence of lipids with a shorter chain length in TC- sEVs. This observation together with previously published reports indicates the effect of A β association to EV membrane fluidity by changing the structure of EV membrane lipids [94].

Table 3. Analysis of lipids saturation and structure.

sEVs group	$I_{2878} \text{ cm}^{-1}$	Degree of Unsaturation (CH _{2 sym.} - CH _{2 asym.}) (ratio $I_{2845}/I_{2878} \text{ cm}^{-1}$)	Chain length prediction (CH ₂ /CH ₃) (ratio $I_{2845}/I_{2930} \text{ cm}^{-1}$)
TC- sEVs	32.06708	0.37336	0.41045
TC+ sEVs	45.10705	0.26995	1.35690
osEVs	34.37304	0.36756	1.09376

5.5 Discussion

AD is a neurodegenerative disease that remains challenging to diagnose in early stages. This prognostic uncertainty of existing diagnostic methods in combination with high costs and invasiveness of current diagnostic procedures further emphasizes the importance of developing sensitive and accurate alternative tests for early AD diagnosis. The overall goal of the study was

to explore the use of sEVs as carriers of toxic proteins. We used Raman spectroscopy to characterize sEVs associated with A β protein as potential biomarkers for AD diagnosis. First, we demonstrated a clearly different biochemical profile of A β associated sEVs compared to the control sEVs groups. In particular, intense peaks at 1650 cm⁻¹ and 2930 cm⁻¹ and their similarities with the spectra of pure A β protein indicate the presence of the A β protein in TC- sEVs. On the contrary, less intense, or lacking bands at these positions in TC+ sEVs and osEVs confirm the hypothesis that these peaks are associated with A β protein. The observed differences in the PCA results in the Amide I and “high-wavenumber regions” of the spectra can be explained by additional contributions from other proteins in sEVs cargo in the Amide I region, as well as a lower overall signal-to-noise ratio in this region compared to the “high-wavenumber region”.

In order to evaluate *a priori* the ability of Raman spectroscopy to detect A β in our sEVs we performed an estimate of the number of A β molecules in our laser spot. First, we calculated the number of A β molecules per sEV based on published data [22]. Fiandaca et al [22]. reported the A β ₄₂ concentration (pg/ml) in total exosomes solution and the number of exosomes per ml. To determine the mass of A β ₄₂ per sEV, we divided the A β concentration (expressed in pg/ml) by the number of exosomes per ml. Next, we converted the mass of A β to the number of molecules per sEV by first converting the mass of A β to moles using the molar mass and further converting to the number of molecules using the Avogadro’s number. We applied this procedure to the values reported in the aforementioned study. The reported concentration of A β ₄₂ is 18.5 pg/ml in exosomes (2.78 \times 10⁹ particles/ml) isolated from plasma of AD patients (n=3) and 0.83 pg/ml in exosomes (3.49 \times 10⁹ particles/ml) extracted from age matching healthy individuals (n=3). We used the values of the exosomal A β ₄₂ protein concentration extracted from AD patients’ plasma to estimate the concentration of the protein in our TC- sEVs. The concentration of A β ₄₂ protein obtained from the analysis of healthy controls was used to calculate the protein concentration in TC+ sEVs and osEVs. Beginning with the number of A β molecules per one sEV in TC-/+ sEVs and osEVs solutions, we calculated approximately 885 A β molecules/sEV, 31.5 molecules/sEV, and 30 molecules/sEV, respectively. The calculated values indicate a higher load of A β in TC- sEVs. Next, knowing the number of A β molecules per sEV we can calculate the expected number of A β molecules in our laser spot by assuming that the laser spot is a cylinder with 0.5 μ m radius and 2 μ m height and the sample is composed of concentrated sEVs filling the laser

beam. Then, we calculated the estimated volume of one sEV of each group based on the mean size of sEVs analyzed by NTA. Subsequently, we calculated the number of sEVs of each group in the laser spot described above. The estimated number of A β molecules in the laser beam spot is 6.8×10^5 A β molecules for TC- sEVs, 2.1×10^2 A β molecules for TC+ sEV, and 1.7×10^2 A β molecules for osEVs. These estimates are supported by the differences of Raman intensities, where a linear relationship is expected to the number of molecules in the analyte. It is important to note that the 2930 cm^{-1} peak corresponds to overall protein concentration within analyzed sEVs. However, the main difference between TC- MC65 cells and TC+ MC65 cells is the presence of tetracycline and overexpression of A β in TC- MC65 cells. This indicates that the isolated sEVs will have mainly the same molecular composition and the major variability is the presence of A β in TC-sEVs as detected by Raman spectroscopy.

Next, the deconvolution of the Amide I region of TC-sEVs showed that A β associated with sEVs is in an α -helical conformational form and in the size of a monomer or a small oligomer. These findings may shine light on a potential mechanism of propagation of neurodegeneration by sEVs carrying toxic oligomers. There is no consensus in the field regarding the structure of the toxic oligomers. The process of transformation of the monomers into toxic oligomers has been shown to be structure dependent. Specifically, it has been noted that toxic oligomers, as well as A β fibrils, have a β -sheet enriched secondary structure that provides a high adherence site for further fibrillation [95-97]. Conversely, a number of studies showed that early oligomers of A β and α -synuclein have an α -helical secondary structure and are prompted by helix-helix interactions [51, 98]. This knowledge and our results further suggest that sEVs may be involved in toxic oligomers spread within the neurons in CNS.

In addition, we observed differences in the lipid structures of sEVs. The lipids with longer fatty acid chains are prevalent in control sEVs groups, TC+ sEVs, and osEVs. On the other hand, TC-sEVs have shorter fatty acid chain lengths. Since the main difference between TC- sEVs and TC+ sEVs is the presence of the A β protein, we suggest that the association of A β protein with plasma membrane alters plasma membrane fluidity. The plasma membrane fluidity depends on several factors, such as degree of fatty acids saturation, length of fatty acid tail, cholesterol content, and temperature. Specifically, the lengths of fatty acids tails affect the membrane rigidity by creating intermolecular interactions between phospholipid tails. In the case of TC-

sEVs we observe a two-fold reduction of the chain length and as a result, a potential increase in membrane fluidity. However, the cause of this phenomenon remains to be explored. One possible explanation for the increased EV membrane fluidity is the formation of transmembrane oligomeric pore structures that are proposed to occur with the peptide's interaction with the EV plasma membrane. In addition, the length of the fatty acid chain shortens with an increase in temperature. However, this parameter should not affect our results since sEVs from all three groups were analyzed under the same experimental conditions.

Overall, our results confirm that A β protein is present in sEVs and can be detected *via* Raman spectroscopy. Moreover, our study uncovered the role of A β protein in the plasma membrane fluidity, paving the way for other studies on this topic. Future studies using clinical samples of AD patients will be necessary to demonstrate the potential of sEVs for early AD diagnosis. Further, studies of the sEVs derived from AD patients and healthy controls via Raman spectroscopy will possibly indicate spectral biomarkers that may correlate to the development of AD. The analysis of molecular conformation of sEV-associated A β protein is particularly important in understanding the role of sEVs in the propagation of neurodegeneration as it has been previously proposed in the literature. Potential pathologies underlying AD other than misfolded proteins and their conformers can be explored via Raman spectroscopy in sEVs from clinical samples. For instance, a comparison of the metal ions contents in EVs that has been shown to correlate with aggregation of A β protein and deposition of plaques. Moreover, another area of great interest is exploring lipidomic changes that may contribute to the disease development and may potentially be detected in EVs molecular content via Raman spectroscopy. The main drawback of the technique that limits its translation to clinic is the relatively low Raman signal. Nonetheless, this limitation can potentially be addressed by technologies aimed at enhancing Raman signals such as plasmonic nanomaterials in surface enhanced Raman spectroscopy, or coherent Raman techniques.

Conflict of interest

The authors declare that the research was conducted in the absence of any commercial or financial relationships that could be construed as a potential conflict of interest.

Acknowledgments

This work was financially supported by the Natural Sciences and Engineering Research Council of Canada (NSERC), Discovery Grant RGPIN-2018-05675 (to S.W.-H.); M.I. acknowledges the Bolashak International Scholarship for PhD studies; T.R. acknowledges The Sigrid Juselius Foundation, Helsinki, Finland; R.M. and R.P.C. acknowledge funding support from the NIH (1R01CA241666); TMD acknowledges funding support from the Van Berkomp foundation, the CQDM and the McGill Healthy Brains for Healthy Lives. We also acknowledge Dr Carol Chen and Narges Abdian for prior work establishing and profiling the AIW002-02 iPSC used for MBO generation.

References

1. R. J. O'Brien and P. C. Wong, *Annu. Rev. Neurosci.*, 2011, 34, 185 —204.
2. T. A. Bayer, O. Wirths, K. Majtényi, T. Hartmann, G. Multhaup, K. Beyreuther and C. Czech, *Brain Pathol.*, 2001, 11, 1 —11.
3. S. G. Younkin *J. Physiol.*, 1998, 92, 289 —292.
4. L. Rajendran, M. Honsho, T. R. Zahn, P. Keller, K. D. Geiger, P. Verkade and K. Simons, *Proc. Natl. Acad. Sci. U. S. A.*, 2006, 103, 11172 —11177.
5. T. Zheng, J. Pu, Y. Chen, Y. Mao, Z. Guo, H. Pan, L. Zhang, H. Zhang, B. Sun and B. Zhang, *Front. Aging Neurosci.*, 2017, 9, 12.
6. C. Théry, L. Zitvogel and S. Amigorena, *Nat. Rev. Immunol.*, 2002, 2, 569 —579.
7. F. Jansen, G. Nickenig and N. Werner, *Circ. Res.*, 2017, 120, 1649 —1657.
8. R. Kalluri *J. Clin. Invest.*, 2016, 126, 1208 —1215.
9. M.-J. Lee, D.-H. Park and J.-H. Kang, *Ann. Pediatr. Endocrinol. Metab.*, 2016, 21, 119.
10. D. M. Pegtel, L. Peferoen and S. Amor, *Philos. Trans. R. Soc., B*, 2014, 369, 20130516.
11. C. Caruso Bavisotto, F. Scalia, A. Marino Gammazza, D. Carlisi, F. Bucchieri, E. Conway de Macario, A. J. L. Macario, F. Cappello and C. Campanella, *Int. J. Mol. Sci.*, 2019, 20, 434.
12. A. Anel, A. Gallego-Lleyda, D. de Miguel, J. Naval and L. Martínez-Lostao, *Cells*, 2019, 8, 154.
13. L. Tan, H. Wu, Y. Liu, M. Zhao, D. Li and Q. Lu, *Autoimmunity*, 2016, 49, 357 —365.
14. C. Théry et.al., *J. Extracell. Vesicles*, 2018, 7, 1535750.
15. S. A. Bellingham, B. Guo, B. Coleman and A. F. Hill, *Front. Physiol.*, 2012, 3, 124.
16. L. J. Vella, R. A. Sharples, R. M. Nisbet, R. Cappai and A. F. Hill, *Eur. Biophys. J.*, 2008, 37, 323 —332.
17. M. Perrotte, M. Haddad, A. Le Page, E. H. Frost, T. Fulöp and C. Ramassamy, *Neurobiol. Aging*, 2020, 86, 102 —111.

18. D. J. Cha, D. Mengel, M. Mustapic, W. Liu, D. J. Selkoe, D. Kapogiannis, D. Galasko, R. A. Rissman, D. A. Bennett and D. M. Walsh, *Front. Neurosci.*, 2019, 13, 1208.
19. S. A. Bellingham, B. M. Coleman and A. F. Hill, *Nucleic Acids Res.*, 2012, 40 , 10937 —10949.
20. A. F. Hill *J. Neurosci.*, 2019, 39, 9269 —9273.
21. M. Sardar Sinha, A. Ansell-Schultz, L. Civitelli, C. Hildesjö, M. Larsson, L. Lannfelt, M. Ingelsson and M. Hallbeck, *Acta Neuropathol.*, 2018, 136, 41 —56.
22. M. S. Fiandaca, D. Kapogiannis, M. Mapstone, A. Boxer, E. Eitan, J. B. Schwartz, E. L. Abner, R. C. Petersen, H. J. Federoff and B. L. Miller, *J. Alzheimer's Dis.*, 2015, 11, 600-7.e1.
23. D. Kapogiannis, M. Mustapic, M. D. Shardell, S. T. Berkowitz, T. C. Diehl, R. D. Spangler, J. Tran, M. P. Lazaropoulos, S. Chawla, S. Gulyani, E. Eitan, Y. An, C. W. Huang, E. S. Oh, C. G. Lyketsos, S. M. Resnick, E. J. Goetzl and L. Ferrucci, *JAMA Neurol.*, 2019, 76, 1340 —1351.
24. P. Spitzer, L.-M. Mulzer, T. J. Oberstein, L. E. Munoz, P. Lewczuk, J. Kornhuber, M. Herrmann and J. M. Maler, *Sci. Rep.*, 2019, 9, 7089.
25. C. Z. J. Lim, Y. Zhang, Y. Chen, H. Zhao, M. C. Stephenson, N. R. Y. Ho, Y. Chen, J. Chung, A. Reilhac, T. P. Loh, C. L. H. Chen and H. Shao, *Nat. Commun.*, 2019, 10, 1144.
26. D. Bachurski, M. Schuldner, P.-H. Nguyen, A. Malz, K. S. Reiners, P. C. Grenzi, F. Babatz, A. C. Schauss, H. P. Hansen, M. Hallek and E. Pogge von Strandmann, *J. Extracell. Vesicles*, 2019, 8, 1596016.
27. R. Linares, S. Tan, C. Gounou and A. R. Brisson, *Exosomes and Microvesicles*, Springer, 2017, pp. 43–54.
28. S. Sharma, M. LeClaire and J. K. Gimzewski, *Nanotechnology*, 2018, 29, 132001.
29. C. Gardiner, D. D. Vizio, S. Sahoo, C. Théry, K. W. Witwer, M. Wauben and A. F. Hill, *J. Extracell. Vesicles*, 2016, 5, 32945 Search PubMed.
30. M. S. Panagopoulou, A. W. Wark, D. J. S. Birch and C. D. Gregory, *J. Extracell. Vesicles*, 2020, 9, 1710020 Search PubMed.
31. M. P. Bebelman, P. Bun, S. Huvneers, G. van Niel, D. M. Pegtel and F. J. Verweij, *Nat. Protoc.*, 2020, 15, 102 —121.
32. S. Y. Kim, D. Khanal, B. Kalionis and W. Chrzanowski, *Nat. Protoc.*, 2019, 14, 576 —593.
33. T. Rojalin, B. Phong, H. J. Koster and R. P. Carney, 2019, 7.
34. A. Gualerzi, S. A. A. Kooijmans, S. Niada, S. Picciolini, A. T. Brini, G. Camussi and M. Bedoni, *J. Extracell. Vesicles*, 2019, 8, 1568780.
35. G. Devitt, K. Howard, A. Mudher and S. Mahajan, *ACS Chem. Neurosci.*, 2018, 9, 404 —420.
36. Y. An, T. Jin, Y. Zhu, F. Zhang and P. He, *Biosens. Bioelectron.*, 2019, 142, 111503.
37. N. Colthup. *Introduction to infrared and Raman spectroscopy*, Elsevier, 2012.
38. F. Lavialle, S. Deshayes, F. Gonnet, E. Larquet, S. G. Kruglik, N. Boisset, R. Daniel, A. Alfsen and I. Tatischeff, *Int. J. Pharm.*, 2009, 380, 206 —215.
39. Z. J. Smith, C. Lee, T. Rojalin, R. P. Carney, S. Hazari, A. Knudson, K. Lam, H. Saari, E. L. Ibañez, T. Viitala, T. Laaksonen, M. Yliperttula and S. Wachsmann-Hogiu, *J. Extracell. Vesicles*, 2015, 4, 28533.

40. I. Tatischeff, E. Larquet, J. M. Falcón-Pérez, P.-Y. Turpin and S. G. Kruglik, *J. Extracell. Vesicles*, 2012, 1, 19179.
41. C. Krafft, K. Wilhelm, A. Eremin, S. Nestel, N. von Bubnoff, W. Schultze-Seemann, J. Popp and I. Nazarenko, *Nanotechnology, Biology and Medicine*, 2017, 13, 835 —841.
42. W. Lee, A. Nanou, L. Rikkert, F. A. W. Coumans, C. Otto, L. W. M. M. Terstappen and H. L. Offerhaus, *Anal. Chem.*, 2018, 90, 11290 —11296.
43. A. Gualerzi, S. Niada, C. Giannasi, S. Picciolini, C. Morasso, R. Vanna, V. Rossella, M. Masserini, M. Bedoni and F. Ciceri, *Sci. Rep.*, 2017, 7, 1 —11.
44. H. Zhang, A. C. Silva, W. Zhang, H. Rutigliano and A. Zhou, *PloS One*, 2020, 15, e0235214.
45. M. Roman, A. Kamińska, A. Drożdż, M. Platt, M. Kuźniewski, M. T. Małecki, W. M. Kwiatek, C. Paluszkiwicz and E. Ł. Stępień, *Nanotechnology, Biology and Medicine*, 2019, 17, 137 —149.
46. P. Beekman, A. Enciso-Martinez, H. S. Rho, S. P. Pujari, A. Lenferink, H. Zuilhof, L. W. M. M. Terstappen, C. Otto and S. Le Gac, *Lab Chip*, 2019, 19, 2526 —2536.
47. D. Kuroski, R. P. Van Duyne and I. K. Lednev, *Analyst*, 2015, 140, 4967 —4980.
48. D. Röhr, B. D. C. Boon, M. Schuler, K. Kremer, J. J. M. Hoozemans, F. H. Bouwman, S. F. El-Mashtoly, A. Nabers, F. Großerueschkamp, A. J. M. Rozemuller and K. Gerwert, *Acta Neuropathol. Commun.*, 2020, 8, 222.
49. M. Ji, M. Arbel, L. Zhang, C. W. Freudiger, S. S. Hou, D. Lin, X. Yang, B. J. Bacskai and X. S. Xie, *Sci. Adv.*, 2018, 4, eaat7715.
50. N. C. Maiti, M. M. Apetri, M. G. Zagorski, P. R. Carey and V. E. Anderson, *J. Am. Chem. Soc.*, 2004, 126, 2399 —2408.
51. M. M. Apetri, N. C. Maiti, M. G. Zagorski, P. R. Carey and V. E. Anderson, *J. Mol. Biol.*, 2006, 355, 63 —71.
52. G. Ramachandran, E. A. Milán-Garcés, J. B. Udgaonkar and M. Puranik, *Biochemistry*, 2014, 53, 6550 —6565.
53. E. Ryzhikova, O. Kazakov, L. Halamkova, D. Celmins, P. Malone, E. Molho, E. A. Zimmerman and I. K. Lednev, *J. Biophot.*, 2015, 8, 584 —596.
54. C. W. Ong, Z. X. Shen, Y. He, T. Lee and S. H. Tang, *J. Raman Spectrosc.*, 1999, 30, 91 —96.
55. N. Mammadova, C. M. Summers, R. D. Kokemuller, Q. He, S. Ding, T. Baron, C. Yu, R. J. Valentine, D. S. Sakaguchi and A. G. Kanthasamy, *Neurobiol. Dis.*, 2019, 121, 1 —16.
56. M. Paraskevaïdi, C. L. M. Morais, D. E. Halliwell, D. M. A. Mann, D. Allsop, P. L. Martin-Hirsch and F. L. Martin, *ACS Chem. Neurosci.*, 2018, 9, 2786 —2794.
57. A. Huefner, W.-L. Kuan, S. L. Mason, S. Mahajan and R. A. Barker, *Chem. Sci.*, 2020, 11, 525 —533.
58. A. Gualerzi, S. Picciolini, C. Carlomagno, F. Terenzi, S. Ramat, S. Sorbi and M. Bedoni, *Nanotechnology, Biology and Medicine*, 2019, 22, 102097.
59. C. F. Morasso, D. Sproviero, M. C. Mimmi, M. Giannini, S. Gagliardi, R. Vanna, L. Diamanti, S. Bernuzzi, F. Piccotti and M. Truffi, *Nanotechnology, Biology and Medicine*, 2020, 102249.
60. C. Lee, R. P. Carney, S. Hazari, Z. J. Smith, A. Knudson, C. S. Robertson, K. S. Lam and S. Wachsmann-Hogiu, *Nanoscale*, 2015, 7, 9290 —9297.

61. S. Suarasan, J. Liu, M. Imanbekova, T. Rojalín, S. Hilt, J. C. Voss and S. Wachsmann-Hogiu, *J. Mater. Chem. B*, 2020, 8, 8845 —8852.
62. M. Avella-Oliver, R. Puchades, S. Wachsmann-Hogiu and A. Maquieira, *Sens. Actuators, B*, 2017, 252, 657 —662.
63. M. Kahraman, P. Daggumati, O. Kurtulus, E. Seker and S. Wachsmann-Hogiu, *Sci. Rep.*, 2013, 3, 3396.
64. T. Rojalín, H. J. Koster, J. Liu, R. R. Mizenko, D. Tran, S. Wachsmann-Hogiu and R. P. Carney, *ACS Sens.*, 2020, 5, 2820 —2833.
65. B. L. Sopher, K.-i. Fukuchi, A. C. Smith, K. A. Leppig, C. E. Furlong and G. M. Martin, *Mol. Brain Res.*, 1994, 26, 207 —217.
66. N.-V. Mohamed, M. Mathur, R. da Silva, L. Beitel, E. Fon and T. Durcan, *MNI Open Res.*, 2019, 3, 1.
67. Y. Yuana, A. N. Böing, A. E. Grootemaat, E. van der Pol, C. M. Hau, P. Cizmar, E. Buhr, A. Sturk and R. Nieuwland, *J. Extracell. Vesicles*, 2015, 4, 29260.
68. Y. Cheng, Q. Zeng, Q. Han and W. Xia, *Protein Cell*, 2019, 10, 295 —299.
69. E. Valera, R. Dargusch, P. A. Maher and D. Schubert, *J. Neurosci.*, 2013, 33, 10512 —10525.
70. A. Currais, O. Quehenberger, A. M Armando, D. Daugherty, P. Maher and D. Schubert, *npj Aging Mech. Dis.*, 2016, 2, 16012.
71. P. F. Copenhaver, T. S. Anekonda, D. Musashe, K. M. Robinson, J. M. Ramaker, T. L. Swanson, T. L. Wadsworth, D. Kretschmar, R. L. Woltjer and J. F. Quinn, *Dis. Models Mech.*, 2011, 4, 634 —648.
72. K. Laulagnier, C. Motta, S. Hamdi, S. Roy, F. Fauvelle, J.-F. Pageaux, T. Kobayashi, J.-P. Salles, B. Perret, C. Bonnerot and M. Record, *Biochem. J.*, 2004, 380, 161 —171.
73. I. Parolini, C. Federici, C. Raggi, L. Lugini, S. Palleschi, A. De Milito, C. Coscia, E. Iessi, M. Logozzi, A. Molinari, M. Colone, M. Tatti, M. Sargiacomo and S. Fais, *J. Biol. Chem.*, 2009, 284, 34211 —34222.
74. L. Rajendran, M. Honsho, T. R. Zahn, P. Keller, K. D. Geiger, P. Verkade and K. Simons, *Proc. Natl. Acad. Sci.*, 2006, 103, 11172 —11177.
75. M.-S. García-Ayllón, I. Lopez-Font, C. P. Boix, J. Fortea, R. Sánchez-Valle, A. Lleó, J.-L. Molinuevo, H. Zetterberg, K. Blennow and J. Sáez-Valero, *Sci. Rep.*, 2017, 7, 2477.
76. H. Jeong, H. Shin, J. Yi, Y. Park, J. Lee, Y. Gianchandani and J. Park, *Lab Chip*, 2019, 19, 3326 —3336.
77. S. Zou, M. Hou, J. Li, L. Ma and Z. Zhang, *Sci. Rep.*, 2017, 7, 6186.
78. R. Yasukuni, R. Gillibert, M. N. Triba, R. Grinyte, V. Pavlov and M. Lamy de la Chapelle, *Nanophotonics*, 2019, 8, 1477 —1483.
79. B. Hernández, F. Pflüger, S. G. Kruglik and M. Ghomi, *J. Raman Spectrosc.*, 2013, 44, 827 —833.
80. S. K. Teh, W. Zheng, D. P. Lau and Z. Huang, *Analyst*, 2009, 134, 1232 —1239.
81. J. Bandekar *Biochim. Biophys. Acta, Protein Struct. Mol. Enzymol.*, 1992, 1120, 123 —143.
82. S. P. Verma and D. F. H. Wallach, *Biochim. Biophys. Acta, Lipids Lipid Metab.*, 1977, 486, 217 —227.
83. I. Notingher, S. Verrier, S. Haque, J. M. Polak and L. L. Hench, *Biopolymers*, 2003, 72, 230 —240.
84. D. Song, T. Chen, S. Wang, S. Chen, H. Li, F. Yu, J. Zhang and Z. Zhang, *Analyst*, 2020, 145, 626 —635.

85. A. Rygula, K. Majzner, K. M. Marzec, A. Kaczor, M. Pilarczyk and M. Baranska, *J. Raman Spectrosc.*, 2013, 44, 1061 —1076.
86. L. J. Lis, S. C. Goheen, J. W. Kauffman and D. F. Shriver, *Biochim. Biophys. Acta, Nucleic Acids Protein Synth.*, 1976, 443, 331 —338.
87. B. Shivu, S. Seshadri, J. Li, K. A. Oberg, V. N. Uversky and A. L. Fink, *Biochemistry*, 2013, 52, 5176 —5183.
88. M. Coles, W. Bicknell, A. A. Watson, D. P. Fairlie and D. J. Craik, *Biochemistry*, 1998, 37, 11064 —11077.
89. M. Ji, D. A. Orringer, C. W. Freudiger, S. Ramkissoon, X. Liu, D. Lau, A. J. Golby, I. Norton, M. Hayashi and N. Y. R. Agar, *Sci. Transl. Med.*, 2013, 5, 201ra119.
90. I. Anna, P. Bartosz, P. Lech and A. Halina, *Oncotarget*, 2017, 8, 85290.
91. K. Larsson and R. P. Rand, *Biochim. Biophys. Acta, Lipids Lipid Metab.*, 1973, 326, 245 —255.
92. J. Kiskis, H. Fink, L. Nyberg, J. Thyr, J.-Y. Li and A. Enejder, *Sci. Rep.*, 2015, 5, 13489.
93. L. E. Jamieson, A. Li, K. Faulds and D. Graham, *R. Soc. Open Sci.*, 2018, 5, 181483.
94. W. Gibson Wood, G. P. Eckert, U. Igbavboa and W. E. Müller, *Biochim. Biophys. Acta, Biomembr.*, 2003, 1610, 281 —290.
95. J. C. Stroud, C. Liu, P. K. Teng and D. Eisenberg, 2012, 109, 77177722.
96. L. Yu, R. Edalji, J. E. Harlan, T. F. Holzman, A. P. Lopez, B. Labkovsky, H. Hillen, S. Barghorn, U. Ebert, P. L. Richardson, L. Miesbauer, L. Solomon, D. Bartley, K. Walter, R. W. Johnson, P. J. Hajduk and E. T. Olejniczak, *Biochemistry*, 2009, 48, 1870 —1877.
97. E. Cerf, R. Sarroukh, S. Tamamizu-Kato, L. Breydo, S. Derclaye, Y. F. Dufrière, V. Narayanaswami, E. Goormaghtigh, J. M. Ruyschaert and V. Raussens, *Biochem. J.*, 2009, 421, 415 —423.
98. A. Abedini and D. P. Raleigh, *Phys. Biol.*, 2009, 6, 015005.

Chapter VI. Discussion

The comprehensive literature review presented in Chapter II shows that optical label-free methods are currently complementary to conventional EV characterization methods. The anticipation of the usage of both conventional technologies and emerging novel methods is important especially when the users need to analyze complex analytes such as EVs.

Label-free optical methodologies enhance the growing field of EV research by providing effective tools for disease specific biomarkers discovery and simultaneous detection of multiple markers of disease specific molecular fingerprints in small volumes of samples. In the EV research field NTA, SPR, and flow cytometry gained the most popularity among optical label-free technologies¹. EV morphological features such as size, shape, and concentration as well as their biochemical content have been most successfully characterized using label-free optical technologies. Furthermore, these technologies have been used for the detection of EV-associated markers of cancer and neurological disorders¹.

EVs exhibit a biocorona which consists of proteins and other molecules. It is a fragile outer shell that surrounds EVs and is proposed to be an external cargo or natural component of EVs¹⁰⁶. It has been suggested that it may play an important role in EV function¹⁰⁷. The thickness of the EV biocorona in one study is found to be approximately 5.3 nm \pm 0.3 nm and is enriched with apolipoproteins, immunoglobulins, albumin, proteoglycans, heparin-binding proteins^{106, 108-110}. Electrostatic and thiol interactions, as well as the surrounding media, affects the formation of EV biocorona^{110, 111}. Current technologies that are used for EV isolation and analysis may disrupt EVs biocorona and essential information it carries^{107, 112}. Hence, it is important to apply methods that have minimal impact on a sample such as optical label-free technologies including Raman spectroscopy and SERS. The non-destructive feature of these technologies, with appropriate sample preparation, may reveal components of biocorona and allow assessment and differentiation of EV internal cargo from components of biocorona.

A further exciting opportunity these new technologies can provide is classification of EVs into subpopulations, that may reveal heterogeneity of EVs and advance our knowledge of EVs functions in health and disease. The limited characterization capabilities of traditional bulk

characterization methodologies make analysis of complex EV heterogeneity challenging. Bulk EV characterization methodologies offer an overall view of EVs present in a sample and are not suitable for EV subpopulations characterization. Identification and analysis of different EV subpopulations, and variations between these subpopulations, may shine light on the genesis and origin of EVs present in a sample. This analysis is important to better understand the role of EVs in the normal physiology and pathology of the disease. Furthermore, standardization of isolation protocols, processing, and analysis methods for different subpopulations of EVs would be a substantial benefit to the field, leading to consistent and accurate results. Determining EVs as clinical biomarkers and the subsequent development of clinical guidelines requires quantitative methods of analysis. However, differentiation between the accuracy of a specific biosensing technique and the accuracy of the EVs themselves as biomarkers of pathology is not always possible to establish. This ambiguity is a key obstacle to use EVs in clinical settings. A lot of effort has been made to establish EV-associated biomarkers of disease. To date, there is only one EV-based biomarker test that has been approved by public health authorities. The ExoDX prostate cancer test is used for diagnosis of prostate cancer in men with elevated prostate specific antigen. The test utilizes exosomal RNA and DNA level to assess the risk of cancer development and further necessity to perform prostate biopsy. This technology is an advancement in prostate cancer diagnosis. The challenge is to establish EV-associated biomarkers for other cancer types and neurological disorders.

Another challenge that needs to be discussed in regard to EV characterization methodologies is the analysis of the acquired datasets. The importance of this analysis lies on providing valuable predictive information. One of the promising, emerging approaches to detect key features in large data sets and classify EV samples as well as discriminate EV subpopulations is machine learning (ML). ML algorithms have been employed for classifying clinical samples as well as for investigating underlying patterns of large and complex datasets that are typically encountered in heterogeneous EVs samples. For instance, microscopy images^{113, 114}, spectral data from Raman spectroscopy¹¹⁵⁻¹¹⁷ and SERS^{118, 119}, proteomic¹²⁰, and genomic data¹²¹ are all analyzed and processed into various clusters and subpopulations. Both supervised and unsupervised ML algorithms have been applied in EV research. The supervised algorithms are trained on datasets where each training example is explicitly labeled with its corresponding output value. This is

specifically useful in clinical cases, where diagnostic criteria or biomarkers are known, and the objective is a predictive model. Notably, these ML models have been utilized for the analysis of EV-associated molecules related to cancer¹²²⁻¹²⁷ and neurodegenerative diseases^{120, 128, 129}. Unsupervised ML algorithms are not trained on pre-labeled datasets and therefore the operators must interpret data patterns on their own. PCA, K-Means clustering, and hierarchical clustering are examples of unsupervised ML that are used in EV research^{130, 131, 132}. The most appealing aspect of unsupervised learning is the possibility to discover previously unknown underlying patterns within datasets that can be identified without human input. This approach is particularly beneficial in biomarker discovery studies. Another approach that is less common in the EV research field is semi-supervised ML analysis. It combines labeled and unlabeled data to construct a learning model and is typically used when a dataset contains predominantly unlabeled data.

ML includes a subclass that utilizes neural networks for processing large-scale data sets termed deep learning (DL). In DL, created layers mimic the interconnection of neurons in the human brain. This approach has been applied to develop predictive classification models with the ability to make more “human-like” decisions. The application of DL in EV research is less common. One of the examples using DL is a recent study by Shin et al. that classified cancer EVs from healthy patients’ derived EVs¹³³. The SERS spectra-trained DL algorithms were able to stratify lung cancer cell line EVs from human pulmonary alveolar epithelial cell line EVs, that are considered as a healthy control in this study, with 95% accuracy and as healthy control EVs and was able to stratify them. Moreover, the developed DL model is tested using EVs isolated clinical samples and was able to predict lung cancer for all patients (stages 1A, 1B, and 2B) with an AUC of 0.912. Interestingly, for stage 1 patients lung cancer is predicted with an AUC of 0.910. This demonstrates the potential for early-stage noninvasive diagnostics.

Overall, despite many challenges, the field of label-free optical methods for EV characterization will grow in significance and offer new tools and possibilities for liquid biopsy applications, biomarker discovery, standardized sample handling and isolation, technological improvements in optics, and advanced data analysis methodologies. Integration of ML and DL into further studies

of EV subpopulations is an important avenue to determine clinically viable diagnostic methods based on optical label-free techniques.

6.1 Morphological and biochemical characterization of micro- and nanoparticles including EVs using developed techniques.

The next part of the discussion section is dedicated to the original research articles that demonstrate morphological and biochemical characterization of micro- and nanoparticles.

The lens-free dark-field microscopy directly on a CMOS sensor is a novel technique that, in accordance with the Fresnel equations of reflection, results contrast reversal. The images of the objects acquired using this technique are similar to ones acquired using traditional dark-field microscopy. Specifically, a larger fraction of light intensity is reflected when the incident light propagates at angles of illumination close to 90° from a medium with a lower refractive index (such as air) to a higher refractive index (such as plastic). The background recorded by the CMOS sensor depends directly on the intensity of reflected light. The low background intensities observed when most of the incident light is reflected. The images of the objects using this dark-field mode have reversal of the contrast of the object when opposed to the images recorded using bright field illumination mode. The proof-of-concept experiments using polystyrene beads with size ranging from $1.6\ \mu\text{m}$ to $7\ \mu\text{m}$ show a three- to four-fold reduction of the background at illumination angles close to 90° vs. 0° . The surface geometry of the imaging sensor may affect the reflectance. The flattening of the CMOS imaging surface by chemical or physical methods is expected to improve the background reduction factor.

Next, interesting modality that is developed as a part of RDFM platform is shadow-based measurements of object's height. Illuminating the polystyrene spheres of various size at oblique angles ranging between 0° and 85° result in a formation of the objects' geometrical shadow. Using simple geometrical calculations, we are able to quantify approximate height of the polystyrene spheres based on their geometrical shadows.

The results of proof-of-concept experiments encouraged us to apply the RDFM technology for analysis of biological samples. For this, single cells of *E. gracilis* algae were imaged in both shadow and dark-field microscopy modes. The obtained images allow for the calculation of *E.*

gracilis approximate height (~5 μm) and length (10-11 μm) that is found to be true to the size of the microorganism determined by other microscopy techniques¹³⁴. Moreover, the RDFM method enabled quantification of 3D morphological features within large clusters of *E. gracilis*. The analysis of *S. epidermidis* cells that typically smaller than *E. gracilis* cells further validated the use of the platform for detecting and quantifying small, micrometer-sized biological objects.

In the EV research field RDFM methodology can be applied for detection and characterization of morphological features of EVs such as size and shape. These morphological features are currently characterized using various traditional methods such as NTA, AFM, EM, etc. The RDFM complements these techniques and offers morphological analysis of EVs at lower cost, with relatively simple experimental set-up. At this point of time, the platform is able to analyse large vesicles or clusters of small vesicles. However, improvements in optical technologies and the subsequent reduction of imaging sensors' pixel size may allow the application of RDFM for small EV characterization. Additionally, the drying of EVs on the surface of the imaging sensor may affect the morphological features of EVs. The change in morphology of EVs due to fixation is observed during TEM when EVs are fixed on the surface of the carbon grid. The resulting images show cup-shaped morphology as an artefact of EV dehydration¹³⁵. This shortcoming needs to be addressed in future studies by possible incorporating the microfluidic chip onto the CMOS sensor.

In addition to EV analysis, RDFM can be useful in cancer research to understand different states of cancerous cells based on the variability in cellular thickness and cytoplasm-to-nucleus ratios that subsequently result in morphological differences and changes in cell mechanics¹³⁶. These alterations in cell morphology occur particularly during metastasis, tissue generation, and cancer cell-drug molecule interactions^{137, 138}. These effects are challenging to be axially resolved for large FOV using a conventional microscopy technique without fluorescence or even with fluorescence require confocal microscopy with extensive image post-processing and sample labeling¹³⁹. In addition, quantitative phase imaging (QPI) is used to characterize morphological alterations of the cancer cells. The QPI, unlike most of the conventional techniques microscopy techniques used in cancer research, can analyse live and unlabeled cells¹⁴⁰. Nevertheless, the need to perform image-post processing, in addition to the extensive image acquisition process

and the high cost of the equipment, limits the application of the QPI method. The RDFM technique would fall in line with similar 3D on-chip imaging technologies that have been applied for the morphological characterization of cells¹⁴¹.

Overall, the RDFM technology enables morphological analysis of unstained, dried, or fixed biological and non-biological objects with a high spatial resolution (limited to the pixel size) and large field-of-view imaging. The low cost and simplicity of the technique opens up opportunities for its implementation in low-resource environments for biological, medical, food safety, or environmental monitoring applications. The large field-of-view, coupled with the high spatial resolution and improved contrast, makes the system applicable in the pathology field for the imaging of large, fixed (stained or unstained) thin tissue sections or blood or cell culture smears.

Another useful approach that is introduced in this thesis is a size-based trapping, imaging and biochemical characterization of small particles including EVs and polystyrene spheres *via* CMOS TrICC technology. Our theoretical and experimental results demonstrate the presence of hot spots localized in the confined spaces between interconnected microlenses. Previously reported studies support our findings and show that high and uniform SERS enhancement is observed in SERS substrates with periodic arrays of closely spaced nanostructures. On the other hand, SERS substrates with randomly structured surfaces exhibit lower signal enhancement⁵². The coating of a CMOS imaging sensor surface with a thin layer of silver (40 nm) creates plasmonic hot spots between microlenses and allows high amplification of the Raman scattering signal of the EVs. In addition, the observed overall Raman enhancement may have contribution of the lightning rod effect in the funnel-like structures⁵³. Moreover, a higher SERS enhancement can also be explained by minimized⁵⁴ retardation or damping effects for EM fields created in nanogaps within the quasistatic limit⁵⁵.

The hot spots serve both for capturing and biochemical characterization of EVs and other particles of interest. The AFM measurements revealed that their size is approximately 300 nm. This means that only a single or a few EVs could fit in this region that is otherwise also the volume with the highest SERS enhancement. One may argue that bigger particles may concentrate and cover the nanogaps containing EVs such that the signal represents the biochemical content of larger particles as well. However, due to the nature of SERS

enhancement that occurs in close proximity to the plasmonic material, particles that are larger than the size of nanogaps have minimal or no interference to EV SERS signal¹⁷. Previous studies have applied similar concepts of SERS characterization of EVs using nanoplasmonic materials that allow SERS characterization of EVs that fall in the nanogaps between gold nanorods³¹, porous nanoplasmonic scaffolds^{33, 57}, and array of gold-covered graphene pyramids⁵⁸.

Another important characteristic of the hot spots created between adjacent microlenses is their large volumes (extending in the z dimension) that may potentially allow for the probing of molecules that are located at a longer distance from the SERS substrate surface, such as EV intraluminal cargo. This is supported in our measurements of small volumes of brain organoids EVs by detection of specific peaks centered at 1345 cm^{-1} that correlate to nucleic acids vibrational modes⁴⁶ which are mainly part of the intraluminal cargo of EVs⁵⁶. Analysis of SERS spectra in the “fingerprint region” and “high-wavenumber region” revealed chemical constituents typical for both EV membrane and intraluminal content (proteins, lipids, and nucleic acids), and therefore validated the presence of EVs trapped within nanocavities.

Finally, attempts to combine SERS and optical microscopy in one platform have been reported previously, mostly by utilizing research-grade microscopes, which operate on a trade-off mode between spatial resolution and field of view⁹. One recent example is simultaneous SERS measurements and Stochastic Optical Reconstruction Microscopy (STORM) of biological structures and microorganisms⁵⁹⁻⁶¹, which reports high spatial resolution (<50 nm) and chemical information of the analyte but is limited in terms of field of view. The technique is also complex, requires the acquisition of multiple images, and uses computing-intensive image reconstruction algorithms. In our study, the coating of the CMOS imaging sensor with a silver layer did not affect its performance and imaging functions were maintained. The approach is based on lensless imaging with a spatial resolution limited by the pixel size and a field of view limited only by the size of the sensor (as high as 1 cm). We are able to record images of polystyrene beads and dried droplet of EVs. While this modality remains to be explored in the EV analysis settings, we believe that the RDFM technology may allow morphology characterization in addition to chemical analysis. In addition, this device does not need external lenses, can be miniaturized, and is designed to operate in point-of-need applications.

Going beyond EV analysis, combining imaging with SERS on the same platform may enable recording optical microscopy and chemical images of analytes of interest (such as molecules related to infectious diseases, pathogens, food safety, and other applications) placed directly on its surface. This opens up new directions towards biosensor development.

6.2 Optical label-free technologies for identification of EV-associated disease biomarkers

A biomarker as defined by the National Institute of Health is “a characteristic that is objectively measured and evaluated as an indicator of normal biological processes, pathogenic processes, or pharmacological responses to therapeutical intervention”. The development of EV-based biomarkers for diagnosis of cancer and neurological conditions is showing great promise. However, translating laboratory-based findings to the clinic remains challenging. This transition requires the advancement of isolation and analytical methodologies that will enable rapid results acquired in a high-throughput manner. AD is a neurodegenerative disease that remains challenging to diagnose in the early stages. This prognostic uncertainty of existing diagnostic methods in combination with the high costs and invasiveness of current diagnostic procedures further emphasizes the importance of developing sensitive and accurate alternative tests for early AD diagnosis. Moreover, in clinical settings, it is desirable to apply analytical methods that enable sensitive quantification of EVs from small volumes of biofluid. One such method is Raman spectroscopy. Therefore, one of the goals of the thesis was to explore the use of Raman spectroscopy to detect sEV-associated biomarker of AD, A β protein.

In cases when it is necessary to perform analysis of EVs in liquid, one must consider difficulties associated with such measurements. First, the measurement of the Raman spectra of sEVs in liquid presents difficulties due to their Brownian motion, which will cause particles to travel in and out of the laser beam, reducing signal-to-noise ratio. In addition, the laser beam may push particles out of the focal region due to the momentum of incident photons. Another important experimental parameter is the wavelength of the laser. In this thesis two different wavelength are used to collect Raman spectra from probe molecules and EVs. The main explanation for this variety of the choice is determined by the substrate on which samples are placed. Existing literature shows use of the large variety of the substrates including CaF₂ and quartz substrates, and glass substates. SERS spectra of probe molecules placed on a CaF₂ shown in Chapter IV is

collected using 785 nm excitation. The Chapter V introduces Raman spectra of EVs placed on a glass substrate. To minimize glass background, we used 633 nm excitation laser. post-processing background subtraction.

Our results show a clear difference between biochemical profile of sEVs associated with A β compared to the control sEVs groups. The similarity of the intense peaks at 1650 cm⁻¹ and 2930 cm⁻¹ in TC- sEVs Raman spectra to the same peaks in the spectra of pure A β protein indicate the presence of A β protein. On the contrary, the Raman spectra of TC+ sEVs and osEVs exhibit less intense or lacking bands at these positions. The Amide I region of the Raman spectra of sEVs has additional contributions from other proteins in sEV cargo and low signal-to-noise ratio. The “high-wavenumber region” on the other hand, shows strong protein peaks and a high signal-to-noise ratio. The use of unsupervised machine learning algorithms such as PCA in this study is justified by its ability to recognize unknown patterns in the Raman data that is associated to changes in EV molecular cargo isolated from AD cell culture model. Moreover, this approach reduces dimensionality of the large and complex Raman data without the loss of its accuracy.

The conducted study required validation of the A β presence within sEVs. For this, we first performed a theoretical evaluation of the A β concentration within a laser spot. We based our calculations on an A β concentration within EVs published earlier by Fiandaca et al^{89, 142}. By dividing the A β concentration (expressed in pg/ml) by the number of EVs per ml, we determined the mass of A β ₄₂ per sEV. Using Avogadro’s number, we converted the moles of A β to the number of molecules per sEVs. To estimate the concentration of the A β ₄₂ protein in TC- sEVs, we used values found in the aforementioned study. Specifically, the concentration of A β ₄₂ in EVs isolated from AD patients (n=3) was determined by ELISA and reported to be 18.5 pg/ml in EVs (2.78×10⁹ particles/ml). EVs isolated from healthy individuals (n=3) had lower concentrations of EV-associated A β ₄₂ (0.83 pg/ml in EVs (3.49×10⁹ particles/ml)). The concentration of the A β ₄₂ protein is obtained from the analysis of healthy controls and was used to calculate the protein concentration in TC+ sEVs and osEVs. The calculated number of molecules per EV was as follows: TC- sEVs – ~885 A β molecules/sEV, TC+ - ~31.5 molecules/sEV, and osEVs - ~30 molecules/sEV. Subsequently, we calculated the number of sEVs for each group in the laser spot. The estimated number of A β molecules in the laser beam spot is 6.8×10⁵ A β molecules for

TC- sEVs, 2.1×10^2 A β molecules for TC+ sEV, and 1.7×10^2 A β molecules for osEVs. The differences of Raman intensities in Raman spectra collected from TC- sEVs compared to control EV groups support our estimations. It is expected that TC- sEVs and TC+ sEVs have similar composition as they were isolated from the same cell culture. We hypothesised that the major variability between these EV groups will be the presence of A β in TC-sEVs because they were collected when MC65 cells were overexpressing A β . This variation is identified by Raman spectroscopy that reflects linearly the number of molecules in the analyte to Raman intensities.

In addition, our results show that A β associated with sEVs is in an α -helical conformational form and in the size of a monomer or a small oligomer. This is important because the process of transformation of the monomers into toxic oligomers has been shown to be structure dependent. Moreover, these findings may shine a light on a potential mechanism of propagation of neurodegeneration by sEVs carrying toxic oligomers as there is no consensus in the field regarding the structure of the toxic oligomers. Specifically, it has been noted that toxic oligomers, as well as A β fibrils, have a β -sheet enriched secondary structure that provides a high adherence site for further fibrillation¹⁴³⁻¹⁴⁵. Conversely, several studies showed that early oligomers of A β and α -synuclein have an α -helical secondary structure and are prompted by helix-helix interactions^{146, 147}. This knowledge, and our results, further suggest that sEVs may be involved in toxic oligomers spread within the neurons in CNS.

Next interesting observation is the potential affect of the A β on the EV membrane fluidity. The analysis of Raman spectra shows differences in the lipid structures of sEVs. The control sEVs groups, TC+ sEVs, and osEVs, are prevalent in lipids with longer fatty acid chains. On the other hand, TC- sEVs have lipids with shorter fatty acid chain lengths. Since the main difference between TC- sEVs and TC+ sEVs is the presence of the A β protein, it can be suggested that the association of A β protein with plasma membrane alters plasma membrane fluidity. The plasma membrane fluidity depends on several factors, such as degree of fatty acids saturation, length of fatty acid tail, cholesterol content, and temperature. Specifically, the lengths of fatty acids tails affect the membrane rigidity by creating intermolecular interactions between phospholipid tails. In the case of TC- sEVs we observe a two-fold reduction of the chain length, and as a result, a potential increase in membrane fluidity. However, the cause of this phenomenon remains to be explored. One possible explanation for the increased EV membrane fluidity is the formation of

transmembrane oligomeric pore structures that are proposed to occur with the peptide's interaction with the EV plasma membrane. In addition, the length of the fatty acid chain shortens with an increase in temperature. However, this parameter should not affect our results since sEVs from all three groups were analyzed under the same experimental conditions.

We also performed mass spectrometry analysis of sEVs. Mass spectrometry identified APP peptides in both TC- and TC+ sEVs. However, A β ₄₂ peptide is detected only in TC-sEVs. The proteins of amyloidogenic pathway, such as ADAM 10, ADAM TS4, SORL1 and gamma secretase subunit (nicastrin), are detected in TC-sEVs and absent in TC+ sEVs¹⁴⁸⁻¹⁵⁰. The enzymes of tau cleavage, such as glycogen synthase kinase-3 beta, are also detected¹⁵¹. Additionally, the EV markers such as TSG101, CD81, syntenin-1, HSP 70, HSP 90, annexin VII, annexin XI, Rab5 and Rab7 GTPases indicate the endosomal origin of the analysed EVs^{152, 153}. The presence of annexin A, fibronectin, actin, tubulin and Rab11 suggest co-isolation of large EVs such as microvesicles¹⁵⁴.

Overall, our results confirm the hypothesis of the thesis and show that A β protein is present in sEVs and can be detected *via* Raman spectroscopy. Moreover, our study uncovered the role of A β protein in plasma membrane fluidity, paving the way for other studies on this topic. Future studies, using clinical samples of AD patients, will be necessary to demonstrate the potential of sEVs for early AD diagnosis. Analysis of the sEVs derived from AD patients and healthy controls *via* Raman spectroscopy may indicate spectral biomarkers that correlate to the development of AD. The analysis of molecular conformation of sEV-associated A β protein is particularly important in understanding the role of sEVs in the propagation of neurodegeneration as it has been previously proposed in the literature. Raman spectroscopy analysis of sEVs from isolated from clinical samples may enable to explore potential pathologies underlying AD, other than misfolded proteins and their conformers. For instance, a comparison of the metal ions' contents in EVs has been shown to correlate with aggregation of A β protein and deposition of plaques. Moreover, another area of great interest is exploring lipidomic changes that may contribute to the disease development and may potentially be detected in EV molecular content *via* Raman spectroscopy. The main drawback of the technique that limits its translation to clinic is the relatively low Raman signal. Nonetheless, this limitation can potentially be addressed by technologies aimed at enhancing Raman signals such as plasmonic nanomaterials in surface-

enhanced Raman spectroscopy, or coherent Raman techniques. For example, CMOS-TrICC can be further applied for characterization of A β -associated EVs. and may provide higher sensitivity analysis of low copy number molecule such as EV membrane-associated A β . Moreover, ability for size-based trapping of EVs may reveal information about EV heterogeneity and its relevance to the A β .

Another shortcoming of the technique is its inability to specifically detect the molecules of interest. Discrimination of EV-associated molecules from isolation impurities is another challenge that needs to be considered by a researcher while planning the experimental setup of a study. This problem mostly occurs when the target of the analysis is membrane-bound molecules and does not significantly affect characterization of intravesicular molecules.

7. Conclusions and outlook

Together with increased interest in EVs as mediators of cell-cell communication and disease markers, an increase in the technological advancement for the characterization of their molecular cargo is expected. To date, most of the traditional EV characterization methods that perform bulk assessment of EV content are invasive and require a large volume of samples. Therefore, the implementation of efficient methods for non-destructive single/few EV characterization could facilitate further advancements in the understanding of EV biology, functions, and application.

Herein, this thesis presents novel, label-free optical approaches for EV molecular characterization and validates the use of Raman spectroscopy for the identification of EV-associated A β . The small amounts of samples required, the non-invasive label-free detection, sensitivity, and cost convenience of the introduced methodologies, as well as the crucial ability to trap EVs for further analysis, make them advantageous in EV research.

The current state of the developed technologies is limited by spatial resolution and dry sample analysis. The resolution of the CMOS TrICC system is determined by the pixel size of the CMOS imaging sensor and currently is 1.4 μm . At this point, large EVs and clusters of sEVs can be visualized and characterized. However, we believe that with advancements in optical instrumentation, it will be feasible to characterize small EVs. The approach does not require staining, labeling or large volumes of a sample, which makes it appealing for the EV research

field. Other advantages of the technology are its straightforward sample preparation, and its low cost mainly due to the inexpensive CMOS imaging sensor and custom-built multi-angle illumination stage.

Another limitation of the describe technologies is a necessity to immobilize the samples including EVs, polystyrene spheres and microorganisms by air drying them on the surface of the substrate. This method enables additional *in situ* separation of small EVs from large EVs and isolation contaminants. It also allows size-based separation of EVs due to convective currents inside the droplet that cause concentration of small particles on the edge of drying droplet. On the other hand, the large particles are condensed in the middle of the dried droplet. While this approach of sample processing provides a stable, reproducible way of measuring Raman spectra of EVs, certain experimental settings may require analysis of EVs in liquid samples, as being closer to physiological conditions. While these opportunities for the developed methodologies remain to be explored, we believe the integration of microfluidic technologies is one of the possible ways to make liquid measurements feasible.

With further advancements in optical technologies such as reduction of the signal to noise ratio of the spectrometers; reduction of the pixel size of the CMOS imaging sensors; improvement of a quantum efficiency of the imaging devices including CCD and CMOS sensors; increased spectral resolution of the Raman spectrometer; will only increase efficacy of the developed platforms.

I foresee that the emphasis of future developments will be on the advancements of non-invasive and non-destructive methods for EV biology characterization. Therefore, the next step will be the adaptation of the newly developed technologies for the characterization of EVs in physiological conditions.

Another important aspect of further development is understanding EV heterogeneity. CMOS-TrICC technology has a great potential to be applied in this particular research direction to explore EV heterogeneity in terms of size and shape, and chemical content. Recent publications highlight the differences in the EV size and their protein cargo, showing that larger EVs have lower total protein amount compared to small EVs¹⁵⁵.

Moreover, potential pathologies underlying AD other than misfolded proteins and their conformers can be explored *via* Raman spectroscopy and SERS in sEVs from clinical samples. For instance, exploring lipidomic changes that may contribute to the disease development and may potentially be detected in EVs molecular content.

In addition, coupling these platforms and other optical label-free methods with Big Data Analysis methods and machine learning algorithms will ultimately broaden the application capabilities to preclinical and clinical studies of EVs. Therefore, we foresee a leading role of these methodologies in future EV research.

Reference list

1. Imanbekova, M.; Suarasan, S.; Lu, Y.; Jurchuk, S.; Wachsmann-Hogiu, S., Recent advances in optical label-free characterization of extracellular vesicles. *Nanophotonics* **2022**.
2. Imanbekova, M.; Perumal, A. S.; Kheireddine, S.; Nicolau, D. V.; Wachsmann-Hogiu, S., Lensless, reflection-based dark-field microscopy (RDFM) on a CMOS chip. *Biomed Opt Express* **2020**, *11* (9), 4942-4959.
3. Imanbekova, M.; Saridag, A. M.; Kahraman, M.; Liu, J.; Caglayan, H.; Wachsmann-Hogiu, S., Complementary Metal-Oxide-Semiconductor-Based Sensing Platform for Trapping, Imaging, and Chemical Characterization of Biological Samples. *ACS Applied Optical Materials* **2022**.
4. Imanbekova, M.; Suarasan, S.; Rojalin, T.; Mizenko, R. R.; Hilt, S.; Mathur, M.; Lepine, P.; Nicouleau, M.; Mohamed, N.-V.; Durcan, T. M.; Carney, R. P.; Voss, J. C.; Wachsmann-Hogiu, S., Identification of amyloid beta in small extracellular vesicles via Raman spectroscopy. *Nanoscale Advances* **2021**, *3* (14), 4119-4132.
5. Mathieu, M.; Martin-Jaular, L.; Lavieu, G.; Théry, C., Specificities of secretion and uptake of exosomes and other extracellular vesicles for cell-to-cell communication. *Nature cell biology* **2019**, *21* (1), 9-17.
6. Zaborowski, M. P.; Balaj, L.; Breakefield, X. O.; Lai, C. P., Extracellular Vesicles: Composition, Biological Relevance, and Methods of Study. *BioScience* **2015**, *65* (8), 783-797.
7. Yáñez-Mó, M.; Siljander, P. R. M.; Andreu, Z.; Bedina Zavec, A.; Borràs, F. E.; Buzas, E. I.; Buzas, K.; Casal, E.; Cappello, F.; Carvalho, J.; Colás, E.; Cordeiro-da Silva, A.; Fais, S.; Falcon-Perez, J. M.; Ghobrial, I. M.; Giebel, B.; Gimona, M.; Graner, M.; Gursel, I.; Gursel, M.; Heegaard, N. H. H.; Hendrix, A.; Kierulf, P.; Kokubun, K.; Kosanovic, M.; Kralj-Iglic, V.; Krämer-Albers, E.-M.; Laitinen, S.; Lässer, C.; Lener, T.; Ligeti, E.; Linē, A.; Lipps, G.; Llorente, A.; Lötval, J.; Manček-Keber, M.; Marcilla, A.; Mittelbrunn, M.; Nazarenko, I.; Nolte-‘t Hoen, E. N. M.; Nyman, T. A.; O'Driscoll, L.; Olivan, M.; Oliveira, C.; Pállinger, É.; del Portillo, H. A.; Reventós, J.; Rigau, M.; Rohde, E.; Sammar, M.; Sánchez-Madrid, F.; Santarém, N.; Schallmoser, K.; Stampe Ostenfeld, M.; Stoorvogel, W.; Stukelj, R.; Van der Grein, S. G.; Helena Vasconcelos, M.; Wauben, M. H. M.; De Wever, O., Biological properties of extracellular vesicles and their physiological functions. *J Extracell Vesicles* **2015**, *4* (1), 27066.
8. van Niel, G.; D'Angelo, G.; Raposo, G., Shedding light on the cell biology of extracellular vesicles. *Nature Reviews Molecular Cell Biology* **2018**, *19*, 213.
9. Stahl, P. D.; Raposo, G., Extracellular Vesicles: Exosomes and Microvesicles, Integrators of Homeostasis. *Physiology* **2019**, *34* (3), 169-177.
10. Anand, S.; Samuel, M.; Kumar, S.; Mathivanan, S., Ticket to a bubble ride: Cargo sorting into exosomes and extracellular vesicles. *Biochimica et Biophysica Acta (BBA) - Proteins and Proteomics* **2019**, *1867* (12), 140203.
11. Battistelli, M.; Falcieri, E., Apoptotic Bodies: Particular Extracellular Vesicles Involved in Intercellular Communication. *Biology (Basel)* **2020**, *9* (1).

12. Malkin, E. Z.; Bratman, S. V., Bioactive DNA from extracellular vesicles and particles. *Cell Death & Disease* **2020**, *11* (7), 584.
13. Raposo, G.; Stoorvogel, W., Extracellular vesicles: Exosomes, microvesicles, and friends. *Journal of Cell Biology* **2013**, *200* (4), 373-383.
14. Skotland, T.; Sagini, K.; Sandvig, K.; Llorente, A., An emerging focus on lipids in extracellular vesicles. *Adv Drug Deliv Rev* **2020**, *159*, 308-321.
15. Crescitelli, R.; Lässer, C.; Szabó, T. G.; Kittel, A.; Eldh, M.; Dianzani, I.; Buzás, E. I.; Lötvall, J., Distinct RNA profiles in subpopulations of extracellular vesicles: apoptotic bodies, microvesicles and exosomes. *J Extracell Vesicles* **2013**, *2* (1), 20677.
16. Caruso, S.; Poon, I. K., Apoptotic cell-derived extracellular vesicles: more than just debris. *Frontiers in immunology* **2018**, *9*, 1486.
17. Raposo, G.; Stahl, P. D., Extracellular vesicles: a new communication paradigm? *Nature Reviews Molecular Cell Biology* **2019**, *20* (9), 509-510.
18. Ratajczak, J.; Miekus, K.; Kucia, M.; Zhang, J.; Reca, R.; Dvorak, P.; Ratajczak, M., Embryonic stem cell-derived microvesicles reprogram hematopoietic progenitors: evidence for horizontal transfer of mRNA and protein delivery. *Leukemia* **2006**, *20* (5), 847-856.
19. Valadi, H.; Ekström, K.; Bossios, A.; Sjöstrand, M.; Lee, J. J.; Lötvall, J. O., Exosome-mediated transfer of mRNAs and microRNAs is a novel mechanism of genetic exchange between cells. *Nature cell biology* **2007**, *9* (6), 654-659.
20. Skog, J.; Würdinger, T.; Van Rijn, S.; Meijer, D. H.; Gainche, L.; Curry, W. T.; Carter, B. S.; Krichevsky, A. M.; Breakefield, X. O., Glioblastoma microvesicles transport RNA and proteins that promote tumour growth and provide diagnostic biomarkers. *Nature cell biology* **2008**, *10* (12), 1470-1476.
21. van Niel, G.; Carter, D. R. F.; Clayton, A.; Lambert, D. W.; Raposo, G.; Vader, P., Challenges and directions in studying cell–cell communication by extracellular vesicles. *Nature Reviews Molecular Cell Biology* **2022**, *23* (5), 369-382.
22. Muralidharan-Chari, V.; Clancy, J. W.; Sedgwick, A.; D'Souza-Schorey, C., Microvesicles: mediators of extracellular communication during cancer progression. *J Cell Sci* **2010**, *123* (Pt 10), 1603-11.
23. Jansen, F.; Nickenig, G.; Werner, N., Extracellular vesicles in cardiovascular disease: potential applications in diagnosis, prognosis, and epidemiology. *Circulation research* **2017**, *120* (10), 1649-1657.
24. Dujardin, S.; Bégard, S.; Caillierez, R.; Lachaud, C.; Delattre, L.; Carrier, S.; Loyens, A.; Galas, M. C.; Bousset, L.; Melki, R.; Aurégan, G.; Hantraye, P.; Brouillet, E.; Buée, L.; Colin, M., Ectosomes: a new mechanism for non-exosomal secretion of tau protein. *PLoS One* **2014**, *9* (6), e100760.
25. Joshi, P.; Turola, E.; Ruiz, A.; Bergami, A.; Libera, D. D.; Benussi, L.; Giussani, P.; Magnani, G.; Comi, G.; Legname, G.; Ghidoni, R.; Furlan, R.; Matteoli, M.; Verderio, C., Microglia convert aggregated amyloid- β into neurotoxic forms through the shedding of microvesicles. *Cell Death Differ* **2014**, *21* (4), 582-93.

26. Schiller, M.; Parcina, M.; Heyder, P.; Foermer, S.; Ostrop, J.; Leo, A.; Heeg, K.; Herrmann, M.; Lorenz, H. M.; Bekeredjian-Ding, I., Induction of type I IFN is a physiological immune reaction to apoptotic cell-derived membrane microparticles. *J Immunol* **2012**, *189* (4), 1747-56.
27. Schiller, M.; Bekeredjian-Ding, I.; Heyder, P.; Blank, N.; Ho, A. D.; Lorenz, H. M., Autoantigens are translocated into small apoptotic bodies during early stages of apoptosis. *Cell Death Differ* **2008**, *15* (1), 183-91.
28. Santavanond, J. P.; Rutter, S. F.; Atkin-Smith, G. K.; Poon, I. K. H., Apoptotic Bodies: Mechanism of Formation, Isolation and Functional Relevance. *Subcell Biochem* **2021**, *97*, 61-88.
29. Park, S. J.; Kim, J. M.; Kim, J.; Hur, J.; Park, S.; Kim, K.; Shin, H.-J.; Chwae, Y.-J., Molecular mechanisms of biogenesis of apoptotic exosome-like vesicles and their roles as damage-associated molecular patterns. *Proceedings of the National Academy of Sciences* **2018**, *115* (50), E11721-E11730.
30. Gregory, C. D.; Dransfield, I., Apoptotic tumor cell-derived extracellular vesicles as important regulators of the onco-regenerative niche. *Frontiers in immunology* **2018**, *9*, 1111.
31. Szatanek, R.; Baj-Krzyworzeka, M.; Zimoch, J.; Lekka, M.; Siedlar, M.; Baran, J., The Methods of Choice for Extracellular Vesicles (EVs) Characterization. *Int J Mol Sci* **2017**, *18* (6).
32. Liangsupree, T.; Multia, E.; Riekkola, M.-L., Modern isolation and separation techniques for extracellular vesicles. *Journal of Chromatography A* **2021**, *1636*, 461773.
33. Ramirez, M. I.; Amorim, M. G.; Gadelha, C.; Milic, I.; Welsh, J. A.; Freitas, V. M.; Nawaz, M.; Akbar, N.; Couch, Y.; Makin, L.; Cooke, F.; Vettore, A. L.; Batista, P. X.; Freezor, R.; Pezuk, J. A.; Rosa-Fernandes, L.; Carreira, A. C. O.; Devitt, A.; Jacobs, L.; Silva, I. T.; Coakley, G.; Nunes, D. N.; Carter, D.; Palmisano, G.; Dias-Neto, E., Technical challenges of working with extracellular vesicles. *Nanoscale* **2018**, *10* (3), 881-906.
34. Kornilov, R.; Puhka, M.; Mannerström, B.; Hiidenmaa, H.; Peltoniemi, H.; Siljander, P.; Seppänen-Kaijansinkko, R.; Kaur, S., Efficient ultrafiltration-based protocol to deplete extracellular vesicles from fetal bovine serum. *J Extracell Vesicles* **2018**, *7* (1), 1422674-1422674.
35. Chen, Y.; Zhu, Q.; Cheng, L.; Wang, Y.; Li, M.; Yang, Q.; Hu, L.; Lou, D.; Li, J.; Dong, X., Exosome detection via the ultrafast-isolation system: EXODUS. *Nature Methods* **2021**, *18* (2), 212-218.
36. Zhang, H.; Freitas, D.; Kim, H. S.; Fabijanic, K.; Li, Z.; Chen, H.; Mark, M. T.; Molina, H.; Martin, A. B.; Bojmar, L., Identification of distinct nanoparticles and subsets of extracellular vesicles by asymmetric flow field-flow fractionation. *Nature cell biology* **2018**, *20* (3), 332-343.
37. Verweij, F. J.; Balaj, L.; Boulanger, C. M.; Carter, D. R. F.; Compeer, E. B.; D'Angelo, G.; El Andaloussi, S.; Goetz, J. G.; Gross, J. C.; Hyenne, V.; Krämer-Albers, E.-M.; Lai, C. P.; Loyer, X.; Marki, A.; Momma, S.; Nolte-'t Hoen, E. N. M.; Pegtel, D. M.; Peinado, H.; Raposo, G.; Rilla, K.; Tahara, H.; Théry, C.; van Royen, M. E.; Vandenbroucke, R. E.; Wehman, A. M.; Witwer, K.; Wu, Z.; Wubbolts, R.; van Niel, G., The power of imaging to understand extracellular vesicle biology in vivo. *Nature Methods* **2021**, *18* (9), 1013-1026.
38. Gardiner, C.; Vizio, D. D.; Sahoo, S.; Théry, C.; Witwer, K. W.; Wauben, M.; Hill, A. F., Techniques used for the isolation and characterization of extracellular vesicles: results of a worldwide survey. *J Extracell Vesicles* **2016**, *5* (1), 32945.

39. Gonçalves, M. S. T., Fluorescent labeling of biomolecules with organic probes. *Chemical reviews* **2009**, *109* (1), 190-212.
40. Vallabhajosula, S.; Lyden, D.; Selgas, H. P.; Nikolopoulou, A. *Radiolabeled Exosomes for the Early Detection of Metastases and to Predict Breast Cancer Premetastatic Niche*; CORNELL UNIV MEDICAL COLL (WEILL) NEW YORK: 2015.
41. Dominkuš, P. P.; Stenovec, M.; Sitar, S.; Lasič, E.; Zorec, R.; Plemenitaš, A.; Žagar, E.; Kreft, M.; Lenassi, M., PKH26 labeling of extracellular vesicles: Characterization and cellular internalization of contaminating PKH26 nanoparticles. *Biochimica et Biophysica Acta (BBA)-Biomembranes* **2018**, *1860* (6), 1350-1361.
42. Morales-Kastresana, A.; Telford, B.; Musich, T. A.; McKinnon, K.; Clayborne, C.; Braig, Z.; Rosner, A.; Demberg, T.; Watson, D. C.; Karpova, T. S., Labeling extracellular vesicles for nanoscale flow cytometry. *Scientific reports* **2017**, *7* (1), 1-10.
43. Rautaniemi, K.; Zini, J.; Löfman, E.; Saari, H.; Haapalehto, I.; Laukka, J.; Vesamäki, S.; Efimov, A.; Yliperttula, M.; Laaksonen, T.; Vuorimaa-Laukkanen, E.; Lisitsyna, E. S., Addressing challenges in the removal of unbound dye from passively labelled extracellular vesicles. *Nanoscale Advances* **2022**, *4* (1), 226-240.
44. Théry, C.; Witwer, K. W.; Aikawa, E.; Alcaraz, M. J.; Anderson, J. D.; Andriantsitohaina, R.; Antoniou, A.; Arab, T.; Archer, F.; Atkin-Smith, G. K.; Ayre, D. C.; Bach, J.-M.; Bachurski, D.; Baharvand, H.; Balaj, L.; Baldacchino, S.; Bauer, N. N.; Baxter, A. A.; Bebawy, M.; Beckham, C.; Zavec, A. B.; Benmoussa, A.; Berardi, A. C.; Bergese, P.; Bielska, E.; Blenkiron, C.; Bobis-Wozowicz, S.; Boilard, E.; Boireau, W.; Bongiovanni, A.; Borràs, F. E.; Bosch, S.; Boulanger, C. M.; Breakefield, X.; Breglio, A. M.; Brennan, M. Á.; Brigstock, D. R.; Brisson, A.; Broekman, M. L. D.; Bromberg, J. F.; Bryl-Górecka, P.; Buch, S.; Buck, A. H.; Burger, D.; Busatto, S.; Buschmann, D.; Bussolati, B.; Buzás, E. I.; Byrd, J. B.; Camussi, G.; Carter, D. R. F.; Caruso, S.; Chamley, L. W.; Chang, Y.-T.; Chen, C.; Chen, S.; Cheng, L.; Chin, A. R.; Clayton, A.; Clerici, S. P.; Cocks, A.; Cocucci, E.; Coffey, R. J.; Cordeiro-da-Silva, A.; Couch, Y.; Coumans, F. A. W.; Coyle, B.; Crescitelli, R.; Criado, M. F.; D'Souza-Schorey, C.; Das, S.; Chaudhuri, A. D.; Candia, P. d.; Junior, E. F. D. S.; Wever, O. D.; Portillo, H. A. d.; Demaret, T.; Deville, S.; Devitt, A.; Dhondt, B.; Vizio, D. D.; Dieterich, L. C.; Dolo, V.; Rubio, A. P. D.; Dominici, M.; Dourado, M. R.; Driedonks, T. A. P.; Duarte, F. V.; Duncan, H. M.; Eichenberger, R. M.; Ekström, K.; Andaloussi, S. E. L.; Elie-Caille, C.; Erdbrügger, U.; Falcón-Pérez, J. M.; Fatima, F.; Fish, J. E.; Flores-Bellver, M.; Försonits, A.; Frelet-Barrand, A.; Fricke, F.; Fuhrmann, G.; Gabrielsson, S.; Gámez-Valero, A.; Gardiner, C.; Gärtner, K.; Gaudin, R.; Ghossein, Y. S.; Giebel, B.; Gilbert, C.; Gimona, M.; Giusti, I.; Goberdhan, D. C. I.; Görgens, A.; Gorski, S. M.; Greening, D. W.; Gross, J. C.; Gualerzi, A.; Gupta, G. N.; Gustafson, D.; Handberg, A.; Haraszti, R. A.; Harrison, P.; Hegyesi, H.; Hendrix, A.; Hill, A. F.; Hochberg, F. H.; Hoffmann, K. F.; Holder, B.; Holthofer, H.; Hosseinkhani, B.; Hu, G.; Huang, Y.; Huber, V.; Hunt, S.; Ibrahim, A. G.-E.; Ikezu, T.; Inal, J. M.; Isin, M.; Ivanova, A.; Jackson, H. K.; Jacobsen, S.; Jay, S. M.; Jayachandran, M.; Jenster, G.; Jiang, L.; Johnson, S. M.; Jones, J. C.; Jong, A.; Jovanovic-Taliman, T.; Jung, S.; Kalluri, R.; Kano, S.-i.; Kaur, S.; Kawamura, Y.; Keller, E. T.; Khamari, D.; Khomyakova, E.; Khvorova, A.; Kierulf, P.; Kim, K. P.; Kislinger, T.; Klingeborn, M.; Ii, D. J. K.; Kornek, M.;

Kosanović, M. M.; Kovács, Á. F.; Krämer-Albers, E.-M.; Krasemann, S.; Krause, M.; Kurochkin, I. V.; Kusuma, G. D.; Kuypers, S.; Laitinen, S.; Langevin, S. M.; Languino, L. R.; Lannigan, J.; Lässer, C.; Laurent, L. C.; Lavieu, G.; Lázaro-Ibáñez, E.; Lay, S. L.; Lee, M.-S.; Lee, Y. X. F.; Lemos, D. S.; Lenassi, M.; Leszczynska, A.; Li, I. T. S.; Liao, K.; Libregts, S. F.; Ligeti, E.; Lim, R.; Lim, S. K.; Linē, A.; Linnemannstōns, K.; Llorente, A.; Lombard, C. A.; Lorenowicz, M. J.; Lőrincz, Á. M.; Lōtvall, J.; Lovett, J.; Lowry, M. C.; Loyer, X.; Lu, Q.; Lukomska, B.; Lunavat, T. R.; Maas, S. L. N.; Malhi, H.; Marcilla, A.; Mariani, J.; Mariscal, J.; Martens-Uzunova, E. S.; Martin-Jaular, L.; Martinez, M. C.; Martins, V. R.; Mathieu, M.; Mathivanan, S.; Maugeri, M.; McGinnis, L. K.; McVey, M. J.; Jr, D. G. M.; Meehan, K. L.; Mertens, I.; Minciacchi, V. R.; Möller, A.; Jørgensen, M. M.; Morales-Kastresana, A.; Morhayim, J.; Mullier, F.; Muraca, M.; Musante, L.; Mussack, V.; Muth, D. C.; Myburgh, K. H.; Najrana, T.; Nawaz, M.; Nazarenko, I.; Nejsun, P.; Neri, C.; Neri, T.; Nieuwland, R.; Nimrichter, L.; Nolan, J. P.; Hoen, E. N. M. N.-t.; Hooten, N. N.; O’Driscoll, L.; O’Grady, T.; O’Loghlen, A.; Ochiya, T.; Olivier, M.; Ortiz, A.; Ortiz, L. A.; Osteikoetxea, X.; Østergaard, O.; Ostrowski, M.; Park, J.; Pegtel, D. M.; Peinado, H.; Perut, F.; Pfaffl, M. W.; Phinney, D. G.; Pieters, B. C. H.; Pink, R. C.; Pisetsky, D. S.; Strandmann, E. P. v.; Polakovicova, I.; Poon, I. K. H.; Powell, B. H.; Prada, I.; Pulliam, L.; Quesenberry, P.; Radeghieri, A.; Raffai, R. L.; Raimondo, S.; Rak, J.; Ramirez, M. I.; Raposo, G.; Rayyan, M. S.; Regev-Rudzki, N.; Ricklefs, F. L.; Robbins, P. D.; Roberts, D. D.; Rodrigues, S. C.; Rohde, E.; Rome, S.; Rouschop, K. M. A.; Rughetti, A.; Russell, A. E.; Saá, P.; Sahoo, S.; Salas-Huenuleo, E.; Sánchez, C.; Saugstad, J. A.; Saul, M. J.; Schiffelers, R. M.; Schneider, R.; Schøyen, T. H.; Scott, A.; Shahaj, E.; Sharma, S.; Shatnyeva, O.; Shekari, F.; Shelke, G. V.; Shetty, A. K.; Shiba, K.; Siljander, P. R. M.; Silva, A. M.; Skowronek, A.; Ii, O. L. S.; Soares, R. P.; Sōdar, B. W.; Soekmadji, C.; Sotillo, J.; Stahl, P. D.; Stoorvogel, W.; Stott, S. L.; Strasser, E. F.; Swift, S.; Tahara, H.; Tewari, M.; Timms, K.; Tiwari, S.; Tixeira, R.; Tkach, M.; Toh, W. S.; Tomasini, R.; Torrecilhas, A. C.; Tosar, J. P.; Toxavidis, V.; Urbanelli, L.; Vader, P.; Balkom, B. W. M. v.; Grein, S. G. v. d.; Deun, J. V.; Herwijnen, M. J. C. v.; Keuren-Jensen, K. V.; Niel, G. v.; Royen, M. E. v.; Wijnen, A. J. v.; Vasconcelos, M. H.; Jr, I. J. V.; Veit, T. D.; Vella, L. J.; Velot, É.; Verweij, F. J.; Vestad, B.; Viñas, J. L.; Visnovitz, T.; Vukman, K. V.; Wahlgren, J.; Watson, D. C.; Wauben, M. H. M.; Weaver, A.; Webber, J. P.; Weber, V.; Wehman, A. M.; Weiss, D. J.; Welsh, J. A.; Wendt, S.; Wheelock, A. M.; Wiener, Z.; Witte, L.; Wolfram, J.; Xagorari, A.; Xander, P.; Xu, J.; Yan, X.; Yáñez-Mó, M.; Yin, H.; Yuana, Y.; Zappulli, V.; Zarubova, J.; Žėkas, V.; Zhang, J.-y.; Zhao, Z.; Zheng, L.; Zheutlin, A. R.; Zickler, A. M.; Zimmermann, P.; Zivkovic, A. M.; Zocco, D.; Zuba-Surma, E. K., Minimal information for studies of extracellular vesicles 2018 (MISEV2018): a position statement of the International Society for Extracellular Vesicles and update of the MISEV2014 guidelines. *J Extracell Vesicles* **2018**, 7 (1), 1535750.

45. Lai, C. P.; Kim, E. Y.; Badr, C. E.; Weissleder, R.; Mempel, T. R.; Tannous, B. A.; Breakefield, X. O., Visualization and tracking of tumour extracellular vesicle delivery and RNA translation using multiplexed reporters. *Nature communications* **2015**, 6 (1), 1-12.

46. Sung, B. H.; von Lersner, A.; Guerrero, J.; Krystofiak, E. S.; Inman, D.; Pelletier, R.; Zijlstra, A.; Ponik, S. M.; Weaver, A. M., A live cell reporter of exosome secretion and uptake reveals pathfinding behavior of migrating cells. *Nature communications* **2020**, *11* (1), 1-15.
47. Bebelman, M. P.; Smit, M. J.; Pegtel, D. M.; Baglio, S. R., Biogenesis and function of extracellular vesicles in cancer. *Pharmacology & Therapeutics* **2018**, *188*, 1-11.
48. Hill, A. F., Extracellular Vesicles and Neurodegenerative Diseases. *The Journal of neuroscience : the official journal of the Society for Neuroscience* **2019**, *39* (47), 9269-9273.
49. Vandendriessche, C.; Kapogiannis, D.; Vandenbroucke, R. E., Biomarker and therapeutic potential of peripheral extracellular vesicles in Alzheimer's disease. *Advanced Drug Delivery Reviews* **2022**, *190*, 114486.
50. Canada, P. H. A. o. *A Dementia Strategy for Canada: Together We Aspire*; 2019.
51. Chen, X.-Q.; Mobley, W. C., Alzheimer Disease Pathogenesis: Insights From Molecular and Cellular Biology Studies of Oligomeric A β and Tau Species. *Frontiers in Neuroscience* **2019**, *13*.
52. Gonzalez-Garcia, M.; Fusco, G.; De Simone, A., Membrane Interactions and Toxicity by Misfolded Protein Oligomers. *Front Cell Dev Biol* **2021**, *9*.
53. Combs, C. K.; Karlo, J. C.; Kao, S.-C.; Landreth, G. E., β -Amyloid Stimulation of Microglia and Monocytes Results in TNF α -Dependent Expression of Inducible Nitric Oxide Synthase and Neuronal Apoptosis. *The Journal of Neuroscience* **2001**, *21* (4), 1179-1188.
54. Hampel, H.; Hardy, J.; Blennow, K.; Chen, C.; Perry, G.; Kim, S. H.; Villemagne, V. L.; Aisen, P.; Vendruscolo, M.; Iwatsubo, T.; Masters, C. L.; Cho, M.; Lannfelt, L.; Cummings, J. L.; Vergallo, A., The Amyloid- β Pathway in Alzheimer's Disease. *Molecular Psychiatry* **2021**, *26* (10), 5481-5503.
55. DeTure, M. A.; Dickson, D. W., The neuropathological diagnosis of Alzheimer's disease. *Mol Neurodegener* **2019**, *14* (1), 32.
56. Klunk, W. E.; Engler, H.; Nordberg, A.; Wang, Y.; Blomqvist, G.; Holt, D. P.; Bergström, M.; Savitcheva, I.; Huang, G. F.; Estrada, S., Imaging brain amyloid in Alzheimer's disease with Pittsburgh Compound-B. *Annals of Neurology: Official Journal of the American Neurological Association and the Child Neurology Society* **2004**, *55* (3), 306-319.
57. Bateman, R. J.; Munsell, L. Y.; Morris, J. C.; Swarm, R.; Yarasheski, K. E.; Holtzman, D. M., Human amyloid- β synthesis and clearance rates as measured in cerebrospinal fluid in vivo. *Nature medicine* **2006**, *12* (7), 856-861.
58. Blennow, K.; Zetterberg, H., Understanding biomarkers of neurodegeneration: Ultrasensitive detection techniques pave the way for mechanistic understanding. *Nat Med* **2015**, *21* (3), 217-9.
59. Shi, M.; Sheng, L.; Stewart, T.; Zabetian, C. P.; Zhang, J., New windows into the brain: Central nervous system-derived extracellular vesicles in blood. *Progress in Neurobiology* **2019**, *175*, 96-106.
60. Rajendran, L.; Honsho, M.; Zahn, T. R.; Keller, P.; Geiger, K. D.; Verkade, P.; Simons, K., Alzheimer's disease β -amyloid peptides are released in association with exosomes. **2006**, *103* (30), 11172-11177.

61. Goetzl, E. J.; Boxer, A.; Schwartz, J. B.; Abner, E. L.; Petersen, R. C.; Miller, B. L.; Kapogiannis, D. J. N., Altered lysosomal proteins in neural-derived plasma exosomes in preclinical Alzheimer disease. **2015**, *85* (1), 40-47.
62. Goetzl, E. J.; Boxer, A.; Schwartz, J. B.; Abner, E. L.; Petersen, R. C.; Miller, B. L.; Carlson, O. D.; Mustapic, M.; Kapogiannis, D., Low neural exosomal levels of cellular survival factors in Alzheimer's disease. *Ann Clin Transl Neurol* **2015**, *2* (7), 769-773.
63. Goetzl, E. J.; Mustapic, M.; Kapogiannis, D.; Eitan, E.; Lobach, I. V.; Goetzl, L.; Schwartz, J. B.; Miller, B. L., Cargo proteins of plasma astrocyte-derived exosomes in Alzheimer's disease. *FASEB J* **2016**, *30* (11), 3853-3859.
64. Goetzl, E. J.; Abner, E. L.; Jicha, G. A.; Kapogiannis, D.; Schwartz, J. B., Declining levels of functionally specialized synaptic proteins in plasma neuronal exosomes with progression of Alzheimer's disease. *FASEB J* **2018**, *32* (2), 888-893.
65. Hamlett, E. D.; Goetzl, E. J.; Ledreux, A.; Vasilevko, V.; Boger, H. A.; LaRosa, A.; Clark, D.; Carroll, S. L.; Carmona-Iragui, M.; Fortea, J.; Mufson, E. J.; Sabbagh, M.; Mohammed, A. H.; Hartley, D.; Doran, E.; Lott, I. T.; Granholm, A.-C., Neuronal exosomes reveal Alzheimer's disease biomarkers in Down syndrome. *Alzheimers Dement* **2017**, *13* (5), 541-549.
66. Goetzl, E. J.; Nogueras-Ortiz, C.; Mustapic, M.; Mullins, R. J.; Abner, E. L.; Schwartz, J. B.; Kapogiannis, D., Deficient neurotrophic factors of CSPG4-type neural cell exosomes in Alzheimer disease. **2019**, *33* (1), 231-238.
67. Gomes, D. E.; Witwer, K. W., LICAM-associated extracellular vesicles: A systematic review of nomenclature, sources, separation, and characterization. *Journal of Extracellular Biology* **2022**, *1* (3), e35.
68. Anastasi, F.; Masciandaro, S. M.; Carratore, R. D.; Dell'Anno, M. T.; Signore, G.; Falleni, A.; McDonnell, L. A.; Bongioanni, P., Proteomics profiling of neuron-derived small extracellular vesicles from human plasma: Enabling single-subject analysis. *Int J Mol Sci* **2021**, *22* (6), 2951.
69. Cha, D. J.; Mengel, D.; Mustapic, M.; Liu, W.; Selkoe, D. J.; Kapogiannis, D.; Galasko, D.; Rissman, R. A.; Bennett, D. A.; Walsh, D. M., miR-212 and miR-132 are downregulated in neurally derived plasma exosomes of Alzheimer's patients. *Frontiers in neuroscience* **2019**, *13*, 1208.
70. Gu, D.; Liu, F.; Meng, M.; Zhang, L.; Gordon, M. L.; Wang, Y.; Cai, L.; Zhang, N., Elevated matrix metalloproteinase-9 levels in neuronal extracellular vesicles in Alzheimer's disease. *Ann Clin Transl Neurol* **2020**, *7* (9), 1681-1691.
71. Mullins, R. J.; Mustapic, M.; Goetzl, E. J.; Kapogiannis, D., Exosomal biomarkers of brain insulin resistance associated with regional atrophy in Alzheimer's disease. *Human brain mapping* **2017**, *38* (4), 1933-1940.
72. Zhao, A.; Li, Y.; Yan, Y.; Qiu, Y.; Li, B.; Xu, W.; Wang, Y.; Liu, J.; Deng, Y., Increased prediction value of biomarker combinations for the conversion of mild cognitive impairment to Alzheimer's dementia. *Transl Neurodegener* **2020**, *9* (1), 30.

73. Yuyama, K.; Takahashi, K.; Usuki, S.; Mikami, D.; Sun, H.; Hanamatsu, H.; Furukawa, J.; Mukai, K.; Igarashi, Y., Plant sphingolipids promote extracellular vesicle release and alleviate amyloid- β pathologies in a mouse model of Alzheimer's disease. *Scientific Reports* **2019**, *9* (1), 16827.
74. Winston, C. N.; Goetzl, E. J.; Akers, J. C.; Carter, B. S.; Rockenstein, E. M.; Galasko, D.; Masliah, E.; Rissman, R. A., Prediction of conversion from mild cognitive impairment to dementia with neuronally derived blood exosome protein profile. *Alzheimer's & Dementia: Diagnosis, Assessment & Disease Monitoring* **2016**, *3*, 63-72.
75. Norman, M.; Ter-Ovanesyan, D.; Trieu, W.; Lazarovits, R.; Kowal, E. J. K.; Lee, J. H.; Chen-Plotkin, A. S.; Regev, A.; Church, G. M.; Walt, D. R., L1CAM is not associated with extracellular vesicles in human cerebrospinal fluid or plasma. *Nature Methods* **2021**, *18* (6), 631-634.
76. Altevogt, P.; Ben-Ze'ev, A.; Gavert, N.; Schumacher, U.; Schäfer, H.; Sebens, S., Recent insights into the role of L1CAM in cancer initiation and progression. *International Journal of Cancer* **2020**, *147* (12), 3292-3296.
77. Pegtel, D. M.; Peferoen, L.; Amor, S., Extracellular vesicles as modulators of cell-to-cell communication in the healthy and diseased brain. *Philosophical Transactions of the Royal Society B: Biological Sciences* **2014**, *369* (1652), 20130516.
78. Paolicelli, R. C.; Bergamini, G.; Rajendran, L. J. N., Cell-to-cell communication by extracellular vesicles: focus on microglia. **2018**.
79. Janas, A. M.; Sapoń, K.; Janas, T.; Stowell, M. H. B.; Janas, T., Exosomes and other extracellular vesicles in neural cells and neurodegenerative diseases. *Biochimica et Biophysica Acta (BBA) - Biomembranes* **2016**, *1858* (6), 1139-1151.
80. Sardar Sinha, M.; Ansell-Schultz, A.; Civitelli, L.; Hildesjö, C.; Larsson, M.; Lannfelt, L.; Ingelsson, M.; Hallbeck, M., Alzheimer's disease pathology propagation by exosomes containing toxic amyloid-beta oligomers. *Acta Neuropathologica* **2018**, *136* (1), 41-56.
81. Li, T.-R.; Wang, X.-N.; Sheng, C.; Li, Y.-X.; Li, F. Z.-T.; Sun, Y.; Han, Y., Extracellular vesicles as an emerging tool for the early detection of Alzheimer's disease. *Mechanisms of Ageing and Development* **2019**, *184*, 111175.
82. Lim, C. Z. J.; Zhang, Y.; Chen, Y.; Zhao, H.; Stephenson, M. C.; Ho, N. R. Y.; Chen, Y.; Chung, J.; Reilhac, A.; Loh, T. P.; Chen, C. L. H.; Shao, H., Subtyping of circulating exosome-bound amyloid β reflects brain plaque deposition. *Nature Communications* **2019**, *10* (1), 1144.
83. Huang, Y.; Driedonks, T. A. P.; Cheng, L.; Rajapaksha, H.; Turchinovich, A.; Routenberg, D. A.; Nagaraj, R.; Redding-Ochoa, J.; Arab, T.; Powell, B. H.; Pletnikova, O.; Troncoso, J. C.; Zheng, L.; Hill, A. F.; Mahairaki, V.; Witwer, K. W., Relationships of ϵ APOE Genotypes With Small RNA and Protein Cargo of Brain Tissue Extracellular Vesicles From Patients With Late-Stage AD. *Neurology Genetics* **2022**, *8* (6), e200026.
84. Huang, Y.; Driedonks, T. A. P.; Cheng, L.; Rajapaksha, H.; Routenberg, D. A.; Nagaraj, R.; Redding, J.; Arab, T.; Powell, B. H.; Pletniková, O.; Troncoso, J. C.; Zheng, L.; Hill, A. F.; Mahairaki, V.; Witwer, K.

W., Brain Tissue-Derived Extracellular Vesicles in Alzheimer's Disease Display Altered Key Protein Levels Including Cell Type-Specific Markers. *Journal of Alzheimer's Disease* **2022**, *90*, 1057-1072.

85. Ruan, Z.; Pathak, D.; Venkatesan Kalavai, S.; Yoshii-Kitahara, A.; Muraoka, S.; Bhatt, N.; Takamatsu-Yukawa, K.; Hu, J.; Wang, Y.; Hersh, S.; Ericsson, M.; Gorantla, S.; Gendelman, H. E.; Kaye, R.; Ikezu, S.; Luebke, J. I.; Ikezu, T., Alzheimer's disease brain-derived extracellular vesicles spread tau pathology in interneurons. *Brain* **2021**, *144* (1), 288-309.

86. Vingtdoux, V.; Hamdane, M.; Loyens, A.; Gelé, P.; Drobeck, H.; Bégard, S.; Galas, M.-C.; Delacourte, A.; Beauvillain, J.-C.; Buée, L.; Sergeant, N., Alkalinizing Drugs Induce Accumulation of Amyloid Precursor Protein By-products in Luminal Vesicles of Multivesicular Bodies ^{*} *Journal of Biological Chemistry* **2007**, *282* (25), 18197-18205.

87. Sharples, R. A.; Vella, L. J.; Nisbet, R. M.; Naylor, R.; Perez, K.; Barnham, K. J.; Masters, C. L.; Hill, A. F., Inhibition of γ -secretase causes increased secretion of amyloid precursor protein C-terminal fragments in association with exosomes. *The FASEB Journal* **2008**, *22* (5), 1469-1478.

88. Perez-Gonzalez, R.; Gauthier, S. A.; Kumar, A.; Levy, E., The Exosome Secretory Pathway Transports Amyloid Precursor Protein Carboxyl-terminal Fragments from the Cell into the Brain Extracellular Space ^{*}. *Journal of Biological Chemistry* **2012**, *287* (51), 43108-43115.

89. Fiandaca, M. S.; Kapogiannis, D.; Mapstone, M.; Boxer, A.; Eitan, E.; Schwartz, J. B.; Abner, E. L.; Petersen, R. C.; Federoff, H. J.; Miller, B. L. J. A. s.; Dementia, Identification of preclinical Alzheimer's disease by a profile of pathogenic proteins in neurally derived blood exosomes: A case-control study. **2015**, *11* (6), 600-607. e1.

90. Jia, L.; Qiu, Q.; Zhang, H.; Chu, L.; Du, Y.; Zhang, J.; Zhou, C.; Liang, F.; Shi, S.; Wang, S.; Qin, W.; Wang, Q.; Li, F.; Wang, Q.; Li, Y.; Shen, L.; Wei, Y.; Jia, J., Concordance between the assessment of A β 42, T-tau, and P-T181-tau in peripheral blood neuronal-derived exosomes and cerebrospinal fluid. *Alzheimer's & Dementia* **2019**, *15* (8), 1071-1080.

91. Kapogiannis, D.; Mustapic, M.; Shardell, M. D.; Berkowitz, S. T.; Diehl, T. C.; Spangler, R. D.; Tran, J.; Lazaropoulos, M. P.; Chawla, S.; Gulyani, S.; Eitan, E.; An, Y.; Huang, C. W.; Oh, E. S.; Lyketsos, C. G.; Resnick, S. M.; Goetzl, E. J.; Ferrucci, L., Association of Extracellular Vesicle Biomarkers With Alzheimer Disease in the Baltimore Longitudinal Study of Aging. *JAMA neurology* **2019**, *76* (11), 1340-51.

92. Li, T.-R.; Yao, Y.-X.; Jiang, X.-Y.; Dong, Q.-Y.; Yu, X.-F.; Wang, T.; Cai, Y.-N.; Han, Y., β -Amyloid in blood neuronal-derived extracellular vesicles is elevated in cognitively normal adults at risk of Alzheimer's disease and predicts cerebral amyloidosis. *Alzheimers Res Ther* **2022**, *14* (1), 66.

93. Perrotte, M.; Haddad, M.; Le Page, A.; Frost, E. H.; Fulöp, T.; Ramassamy, C., Profile of pathogenic proteins in total circulating extracellular vesicles in mild cognitive impairment and during the progression of Alzheimer's disease. *Neurobiol Aging* **2020**, *86*, 102-111.

94. Serrano-Pertierra, E.; Oliveira-Rodríguez, M.; Matos, M.; Gutiérrez, G.; Moyano, A.; Salvador, M.; Rivas, M.; Blanco-López, M. C., Extracellular Vesicles: Current Analytical Techniques for Detection and Quantification. *Biomolecules* **2020**, *10* (6).
95. Paraskevaïdi, M.; Morais, C. L. M.; Halliwell, D. E.; Mann, D. M. A.; Allsop, D.; Martin-Hirsch, P. L.; Martin, F. L., Raman Spectroscopy to Diagnose Alzheimer's Disease and Dementia with Lewy Bodies in Blood. *ACS Chem Neurosci* **2018**, *9* (11), 2786-2794.
96. Carota, A. G.; Campanella, B.; Del Carratore, R.; Bongioanni, P.; Giannelli, R.; Legnaioli, S., Raman spectroscopy and multivariate analysis as potential tool to follow Alzheimer's disease progression. *Analytical and Bioanalytical Chemistry* **2022**, *414* (16), 4667-4675.
97. Ryzhikova, E.; Ralbovsky, N. M.; Sikirzhyski, V.; Kazakov, O.; Halamkova, L.; Quinn, J.; Zimmerman, E. A.; Lednev, I. K., Raman spectroscopy and machine learning for biomedical applications: Alzheimer's disease diagnosis based on the analysis of cerebrospinal fluid. *Spectrochimica Acta Part A: Molecular and Biomolecular Spectroscopy* **2021**, *248*, 119188.
98. Ralbovsky, N. M.; Halámková, L.; Wall, K.; Anderson-Hanley, C.; Lednev, I. K., Screening for Alzheimer's disease using saliva: a new approach based on machine learning and Raman hyperspectroscopy. *Journal of Alzheimer's Disease* **2019**, *71* (4), 1351-1359.
99. Yang, J. K.; Hwang, I. J.; Cha, M. G.; Kim, H. I.; Yim, D.; Jeong, D. H.; Lee, Y. S.; Kim, J. H., Reaction Kinetics-Mediated Control over Silver Nanogap Shells as Surface-Enhanced Raman Scattering Nanoprobes for Detection of Alzheimer's Disease Biomarkers. *Small* **2019**, *15* (19), 1900613.
100. Yang, S. J.; Lee, J. U.; Jeon, M. J.; Sim, S. J., Highly sensitive surface-enhanced Raman scattering-based immunosensor incorporating half antibody-fragment for quantitative detection of Alzheimer's disease biomarker in blood. *Analytica Chimica Acta* **2022**, *1195*, 339445.
101. Clarke, E. J.; Lima, C.; Anderson, J. R.; Castanheira, C.; Beckett, A.; James, V.; Hyett, J.; Goodacre, R.; Peffers, M. J., Optical photothermal infrared spectroscopy can differentiate equine osteoarthritic plasma extracellular vesicles from healthy controls. *Analytical Methods* **2022**, *14* (37), 3661-3670.
102. Lozano-Andrés, E.; Enciso-Martinez, A.; Gijbers, A.; Libregts, S. F. W. M.; Pinheiro, C.; Van Niel, G.; Hendrix, A.; Peters, P. J.; Otto, C.; Arkesteijn, G. J. A.; Wauben, M. H. M., Physical association of low density lipoprotein particles and extracellular vesicles unveiled by single particle analysis. *bioRxiv* **2022**, 2022.08.31.506022.
103. Xie, Y.; Su, X.; Wen, Y.; Zheng, C.; Li, M., Artificial Intelligent Label-Free SERS Profiling of Serum Exosomes for Breast Cancer Diagnosis and Postoperative Assessment. *Nano Letters* **2022**, *22* (19), 7910-7918.
104. Liangsupree, T.; Multia, E.; Saarinen, J.; Ruiz-Jimenez, J.; Kemell, M.; Riekkola, M.-L., Raman spectroscopy combined with comprehensive gas chromatography for label-free characterization of plasma-derived extracellular vesicle subpopulations. *Analytical Biochemistry* **2022**, *647*, 114672.
105. Flynn, J. D.; McGlinchey, R. P.; Walker, R. L., 3rd; Lee, J. C., Structural features of α -synuclein amyloid fibrils revealed by Raman spectroscopy. *J Biol Chem* **2018**, *293* (3), 767-776.

106. Tóth, E. Á.; Turiák, L.; Visnovitz, T.; Cserép, C.; Mázló, A.; Sódar, B. W.; Försönits, A. I.; Petővári, G.; Sebestyén, A.; Komlósi, Z., Formation of a protein corona on the surface of extracellular vesicles in blood plasma. *J Extracell Vesicles* **2021**, *10* (11), e12140.
107. Wolf, M.; Poupardin, R. W.; Ebner-Peking, P.; Andrade, A. C.; Blöchl, C.; Obermayer, A.; Gomes, F. G.; Vari, B.; Maeding, N.; Eminger, E.; Binder, H.-M.; Raninger, A. M.; Hochmann, S.; Brachtl, G.; Spittler, A.; Heuser, T.; Ofir, R.; Huber, C. G.; Aberman, Z.; Schallmoser, K.; Volk, H.-D.; Strunk, D., A functional corona around extracellular vesicles enhances angiogenesis, skin regeneration and immunomodulation. *J Extracell Vesicles* **2022**, *11* (4), e12207.
108. Varga, Z.; Fehér, B.; Kitka, D.; Wacha, A.; Bóta, A.; Berényi, S.; Pipich, V.; Fraikin, J.-L., Size measurement of extracellular vesicles and synthetic liposomes: the impact of the hydration shell and the protein corona. *Colloids and Surfaces B: Biointerfaces* **2020**, *192*, 111053.
109. Meneghetti, M. C.; Hughes, A. J.; Rudd, T. R.; Nader, H. B.; Powell, A. K.; Yates, E. A.; Lima, M. A., Heparan sulfate and heparin interactions with proteins. *J R Soc Interface* **2015**, *12* (110), 20150589.
110. Buzás, E. I.; Tóth, E. Á.; Sódar, B. W.; Szabó-Taylor, K. É. In *Molecular interactions at the surface of extracellular vesicles*, Seminars in immunopathology, Springer: 2018; pp 453-464.
111. Santucci, L.; Bruschi, M.; Del Zotto, G.; Antonini, F.; Ghiggeri, G. M.; Panfoli, I.; Candiano, G., Biological surface properties in extracellular vesicles and their effect on cargo proteins. *Scientific reports* **2019**, *9* (1), 1-12.
112. Buzas, E. I., Opportunities and challenges in studying the extracellular vesicle corona. *Nature Cell Biology* **2022**, *24* (9), 1322-1325.
113. Kuypers, S.; Smisdom, N.; Pintelon, I.; Timmermans, J. P.; Ameloot, M.; Michiels, L.; Hendrix, J.; Hosseinkhani, B., Unsupervised Machine Learning-Based Clustering of Nanosized Fluorescent Extracellular Vesicles. *Small* **2021**, *17* (5), 2006786.
114. Cansever Mutlu, E.; Kaya, M.; Küçük, I.; Ben-Nissan, B.; Stamboulis, A., Exosome Structures Supported by Machine Learning Can Be Used as a Promising Diagnostic Tool. *Materials* **2022**, *15* (22), 7967.
115. Qin, Y.-F.; Lu, X.-Y.; Shi, Z.; Huang, Q.-S.; Wang, X.; Ren, B.; Cui, L., Deep Learning-Enabled Raman Spectroscopic Identification of Pathogen-Derived Extracellular Vesicles and the Biogenesis Process. *Anal Chem* **2022**, *94* (36), 12416-12426.
116. Uthamacumaran, A.; Elouatik, S.; Abdouh, M.; Berteau-Rainville, M.; Gao, Z.-h.; Arena, G., Machine learning characterization of cancer patients-derived extracellular vesicles using vibrational spectroscopies: results from a pilot study. *Applied Intelligence* **2022**, *52* (11), 12737-12753.
117. Lee, W.; Lenferink, A. T. M.; Otto, C.; Offerhaus, H. L., Classifying Raman spectra of extracellular vesicles based on convolutional neural networks for prostate cancer detection. *Journal of Raman Spectroscopy* **2020**, *51* (2), 293-300.

118. Kazemzadeh, M.; Hisey, C. L.; Artuyants, A.; Blenkiron, C.; Chamley, L. W.; Zargar-Shoshtari, K.; Xu, W.; Broderick, N. G. R., Space curvature-inspired nanoplasmonic sensor for breast cancer extracellular vesicle fingerprinting and machine learning classification. *Biomed Opt Express* **2021**, *12* (7), 3965-3981.
119. Culum, N. M.; Cooper, T. T.; Lajoie, G. A.; Dayarathna, T.; Pasternak, S. H.; Liu, J.; Fu, Y.; Postovit, L.-M.; Laguné-Labarthe, F., Characterization of ovarian cancer-derived extracellular vesicles by surface-enhanced Raman spectroscopy. *Analyst* **2021**, *146* (23), 7194-7206.
120. Muraoka, S.; DeLeo, A. M.; Sethi, M. K.; Yukawa-Takamatsu, K.; Yang, Z.; Ko, J.; Hogan, J. D.; Ruan, Z.; You, Y.; Wang, Y.; Medalla, M.; Ikezu, S.; Chen, M.; Xia, W.; Gorantla, S.; Gendelman, H. E.; Issadore, D.; Zaia, J.; Ikezu, T., Proteomic and biological profiling of extracellular vesicles from Alzheimer's disease human brain tissues. *Alzheimer's & Dementia* **2020**, *16* (6), 896-907.
121. Liu, C.; Li, B.; Lin, H.; Yang, C.; Guo, J.; Cui, B.; Pan, W.; Feng, J.; Luo, T.; Chu, F.; Xu, X.; Zheng, L.; Yao, S., Multiplexed analysis of small extracellular vesicle-derived mRNAs by droplet digital PCR and machine learning improves breast cancer diagnosis. *Biosensors and Bioelectronics* **2021**, *194*, 113615.
122. Yin, P.; Li, G.; Zhang, B.; Farjana, H.; Zhao, L.; Qin, H.; Hu, B.; Ou, J.; Tian, J., Facile PEG-based isolation and classification of cancer extracellular vesicles and particles with label-free surface-enhanced Raman scattering and pattern recognition algorithm. *Analyst* **2021**, *146* (6), 1949-1955.
123. Zlotogorski-Hurvitz, A.; Dekel, B. Z.; Malonek, D.; Yahalom, R.; Vered, M., FTIR-based spectrum of salivary exosomes coupled with computational-aided discriminating analysis in the diagnosis of oral cancer. *J Cancer Res Clin Oncol* **2019**, *145* (3), 685-694.
124. Carmicheal, J.; Hayashi, C.; Huang, X.; Liu, L.; Lu, Y.; Krasnoslobodtsev, A.; Lushnikov, A.; Kshirsagar, P. G.; Patel, A.; Jain, M.; Lyubchenko, Y. L.; Lu, Y.; Batra, S. K.; Kaur, S., Label-free characterization of exosome via surface enhanced Raman spectroscopy for the early detection of pancreatic cancer. *Nanomedicine* **2019**, *16*, 88-96.
125. Rojalín, T.; Koster, H. J.; Liu, J.; Mizenko, R. R.; Tran, D.; Wachsmann-Hogiu, S.; Carney, R. P., Hybrid Nanoplasmonic Porous Biomaterial Scaffold for Liquid Biopsy Diagnostics Using Extracellular Vesicles. *ACS Sensors* **2020**, *5* (9), 2820-2833.
126. del Real Mata, C.; Jeanne, O.; Jalali, M.; Lu, Y.; Mahshid, S., Nanostructured-Based Optical Readouts Interfaced with Machine Learning for Identification of Extracellular Vesicles. *Advanced Healthcare Materials* **2022**, *n/a* (n/a), 2202123.
127. Nicoliche, C. Y. N.; de Oliveira, R. A. G.; da Silva, G. S.; Ferreira, L. F.; Rodrigues, I. L.; Faria, R. C.; Fazzio, A.; Carrilho, E.; de Pontes, L. G.; Schleder, G. R.; Lima, R. S., Converging Multidimensional Sensor and Machine Learning Toward High-Throughput and Biorecognition Element-Free Multidetermination of Extracellular Vesicle Biomarkers. *ACS Sensors* **2020**, *5* (7), 1864-1871.
128. Pasetto, L.; Callegaro, S.; Corbelli, A.; Fiordaliso, F.; Ferrara, D.; Brunelli, L.; Sestito, G.; Pastorelli, R.; Bianchi, E.; Cretich, M.; Chiari, M.; Potrich, C.; Moglia, C.; Corbo, M.; Sorarù, G.; Lunetta, C.; Calvo, A.; Chiò, A.; Mora, G.; Pennuto, M.; Quattrone, A.; Rinaldi, F.; D'Agostino, V. G.; Basso, M.; Bonetto, V.,

- Decoding distinctive features of plasma extracellular vesicles in amyotrophic lateral sclerosis. *Mol Neurodegener* **2021**, *16* (1), 52.
129. Vacchi, E.; Burrello, J.; Di Silvestre, D.; Burrello, A.; Bolis, S.; Mauri, P.; Vassalli, G.; Cereda, C. W.; Farina, C.; Barile, L.; Kaelin-Lang, A.; Melli, G., Immune profiling of plasma-derived extracellular vesicles identifies Parkinson disease. *Neurology - Neuroimmunology Neuroinflammation* **2020**, *7* (6), e866.
130. Kruglik, S. G.; Royo, F.; Guigner, J.-M.; Palomo, L.; Seksek, O.; Turpin, P.-Y.; Tatischeff, I.; Falcón-Pérez, J. M., Raman tweezers microspectroscopy of circa 100 nm extracellular vesicles. *Nanoscale* **2019**, *11* (4), 1661-1679.
131. Zhang, H.; Silva, A. C.; Zhang, W.; Rutigliano, H.; Zhou, A., Raman Spectroscopy characterization extracellular vesicles from bovine placenta and peripheral blood mononuclear cells. *PLOS ONE* **2020**, *15* (7), e0235214.
132. Dash, M.; Palaniyandi, K.; Ramalingam, S.; Sahabudeen, S.; Raja, N. S., Exosomes isolated from two different cell lines using three different isolation techniques show variation in physical and molecular characteristics. *Biochim Biophys Acta Biomembr* **2021**, *1863* (2), 183490.
133. Shin, H.; Oh, S.; Hong, S.; Kang, M.; Kang, D.; Ji, Y.-g.; Choi, B. H.; Kang, K.-W.; Jeong, H.; Park, Y.; Hong, S.; Kim, H. K.; Choi, Y., Early-Stage Lung Cancer Diagnosis by Deep Learning-Based Spectroscopic Analysis of Circulating Exosomes. *ACS Nano* **2020**, *14* (5), 5435-5444.
134. Pal, R.; Choudhury, A. K., *An introduction to phytoplanktons: diversity and ecology*. Springer: 2014.
135. Rikkert, L. G.; Nieuwland, R.; Terstappen, L.; Coumans, F. A. W., Quality of extracellular vesicle images by transmission electron microscopy is operator and protocol dependent. *J Extracell Vesicles* **2019**, *8* (1), 1555419.
136. Pathak, A.; Kumar, S., Independent regulation of tumor cell migration by matrix stiffness and confinement. *Proc Natl Acad Sci U S A* **2012**, *109* (26), 10334-10339.
137. Domura, R.; Sasaki, R.; Ishikawa, Y.; Okamoto, M., Cellular Morphology-Mediated Proliferation and Drug Sensitivity of Breast Cancer Cells. *J Funct Biomater* **2017**, *8* (2), 18.
138. Walker, C.; Mojares, E.; Del Río Hernández, A., Role of Extracellular Matrix in Development and Cancer Progression. *Int J Mol Sci* **2018**, *19* (10), 3028.
139. Pampaloni, F.; Reynaud, E. G.; Stelzer, E. H. K., The third dimension bridges the gap between cell culture and live tissue. *Nature Reviews Molecular Cell Biology* **2007**, *8* (10), 839-845.
140. Park, Y.; Depeursinge, C.; Popescu, G., Quantitative phase imaging in biomedicine. *Nature Photonics* **2018**, *12* (10), 578-589.
141. Zhang, Y.; Shin, Y.; Sung, K.; Yang, S.; Chen, H.; Wang, H.; Teng, D.; Rivenson, Y.; Kulkarni, R. P.; Ozcan, A., 3D imaging of optically cleared tissue using a simplified CLARITY method and on-chip microscopy. *Science Advances* **2017**, *3* (8), e1700553.
142. Ji, M.; Orringer, D. A.; Freudiger, C. W.; Ramkissoon, S.; Liu, X.; Lau, D.; Golby, A. J.; Norton, I.; Hayashi, M.; Agar, N. Y. R., Rapid, label-free detection of brain tumors with stimulated Raman scattering microscopy. *Science translational medicine* **2013**, *5* (201), 201ra119-201ra119.

143. Stroud, J. C.; Liu, C.; Teng, P. K.; Eisenberg, D., Toxic fibrillar oligomers of amyloid- β have cross- β structure. *2012*, *109* (20), 7717-7722.
144. Yu, L.; Edalji, R.; Harlan, J. E.; Holzman, T. F.; Lopez, A. P.; Labkovsky, B.; Hillen, H.; Barghorn, S.; Ebert, U.; Richardson, P. L.; Miesbauer, L.; Solomon, L.; Bartley, D.; Walter, K.; Johnson, R. W.; Hajduk, P. J.; Olejniczak, E. T., Structural characterization of a soluble amyloid beta-peptide oligomer. *Biochemistry* **2009**, *48* (9), 1870-7.
145. Cerf, E.; Sarroukh, R.; Tamamizu-Kato, S.; Breydo, L.; Derclaye, S.; Dufrière, Y. F.; Narayanaswami, V.; Goormaghtigh, E.; Ruyschaert, J. M.; Raussens, V., Antiparallel beta-sheet: a signature structure of the oligomeric amyloid beta-peptide. *The Biochemical journal* **2009**, *421* (3), 415-23.
146. Abedini, A.; Raleigh, D. P., A role for helical intermediates in amyloid formation by natively unfolded polypeptides? *Phys Biol* **2009**, *6* (1), 015005-015005.
147. Apetri, M. M.; Maiti, N. C.; Zagorski, M. G.; Carey, P. R.; Anderson, V. E., Secondary Structure of α -Synuclein Oligomers: Characterization by Raman and Atomic Force Microscopy. *Journal of Molecular Biology* **2006**, *355* (1), 63-71.
148. O'Brien, R. J.; Wong, P. C., Amyloid Precursor Protein Processing and Alzheimer's Disease. *Annu Rev Neurosci* **2011**, *34* (1), 185-204.
149. Tomita, T.; Matsuzaki, M.; Kaneko, N.; Yokoyama, M.; Yoshizawa, Y.; Iwamoto, S.; Tanaka, K., Identification of ADAMTS4 as an APP-cleaving enzyme at 669 site in the APP669-711 production pathway. *Alzheimer's & Dementia* **2020**, *16* (S5), e039194.
150. Nhan, H. S.; Chiang, K.; Koo, E. H., The multifaceted nature of amyloid precursor protein and its proteolytic fragments: friends and foes. *Acta Neuropathologica* **2015**, *129* (1), 1-19.
151. Quinn, J. P.; Corbett, N. J.; Kellett, K. A. B.; Hooper, N. M., Tau Proteolysis in the Pathogenesis of Tauopathies: Neurotoxic Fragments and Novel Biomarkers. *J Alzheimers Dis* **2018**, *63* (1), 13-33.
152. Jeppesen, D. K.; Fenix, A. M.; Franklin, J. L.; Higginbotham, J. N.; Zhang, Q.; Zimmerman, L. J.; Liebler, D. C.; Ping, J.; Liu, Q.; Evans, R.; Fissell, W. H.; Patton, J. G.; Rome, L. H.; Burnette, D. T.; Coffey, R. J., Reassessment of Exosome Composition. *Cell* **2019**, *177* (2), 428-445.e18.
153. Kugeratski, F. G.; Hodge, K.; Lilla, S.; McAndrews, K. M.; Zhou, X.; Hwang, R. F.; Zanivan, S.; Kalluri, R., Quantitative proteomics identifies the core proteome of exosomes with syntenin-1 as the highest abundant protein and a putative universal biomarker. *Nat Cell Biol* **2021**, *23* (6), 631-641.
154. Kowal, J.; Arras, G.; Colombo, M.; Jouve, M.; Morath, J. P.; Prindal-Bengtson, B.; Dingli, F.; Loew, D.; Tkach, M.; Théry, C., Proteomic comparison defines novel markers to characterize heterogeneous populations of extracellular vesicle subtypes. *Proceedings of the National Academy of Sciences* **2016**, *113* (8), E968-E977.
155. Zendrini, A.; Guerra, G.; Sagini, K.; Vagner, T.; Di Vizio, D.; Bergese, P., On the surface-to-bulk partition of proteins in extracellular vesicles. *Colloids and Surfaces B: Biointerfaces* **2022**, *218*, 112728.